LOW-K MATERIALS ENGINEERING FOR 10 NM TECHNOLOGY NODE AND BEYOND

Mikhail Krishtab

Supervisor(s):
Prof. Dr. Stefan De Gendt
Prof. Dr. Rob Ameloot

Members of the Examination Committee:
Prof. Dr. Steven De Feyter
Prof. Dr. Pascal Van Der Voort
Dr. Silvia Armini
Dr. Jean-Francois de Marneffe
Prof. Dr. Annelies Delabie, chair

Dissertation presented in partial fulfilment of the requirements for the degree of Doctor of Science.

In collaboration with: Imec vzw
Kapeldreef 75, 3001 Leuven, Belgium

November 2022

© 2022 KU Leuven – Faculty of Science
Uitgegeven in eigen beheer, Mikhail Krishtab, Leuven, België

Alle rechten voorbehouden. Niets uit deze uitgave mag worden vermenigvuldigd en/of openbaar gemaakt worden door middel van druk, fotokopie, microfilm, elektronisch of op welke andere wijze ook zonder voorafgaandelijke schriftelijke toestemming van de uitgever.

All rights reserved. No part of the publication may be reproduced in any form by print, photoprint, microfilm, electronic or any other means without written permission from the publisher.

Preface

The PhD research has been an integral and substantial part of my life for many years. These were years filled with exciting experiments, thrilling ideas and hypotheses, thought-provoking discussions, fruitful collaborations, and everyday learning. I had the privilege to meet a lot of talented and passionate people who in one way or another shaped my views and helped me to become the researcher I am now.

It would be impossible to count all the people who contributed to my PhD research and beyond. Nonetheless, I would like to highlight a few people without whom I would not have had a chance to obtain an honorable PhD title in a renowned EU university.

First of all, I am deeply thankful to Prof. Mikhail Baklanov, who believed in me and supported me since my first steps on the Belgian ground in April 2010 as an internship student. My truly accidental appearance at imec at that moment and the support I received there was a turning point in my whole life. I am also very grateful to Silvia Armini and Jean-Francois de Marneffe for their passionate supervision of my research.

The completion of my PhD would be impossible without the patient guidance of Prof. Stefan De Gendt, whose advice helped me to pass such critical steps of every successful PhD research as publishing research papers, thesis writing and eventually defending it.

Prof. Rob Ameloot whose research group I was honored to join at the final phase of my PhD research is another person to whom I am profoundly grateful. The change in the research environment allowed me to experience better the dynamics and livelihood of the university research. Working in his group let me explore the new research dimensions not easily accessible at imec such as the design and construction of custom experiment set-ups and

performing experiments at synchrotron facilities. I do also greatly appreciate Rob's wise guidance and support of my research initiatives.

A lot more colleagues and friends from imec and KU Leuven should be mentioned here. If you are reading this preface part, you are very likely one of them. Thank you!

Finally, I would like to thank my parents and Alisa for believing in my ability to defend the thesis even after the sometimes frustrating multi-year delay.

Mikhail Krishtab Leuven, November 2022

Summary

A simple and yet indispensable part of every microelectronics chip is a multi-level wiring (interconnect) system built on top of the semiconductor device layer. This system is responsible for signal transmission between functional nodes of an integrated circuit. While in the early days of microelectronics the IC performance was largely defined by the operational speed of the devices built within the semiconductor surface, the decades of exponential increase in the device density led to the situation where the signal propagation delay became comparable to the device switching rate thus limiting the overall computational performance of a chip. Moreover, the electrical interconnects are responsible for more than 50% consumption of the total power in today's microprocessor which poses a great challenge for energy-efficient computation, like in handheld devices.

There are multiple innovative solutions being developed for the alleviation of the above interconnect challenges at different levels starting from the system level and going down to the materials level, which compose the on-chip interconnects – metals and dielectrics. The seminal transition from a traditional metallization scheme based on Al and SiO_2 to a damascene processing featuring more conductive Cu metal and less polarizable low-k dielectrics occurred in the late 90s. While Cu is still a metal of choice in today's most advanced interconnects, no single low-k dielectric material can be termed as a universal insulation solution. The long list of sometimes self-contradicting requirements for an optimal low-k dielectric in combination with multiple diverse classes of dielectric materials led to extensive research ranging from simple evaluation of new material candidates to exploration of novel material integration schemes.

The current work explores two classes of low-k dielectrics – spin-on organosilica glasses (SOG) and metal-organic frameworks.

The porous SOGs have been under evaluation since the beginning of nillies, but the early versions failed to compete with analogous PECVD SiOCH dielectrics. Only when the highly porous ultra-low-k dielectrics with k-values below 2.5 were considered, the SOGs got a second chance thanks to the possibility to fine-tune the composition of organosilica matrix and to better control over the pore structure compared to the PECVD analogs. As SOG materials can be considered a relatively mature class of dielectrics, the full spectrum of material properties as well as their integration into a damascene metallization layer has been explored.

Since one of the key properties of low-k dielectrics is the balance between k-value and mechanical strength, the effects of pore structure as well as of the organosilica matrix composition on Young's modulus and cohesion strength have been studied in SOGs. The pore structure was modulated by exchanging the type of polyethylene oxide (PEO)-based surfactant used as a porogen in the original sol solution. Similarly, the composition of the organosilica backbone was adjusted by adding to the sol various organosilica esters including carbon chains in the form of terminal or bridging functional groups. The analysis of porosity and pore size distribution of the prepared SOGs by ellipsometric porosimetry along with the characterization of mechanical properties by nanoindentation and 4-point-bending test allowed concluding on the importance of reduced pore dimensions for enhancement in material's crack resistance. The same set of evaluation techniques complemented with quantitative IR-spectroscopy analysis was used to demonstrate the key role of matrix connectivity in the improvement of the material's Young's modulus and fracture toughness.

Besides the k-value and mechanical properties, one of the key intrinsic parameters of a low-k dielectric is its ability to resist the charge transfer, which adds up to the chip power consumption and is largely responsible for the electrical reliability failure. One of the contributions to the leakage current in porous organosilica materials are residues from the sacrificial organic phase,

which is particularly difficult to eliminate in the case of typical PECVD SiOCH dielectrics. The analysis of the PEO-based surfactant thermal decomposition in the porous SOG dielectric under study clearly showed that incomplete removal of the surfactant results in increased leakage current associated with carbon-based defect states in the dielectric's band gap. In turn, the combination of thermal annealing with successive UV-curing allows not only to shorten the SOG material preparation time due to the accelerated sacrificial carbon removal but also results in a residue-free organosilica backbone with improved insulating properties.

The integration of highly porous SOG dielectrics in on-chip interconnects is associated with multiple challenges related to undesirable in-diffusion of processing gases/liquids, plasma species, or interfacial materials inside the porous network. Such in-depth modification of low-k dielectrics results in the integration of a dielectric material with noticeably degraded electrical properties. In the scope of this work, the concept of using surfactant residues for the protection of the organosilica backbone has been explored with respect to plasma-induced damage during SOG material etching and to the damage caused by the formation of continuous PVD TaN/Ta metal barrier. It has been shown that retention of the organic template residues uniformly distributed throughout the porous layer enables damage-free plasma etching and helps to achieve pore sealing with thinner PVD metal barriers. The successive single damascene integration study further demonstrated the applicability of the proposed template residue-based protection strategy.

Another category of low-k dielectric materials studied in this work are zeolitic imidazolate frameworks (ZIFs), a sub-class of metal-organic frameworks (MOFs) exhibiting exceptionally high thermal and chemical stability. Unlike organosilica dielectrics, the research on MOFs as low-k dielectrics is still in its infancy, and the majority of the published work focuses on the assessment of intrinsic dielectric properties of various MOFs. The current work makes a step forward by additionally evaluating the integration

of ZIF-8 and ZIF-67 materials in on-chip interconnects. The central spot in the proposed integration scheme belongs to a novel MOF-CVD deposition process which consists in the solvent-free conversion of metal oxide in the respective MOF layer. The conversion of a metal oxide precursor layer deposited over a pre-formed pattern demonstrated the seamless filling of narrow trenches with the crystalline ZIF-8/ZIF-67 dielectric. The good balance of k-value and Young's modulus of ZIF dielectrics (on par with traditional organosilica dielectrics) in combination with the good gap-filling performance makes ZIF dielectrics appealing for integration into ruthenium-based metallization where Ru pattern is formed before the insulation layer.

To summarize, the performed research demonstrates that both porous spin-on organosilica glasses and metal-organic frameworks can provide a viable alternative to PECVD SiOCH low-k dielectrics used in the modern on-chip interconnects. The precise control over the backbone composition and the pore volume distribution in porous SOGs allows the preparation of coatings with superior mechanical properties. At the same time, the controlled decomposition of the sacrificial porogen phase in SOGs allows a sizable reduction in the integration-induced damage thus enabling the incorporation of highly porous dielectrics in the classical damascene interconnects. On the other hand, metal-organic frameworks featured with intrinsic crystallinity, microporosity, relatively high Young's modulus, and low dielectric constant have been found to be a good candidate for integration in the post-damascene interconnects where void-free gap-filling of high-aspect-ratio trenches in-between metal wires becomes an essential requirement to a low-k dielectric.

Samenvatting

Een eenvoudig en toch onmisbaar onderdeel van elke micro-elektronicachip is een meerlaags bedradingssysteem dat bovenop de laag van de actieve halfgeleider componenten (i.e. transistors, ..) is gebouwd. Dit systeem is verantwoordelijk voor de signaaloverdracht tussen functionele knooppunten van een geïntegreerde schakeling. Terwijl in de begindagen van de micro-elektronica, de IC-prestaties grotendeels werden bepaald door de actieve halfgeleider componenten die in het halfgeleideroppervlak waren gebouwd, leidden de decennia van exponentiële toename van de miniaturisatie tot de situatie waarin de signaal transmissie vergelijkbaar werd met de schakelsnelheid van de transistor, en de algemene rekenprestaties van een chip beinvloedt. Bovendien zijn de elektrische verbindingen verantwoordelijk voor meer dan 50% van het totale vermogen in de huidige microprocessor, wat een grote uitdaging vormt voor energiezuinige berekeningen.

Er worden meerdere innovatieve oplossingen beschouwd voor de bovenstaande uitdagingen op verschillende niveaus, te beginnen vanaf het systeemniveau tot de materialen die de on-chip-interconnecties vormen – zijnde metalen en diëlektrica. De baanbrekende overgang van een traditioneel metallisatieschema op basis van Al en SiO_2 naar een damasceen gebaseerde integratie met meer geleidend Cu-metaal en een minder polariseerbaar lage-k-diëlektricum vond plaats in de late jaren 90. Hoewel Cu nog steeds het metaal bij uitstek is in de meest geavanceerde interconnecties van vandaag, voldoet geen enkel lage-k diëlektrisch materiaal als een universele isolatieoplossing. De lange lijst van soms tegenstrijdige vereisten voor een optimaal lage-k diëlektricum gerelateerd aan meerdere verschillende klassen van diëlektrische materialen leidde tot uitgebreid onderzoek, variërend van eenvoudige evaluatie van nieuwe materiaalkandidaten tot verkenning van nieuwe materiaalintegratieschema's.

Het huidige werk onderzoekt twee types van low-k diëlektrica: spin-on organosilica glass (SOG) en metaal-organische structuren.

De poreuze SOG's worden sinds het begin van de nillies geëvalueerd, maar de eerste versies konden niet concurreren met PECVD SiOCH-diëlektrica. Pas wanneer de zeer poreuze ultra-low-k diëlektrica met k-waarden lager dan 2,5 in overweging werden genomen, krijgen de SOG's een tweede kans; dit dankzij de mogelijkheid om de samenstelling van de organosilica-matrix te verfijnen en aldus een betere controle over de poriestructuur te bekomenin vergelijking met de PECVD-analogen. Aangezien SOG-materialen kunnen worden beschouwd als een relatief volwassen klasse van diëlektrica, is het volledige spectrum van materiaaleigenschappen en hun integratie in een damasceen metallisatie schema onderzocht.

Omdat 1 van de belangrijkste eigenschappen van diëlektrica met lage k de balans is tussen k-waarde en mechanische sterkte, werden de effecten van poriestructuur en van de organosilica-matrixsamenstelling op Young's modulus en cohesiesterkte bestudeerd in SOG's. De poriestructuur werd gemoduleerd door het type op polyethyleenoxide (PEO) gebaseerde oppervlakteactieve porogeen materialen in de oorspronkelijke sol-oplossing uit te wisselen. Evenzo werd de samenstelling van de organosilica-matrix aangepast door aan de sol verschillende organosilica-esters toe te voegen, waaronder koolstofketens met terminale of brugvormende functionele groepen. De analyse van porositeit en poriegrootteverdeling van de bereide SOG's door ellipsometrische porosimetrie, samen met de karakterisering van mechanische eigenschappen door nano-indentatie en 4-puntsbuigtest, maakte het mogelijk om conclusies te trekken over het belang van verminderde porieafmetingen voor verbetering van de scheurweerstand van het materiaal. Dezelfde reeks evaluatietechnieken, aangevuld met kwantitatieve IR-spectroscopie-analyse, werd gebruikt om de sleutelrol van

matrixconnectiviteit bij de verbetering van de Young's modulus en breuktaaiheid van het materiaal aan te tonen.

Naast de k-waarde en mechanische eigenschappen, is een van de belangrijkste intrinsieke parameters van een diëlektricum met lage k het vermogen om de ladingsoverdracht te weerstaan, wat het stroomverbruik van de chip bepaalt en grotendeels verantwoordelijk is voor het falen van de elektrische betrouwbaarheid. Een van de bijdragen aan de lekstroom in poreuze organosilicamaterialen zijn de residuen van de sacrificiele organische fase, die bijzonder moeilijk te elimineren is in het geval van typische PECVD SiOCH-diëlektrica. De analyse van de op PEO gebaseerde thermische degradatie van oppervlakteactieve stoffen in het onderzochte poreuze SOG-diëlektricum toonde duidelijk aan dat onvolledige verwijdering van de oppervlakteactieve stof resulteert in verhoogde lekstroom geassocieerd met op koolstof gebaseerde defect niveaus in de band structuur van het diëlektricum. De combinatie van thermische behandelingmet opeenvolgende UV-uitharding zorgt er op zijn beurt voor dat niet alleen de voorbereidingstijd van het SOG-materiaal wordt verkort vanwege de versnelde verwijdering van de organische fase, maar resulteert ook in een residuvrije organosilica-ruggengraat met verbeterde isolerende eigenschappen.

De integratie van zeer poreuze SOG-diëlektrica in on-chip-interconnecties gaat gepaard met meerdere uitdagingen die verband houden met ongewenste diffusie van precursor gassen/vloeistoffen, plasmaspecies, e.d.m.binnen het poreuze netwerk. Een dergelijke wijziging van diëlektrica met lage k resulteert in de integratie van een diëlektrisch materiaal met merkbaar verslechterde elektrische eigenschappen. In het kader van dit werk is het concept van het gebruik van residuen van oppervlakte actieve stoffen voor de bescherming van de organosilica-ruggengraat onderzocht, specifiej met betrekking tot plasma-geïnduceerde schade tijdens het etsen van SOG-materiaal en de schade veroorzaakt door de vorming van een continue PVD TaN/Ta-metaalbarrière. Het is aangetoond dat retentie van de organische

templateresiduen die gelijkmatig over de poreuze laag zijn verdeeld, schadevrij plasma-etsen mogelijk maakt. Dithelpt bij het bereiken van porieafdichting met dunnere PVD-metalen barrières. De opeenvolgende enkelvoudige damasceen integratiestudie toonde verder de toepasbaarheid van de op templateresiduen gebaseerde beschermingsstrategie aan.

Een andere categorie van diëlektrische materialen die in dit werk als lage-k diëlektrische kandidaten worden bestudeerd, zijn zeolitische imidazolaat structuren (ZIF's), een subklasse van metaal-organische structuren (MOF's) die een uitzonderlijk hoge thermische en chemische stabiliteit vertonen. In tegenstelling tot organosilica-diëlektrica staat het onderzoek naar MOF's als low-k-diëlektrica nog in de kinderschoenen, en het grootste deel van het gepubliceerde werk richt zich op de beoordeling van intrinsieke diëlektrische eigenschappen van verschillende MOF's. Het huidige werk maakt een stap voorwaarts door bovendien de integratie van ZIF-8- en ZIF-67-materialen in on-chip-interconnecties te evalueren. De centrale plek in het voorgestelde integratieschema behoort tot een nieuw MOF-CVD-depositieproces dat bestaat uit de oplosmiddelvrije omzetting van metaaloxide in de respectieve MOF-laag. De conversie van een metaaloxide-precursorlaag afgezet over een voorgevormd patroon toonde de naadloze vulling van smalle geulen met het kristallijne ZIF-8/ZIF-67 diëlektricum aan. De goede balans van k-waarde en Young's modulus van ZIF-diëlektrica (vergelijkbaar met traditionele organosilica-diëlektrica) in combinatie met de goede vullende prestaties maakt ZIF-diëlektrica aantrekkelijk voor integratie in op ruthenium gebaseerde metallisatie schema's waar het Ru-patroon wordt gevormd vóór de isolatielaag .

Samenvattend toont het uitgevoerde onderzoek aan dat zowel poreuze spin-on organosilica-materialen als metaal-organische structuren een levensvatbaar alternatief kunnen bieden voor PECVD SiOCH low-k-diëlektrica die worden gebruikt in de moderne on-chip-interconnecties. De nauwkeurige controle over de samenstelling van de ruggengraat en de

verdeling van het porievolume in poreuze SOG's maakt de bereiding van coatings met superieure mechanische eigenschappen mogelijk. Tegelijkertijd maakt de gecontroleerde ontleding van de sacrificiele porogeenfase in SOG's een aanzienlijke vermindering van de door integratie geïnduceerde schade mogelijk, waardoor de opname van zeer poreuze diëlektrica in de klassieke damascene-interconnecties mogelijk wordt. Aan de andere kant bleken metaal-organische structuren met intrinsieke kristalliniteit, microporositeit, relatief hoge Young's modulus en lage diëlektrische constante een goede kandidaat te zijn voor integratie in de post-damasceen interconnecties waar conformele en volledige vulling van hoge -aspect-ratio structuren tussen metaaldraden een essentiële vereiste is voor een low-k diëlektricum oplossingen.

List of abbreviations

3MS	Trimethyl-silane
4MS	Tetramethyl-silane
4PB	4-point bending
AC	Alternating current
AFM	Atomic-force microscopy
ALD	Atomic-layer deposition
APM	Ammonia-peroxide mixture
ASD	Area-selective deposition
BEOL	Back-end-of-line
BTESE	1,2-bis-trialkoxysilyl-ethane
CCP	Capacitively coupled plasma
CMOS	Complementary metal-oxide-semiconductor
CMP	Chemical mechanical polishing
CSM	Continuous stiffness measurement
CTAB	Cetyltrimethylammonium bromide
CV	Capacitance-Voltage
CVD	Chemical vapor deposition
DC	Direct current
DCB	Double-cantiliver beam
DD	Dual-damascene
DEMS	Diethoxy-methyl-silane
DEZ	Diethyl zinc
DFT	Density functional theory
DIW	Deionized water
DMDMOS	Dimethyl-dimethoxy-silane
DMDOSH	Dimethyl-dioxysilyl-cyclohexane
DMOMS	Dimethoxy-methyl-silane

DMPCSO	Decamethyl-cylo-pentasiloxane
DMPS	Dimethyl-phenyl-silane
ECD	Electrochemical deposition
EDL	Equivalent damage layer
EDS	Energy dispersive x-ray spectroscopy
EISA	Evaporation-induced self-assembly
EP	Ellipsometric porosimetry
EPC	Effective porogen control
ESR/EPR	Electron spin resonance / Electron paramagnetic resonance
FEOL	Front-end-of-line
FIB	Focused ion beam
FSG	Fluorosilica glass
FTIR	Fourier transform infrared spectroscopy
GI-XRD	Grazing incidence X-ray diffraction
GND	Grounded contact
HAADF	High-angle annular dark field
HB	Hard-bake
HF	Hydrofluoric acid
HM	Hard-mask
HMCTSO	Hexamethyl-cyclo-trisiloxane
HOMO	Highest occupied molecular orbital
IC	Integrated circuit
ICP	Inductively coupled plasma
IPE	Internal photoemission spectroscopy
IR	Infrared frequency range of electromagnetic waves
IRMOF	Isoreticular MOFs (MOF sub-class)
ITRS	International Technology Roadmap for Semiconductors

IV	Voltage-Current
LPSA	Liquid phase self-assembly
LUMO	Lowest unoccupied molecular orbital
MIM	Metal-Insulator-Metal stack
MIS	Metal-Insulator-Semiconductor stack
MOF	Metal-organic frameworks
MOF-CVD	Solvent free MOF depostiion approach
MSQ/MSSQ	Methyl silsesquioxane
MTES	Methyl-triethoxy-silane
MTMS	Methyl-trimethoxy-silane
MW	Molecular weight
NI	Nanoindentation
OCS	Oxycarbosilane material
OMCTS	Octamethyl-cyclo-tetrasiloxane
OSG	Organosilica glass
P4	Post porosity plasma protection
PE	Polyethylene
PEALD	Plasma-enhanced atomic-layer deposition
PECVD	Plasma-enhanced chemical vapor deposition
PEG	Polyethylene glycol
PEO	Polyethylene oxide
PETR	Post-etch template removal
PMMA	Poly(methyl methacrylate)
PMO	Periodic mesoporous organosilica
PSZ	Pure silica zeolites
PVD	Physical vapor deposition
RBS	Rutherford backscattering scpectroscopy
RC	Resistance-Capacitance
RF	Radiofrequency

RI	Refractive index
RMS	Root-mean square
SB	Soft-bake
SD	Single-damascene
SE	Spectroscopic ellipsometry
SEM	Scanning electron microscopy
SHE	Safety, health and environment
SiOCH	Carbon-doped oxide deposited via PECVD
SOG	Spin-on glass
STEM	Scanning transmission electron microscopy
TEM	Transmission electron microscopy
TEOS	Tetraethyl orthosilicate
TMCTS	Tetramethyl-cyclo-tetrasiloxane
TOF-SIMS	Time-of-flight secondary ion mass-spectroscopy
TVTMCTS	Tetravinyl-tetramethyl-cyclo-tetrasiloxane
ULK	Ultra-low-k dielectric (k-value < 2.5)
ULSI	Ultra-large scale integration
UV	Ultraviolet
UV-VIS	Electromagnetic wave frequency range corresponding to ultraviolet and visible light
VUV	Vacuum ultraviolet
XPS	X-ray photoelectron spectroscopy
XRD	X-ray diffraction
YM	Young's modulus
ZIF	Zeolitic imidazolate frameworks

List of symbols

k	Dielectric constant (k-value)
k_{eff}	Effective k-value
ε_0	Vacuum permittivity, F/m
G_c	Energy release rate, J/m^2
d	Film thickness
ρ	Metal resistivity
L	Metal wire length
W	Metal wire width
V	Voltage
I	Current
J	Current density
f	Clock frequency
α	Device activity factor
C	Capacitance
R	Resistance
$\mathbf{E}$	Electric field
$\mathbf{P}$	Polarization
$\boldsymbol{\mu}$	Permanent dipole moment
α_e	Electronic polarizability
α_i	Ionic polarizability
Y	Quantum yield
P	Porosity
P_μ	Microwave power
$\langle r \rangle$	Mean connectivity parameter
$A(k_i)$	Absorbance at wavenumber k_i
D	Dissipation factor
λ	Wavelength

g	g-factor
B	Magnetic field
C_{db}	Carbon dangling bonds (type of EPR defect)
P_{b0}	Dangling Si-bond at the Si/SiO_2 interface (type of EPR defect)
S_1	Singlet state
T_1	Triplet state
$h\nu$	Photon energy
ΔG	Gibbs free energy of a reaction
ΔH	Enthalpy of a reaction
Δ, ψ	Ellipsometric angles
C_{db}	Carbon dangling bonds (type of EPR defect)

Table of contents

Preface 2
Summary 4
Samenvatting 8
List of abbreviations 14
List of symbols 18
Table of contents 20
Chapter 1. Introduction 24
  1.1 Advanced on-chip interconnects 24
    1.1.1 Interconnects performance 26
    1.1.2 Interconnects fabrication routes 31
  1.2 Low-k dielectric materials 37
    1.2.1 Low-k dielectric materials: definition and requirement 37
    1.2.2 Historical view on low-k dielectrics 43
    1.2.3 Perspective low-k dielectrics 52
  1.3 Scope of the work 56
Chapter 2. Materials and methods 58
  2.1 Synthesis of low-k dielectrics under study 58
    2.1.1 Self-assembly based organosilica dielectrics. 58
    2.1.2 Zeolitic imidazolate frameworks. 60
  2.2 Low-k dielectrics characterization 63
Chapter 3. Self-assembly based organosilica spin-on low-k dielectrics 72
  3.1. Chapter introduction 72
  3.2 Correlation between pore dimensions and cohesion strength 76
    Abstract 76
    3.2.1 Introduction 76
    3.2.2 Experimental details 77
    3.2.3 Results and discussion 78

3.2.4 Conclusions 83
3.3 Impact of linking and terminal organic groups on mechanical properties of self-assembly based low-k dielectrics 84
Abstract 84
3.3.1 Introduction 84
3.3.2 Experimental details 86
3.3.3 Results and discussion 87
3.3.4 Conclusions 101
3.4 Leakage Current induced by Surfactant Residues in Self-assembly based Ultra Low-k Dielectric Materials 104
Abstract 104
3.4.1 Introduction 104
3.4.2 Experimental details 106
3.4.3 Results and discussion 107
3.4.4 Conclusions 116
3.5 Surfactant residues as protective coating against plasma-induced low-k damage 118
Abstract 118
3.4.1 Introduction 119
3.4.2 Template management strategy 125
3.4.3 Plasma-induced damage mitigation 131
3.4.3.1 Ar/SF_6 plasma 132
3.4.3.2 Ar/CF_4 plasma 138
3.4.4 VUV radiation-induced damage 142
3.4.5 Conclusions 149
3.6 Metal barrier induced damage in self-assembly based organosilica low-k dielectrics and its reduction by organic template residues 152
Abstract 152
3.6.1 Introduction 152
3.6.2 Experiment details 154

3.6.3 Results and discussion 157
3.6.3.1 PVD TaN/Ta barrier damage in template-free low-k dielectric 157
3.6.3.2 PVD TaN/Ta barrier damage in low-k dielectric with template residues 164
3.6.3.3 Damascene integration using template residue retention .. 168
3.6.4 Conclusions.. 178
3.7 Chapter summary 180

Chapter 4. Zeolitic imidazolate frameworks as low-k dielectrics 182
4.1. Chapter introduction.. 182
4.2 Vapor-deposited zeolitic imidazolate frameworks as gap-filling ultra-low-k dielectrics 184
Abstract.. 184
4.2.1 Introduction.. 184
4.2.2 Experiment details 188
4.2.3 Results and discussion 193
4.2.4 Conclusions.. 204
4.3. Chapter summary 205

Chapter 5. General conclusions and outlook 206
5.1 General conclusions 206
5.2 Outlook.. 209

Appendix A 212
Supporting information for Chapter 3.6 212
Supporting information for Chapter 4.2 220

Appendix B.. 232
Safety, Health and Environment (SHE) 232

Scientific activity.. 234
Bibliography.. 242

Chapter 1. Introduction

This chapter provides an overview of the on-chip interconnects structure and its performance link to the properties of constituting materials. The chapter gives a definition of low-k dielectrics, describes the previous and current generations of low-k materials, and highlights the potential material candidates for future integration into the interconnects.

1.1 Advanced on-chip interconnects

Every chip residing in our mobile devices, wearables, cars, *etc*. has a complex yet modular architecture the core of which consists of rather simple active and passive components formed at the surface of a semiconductor crystal. The concept of building devices on a surface of a semiconductor single crystal was conceived in the early 60s and has been evolving ever since.[1,2]

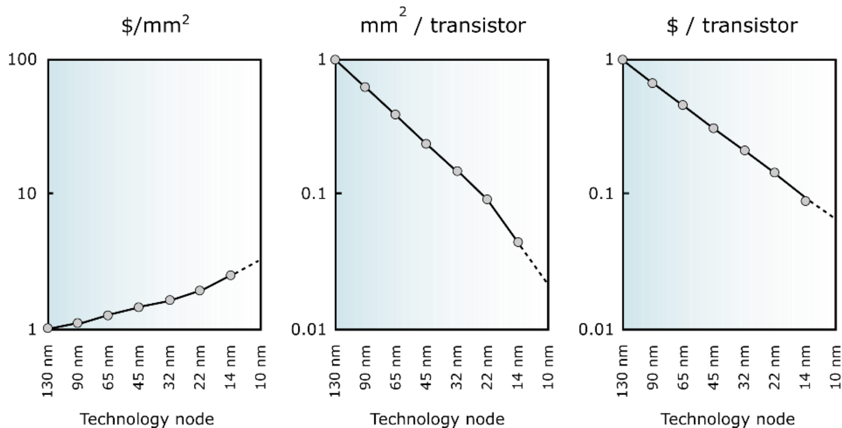

Figure 1.1. The economic driver behind Moore's law. The impact of down-scaling on the cost of a fabricated wafer, on the area per transistor, and the cost of a single transistor. The prices are normalized. Adapted from Intel's keynote presentation "Moore's Law at Fifty: No End in Sight" at DAC2015.

The rapid evolution of ICs in the form of geometrical down-scaling of device components was catalyzed by a win-win situation for both society as well as for the companies advancing the field (Figure 1.1).[3,4] On one hand, packing more transistors per 1 mm^2 allows semiconductor companies to generate more profit per silicon wafer. On the other hand, this continuous increase in the transistor's density every technology node makes electronics more affordable. The latter additionally leads to the expansion of microelectronics products to new market niches. As a result, over the past decades, semiconductor technology became one of the most critical resources of today's information-centered society.

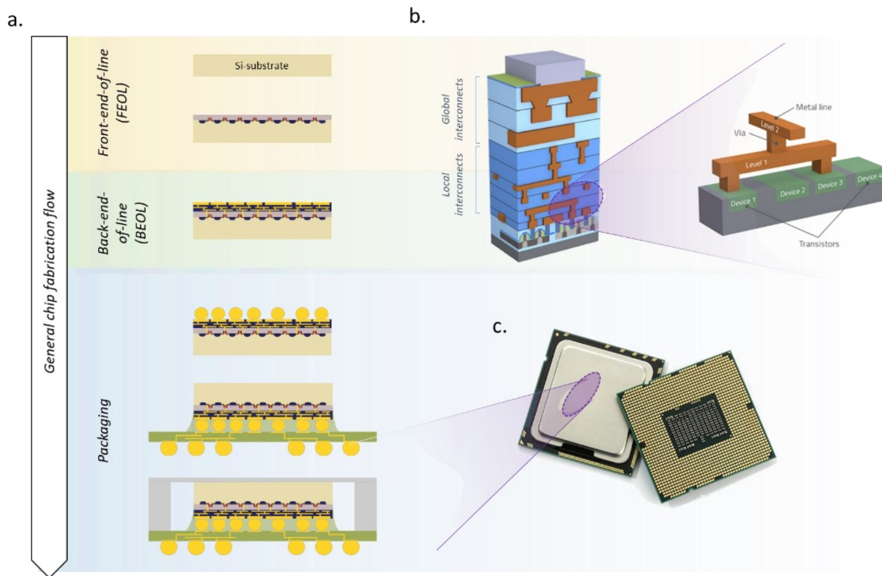

Figure 1.2. Fabrication of IC chip and its structure: (a) general chip fabrication steps starting from a silicon wafer; (b) schematic representation of the IC on-chip cut-out featuring FEOL and BEOL parts; (c) Fully packaged IC chip.

The fabrication cycle of a modern IC chip typically includes three consecutive processing stages (Figure 1.2):

1) *Front-end-of-line* (FEOL) processes are responsible for the formation of a device layer at the surface of a semiconductor wafer.
2) *Back-end-of-line* (BEOL) processes are aimed to construct on-chip interconnects connecting the devices into functional electric circuits with the fabrication of multiple metallization layers (metal wiring levels vertically connected by vias). The stack is finalized with the formation of bond pads on top.
3) *Chip packaging* consists in the formation of solder bumps and the attachment of a chip to an interposer layer. Alternatively, chips could also be stacked before they are placed on the interposer. The assembly is then encapsulated into a resin or is covered with a metallic cover allowing better heat dissipation (Figure 1.2c).

Despite the conceptual simplicity of on-chip interconnects the only role of which is to ensure the propagation of signal (digital “1”’s and “0”’s) between functional units, the scale at which the wiring should be implemented to be consistent with the continuously increasing device density makes the task far from trivial. As the number of transistors per 1 cm^2 in modern logic chips amounts to billions, the total wire length reaches several kilometers.[5] This creates multiple down-scaling challenges such as signal propagation delays, increased power consumption, and signal reliability. These key metrics are directly linked to the performance of on-chip interconnects.

1.1.1 Interconnects performance

The performance of on-chip interconnects can be associated with the three following circuit parameters – signal propagation latency, cross-talk

noise resistance, and power consumption. The next paragraphs highlight the link of these key parameters to the properties of the insulation medium.

RC-delay. The functioning of ICs assumes communication of various circuit nodes between each other via charging/discharging of the wiring connecting them. The time required for this process is defined by the product of line resistance (*R*) and capacitance (*C*). To roughly assess this parameter, it is helpful to simplify the interconnects structure as proposed by Bohr (Figure 1. 3a).[6] The model considers a cross-section of generalized interconnects consisting of conductive lines surrounded by an insulator. Then the resistance and capacitance can be defined as:

$$R = \frac{\rho L}{T_L W} \tag{1.1}$$

$$C = 2(C_L + C_{IL}) = 2k\varepsilon_0 L\left(\frac{T_L}{S} - \frac{W}{T_{IL}}\right) \tag{1.2}$$

where ρ – metal resistivity, k - dielectric constant of the insulation media, L – length, T_L – height/thickness, W – width of the metal wire, S and T_{IL} – the distance between the metal line and metallization layers, respectively.

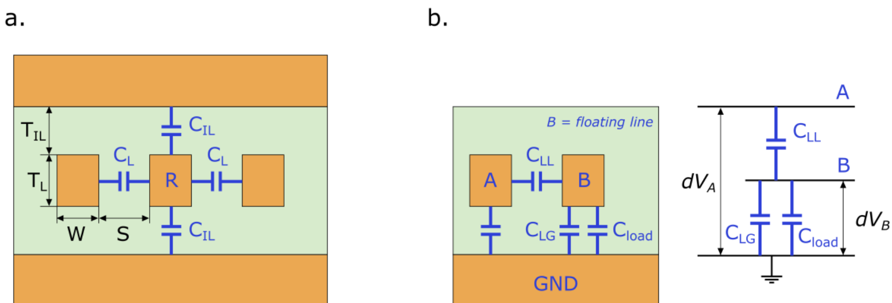

Figure 1.3. Simplified equivalent circuit of a single interconnects layer used for estimation of (a) RC-delay, (b) cross-talk noise.

As follows from the above equations, the RC-delay is a function of intrinsic material characteristics such as metal resistivity and the insulator's k-value as well as interconnects geometry. With the increase of transistor density, the lateral dimensions *W* and *S* shrink which results in higher *R* and *C*. This becomes critical when the signal propagation delay in the interconnects exceeds the delay associated with transistor switching (gate delay) since at this point the overall chip performance is limited by the on-chip interconnects. Such crossover point occurred in chips built under 250 nm technology node (Figure 1.4).

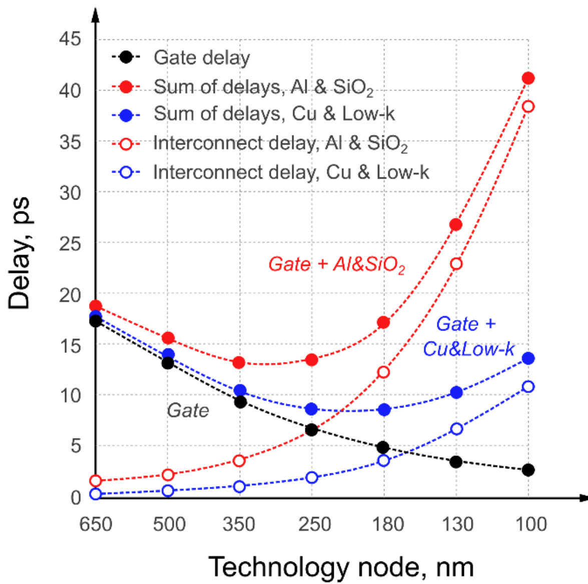

Figure 1.4. Signal propagation delay in interconnects featuring different metal/dielectric combinations in comparison with gate delay for various technology nodes.

There are several ways to address the issue at the material and system levels. On the system level, the interconnects delay can be reduced by the introduction of repeaters, which effectively shorten the wire length.[7] On the material level, metals with lower resistivity and dielectrics with lower k-value need to be introduced.

The traditionally used aluminum wiring was replaced with copper metallization in the late 90s.[8] As the metal wire dimensions approach 20 nm, the effective resistivity of copper drastically increases as compared to the bulk value due to enhanced electron scattering at the interfaces. Moreover, the barrier layer encapsulating copper wires occupies additional conductor volume thus worsening the confinement effect on resistivity. This made alternative metals such as ruthenium and molybdenum considered for integration in the future technology nodes.[9–11]

The original SiO_2 insulation was replaced by materials with lower dielectric constant, so-called low-k dielectrics.[12–14] A wide range of materials has been tested over the last two decades as candidates for integration into on-chip interconnects. Nonetheless, only silica-based dielectrics have been used in commercial chips so far. The originally very optimistic ITRS roadmap outlining the pace of effective k-value down-scaling (Figure 1.5) needed to be revised several times due to numerous integration challenges discussed in p. 1.1.2. The red zone in the ITRS 2013 roadmap highlighting the range of k-values below 2.4 which could not be achieved in fully integrated interconnects test vehicles is largely valid up to these days.

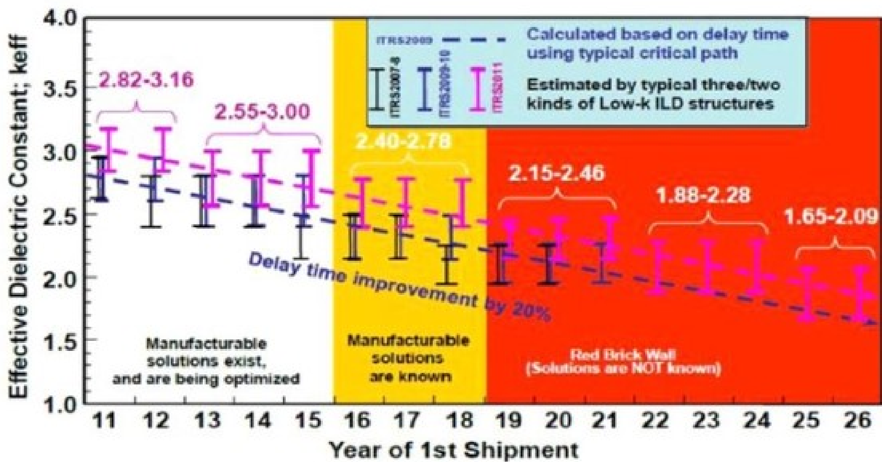

Figure 1.5. The pace of k-value down-scaling in low-k materials according to ITRS roadmap (ITRS 2013 Edition for Interconnect).

Crosstalk noise. The crosstalk noise in interconnects is associated with partial charging of neighboring wires due to capacitive coupling between them.[15,16] Using a simplified interconnects block and corresponding equivalent circuit featuring two wires A (charged) and B (floating) in Figure 1. 3b, one can define the voltage drop ΔV_B on the wire B induced by voltage change ΔV_A on wire A:

$$\Delta V_B = \frac{C_{LL}}{C_{LL} + C_{LG} + C_{load}} \Delta V_A \tag{1.3}$$

where C_{LL} is the interline capacitance, C_{LG} is the capacitance of the metal line with respect to the ground (GND) and C_{load} is the output capacitance of the transistor.

Based on equation 1.3., the crosstalk noise is proportional to the interline capacitance which in turn linearly scales with the dielectric constant of the insulation media. Besides the introduction of the low-k materials, the cross-talk noise can be also reduced by appropriate adjustment of the interconnects geometry.

Power consumption. The power consumption of an IC chip is a critical parameter given the demand for portable devices, issues with excessive heat management, and environmental concerns. CMOS chips may have two contributions to power consumption – dynamic power and static power.[17] The static power consumption is associated with device imperfections such as various leakage sources (e. g. leakage between wires in on-chip interconnects). The dynamic power P_{dyn} is the power related to the actual functioning of the chip and is consumed during the charging and discharging of appropriate nodes in the CMOS circuit every clock cycle. It can be approximated by the following expression:

$$P_{dyn} = \frac{1}{T}\int_0^T iVdt = \frac{V}{T}\int_0^T idt = V\frac{Q}{T} = \alpha C V^2 f \tag{1.4}$$

where V is the power supply voltage, f is the clock frequency, C is the capacitance associated with the switching circuit node and α is the activity ratio taking into account the fact that the device switching doesn't happen every clock cycle. From the above expression, one can see that the power consumption of a CMOS chip can be reduced not only by going to the lower voltage and frequencies (i. e. by lowering the chip performance) but also by reducing the capacitive load. Therefore, from the interconnects materials perspective, the lower power consumption can be achieved by the integration of dielectrics with intrinsically low leakage current and low k-value.

1.1.2 Interconnects fabrication routes

The fabrication of on-chip interconnects represents a cyclic process flow. During each cycle, a single metallization layer consisting of wire and via levels is constructed.

Aluminum-based interconnects. For a long time since the invention of ICs, the wiring above the silicon surface was made of aluminum surrounded by silicon oxide. At these first technology nodes with just a couple of metallization layers, the processes were relying on the conformal deposition of SiO_2 and etching of Al in the pre-defined locations. As the number of the metallization layers has been increasing, the process experienced two major innovations: 1) the addition of planarization steps after fabrication of each via and wire levels by newly developed chemical-mechanical polishing process (CMP)[18] and 2) the introduction of tungsten plugs (or vias) connecting the aluminum wires in the adjacent metallization layers.[19] The planarized topography of the layers helped to mitigate the pattern placement reliability and depth-of-focus limitations in advanced lithography. The CVD W process enabled seamless gap-filling of high-aspect-ratio contact plugs (> 3:1) thus reducing the parasitic capacitance between the adjacent wiring levels. The integration of tungsten was accompanied by the development of the first

damascene process, i. e. a process during which the excess of metal is deposited within the pattern formed in a dielectric layer with the overburden being removed at later stages. The latter was realized by a CMP process. Besides tungsten, Ti/TiN adhesion/diffusion barrier layer was introduced at the interface between Al and W.[20] The example of such metallization is shown in Figure 1.6 as Al.1.

Copper-based interconnects. Despite the introduced changes, more significant modification of the integration scheme and the material base was urged by the rising RC-delay concerns, poor electromigration performance of Al, and high production costs. Among potential metal candidates, copper Cu looked like a reasonable choice accounting for its ~30% lower bulk resistivity and better resistance to electromigration.[21] However, the introduction of copper could not be achieved by a simple replication of the Al technology due to two major Cu integration-related drawbacks namely 1) the difficulty of Cu etching in plasma at low temperatures and 2) the high diffusivity of Cu in SiO_2 and Si. Cu atoms form deep acceptor levels in the bandgap of Si crystal thus reducing the minority carrier lifetime and increasing the junction leakage current.[22] Both issues have been addressed in a dual-damascene process for Cu-metallization developed by IBM in 1998.[8] As can be seen in Figure 1.6, the process extended the damascene concept originally proposed for W vias to copper, which was deposited by electroplating simultaneously at the via and wire level. This allowed to achieve more reliable interconnects with reduced resistivity and lower fabrication costs. These advantages helped the damascene approach to become an industry standard for the next generations of interconnects up until today.

Figure 1.6. Comparison of various metallization routes.

As can be seen in Figure 1.6 DD.1. the damascene process flow assumes plasma etching being applied exclusively to the dielectric with Cu being deposited via electroplating. The successive polishing process of the relatively soft Cu material was one of the major challenges overcome during the process development. As well as in the case of W, the Cu wire needed to be encapsulated. The metal and dielectric barriers encapsulating the Cu metallization are deposited to ensure that Cu doesn't diffuse to the device layer.

While the approach originally developed for SiO_2/Cu metallization was working great on dense materials, low-k dielectrics were strongly unfavored due to multiple challenges posed by the damascene processing.[23,13] The most common issues for the integration of low-k dielectrics into interconnects related to the damascene process flow are highlighted in Figure 1.7.

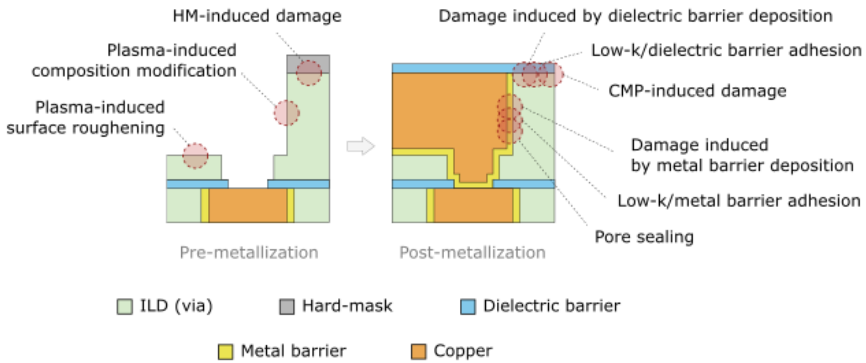

Figure 1.7. Low-k integration challenges for the dual-damascene integration scheme.

The challenges stem from the porous nature of low-k materials which makes them particularly susceptible to aggressive media such as plasma since the effect would not be limited to the surface, but would extend to the bulk of the material, especially when the dielectric spacings are relatively small (on

the order of few tens of nm). The challenges associated with plasma processing of porous dielectrics and potential solutions mitigating the plasma-induced damage are discussed in detail in p. 3.4.1. The discussion on the less explored issue with the formation of a thin continuous metal barrier layer over the surface of highly porous low-k material is provided in p. 3. 6.1.

Ruthenium-based interconnects. As copper metallization becomes less attractive at wire dimensions below 20 nm due to substantially increased resistivity, metallization routes for the integration of alternative metals such as ruthenium have been developed and are currently being considered for implementation in future technology nodes. An example of such a route is the so-called semi-damascene process flow featuring direct Ru metal etch (Figure 1.8).[24]

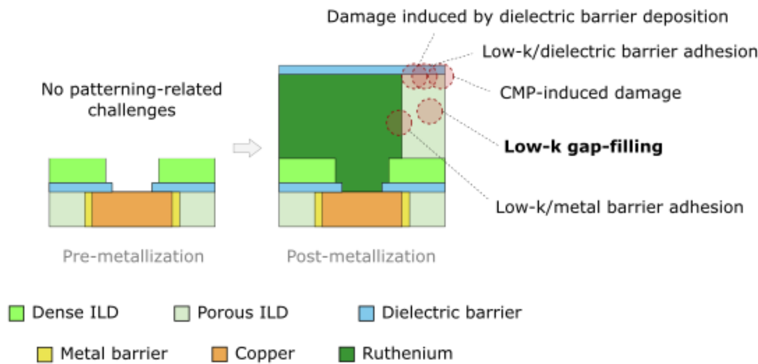

Figure 1.8. Low-k integration challenges for semi-damascene Ru metallization scheme.

In this route, the dielectric at the via level is patterned by plasma analogous to the damascene process flow. However, at the wire level, the dielectric is filling the pattern etched in Ru. This fact allows the integration of new types of low-k dielectrics which could not sustain the integration with direct exposure to patterning plasma. On the other hand, the integration scheme requires the low-k dielectric to have good gap-filling properties which

is particularly challenging for the currently used PECVD SiOCH low-k dielectrics.

Finally, one should note that more exotic low-k integration schemes have been proposed in recent years to address the pattern alignment issues. These schemes rely on area-selective deposition of low-k dielectric and also imply minimal process damage to the ULK material.[25]

1.2 Low-k dielectric materials

In this section, the definition, properties, and types of dielectrics will be considered.

1.2.1 Low-k dielectric materials: definition and requirement

Dielectric constant. The dielectric constant (k-value or relative permittivity (ε_r)) is one of the key characteristics of a material. It is defined as the ratio of the material's permittivity (ε) to the permittivity of a vacuum (ε_0) and serves as a measure of the material's polarizability:

$$k = \varepsilon_r = \frac{\epsilon}{\varepsilon_0} \tag{1.5}$$

The phenomenon of material polarization consists in the induction of charges within the dielectric medium in the presence of an external electric field.[26,27] It is characterized by a vector **P** defined as an average dipole momentum in a unit of volume. On one hand, it can be expressed via macroscopic parameters as electric susceptibility χ_e and external electric field $\mathbf{E}_e$:

$$\mathbf{P} = (k-1)\varepsilon_0\mathbf{E}_e = \chi_e\varepsilon_0\mathbf{E}_e \tag{1.6}$$

On the other hand, one can also express the polarization in terms of microscopic dipole moments **p**:

$$\mathbf{P} = N\mathbf{p} = \alpha N\mathbf{E}_i = \alpha N(\mathbf{E}_e + \mathbf{E}_{eloc}) = \alpha N\left(\mathbf{E}_e + \frac{\mathbf{1}}{\mathbf{3}\varepsilon_0}\mathbf{P}\right) \tag{1.7}$$

where α is polarizability, N is dipole density and $\mathbf{E}_i$ is the internal electric field, which besides the external field component includes an additional local field $\mathbf{E}_{loc}$ contribution created by surrounding charges. By assuming the homogeneity of the charge distribution in the material of interest, Lorentz local field proportional to the polarization is derived. Then, by equating the

above two expressions, one can obtain the Clausius-Mossotti relation explicitly linking the macroscopic dielectric constant parameter to microscopic induced polarization mechanisms:

$$\frac{k-1}{k+2}=\frac{\mathbf{1}}{\mathbf{3}\varepsilon_0}N(\alpha_e+\alpha_i) \tag{1.8}$$

The electronic (α_e) and ionic (α_i) polarization are two major intrinsic polarization mechanisms present in every dielectric medium. Electronic polarization is associated with the displacement of electron cloud with respect to atom nuclei, while ionic polarization is a result of the distortion of material's bonds under an applied electric field.

If the material contains permanent dipoles **μ**, e. g. in the form of adsorbed water or other polar molecules, they will also contribute to the material's polarizability by aligning themself along the external field. This contribution of orientational (or dipolar) polarization to the dielectric's k-value is addressed in the Debye equation:

$$\frac{k-1}{k+2}=\frac{\mathbf{1}}{\mathbf{3}\varepsilon_0}N\left(\alpha_e+\alpha_i+\frac{\mu^2}{3k_BT}\right) \tag{1.9}$$

It is important to note that polarization is a dynamic process, and each of the above polarization types has a characteristic response time to alternating electric field. As the frequency of the external field increases, the contribution of slower polarization mechanisms gets canceled which effectively reduces the dielectric constant (Figure 1. 9). For example, at UV-VIS frequencies, the dielectric constant includes only the contribution from electronic polarizability, and the k-value at these frequencies can be estimated as $\sqrt{n}$, where n is the material's refractive index. Since the typical processor clock frequency is in MHz to GHz range, all the considered polarization mechanisms contribute to the k-value and cannot be ignored during the evaluation of new low-k dielectric candidates.

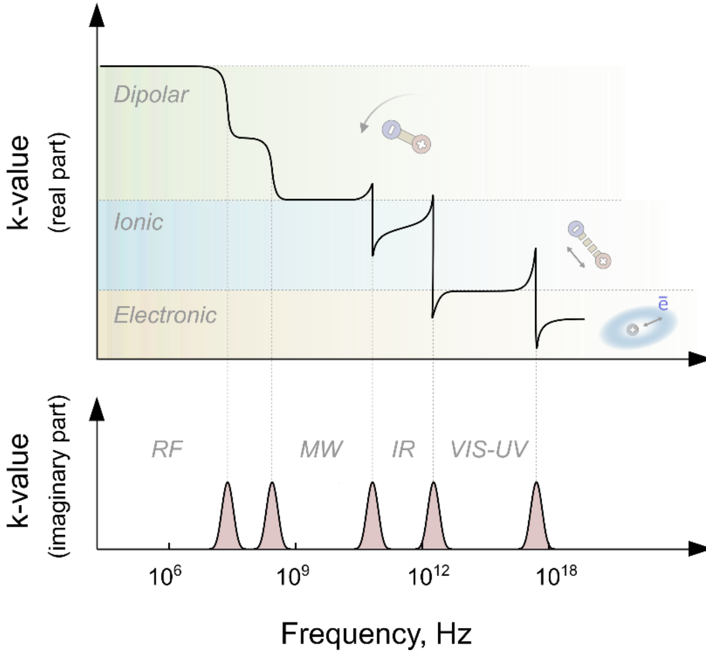

Figure 1.9. Schematic curves of the real and imaginary part of the dielectric constant of a fictive material with two orientation polarization modes and two different ionic polarization modes.

Low-k dielectrics. Silicon oxide has been an insulator of choice since the start of IC fabrication and greatly contributed to the success of silicon-based semiconductor technology. It possesses a unique combination of properties including high thermal and mechanical stability, exceptional dielectric properties, good processability, and can be deposited via a variety of different techniques (thermal, PVD, CVD, PECVD).[12,13]

The necessity to lower the dielectric constant of the insulation medium in advanced on-chip interconnects, gave rise to the search for dielectrics with k-value below that of SiO_2 (k_{SiO2} = 3.9-4.5) broadly termed as low-k dielectrics. Of course, the above definition outlines only the very first necessary condition for a dielectric material to be considered as a candidate for integration into on-chip interconnects. In practice, the dielectric needs to satisfy numerous criteria concerning the material's intrinsic properties. Four categories of desirable

material properties inspired by SiO_2 as an insulation standard are listed in Table 1. 1. Since it is difficult to find a material that would combine all the properties mentioned in the table, some of the criteria may be alleviated by optimizing the material's integration flow. Therefore, it is essential to consider the choice of low-k dielectric material in the context of the chosen metallization scheme.

Table 1.1. Desirable properties of low-k dielectric materials. The inset values show material selection criteria for ultra low-k dielectrics (k < 2.5).

Electrical	Mechanical	Chemical	Thermal
Low k-value (< 2.5)	**High Young's modulus** (> 4 GPa)	High chemical resistance	**High thermal stability** (> 350°C)
Low leakage ($< 1e{-9}$ A/cm^2)	High hardness	Low moisture adsorption	**Low thermal expansion** (~0.5 ppm/K)
Low charge trapping	Good adhesion	Low gas permeability	High thermal conductivity
High electric field strength (> 2 MV/cm)	High cohesion strength	No metal corrosion	
High reliability (t_{BD} > 10 years)	Low stress	High purity	

The Debye equation (1.9) offers two paths to scale down a material's dielectric constant namely (a) lowering the polarizability of its constituents and (b) reducing the material's density (Figure 1.10).

The first approach suggests the construction of a material from low polarizable atoms and bonds. Such atoms ideally should have a minimal

number of unbonded electrons (e. g. sulfur is less preferred than oxygen). The atoms should optimally connect via covalent sigma bonding (e. g. C-C bond has nearly three times lower polarizability compared to C=C). Additionally, it follows from the Debye equation that no polar molecules should be present in the low-k material either in chemisorbed or physisorbed form. Since the low-k dielectric gets exposed to the environment during the integration, the material's hydrophobicity is essential. The replacement of highly polarizable Si-O bonds with Si-F and Si-C in SiO_2 was the first successful strategy to obtain low-k dielectrics with k-values down to ~2.7. The corresponding fluorosilica glass (FSG) and carbon-doped oxide (SiOCH) dielectrics are discussed in p. 1.2.2 and p. 1.2.3, respectively.

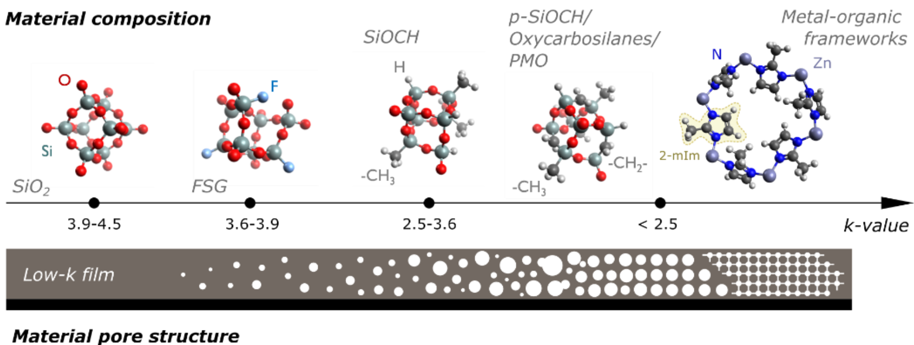

Figure 1.10. Changes in composition and pore structure of low-k materials with down-scaling of dielectric constant.

The introduction of terminal groups into the previously interconnected network of Si-O bonds in FSG and SiOCH materials also results in lower density or microporosity of the films, which additionally contributes to their lower dielectric constant. The incorporation of porosity P in the dielectric material is the most effective way to reduce the dielectric constant. Derived from the Clausius-Mossotti equation, the Lorenz-Lorentz effective medium

approximation allows to estimate the impact of porosity on the material's k-value via the following equation:

$$\frac{k_{eff}-1}{k_{eff}+2}=P\frac{k_{matrix}-1}{k_{matrix}+2}+(1-P)\frac{k_{air}-1}{k_{air}+2}=P\frac{k_{matrix}-1}{k_{matrix}+2} \quad (1.10)$$

where P is porosity, the volume fraction of air in the material, k_{eff} is the dielectric constant of porous material, k_{matrix} is the dielectric constant of the material's matrix or backbone, k_{air}= 1 is the dielectric constant of air filling the pores.[12]

The preparation of highly porous low-k materials via embedding of sacrificial phase (template, porogen) was another essential step in achieving k-values of 2.5 and below in silica-based dielectrics. Since the porosity imparts mechanical weakness, particularly above the percolation threshold found to be around 25% for the SiOCH materials, the research has been focused on optimizing the balance between the k-value and mechanical strength of porous dielectrics. The issues could be partly addressed by ordering the pore arrangement as well as by increasing the bond network connectivity via the addition of carbon in the form of bridging rather than terminal groups. These approaches are discussed in more detail in p. 3.2 and p. 3.3.

An alternative solution to the issues characteristic for highly porous carbon-doped silica dielectrics is to consider other classes of porous materials. For the last two decades, multiple classes of materials have been studied as potential ultra low-k dielectric candidates (k < 2.5) including amorphous carbons, various types of polymers, pure-silica zeolites, *etc*. However, none of the listed materials could provide enough competitive advantages compared to the more industrially mature organosilica-based analogs. So, they are omitted in Figure 1.10.

Recently a relatively novel class of porous materials, metal-organic frameworks (MOFs), gained attention as they combine intrinsic microporosity evenly distributed over the crystalline material with very low density which

compensates for the contribution of relatively high polarizability of the framework's constituents to MOF's dielectric constant. Although conceptually MOF-based dielectrics look appealing, more research is needed to address the possibility of MOF integration in on-chip interconnects.

1.2.2 Fluorosilicate glass

The fluorine-doped SiO_2, or fluorosilica glass (FSG), was the first low-k dielectric that was introduced in high-volume manufacturing in the year 2000 for chip fabrication under 180 nm technology node (k = 3.8).[13,28]

The FSG low-k films inherited PECVD film deposition method previously used for the deposition of SiO_2 coatings. The major difference is the addition of various fluorine-containing precursors (CF_4, C_2F_6, SiF_4, or $FSi(OEt)_3$, *etc.*) to the gas mixture including silicon sources (SiH_4, TEOS) and oxidizing gases (O_2. N_2O, O_3). By varying the Si/F precursor ratio, one can adjust the fluorine content in FSG films.[29]

The resulting films embed Si-F terminal groups which are responsible for the reduction of the material's dielectric constant. Although Si-F bond by itself is not less polar than Si-O, the presence of F bonded to Si modifies the effective charges associated with the normal vibration modes of nearest Si–O–Si bonding groups, which in turn lowers their ionic polarization contribution to FSG k-value.[30] Additionally, the incorporated terminal Si-F groups create micropores which effectively lowers the material's density.[29]

Although it was shown that the increase of the fluorine concentration in the precursor gas mixture allows preparing FSG dielectrics with k-values down to 2.0 and below, the FSG film tends to be unstable at F concentration above ~10%, which is expressed in moisture absorption and fluorine emission upon heating at temperatures below BEOL process temperature limit (400°C).[29,31] Therefore, only FSG dielectrics with k-values above 3.6 could be integrated into the actual ICs.

Since the typical FSG glasses are non-porous, thermally and mechanically stable (YM ~ 50 GPa), minimal changes in the standard SiO_2-based metallization process flow were necessary. The major concern was the release of fluorine by the film during the thermal cycling which was leading to metal corrosion issues.[32,33] On the other hand, FSGs also offer some advantages as compared to the regular PECVD SiO_2. It was noticed that the presence of fluorine during the FSG film deposition allows better gap-filling performance by providing an etching component to the process.[29] This aspect was particularly valuable in the pre-damascene era when FSG deposition was preceded by aluminum patterning.

1.2.3 Organosilica-based dielectrics

The next step in the evolution of SiO_2-based dielectrics was the replacement of fluorine in FSGs with carbon, which eliminated or strongly alleviated corrosion risks, offered wider compositional variability, and allowed to achieve successful integration of dielectrics with k-value down to 2.4 in commercial logic chips.[34]

Over the decades-long history of research into these hybrid dielectrics, many types of various organosilica dielectrics have been explored. The dielectrics are classified into categories based on the deposition approach. (Figure 1.11). So far, the gas-phase deposited (PECVD) SiOCH low-k material is the industry's choice driven by the previous experience in FSG integration, while Spin-on dielectrics are still being considered viable candidates for integration in the future technology nodes.

Although liquid-phase deposition offers several benefits as compared to the PECVD approach, substantial improvement in material properties and integration of SOG dielectrics over PECVD analogs needs to be demonstrated to change the view of the industry. To understand the areas in which the spin-

on dielectrics could outperform, it is important to briefly review the evolution of both material classes up until these days.

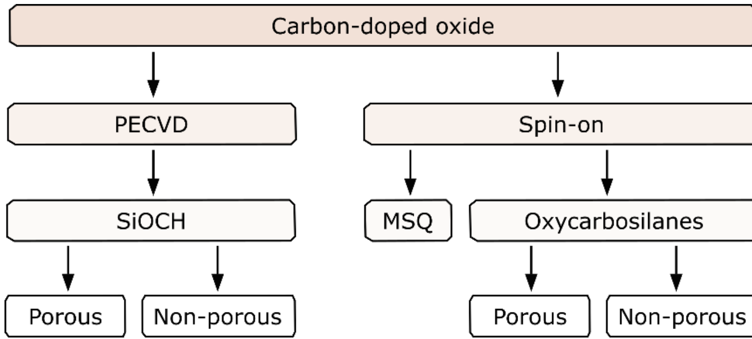

Figure 1.11. Classification of carbon-doped oxide (organosilica-based) low-k dielectrics.

PECVD organosilica dielectrics. PECVD organosilica dielectrics, often denoted as SiOCH referring to the elemental composition of the material, have been explored as low-k dielectric candidates since the late 1990s and have been successfully integrated into on-chip interconnects since 90 nm technology node. The backbone of typical SiOCH dielectrics consists of Si-O-Si bonds responsible for the mechanical stability of the layer and of terminal Si-CH_3 groups adding microporosity and imparting hydrophobicity to the low-k material.[13,35]

The deposition of SiOCH dielectric films features a wide range of precursor mixtures. The first generation of SiOCH dielectrics was deposited from precursor mixtures including oxygen-deficient silicon precursors like tetramethyl-silane (4MS), trimethyl-silane (3MS), dimethyl-phenyl-silane (DMPS), diphenyl-methyl-silane and N_2O or O_2 as oxidizing gases. Since the dissociation of N_2O and O_2 in plasma may lead to uncontrollable oxidation of Si-C bonds, the second generation of SiOCH dielectrics was deposited from the plasma of precursors already embedding the desirable structural units of

the future SiOCH film. These included cyclic siloxane- (hexamethyl-cyclo-trisiloxane (HMCTSO), tetramethyl-cyclo-tetrasiloxane (TMCTS), tetravinyl-tetramethyl-cyclo-tetrasiloxane (TVTMCTS), octamethyl-cyclo-tetrasiloxane (OMCTS), and decamethyl-cylo-pentasiloxane (DMPCSO)) and linear silane-based precursors (dimethoxy-methyl-silane (DMOMS), diethoxy-methyl-silane (DEMS), dimethyl-dimethoxy-silane (DMDMOS), dimethyl-dioxysilyl-cyclohexane (DMDOSH), methyl-triethoxy-silane (MTES)).[36] The properties of the resulting SiOCH film are defined by both precursor design as well as by plasma parameters (deposition temperature, plasma power, chamber pressure, *etc*.). If the plasma conditions favor significant fragmentation of the precursor, the role of the latter in the final structure and composition of SiOCH layer is respectively reduced. By proper precursor selection and optimization of the plasma conditions hydrophobic, thermally stable, and mechanically robust low-k dielectrics with a k-value down to 2.7 could be prepared.

Further down-scaling of dielectric constant can be achieved by the reduction of material's density realized via the following three methods: a) structural modification of the organosilica backbone via precursor design; b) post-deposition modification of SiOCH films; c) co-deposition of organosilica backbone together with labile organic phase (porogen) followed by the additional porogen removal step.

The first approach can be realized by the deposition of SiOCH film from carbon-rich precursors which would substantially lower the density of the organosilica backbone, e. g. from trimethyl-silane and trivinyl-trimethyl-cyclo-trisiloxane.[37] It would be the method of choice for the initial k-value reduction because this method implies no formation of relatively large pores, which represent the major challenge during the integration. Besides the effect on the k-value, the higher carbon content may help in reducing the plasma-induced damage[38] and in enhancing the mechanical properties of the film if the organic groups are introduced in the form of bridges between Si atoms.

The latter phenomenon is particularly well studied in spin-on glass (SOG) dielectrics.[39]

The second method implies extra treatment of SiOCH film with plasma or solution. Examples of this approach are post-treatment of SiOCH with H_2 plasma, which partially replaces Si-CH_3 groups with Si-H thus contributing to the material's microporosity.[40] Alternatively, the dielectric film was shown to drastically change its density upon immersion in an aqueous HF solution. Open porosity up to 67% was measured by ellipsometric porosimetry in originally "non-porous" SiOCH-2.7 films.[41] Since these methods allow relatively poor control over the pore structure and may result in unwanted modification of the dielectric backbone composition, these methods are not used for the preparation of commercial SiOCH dielectrics.

The third most universal k-value reduction method is based on the introduction of subtractive porosity in SiOCH. It is realized by supplying labile molecules to the reactor's chamber in addition to the original organosilane/organosiloxane gas mixture.[36] During the PECVD growth step, the porogen molecules typically represented by unsaturated hydrocarbons or cyclic hydrocarbons featuring labile epoxy groups form organic clusters uniformly distributed throughout the SiOCH layer. In the next step, the sacrificial organics is removed via additional thermal, e-beam, or UV-curing. The UV-curing at elevated temperature and radiation wavelength above 200 nm was shown not only to efficiently remove the porogen phase but also to improve the mechanical properties of SiOCH films due to enhanced silanol condensation.[42] Since the removal of the sacrificial phase may be incomplete resulting in degraded electric reliability of the dielectric, an alternative three-step deposition of SiOCH featuring intermediate remote He/H_2 plasma treatment has been proposed.[43]

Spin-on organosilica glass films (SOGs). Organosilica glass films produced via solution processing provide an alternative to plasma-deposited organosilica dielectrics and have been actively explored for their application

in on-chip interconnects since the late 1990s. As the dielectrics are generally produced via the co-polymerization of various alkoxysilanes, the original functional groups and structural motifs tend to embed in the final film. Although there exists some variability in the bond arrangement in the organosilica backbone depending on the polymerization conditions, the extent of control over the material composition in SOGs stands out as one of the major advantages over SiOCH dielectrics.[13] Another key advantage of spin-on materials is their gap-filling capability which becomes a relevant property for advanced low-k dielectrics to be integrated into ruthenium-based interconnects.[44]

The SOG dielectrics are typically formed via spin-coating of sols – a mixture of pre-oligomerized alkoxysilanes, water, solvent, and catalyst (usually inorganic acid). The oligomers are formed upon mixing, as a result of a balance between hydrolysis and condensation reactions – the basis of sol-gel chemistry (Figure 1.12).[45] The balance is typically controlled via water content, catalyst addition, and temperature. Upon sol spin-coating on a substrate, the film is baked at elevated temperatures (400-450°C) to complete the condensation of silanol (Si-OH) groups.

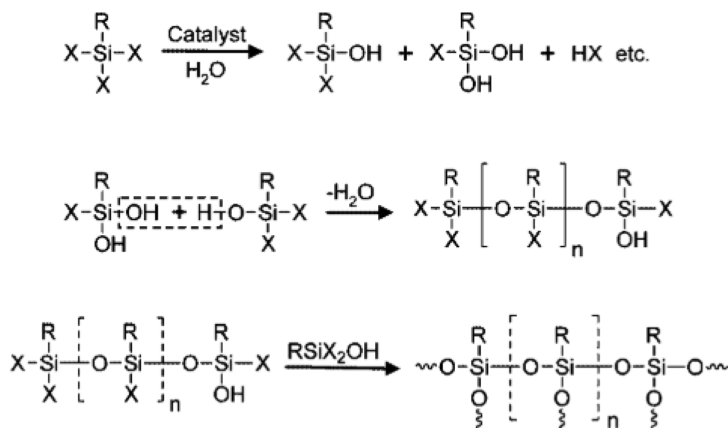

Figure 1.12. Simplified sol-gel reaction scheme, where X = Cl, H, alkoxy; R = alkyl, aryl.

The first common type of studied organosilica coatings is prepared from sols based on methyl-trimethoxy-silane (MTMS) precursor, which adds a single $-CH_3$ group to each embedded orthosilicate unit. The film featuring only MTMS as an organosilica precursor is termed methyl silsesquioxane, or MSQ (sometimes MSSQ).[46] While this type of film exhibits relatively good thermal and chemical stability as well as competitive dielectric properties (k = 2.7-2.8), it suffers from low Young's modulus of 3.8-4.5 GPa as a result of the low connectivity of organosilica matrix in which MTMS precursor tends to form loosely connected cage-like structures.[47] Such bonding structure of the organosilica backbone also implies that MSQ is very brittle, i. e. it has rather poor resistance to the propagation of cracks in the material.

To improve the connectivity of the MSQ backbone without sacrificing its low polarizability, the MTMS was mixed with precursors including alkane-bridges between Si atoms. For example, the addition of 1,2-bis-trialkoxysilyl-ethane (BTESE), allowed to substantially vary Young's modulus with little change in the material's dielectric constant (Figure 1.13).[48]

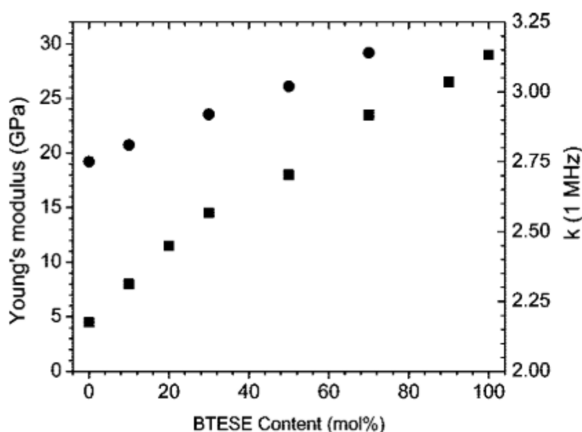

Figure 1.13. Effect of BTESE addition to MTMS. (squares) Young's modulus as a function BTESE content; (circles) dielectric constant as a function of BTESE content.[48]

Further research showed that synthesizing organosilica film from pure carbon-bridged precursors resulting in fully cross-linked organosilica networks is essential for the improvement of mechanical properties such as Young's modulus and cohesion strength.[39,49] This is particularly critical for porous materials. While Young's modulus of porous MSQ dielectrics decreases following power law as a function of material density, the addition of pores into organosilica film consisting of cross-linkable groups only leads to slower linear degradation of Young's modulus (Figure 1.14). A more elaborated discussion on the impact of organosilica matrix composition on film's mechanical properties can be found in p. 3.3.

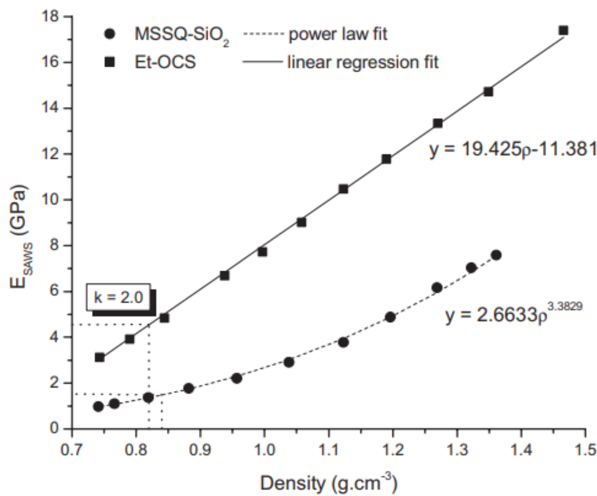

Figure 1.14. Young's modulus for MSSQ-SiO_2 and Et-OCS films as a function of density.[39]

Porosity in SOGs is commonly introduced in two different ways – via self-assembly and via removal of sacrificial material.

The self-assembly approach implies pore creation via controlled assembly of organosilica network either from pre-condensed silica/organosilica particles or via control of the gelation/solvent removal process. Materials exemplifying the latter approach are xerogels and aerogels exhibiting extremely high porosity.[50,51] Despite the attractive k-values obtained in such dielectrics, their integration is challenged by the network hydrophilicity and very large pore dimensions exceeding 10 nm.

In contrast, the addition of sacrificial organics to the sol solution in the form of uniformly sized organic nanoparticles or surfactant molecules allows obtaining better control over the pore size distribution. After the polymerization of the organosilica network around the sacrificial organic template, the latter is removed during the successive calcination step. The use of surfactants as sacrificial organics may provide additional benefits in the form of pore structure ordering caused by evaporation-induced self-assembly (EISA) of ionic or non-ionic surfactants.[52] Depending on the processing conditions, type of surfactant and its concentration, the periodic mesoporous organosilicas (PMO) may feature various pore morphologies.[53–55] The ordered porosity does not only allow to reach higher porosity levels before the structure collapse but also ensures higher mechanical stability at the same level of porosity as compared to dielectrics with random pore distribution.[56]

Removal of organic template from spin-on films may appear an easier task relative to the case of organic porogen in SiOCH dielectrics in which it may potentially be bonded to the organosilica matrix.[57,58] However, as shown in chapter 3.4, the conventional thermal treatment may not be enough for the thorough removal of the sacrificial organics, and an additional UV-curing step may be required to complete the template decomposition.

1.2.3 Metal-organic frameworks

Metal-organic frameworks (MOFs) represent a relatively new class of porous crystalline materials known for their unique combination of composition diversity, high porosity, and well-defined pore structure. The material consists of metal ions or metal oxide clusters connected via multi-topical organic linkers into an ordered network of various topologies (Figure 1.15).[59,60]

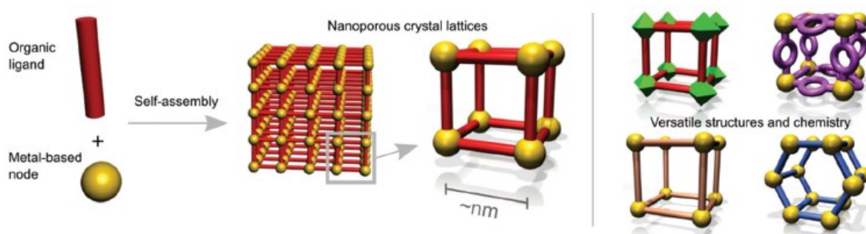

Figure 1.15. Schematic representation of MOF structure.[61]

First synthesized in the form of powder, the material was tested for applications in catalysis[62–64], gas storage and separation[65,66], *etc*. The recent developments in the deposition of MOFs in the form of thin films extended the application field to various types of electronic devices such as FETs, memristors and various types of chemical sensors.[67,68]

Multiple approaches have been employed to form thin films of MOF. These include nucleation of a film from MOF precursor solution, liquid phase epitaxy, electrochemical deposition on electrodes, spin- or dip-coating using a suspension of preformed MOF nanoparticles and conversion of metal oxides into MOFs by supplying organic linker in liquid or gas phase. The latter approach termed MOF-CVD allows solvent-free deposition and ensures good compatibility with other chip fabrication processes (see p. 2.1.2).[69–71]

The combination of low density with crystallographically defined nanosized pores in MOFs makes them a promising candidate for integration into on-chip interconnects as a low-k dielectric. The potential of MOFs as low-k dielectrics in on-chip interconnects has been first assessed by K. Zagorodnjy et al. in 2010 based on theoretical estimates of k-values via the Clausius-Mossotti equation.[72] Despite the crude estimates, the study demonstrated an excellent set of theoretical k-values and bulk modulus for some of the IRMOFs (e. g. reported k-value and bulk modulus for IRMOF-M11 were 1.45 and 12.6 GPa, respectively) which warranted further research in this field. The hypothesis was then supported by multiple experimental reports confirming the low k-value and insulating nature of MOFs.[73–75] The thorough characterization of ZIF-8 MOF films performed by Eslava *et al*. showed that this material with static k-value (@100 kHz) of 2.3 satisfies all the major low-k dielectric criteria such as hydrophobicity, sufficient mechanical strength, and low intrinsic leakage current comparable to that of organosilica materials.[76]

Since MOFs have modular structure thus enabling thousands of different metal node and linker combinations, proper selection of the most suitable low-k material candidates requires a general understanding of how MOF composition and framework topology influence such critical material characteristics as k-value, Young's modulus, and electronic band gap.

According to simulation work by M. R. Ryder *et al*. featuring a series of IRMOF and MOF-74 frameworks,[77] the electronic bandgap of MOFs containing closed-shell metals (e. g. Mg, Zn) is defined by the electronic levels of an organic linker, while for MOFs with metals having open-shell electronic structures (e. g. Co, Ni, Fe), the unoccupied d-orbitals contribute to the positioning of the conduction band. Typically, the latter type of MOFs exhibits a narrower bandgap.

The same theoretical study showed the dominant role of material density in defining the MOF k-value (Figure 1. 16). The nearly linear dependence of

k-value on porosity was also demonstrated experimentally for a range of zeolitic imidazolate frameworks (ZIF).[75]

The measurement of Young's modulus on the series ZIF films revealed its strong correlation with a material density similar to porous organosilica dielectrics (Figure 1. 17).[78] The type of metal forming the framework node (Zn or Co) was reported to have negligible impact, while sterically bulkier organic linkers were found to stiffen the MOF material (at the same framework topology). Also, an increase in connectivity of the metal nodes (coordination number) does clearly contribute to mechanical strength. The UiO-66 material ("metal node-linker" coordination number = 12) has an order of magnitude higher elastic moduli relative to ZIF-8 ("metal node-linker" coordination number = 4) at comparable porosity level.[79]

The "YM-k-value" balance in MOFs with respect to other classes of low-k dielectrics is discussed in p. 3.6.

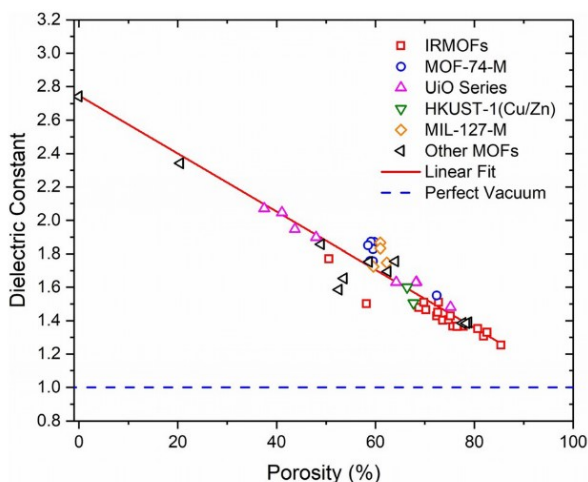

Figure 1.16. Ab-initio simulated static dielectric constant as a function of accessible MOF porosity.[77]

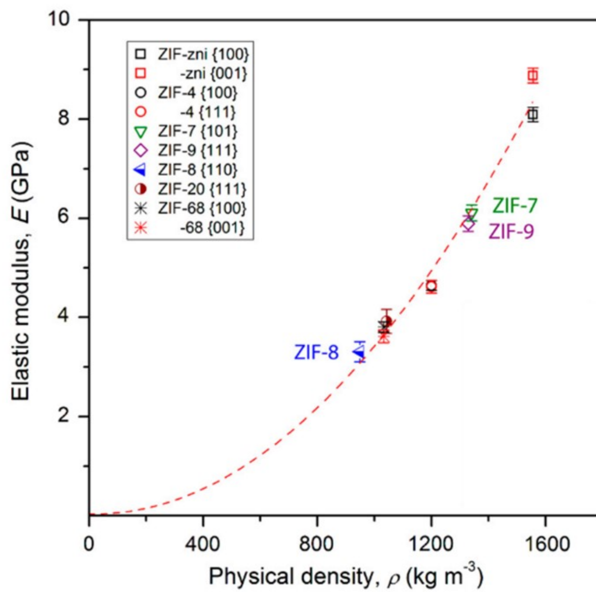

Figure 1.17. Young's modulus as a function of MOF density for a series of ZIFs.[78]

1.3 Scope of the work

The goal of this doctoral thesis research was to examine new classes of porous dielectric materials formed via self-assembly routes as an alternative to the industrial baseline SiOCH low-k dielectrics produced in plasma. The latter PECVD materials seem to have reached their limit in balancing the mechanical stability and dielectric constant, which motivates the search for ultra low-k dielectrics among the conceptually different classes of porous materials. The work has been divided into two directions each featuring a certain class of porous materials characterized by a different degree of maturity with respect to industrial applications (Figure 1.18).

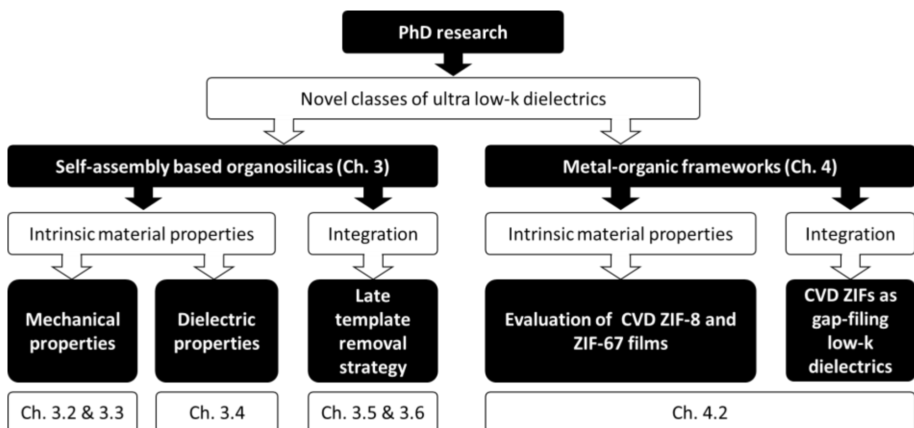

Figure 1.18. General scheme of the PhD research.

The first class of studied materials is self-assembly based spin-on organosilicas. Produced from a sol, they consist of a surfactant-templated organosilica backbone with embedded organic bridges. This class of materials does not step too far from the currently used porous organosilica PECVD dielectrics or extensively studied silsesquioxane films. *Chapter 3* reviews the optimization of the sol composition and the dielectric's integration methodology to enhance its mechanical and dielectric properties as well as to

minimize the process-induced damage associated with plasma patterning and successive formation of a metal barrier on the porous surface.

The second class of studied porous materials is metal-organic frameworks (MOFs) which start being actively explored for their potential applications in micro- and nanoelectronics. While the crystallinity of the frameworks in combination with their high porosity makes them conceptually very interesting as potential low-k insulators, many aspects regarding the actual implementation of this idea remain unclear. For example, questions regarding the criteria for the selection of appropriate MOFs as promising low-k candidates, deposition approaches, and integration concepts remain barely answered. The performed research described in *Chapter 4* sheds light on the above questions using ZIF-8 and ZIF-67 as model MOF materials.

Chapter 2. Materials and methods

The chapter provides an overview of the materials and methods used in this work. The details of the deposition approaches for self-assembly based mesoporous silica and metal-organic frameworks are given in Ch. 2.1.1 and Ch. 2.1.2, respectively. Ch. 2.2 summarizes the methods used to characterize the properties of the low-k dielectric coatings in the form of a table.

2.1 Synthesis of low-k dielectrics under study

2.1.1 Self-assembly based organosilica dielectrics.

The self-assembly based organosilica-based low-k dielectrics, or organosilica glasses (OSGs), used in this work have been prepared by spin-coating of proprietary solutions supplied by SBA Materials Inc.

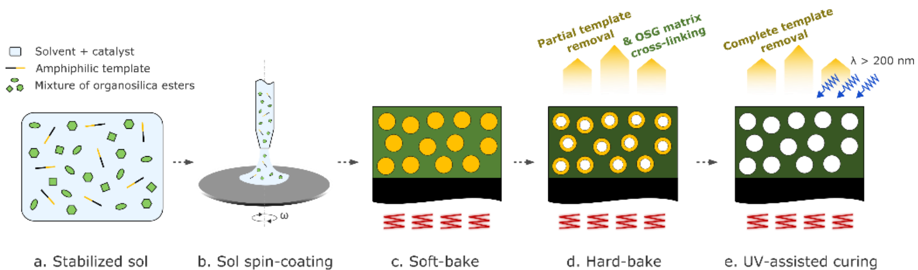

Figure 2.1. General process flow for deposition of self-assembly based organosilica low-k dielectric coatings.

The preparation route for these mesoporous organosilica materials included the following steps (Figure 2.1):

a. ***Sol formulation***. The typical sol included three general components: solvent with added hydrolysis catalyst (typically an inorganic acid), amphiphilic structure directing agent or organic template molecules, a mixture of organosilica esters including TEOS and at least two other esters featuring a single terminal methyl group attached to Si atom and a molecule having a carbon bridge between two Si atoms. The sols were formulated to target the dielectric constant of 2.2 and thickness of ~200 nm for the hard-baked coatings.
b. ***Spin-coating***. Spin-coating was performed by manually dispensing 3 ml of a sol on 300 mm wafer while it is rotating at 100 rpm. The slow sol spreading step is followed by spinning at 1200 rpm.
c. ***Soft-bake***. The wafers after the sol spin-coating are immediately dried on a hot plate at 120°C in air. This step accelerates the matrix crosslinking and fixes the templated pore structure.
d. ***Hard-bake***. The removal of the organic template is performed by annealing at 400°C (if not mentioned otherwise) in N_2. The hard-bake time results in the solidification of the organosilica backbone along with the removal of the sacrificial organics.
e. ***UV-assisted curing***. The complete removal of the organics is realized by means of UV-assisted curing, i. e. annealing of the coating at 400°C while exposing it to UV-radiation with broadband spectrum ($\lambda > 200$ nm). The absence of photons with higher energy helps to minimize the damage of the organosilica matrix.

Although due to the proprietary nature of the employed sols some details about the precursors and their concentrations cannot be fully disclosed, it is important to note that this does not reduce the value or generality of the performed research. The disclosed data concerning the sol composition, which is reported in the corresponding experimental sections of Chapter 3, allows

capturing the link between the sol components of interest and properties under study.

Chapters 3.2 and 3.3 explore the impact of sol components such as organic template and organosilica precursor (step *a* in Figure 2.1), respectively, on the mechanical properties of the hard-baked SOG films.

In contrast, chapters 3.4-3.6 feature a SOG low-k material produced from the same sol (SOG-2.2) and focus on the modification of the hard-bake sequence (steps *d* and *e* in Figure 2.1).

2.1.2 Zeolitic imidazolate frameworks.

The current research on the potential application of MOFs in advanced interconnects was focused on two materials – ZIF-8 and ZIF-67 (Figure 2.2), which belong to a sub-group of zeolitic imidazolate frameworks known for their high thermal and chemical stability.[80] The structural properties of these isostructural materials are summarized in Table 2.1.

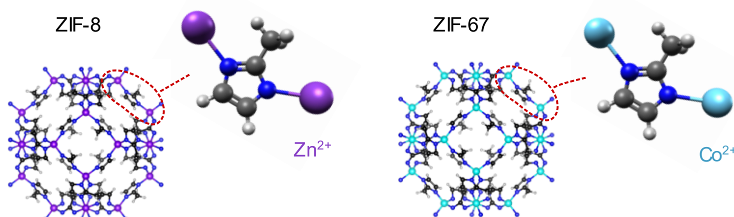

Figure 2.2. Unit cells of ZIF-8 and ZIF-MOFs.

Table 2.1. Structure parameters of isostructural ZIF-8 and ZIF-67 MOFs.[78,81]

Parameter	ZIF-8/ ZIF-67
Lattice constant, nm	~ 1.7
Pore limiting diameter, nm	~ 0.34
Solvent accessible volume (SAV)	~50.4%

While the previous reports have already highlighted the promising combination of ZIF properties for application as insulating material in interconnects, the aspects of MOFs integration into real-world devices have not yet been discussed. In part, this is related to the poor compatibility and scalability of solvothermal synthesis commonly employed for the preparation of various MOFs. In contrast, the solvent-free cleanroom-compatible MOF-CVD approach allows us to demonstrate the growth of MOFs on both blanket and patterns, thus advancing the MOF integration research.

The MOF-CVD method is based on the conversion of the metal oxide precursor layer into porous MOF upon exposure of the film to vapors of organic linker at elevated temperatures.[69,82] In our study, the precursor layers for deposition of ZIF-8 or ZIF-67 were ALD ZnO and oxidized PVD/CVD Co, respectively. The conversion process is schematically shown in Figure 2.3.

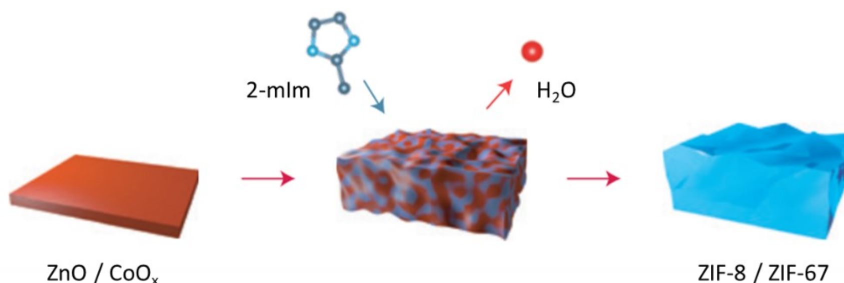

Figure 2.3. MOF-CVD process schematically shown for ZIF-8 and ZIF-67.[69]

The conversion proceeds via an intermediate non-porous mixture phase preceding the MOF crystallization. The latter can be enhanced by the excess of the organic linker or by supplying water vapor.[69,70]

The layers of ALD ZnO and PVD Co were formed on highly-doped p++ Si substrates. ALD ZnO deposition was implemented at 120 °C by 30 cycles of diethyl zinc (DEZ)/H_2O precursor pulses separated by N_2 purge steps

(Savannah S200, Veeco Instruments Inc.). PVD Co film was sputtered on Ar-plasma pre-cleaned Si-substrate (NC7900, Canon Anelva Corp.). Aiming at conformal coverage on patterns, the PVD Co was replaced with CVD Co (Excel platform, Lam Research Corp.).

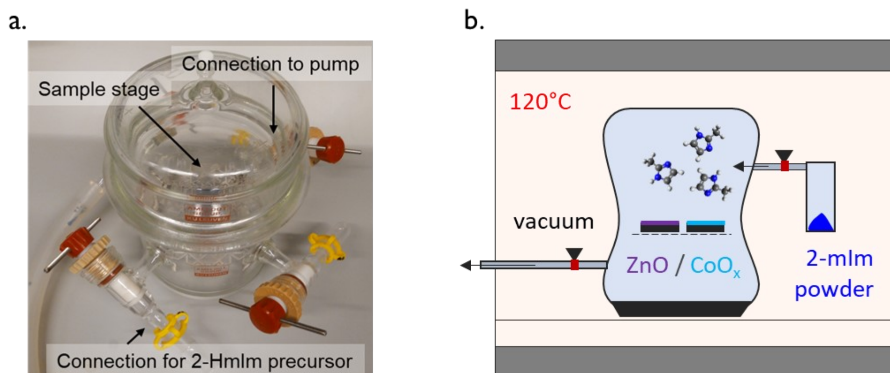

Figure 2.4. MOF-CVD process implementation. (a) Glass reactor and (b) schematic ZnO/CoO_x conversion set-up.

For the conversion to the appropriate ZIF layer, samples with precursor layers were placed in a glassware reactor (Figure 2.4). The glassware reactor was connected to a vacuum pump via a manual valve. Upon assembly, the reactor was checked for leaks. The glass tube containing 2-methylimidazole powder (99%, CAS #693-98-1, Sigma-Aldrich) was connected to one of the ports of the glassware reactor via another manual valve. The whole set-up was placed in a furnace pre-heated at 120 °C. After the temperature stabilization (15 min), the valve to the vacuum pump was opened, and the reactor was evacuated until pressure stabilization below 10 mbar. The vacuum valve was then closed and the valve to the 2-methylimidazole tube opened. The exposure of samples to vapors of 2-methylimidazole was set to 120 min, after which the precursor valve was closed, and the sample area of the reactor was kept under dynamic vacuum for 15 min to remove the unreacted organic linker from the sample surface and pores of formed ZIF films (activation). Finally, the reactor

was let to cool down before the samples could be taken out for further characterization.

2.2 Low-k dielectrics characterization

The characterization techniques used in the current study are classified by the type of information they provide about low-k material and summarized in Table 2.2.

Table 2.2. Techniques for characterization of low-k dielectric thin films in the current study.

Type	Material property	Technique	Measurement details and remarks
Dielectric properties	k-value	Impedance measurements (C-f) on MIS/MIM stacks	The capacitance measurements were done using precision LCR-meter E4980A from Keysight (C_s-R_s mode). The dielectric constant is calculated from series capacitance measured on MIS/MIM stack at 100 kHz (C_s) and thickness of the low-k dielectric layer (d) measured by ellipsometry or via analysis of SEM ross-section: $$k = \frac{dC_S}{\varepsilon_0 S}$$ By adding an extra series capacitor with a dielectric constant of SiO_2 ($k = 4.1$) to the equivalent circuit, one can use the measured C_s to obtain a thickness-independent estimate of the low-k damage depth (see p. 3 in Appendix A). To minimize the impact of the back-side contact resistance, the back of the Si substrates was either covered with Pt, Al, or wetted with InGa eutectic.

		Impedance measurements (C-f) on fork-fork capacitors + 2D capacitance simulation	The capacitance C_s is measured at 100 kHz on 2 cm long 45 nm half-pitch fork-fork capacitors using the same setup. Based on the geometry parameters extracted from TEM cross-section of the same device and assumptions about the dielectric constant of materials other than the low-k dielectric of interest, the capacitance is simulated for a range of k-values (k = 1, 2, 3, 4) using Raphael interconnect solver (Synopsys). Afterward, the effective k-value corresponding to the measured C_s is estimated by interpolation of the simulated capacitance points.
	Leakage current	Volt-Ampere characteristic (I-V) on MIS stacks or fork-fork capacitors	The IV-characteristics were recorded with Agilent 1500A or 4156C parameter analyzers by sweeping voltage from 0V up to 100V. The MIS stacks used for the leakage current analysis had 300 nm thick Al top electrodes and Al layer of the same thickness on the back-side of the Si-substrate. Since the evaporated Al electrodes do not cause any low-k damage, the measured I-V curves reflect the intrinsic properties of the low-k material. The results of leakage current on 2 cm long 45 nm half-pitch fork-fork capacitors fabricated via different single damascene process flows convey information about the process-induced modification of the low-k dielectric phase.
	Defect states	Internal photoemission spectroscopy (IPE)	The photocurrent was recorded on two MIS stacks composed of low-k dielectric on an n-Si substrate and semi-transparent gold electrodes on top. The stacks were irradiated by monochromatic light with photon energies varied over the range 3.1-6.0 eV with a constant

			spectral resolution of 2 nm. The spectra were recorded while applying various positive or negative bias voltages to the gold electrode. The quantum yield *Y* was defined as the photocurrent normalized on the incident photon flux. The measured spectra reflect the positioning of energy band levels in the MIS stack at the respective interfaces as well as of the trap states within the low-k dielectric's bandgap.
	Defect states	Electron spin resonance spectroscopy (ESR)	The ESR measurements were performed in K-band (~20.4 GHz) spectrometer at liquid He temperature (~4.2 K) on the low-k dielectric film deposited on top of a thinned n-Si substrate. Conventional adiabatic first derivative absorption spectra (dP_μ/dB, where P_μ represents the incident microwave power) were recorded at the applied magnetic field B parallel with the [100] normal to the sample surface. Defect densities and g-values were determined using a co-mounted calibrated Si:P marker sample (g = 1.998696±0.00002 at 4.2 K). The g-value of a free electron in a vacuum is 2.00232, while it changes for an unpaired electron inside a molecule due to local interactions. Therefore, the g-value can serve as a fingerprint for the detection of certain molecule fragments, for example, associated with organic residues in low-k dielectric films.
Mechanical	Young's modulus	Nanoindentation (NI)	Nanoindentation measurements were performed using Hysitron TI 950 Triboindenter (Bruker) or Nanoindenter XP system (MTS Systems Corporation) equipped with a cube corner and three-sided pyramid (Berkovich) indenter tip, respectively. Continuous stiffness

			measurements (CSM) were combined with the Li-Vlassak method implemented in a custom MATLAB script to extract the substrate-independent Young's modulus of thin dielectric films deposited on Si-substrate[83].
	Fracture toughness	Nanoindentation (NI)	The fracture toughness of the low-k films was extracted from cube corner indentation tests, which were performed under displacement-control mode with predefined maximum penetration depths between 50 nm and 200 nm in order to generate radial cracks through the film thickness. To calculate the fracture toughness values, the mechanics model developed by Morris and Cook was employed. The model relies on crack geometry and intrinsic low-k film properties including thickness, Young's modulus, and stress as input parameters[84,85]. The crack lengths were measured from high-precision topography maps of the indents and further verified with GHz-scanning acoustic microscopy. The intrinsic low-k film parameters were evaluated using spectroscopic ellipsometry, nanoindentation (see above), and wafer bow measurements, respectively.
	Cohesion & Adhesion strength	4-point bending test (4PB)	The cohesion strength of the low-k films and their adhesion to adjacent barrier layers were estimated by the value of critical energy release rate G_c extracted during a 4-point-bending test performed on a high-precision micromechanical test system from DTS Company (Dauskardt Technical Services). Two types of stacks have been prepared and then glued to another Si-wafer with an epoxy layer:

			1) Si-substrate, 200 nm low-k film, 6 nm PVD TaN/Ta bi-layer, 60 nm PVD Cu seed, 800 nm ECD Cu prepare rectangular test structures of 60 x 5 mm^2 with a notch formed within silicon wafer on which the stack was formed (Fig. 3.1a). 2) Si-substrate, 200 nm low-k film, 5 nm PECVD SiCN, 25 nm PECVD SiCO, 1000 nm CVD SiO_2. Then rectangular pieces of 60 x 5 mm^2 were cleaved with a notch pre-formed on the Si-wafer from the initial stack. To determine the location of the crack both delamination surfaces were analyzed by XPS (Theta300, Al K_α) before and after 500 s Ar sputtering.
Morphological	Pore structure (Open porosity, average pore radius)	Ellipsometric porosimetry (EP)	Ellipsometric porosimetry (EP) measurements were performed on a custom-built tool featuring a vacuum chamber, a spectroscopic ellipsometer (Sentech SE801, 350–850 nm wavelength) mounted on it, and a programmable adsorbate vapor supply platform. The isotherms were recorded at 23 °C (the temperature of the vacuum chamber). The temperature of the liquid sources (toluene, DIW, methanol) was maintained at 25 °C. The equilibration time at each pressure point was set to 30 s.
	Surface roughness	Atomic-force microscopy (AFM)	Atomic force microscopy (AFM) topography images (10 x 20 μm^2, 512 x 1024 pixels) were recorded in tapping mode with Dimension Edge microscope (Bruker). The image corrections (rows alignment, horizontal scars elimination) and plotting were performed with

			Gwyddion 2.44 software. The latter was also used to calculate the arithmetic (R_a) and root-mean-squared (R_q) surface roughness.
	Crystallinity	X-ray diffraction (XRD)	X-Ray diffraction (XRD) patterns were obtained with PANalytical Empyrean diffractometer equipped with Cu Kα X-ray source and Pixcel3D detector. The surface-sensitive grazing incidence X-ray diffraction mode (GI-XRD) was employed with Omega fixed at 0.2° and 2*Theta scanned in the range 5-50° with a step size of 0.05°. The diffractograms were then manually baseline-corrected using b-spline interpolation.
	Pattern geometry	TEM/TEM-EDS	Transmission electron microscopy (TEM) analysis of the fork-fork capacitor cross-section was done on 30-50 nm thick lamellas prepared with dual beam FIB/SEM Helios NanoLab 450HP (FEI). Before the FIB lift-out, the surface of the samples under test was coated with a protective coating consisting of three sequentially deposited layers: a drop-casted organic layer (SoC) soft-baked at 150 °C, e-beam (5 kV) and ion-beam (30 kV) deposited Pt layers. As a last step of the lamella preparation, there was a 5 kV ion beam milling step to reduce the surface damage. The TEM images and EDS element maps were captured with Titan3 G2 60-300 TEM (FEI) operating at 60 kV.
Chemical	Elemental composition at the surface	XPS	X-Ray photoelectron spectroscopy (XPS) measurements were carried out in angle-resolved mode using a Theta300 system (Thermo Fisher Scientific). 16 spectra were recorded at exit angles between 22 and 78 degrees as measured from the normal of the sample. The

			measurements were performed using a monochromatized Al Kα X-ray source (1486.6 eV) and a spot size of 400 micrometers. Standard sensitivity factors were used to convert peak areas to atomic concentrations.
	Elemental depth profiles	TOF SIMS	TOF SIMS depth profiling with TOFSIMS IV from ION-TOF GmbH operating in dual beam configuration.
	Atomic density and depth distribution of metal	RBS	Rutherford backscattering spectroscopy (RBS). The RBS experiments were performed in a random rotation mode using 1.5 MeV He^{+} ions from the 6SDH tandem accelerator (National Electrostatics Corporation) equipped with an Alphatross ion source. The experimental end-station was a 5-axis goniometer developed at the Forshungszentrum Jülich[86]. The angle between the sample normal and the beam was set to 11 degrees. The solid angle of the PIPS detector was 0.42 msr, the scattering angle was 170°. The beam spot was confined to 1x1 mm2. In-house developed analysis software was used to fit the spectra and to deduce the areal density.
	Functional groups	FTIR	IR absorbance spectra were recorded on Nicolet 6700 FTIR spectrometer (Thermo Scientific) in transmission mode with a resolution better than 2 cm^{-1} averaging 100 spectra within the 400-4000 cm^{-1} range. Before the analysis, the substrate spectrum (silicon with 1 nm of thermal oxide on top) was subtracted from the collected spectra. The IR spectra were used for several purposes:

			1) Qualitative monitoring of changes in the concentration of functional groups attributed to an organic template, organosilica matrix, and its damage. 2) Quantification of bond concentrations in organosilica low-k dielectrics.
	Chemical stability	HF-test	The pristine organosilica low-k dielectrics are designed to survive prolonged immersion in 0.5% aqueous HF solution (> 5 min). The removal of protecting methyl groups from the organosilica matrix induced by plasma makes the modified parts of the dielectric soluble. Therefore, the HF-dipping test (aqueous 0.2% HF, 60s) was used to quantify the depth of the plasma damage in thin organosilica low-k films via measurement of the associated thickness loss.

Chapter 3. Self-assembly based organosilica spin-on low-k dielectrics

3.1. Chapter introduction

This chapter summarizes the research performed on self-assembly based spin-on organosilica dielectrics. The first two sub-chapters (3.2 and 3.3) are focused on the enhancement of the dielectric's mechanical properties via optimization of its pore structure and organosilica backbone composition, respectively. The third sub-chapter (3.4) studies the thermal decomposition of an organic template and reveals the effect of template residues left in the pores on the material's electrical properties. The next sub-chapter (3.5) describes the role of the template residues in the protection of the organosilica matrix against damage in patterning fluorocarbon-based plasmas. Similarly, sub-chapter 3.6 looks at the feasibility of the temporarily retained template residues to reduce the low-k material damage caused by the metal barrier deposition. It also addresses concerns related to the applicability of the temporary template residue retention in an actual single damascene metallization process flow. The results shown in the sub-chapters were published in the peer-reviewed journals cited below.

- **M. Krishtab**, K. Vanstreels, T. Savage, M. Koichi, S. De Gendt, and M. Baklanov. Improvement of cohesion strength in ULK OSG materials by pore structure adjustment. *Microelectron. Eng.* 137, 75–78 (2015).

  Personal contribution: Design and arrangement of the experiments, deposition of the low-k dielectric coatings from sols prepared in collaboration with SBA Materials Inc., analysis of pore structure and composition.

***Support from co-authors and other contributors*:** The sols were prepared by T. Savage (SBA Materials), sol spin-coating on 300 mm wafers was optimized by M. Koichi (Tokyo Electron).

- K. Vanstreels, **M. Krishtab**, L. Garcia Gonzalez, S. Armini, Impact of organic linking and terminal groups on the mechanical properties of self-assembly based low-k dielectrics, *Appl. Phys. Lett.* 111 (2017). – *M. Krishtab and K. Vanstreels equally contributed to the published work.*

  ***Personal contribution*:** Design and arrangement of the experiments, optimization of the coating deposition conditions for sols prepared in collaboration with SBA Materials Inc., analysis of pore structure and composition.
  ***Support from co-authors and other contributors*:** The optimization of the low-k coatings deposition was done with a help of L. Garcia Gonzalez, an internship student from LTM CNRS. The characterization of mechanical properties was performed by Kris Vanstreels.

- **M. Krishtab**, V. Afanas'ev, A. Stesmans, S. De Gendt, Leakage current induced by surfactant residues in self-assembly based ultralow-k dielectric materials, *Appl. Phys. Lett.* 111 (2017).

  ***Personal contribution*:** Design and arrangement of the experiments, optimization of the coating deposition conditions for sols prepared by SBA Materials Inc., analysis of pore structure and composition, electrical characterization.
  ***Support from co-authors and other contributors*:** The ESR and IPE measurements were performed in collaboration with Prof. V. Afanas'ev and Prof. A. Stesmans from Department of Physics and Astronomy at KU Leuven.

- **M. Krishtab**, J.-F. de Marneffe, S. De Gendt & M. R. Baklanov. Plasma induced damage mitigation in spin-on self-assembly based ultra low-k dielectrics using template residues. *Appl. Phys. Lett.* 110, 013105 (2017).

  ***Personal contribution*:** Design and arrangement of the experiments, optimization of the coating deposition conditions for sols prepared by SBA Materials Inc., analysis of pore structure and composition, implementation of plasma/VUV exposure tests, evaluation of plasma/VUV-induced damage.
  ***Support from co-authors and other contributors*:** TOF SIMS analysis was done by members of MCA group at imec. The DFT simulation of VUV interaction with model surfactant chains was done by S. Naumov (Leibniz-Institut für Oberflächenmodifizierung, Leipzig, Germany).

- **M. Krishtab**, J.-F. de Marneffe, S. Armini, J. Meersschaut, H. Bender, C. Wilson, S. De Gendt, Metal Barrier Induced Damage in Self-Assembly Based Organosilica Low-k Dielectrics and Its Reduction by Organic Template Residues. *Appl. Surf. Sci.*, 485, 170–178 (2019).

  ***Personal contribution*:** Design and arrangement of the experiments, optimization of the coating deposition conditions for sols prepared by SBA Materials Inc., analysis of pore structure and composition, analysis of low-k damage and pore sealing, electrical characterization.
  ***Support from co-authors and other contributors*:** Some process steps during fabrication of 45 nm half-pitch capacitor structures were performed by imec's p-line operators and engineers. These operations include hard-mask stack deposition, 193 nm immersion lithography, TaN/Ta metal barrier deposition, Cu metallization and CMP. The deposition of TiO_2 hard-mask was optimized with a help of C. Petermann (Merck KGaA). RBS and TEM analysis were done by members of MCA group at imec.

3.2 Correlation between pore dimensions and cohesion strength

Abstract

In this study cohesion strength in low-k dielectric films was enhanced by tuning the pore structure. The correlation between the average size of pores in ultra-low-k materials and cohesion energy was demonstrated by performing a 4-point bending test on multi-layer structures including TaN/Ta metal barrier. Spin-on organosilica films prepared with different templating surfactants were used to alleviate porosity-pore size coupling, which revealed the particular role of pore size with respect to material toughness. The paper also discusses aspects of material design at the precursor level.

3.2.1 Introduction

The growing demand for dielectric constant reduction of insulating materials in interconnects of advanced ULSI chips makes the semiconductor industry consider highly porous films for integration. Apart from benefits in lowering the dielectric permittivity, the introduction of porosity inevitably leads to remarkable degradation of its intrinsic mechanical stability expressed in a decrease of Young's modulus (YM), adhesion, and cohesion strength. While the incorporation of organic bridging groups within the OSG matrix alleviates the issue of fast YM drop, as the porosity of the low-k film increases,[39] the problem of keeping high adhesion and cohesion strength without compromising it with chemical stability persists. Recently, it was also demonstrated with DCB measurements on damascene structures with different via density that weakness of the low-k layer is one of the main mechanisms of mechanical failure, which motivates the search for pathways

to increase the toughness of insulating films.[87] In this work, we investigated the role of structural aspects in cohesion improvement by tuning the pore size in Liquid Phase Self Assembly (LPSA) low-k materials.

3.2.2 Experimental details

A range of low-k dielectric films was prepared from sols based on a mixture of carbon-bridged organosilica precursors and various polyethylene oxide (PEO) based non-ionic surfactants with different molecular weights, which makes it possible to vary the pore size and porosity independently. All sols were spin-coated on top of 300 mm Si wafers with 1 nm of thermally grown SiO_2. The films were subjected to short low-temperature annealing at 150°C for 2 minutes and then hard-baked at 400°C for 90 minutes in a nitrogen atmosphere. The composition of the hard-baked films was checked with FTIR (Nicolet 6800) whereby IR absorbance spectra were collected in the range 400-4000 cm^{-1}. The dielectric constant of selected films was extracted from CV-curves measured on MIS-structures at 100 kHz.[88] The pore structure of the films was analyzed by ellipsometric porosimetry using toluene as an adsorbate.[89] Open porosity and average pore size are used throughout this paper to compare different low-k films. Young's modulus was calculated from the load-displacement curve recorded using a Nanoindenter XP system (MTS Systems Corporation) equipped with a three-sided pyramid (Berkovich) indenter tip. Fracture resistance was estimated by the value of critical energy release rate G_c extracted during the 4-point-bending test (4PB) performed on a high-precision micromechanical test system from DTS Company (Dauskardt Technical Services).[90] A multi-layer stack composed of 200 nm low-k film, 6 nm PVD TaN/Ta bi-layer, 800 nm Cu electroplated on top of 60 nm PVD Cu seed layer was sandwiched between two silicon wafers and used to prepare rectangular test structures of 60 x 5 mm^2 with a notch formed within silicon wafer on which the stack was formed (Fig. 3.1a). To determine the

location of the crack both delamination surfaces were analyzed by XPS (Theta300, Al K_{α}) before and after 500 s sputtering. Typical XPS spectra are shown in Fig. 3.1b. As can be seen, the crack is formed within the low-k layer and is located in proximity to the PVD TaN/Ta layer. So, this setup allows finding a correlation between the cohesion strength of the porous low-k layer and its pore structure parameters.

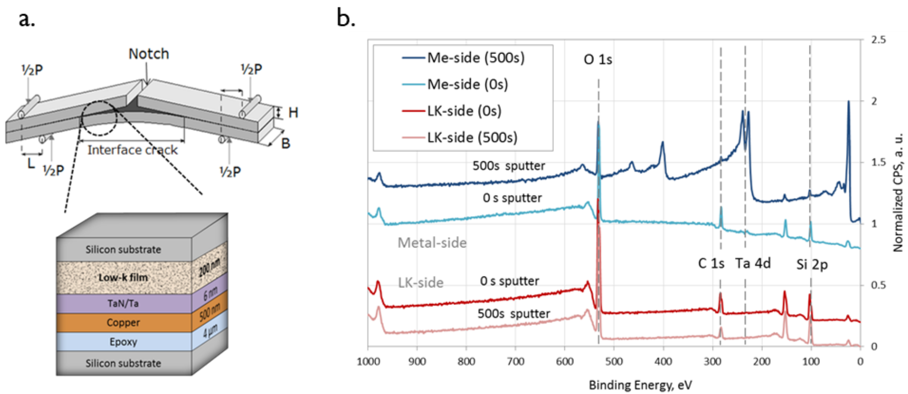

Figure 3.1. (a) Schematic structure of the 4PB-test vehicle and (b) XPS spectra obtained after the 4PB-test on both delamination sides.

3.2.3 Results and discussion

The significance of the pore size as a parameter impacting cohesive failure of OSG films follows from the first tests comparing 4PB results for PECVD and LPSA films (Fig. 3.2). [91] While in PECVD low-k films the effect of pore size may be overshadowed by simultaneous scaling of pore size with porosity,[92] in LPSA materials coupling between these parameters is suppressed and their contribution to the film strengthening can be separated. This is especially apparent for the studied highly porous LPSA films with large pores. The cohesion of these layers was notably lower than for PECVD films which had smaller pore sizes at similar porosity (Fig. 3.2a). At the same

time, the deviation from the linear trend, as seen for data points obtained on PECVD films, disappears when the values of energy release rate are plotted as a function of pore size (Fig. 3.2b). This phenomenon was used as a guideline to increase cohesion strength in LPSA films.

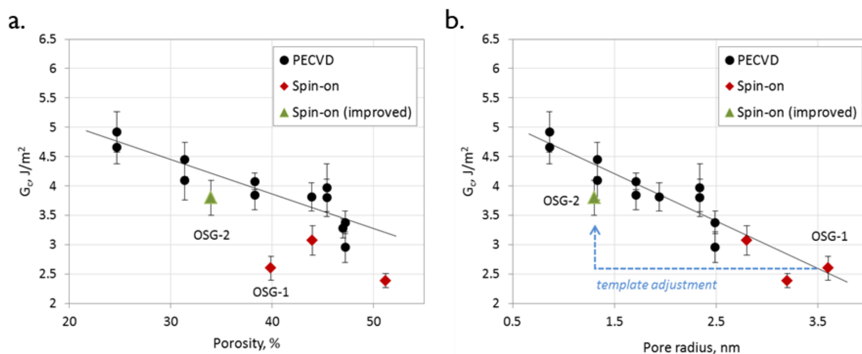

Figure 3.2. Energy release rate measured on PECVD films with different porosity and LPSA low-k materials. The data is plotted as a function of (a) open porosity and (b) pore radius.

To achieve a reduction of pore size in the Spin-on LPSA films and validate the observed correlation, several amphiphilic templates (Template **1-8**) including PEO as hydrophilic molecular block were screened in combination with a fixed composition of organosilica precursors. The template loading was appropriately adjusted to the target dielectric constant of 2.0 for the hard-baked films. The result of this test is shown in Fig. 3.3 as the dependence of the average pore size on the normalized molecular weight of the hydrophobic part of a surfactant molecule. The latter is known to form the core of micellar structures produced in the course of solvent evaporation during the soft-bake step, and it largely determines the dimensions of the pores[93]. As expected, the use of lighter hydrophobic blocks of different chemical nature leads to the incorporation of smaller pores into LPSA film. Since a similar density of the films was maintained throughout the experiment,

the graph gives an idea about the extent to which porosity and pore size can be decoupled for the particular system of precursors and coating conditions. According to Fig. 3.3, low-k films prepared with Template **5** and Template **8** have the largest difference in pore size. It should be mentioned, that apart from the difference in average pore radius, the correlation between the average pore radius and pore size distribution width exists as a result of disordered pore structure. H2-type hysteresis formed by adsorption/desorption isotherms recorded during EP-measurements was observed for all LPSA films used in this study. This means that increase in average pore size is accompanied by a simultaneous broadening of pore size distribution. Therefore, in this work, the average pore radius should be considered as a parameter reflecting both features of pore size distribution in LPSA films – its median and width.

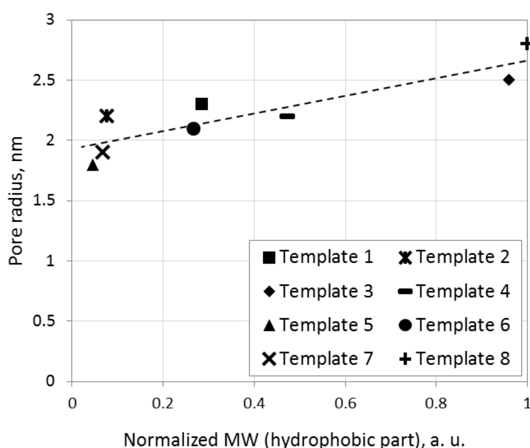

Figure 3.3. Average pore radius as a function of normalized molecular weight (MW) of hydrophobic part of the PEO-based templates.

Two LPSA low-k dielectric films OSG-1 and OSG-2, stemming from sols based on Template **8** and Template **5**, respectively, and designed for dielectric constant of 2.3 were compared with respect to material composition, pore structure and mechanical stability. The properties of the films are

summarized in Table 3.1. In general, there are two major distinctions between the dielectrics – the type of bonding within the organosilica matrix and the size of pores. Each of them may have a considerable effect on the material toughness.

Table 3.1. Properties of LPSA low-k-2.3 films prepared with large (OSG-1) and small (OSG-2) molecular weight templates.

Parameter	OSG-1	OSG-2
C/Si (sol)	0.57	0.55
$-CH_3/-CH_2$ (sol)	0.33	5.00
k-value	2.32	2.30
Young's modulus, GPa	6.04	5.04
Open porosity, %	39.0	34.0
Pore radius, nm	3.6	1.3

The parameters characterizing matrix components such as the ratio between silicon and carbon atoms as well as the distribution of carbon atoms between bridging ($-CH_2-$) and terminal ($-CH_3$) groups are calculated based on the mixture of organosilica precursors and may only indirectly reflect the real composition of the films after the hard-bake step. The composition of hard-baked OSG-1 and OSG-2 layers was analyzed by FTIR (Fig. 3.4). One can notice in Fig. 3.4b, that the absorbance peak featuring terminal $Si-CH_3$ bond is higher for OSG-2, which is consistent with the data in the table. However, the observed peak difference is not as high as one would expect from the mere comparison of $-CH_3/-CH_2-$ ratios indicated in Table 3.1. The discrepancy may be a result of the self-hydrophobization reaction during which total carbon content stays the same while part of the bridging groups is transformed into terminal ones.[53] Regarding the potential impact of the observed trends in the matrix composition, higher network interconnectivity and thereby larger critical energy release rate is expected for OSG-1.[94] Another important

observation is the negligible IR absorbance in the range 3100-3800 cm^{-1} attributed to moisture uptake for both OSG-1 and OSG-2 (Fig. 3.4a). Hydrophobicity of the films is important to exclude or rather alleviate the role of "crack tip - moisture" interaction as the crack propagates within the porous film.[95]

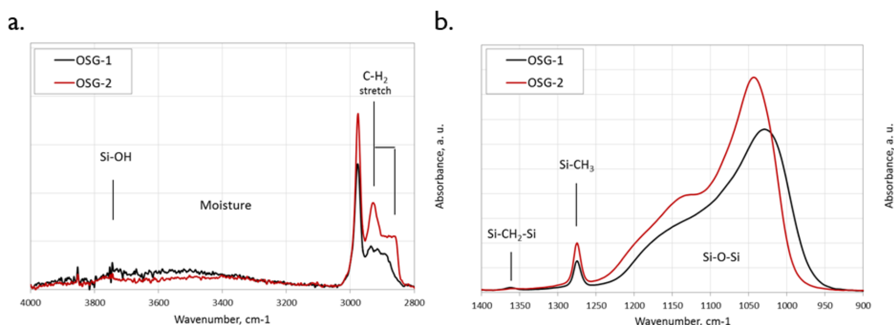

Figure 3.4. FTIR spectra of OSG-1 and OSG-2 films in the ranges (a) sensitive to vibrations of adsorbed moisture and (b) siloxane bonds in the organosilica matrix.

The second parameter of interest and the main focus of this paper, i. e. pore size, exhibits a difference of more than a factor of two between the porous films produced from sol containing large and small molecular weight surfactants. Note, that this difference exceeds the one obtained during the screening test, which can be explained by changed template loading and modified interaction (solubility) of the organosilica matrix with the hydrophilic blocks of the template.

Critical energy release rate values measured on the stacks including layers of OSG-1 and OSG-2 are shown in Figure 3.2. One can see that despite the lower concentration of methylene bridges in the organosilica backbone of OSG-2, this dielectric film reaches the G_c value which is about 35% higher than for OSG-1. Moreover, the measured values of cohesion strength fit well the linear trend initially demonstrated for the PECVD low-k films, thus

confirming the determining role of pore size in retaining material toughness upon the density down-scaling.

3.2.4 Conclusions

The improvement of cohesion strength of organosilica LPSA low-k films was achieved by proper selection of the PEO-based template. By employing a surfactant with a small molecular weight of its hydrophobic block it was possible to reduce the radius of pores below 2 nm and to achieve a 35% increase in cohesion strength. The strong correlation between pore size and material toughness was exemplified by comparing two LPSA low-k films OSG-1 and OSG-2 featuring similar open porosity and more than a two-fold difference in pore dimensions. The better crack growth resistance of OSG-2 film with smaller pores was observed despite remarkably lower interconnectivity of its organosilica backbone as compared to OSG-1, which suggests a prevailing role of the porosity distribution aspects in defining the mechanical robustness of the tested films.

3.3 Impact of linking and terminal organic groups on mechanical properties of self-assembly-based low-k dielectrics

Abstract

The impact of the terminal and linking organic groups on the mechanical stability of self-assembly-based porous ultralow-k dielectrics was investigated by nanoindentation and four-point bending tests in conjunction with quantitative FTIR analysis. Using a set of six porous low-k dielectrics functionalized with alkyl- and aryl-based groups we demonstrated that both elastic and fracture properties can be sensitive to the type of embedded linking or terminal groups. Based on the obtained correlations between the material composition and mechanical properties, two approaches for the improvement of fracture toughness in low-k dielectrics are proposed.

3.3.1 Introduction

The semiconductor industry is continuously improving the performance of microelectronic devices and their functionality through the scaling of integrated circuits and the maximization of transistor density.[12] This encourages the introduction of new materials, processes, chip designs, and packaging strategies into micro-/nano-electronic products. Among these new materials are insulating materials with a dielectric constant (k) less than that of SiO_2, so-called low-k dielectrics. However, finding a good low-k material has proven to be much more challenging than first expected due to a number of integration and reliability issues related to the porous nature of advanced low-k dielectrics.[12] First, there is the need of being compatible with the different lithography, etching, stripping, and cleaning processes that are used

in state-of-the-art integration schemes. Secondly, these materials must also have the sufficient mechanical strength to withstand the high shear stresses as well as harsh chemical environments that are involved during the chemical mechanical polishing process.[96,97] On top of that, since low-k dielectrics exhibit intrinsic tensile stresses and have increased coefficients of thermal expansion compared to SiO_2, thin film cracking and adhesion failure are serious thermal-mechanical reliability issues.[98] Thermo-mechanical deformation of the package during assembly and subsequent packaging reliability tests can induce large local stresses that can initiate and propagate cohesive and/or adhesive cracks in different back-end-of-line (BEOL) layers.[99] In the microelectronics industry, the elastic modulus, fracture cohesive strength, and interfacial adhesion of thin films are commonly used to assess the mechanical behavior, fracture behavior, and process compatibility of interlayer dielectric materials.

Nowadays, the most commonly used low-k dielectrics are porous carbon-doped silicas deposited by plasma enhanced chemical vapor deposition (PECVD) approach. Due to the limited control over the composition of the dielectrics deposited in plasmas, only the simplest implementations of carbon in the form of terminal methyl and bridging methylene groups have been attained so far.[100] In contrast, solution-processed organosilica dielectrics such as self-assembly based oxycarbosilanes allow the incorporation of a wide range of organic groups originating from the corresponding functionality of organosilica ester precursor molecules.[39] This flexibility enables the enhancement of the mechanical robustness of the low-k dielectrics by incorporating organic bridges.[101] In addition, the plasma damage susceptibility of the low-k materials is mitigated by increasing the relative carbon content in the films.[102] Nonetheless, previous studies have been focused on a relatively small number of functional groups, which were limited to short hydrocarbon chains, while larger organic groups would be desirable for the enhancement of the material's chemical stability. In this work, the impact of six different

organic groups on elastic properties, fracture properties, and adhesion of the low-k dielectrics to typical BEOL metal and dielectric barriers are investigated.

3.3.2 Experimental details

A range of low-k dielectric films was prepared from sols containing a mixture of two or three organosilica precursor molecules carrying a single terminal (Si-X) or linking (Si-X-Si) functional group. The reference dielectric coating was prepared from a sol based on two organosilica precursors incorporating Si-CH_3 and Si-CH_2-Si bonds into the organosilica matrix. Other films were prepared by replacing either half of the Si-CH_3 precursor with a precursor featuring a new terminal group or by completely changing the type of linking group precursor in the appropriate solution (Figure 3.5).

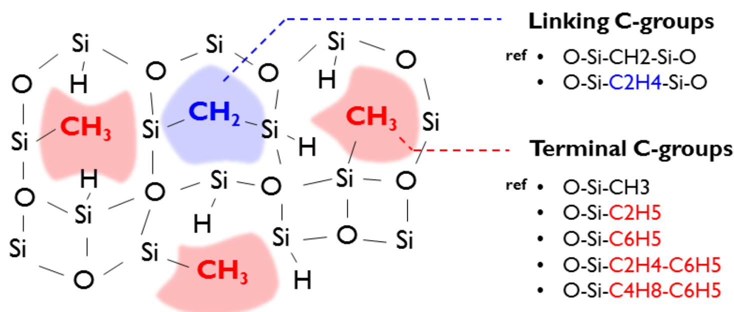

Figure 3.5. The prototypical organosilica matrix structure of the reference SOG material and the list of linking and terminal groups introduced in the modified precursor solution.

The sol also included a sacrificial organic template (porogen) in the form of amphiphilic polyethylene oxide-based molecules (Brij type) which were added to the solution to reach the target porosity in the range of 40-50%. It is important to note that the changes introduced into the solution may not be

simply translated into the same ratios of the functional groups in the deposited low-k layer. The composition of the actual films may be somewhat affected by the induced differences in hydrolysis and condensation reaction rates[103], by the interactions between the new precursor and surfactant micelles[104], by self-hydrophobization reaction during hard-bake[105] and eventually by the successive UV-curing process applied to the hard-baked films for complete removal of surfactant residues[106]. Therefore, to establish a reliable link between the composition of the low-k films and their mechanical properties comprehensive evaluation of the deposited materials was performed.

All the sols were spin-coated on top of 300 mm Si wafers with 1 nm of thermally grown silicon oxide. The films were subjected to short low-temperature annealing at 150°C for 2 min and then hard-baked at 300°C for 300 min in a nitrogen atmosphere. The relatively low temperature of the hard-bake process was chosen to prohibit the self-hydrophobization process which otherwise could consume part of the bridging groups thus changing the pre-defined ratio between the organic terminal and linking groups.[105] On the other hand, the annealing at 300°C resulted in an abundance of the surfactant residues residing inside the pores of hard-baked films. The sacrificial phase was removed during a successive 10 minutes UV-treatment ($\lambda > 200$ nm) performed at 350°C in He/H_2 atmosphere.

3.3.3 Results and discussion

Composition of SOG dielectrics. The structural motifs in the prepared SOG dielectric films were evaluated qualitatively and quantitatively by means of IR absorbance spectra analysis.

The composition of the UV-cured films was assessed by FTIR analysis. IR absorbance spectra were recorded on Nicolet 6700 FTIR spectrometer (Thermo Scientific) with a resolution better than 2 cm^{-1} averaging 100 spectra within the 400-4000 cm^{-1} range. Before the analysis, the substrate spectrum

(silicon with 1 nm of thermal oxide on top) was subtracted from the collected spectra.

At first, the IR absorbance spectra of the films were checked for the presence of target groups and for possible deviation from the ratios imposed by precursor concentrations in the sol. The full spectrum of the reference material is shown in Figure 3.6 and depicts the IR absorption bands of interest. The employed hard-bake and UV-curing conditions were optimized for the reference material to maximize the organosilica matrix cross-linking and minimize the loss of functional organic groups. Therefore, the reference spectrum exhibits negligibly small absorbance from Si-OH and Si-H bond vibrations, respectively. Figure 3.7 shows the detailed IR absorbance spectra of the other five films divided into two groups. The first group includes the films with short aliphatic groups (Si-C_2H_4-Si, Si-C_2H_5), while the second one consists of films containing bulky aryl groups (Si-C_6H_5, Si-C_2H_4-C_6H_5, Si-C_4H_8-C_6H_5).

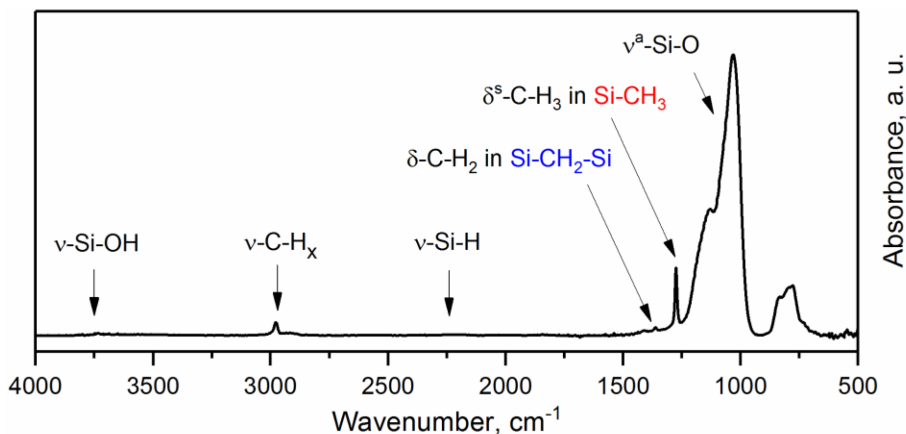

Figure 3.6. IR absorbance spectrum of the reference SOG material (thickness-normalized).

Considering the first group (Figure 3.3a-3.3c), one can conclude that both ethylene-bridged and ethyl-containing films are well cross-linked with Si-OH

bond concentration comparable to the one in the reference film. With respect to the loss of the newly introduced groups, the signal from Si-H bonds was used as an indicator of the organic groups being removed during the UV-curing step (no loss is expected during the hard-bake step at 300°C). This estimate is convenient for comparison between films with different organic groups connected to a silicon atom in the organosilica network, but it might be not very accurate as the formation of Si-H groups may be not the only outcome of the Si-C bond scission. Nonetheless, the formation of the Si-H bond is expected to be promoted by the He/H_2 atmosphere in the UV-curing chamber. According to this criterion, there is no apparent Si-CH_2-CH_2-Si group loss, although M. Redzheb *et al.* showed the principal possibility of such bond degradation under UV irradiation with $\lambda > 200$ nm.[107] In contrast, a part of the terminal ethyl group Si-CH_2-CH_3 was removed during the UV-curing process.

The absorbance spectra of the low-k films from the second group demonstrated the good extent of organosilica matrix cross-linking and the relatively low stability of the aryl-containing groups. Only the film featured with the longest tested aliphatic chain between the silicon atom and benzene ring has a somewhat lower concentration of Si-H bonds, which may be simply a result of bond breaking at a location other than Si-C group anchoring spot. One can also notice a significantly lower signal from Si-O bond in the films with aryl groups, which can be a sign of higher film porosity (this will be confirmed by ellipsometric porosimetry in the following paragraphs). Another important observation is that the ratio between Si-CH_3 and Si-O peaks seems to exceed half of that in the reference material which would be expected from the composition of the precursor solution. This may be also a consequence of higher porosity and thus increased pore surface area in the aryl-containing coatings.

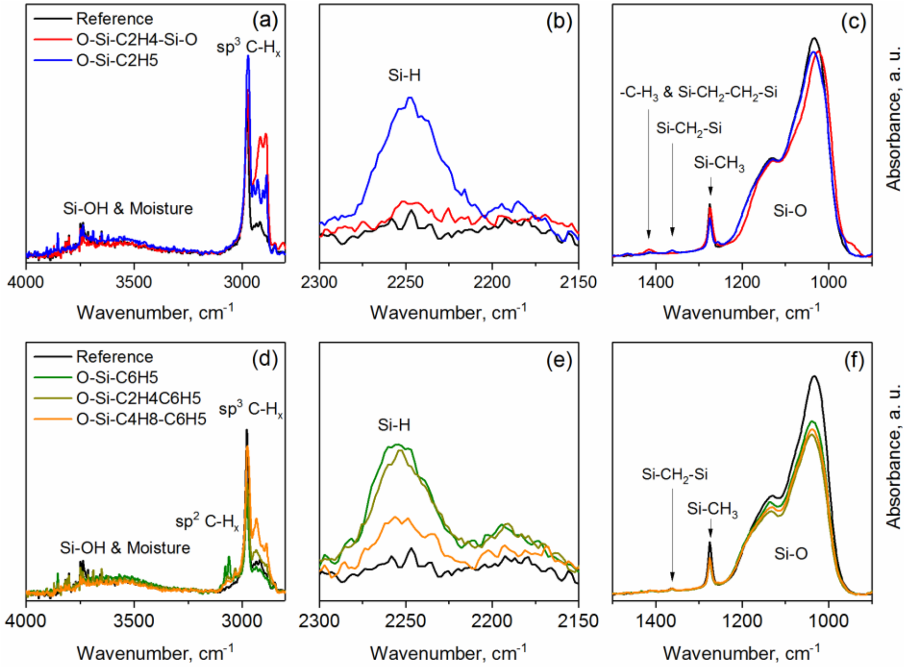

Figure 3.7. IR absorbance spectra of the studied oxycarbosilane coatings (thickness-normalized).

The simple qualitative analysis of the FTIR spectra allowed a crude comparison of the low-k coatings in terms of the presence or absence of the target organic functional groups and with regard to the completeness of the organosilica matrix cross-linking process. However, substantially more valuable information for interpretation of the material's mechanical properties can be obtained from quantitative analysis of IR absorbance, i. e. by extracting the actual concentration of the bonds constituting the organosilica matrix.

The concentration of vibrating bonds Q is linked to the corresponding absorbance in IR spectrum A via the expression derived from the definition of the absorption cross-section and Beer-Lambert law:

$$Q = A_s \int \frac{\alpha(k)}{k} dk \approx \frac{A_s}{k_0} \int_{k_1}^{k_2} \alpha(k) dk = \frac{A_s}{k_0} \int_{k_1}^{k_2} \ln 10 \frac{A(k)}{d} dk$$
$$= \frac{\ln 10 \cdot A_s}{d \cdot k_0} \int_{k_1}^{k_2} A(k) dk \tag{3.1}$$

where α is the absorption coefficient; d is film thickness; A_s is the inverse IR absorption cross-section of an oscillating bond responsible for an absorbance $A(k)$ peak located between k_1 and k_2 and centered at k_0 wavenumber values. The following integration ranges for the groups of interest were defined: 915-1300 cm^{-1} (Si-O), 1240-1310 cm^{-1} ($Si-CH_3$), 1345-1385 cm^{-1} ($Si-CH_2-Si$), 2140-2305 cm^{-1} (Si-H). In the case of the Si-O and $Si-CH_3$ groups, the overlapping peaks were deconvoluted before integration. The values of inverse absorption cross-section for the above groups were taken from the study of Y. Lin *et al*, who estimated them using organosilica low-k dielectrics of similar composition.[108] The absence of accurate inverse IR absorption cross-section values in the literature for ethylene-bridging and aryl-based groups within the organosilica matrix, makes the quantitative analysis of IR absorbance spectra rely on the following assumptions:

a) The concentration of newly introduced terminal groups ($Si-CH_2-CH_3$, $Si-C_6H_5$, $Si-C_2H_4-C_6H_5$, $Si-C_4H_8-C_6H_5$) is equal to the difference between concentrations of $Si-CH_3$ and Si-H bonds detected in the corresponding films. The assumption rests upon equal concentrations of precursors carrying $Si-CH_3$ and a new terminal group in the sol used for the preparation of the films. The connection to Si-H groups additionally supposes that the removal of a new terminal group during the UV-curing step results in the formation of exclusively Si-H bonds.

b) The concentration of $Si-CH_2-CH_2-Si$ is equal to the concentration of $Si-CH_2-Si$ groups in the reference material. The assumption originates

from the proportion of the precursors carrying the linking groups in the corresponding sols.

Although the above simplifications limit the accuracy of the quantitative, they are expected to preserve the trends in connectivity of the studied films, which is crucial for the assessment of mechanical properties. The extracted densities of the linking (Si-O, Si-CH_2-Si/Si-CH_2-CH_2-Si) and terminal (Si-CH_3/Si-C_xH_y, Si-H) bonds are summarized in Table 3.2. Since the bonds in the table represent all the nodes forming the organosilica matrix, one can additionally calculate the mean network connectivity number as an additional characteristic of the porous materials under study. This parameter is often used for the analysis of rigidity percolation threshold in random networks and was also shown to strongly correlate with the bulk modulus of organosilica materials. The mean connectivity parameter (<*r*>) is defined as an average coordination number (*Z*) of atoms or nodes forming a continuous network:

$$\langle r \rangle = \sum_i x_i \cdot Z_i \tag{3.2}$$

where x_i is the fraction of the *i*-atom able to form *Z* bonds. In these calculations, the terminal and linking functional organic groups were treated as single nodes with $Z = 1$ and $Z = 2$, respectively. Finally, to account for the atomistic effects of bonds on mechanical properties, the concentration of linking bonds weighted by the bond formation enthalpy was calculated. The enthalpies for Si-O, Si-C, and C-C were assigned to 452 kJ/mol, 318 kJ/mol, and 346 kJ/mol, respectively.[109]

The last two columns in Table 3.2 are interesting from the point of view that they provide quantitative information about the ratio between the linking and terminal organic groups as well as about the loss of terminal groups during UV-curing, which was earlier associated with the formation of Si-H groups. According to the values of the organic linking groups fraction, the films have a nearly equal number of terminal and linking groups. Regarding the group

loss, in the frameworks of the made assumption, it is equal to double the Si-H fraction values. This means that under the current UV-curing conditions, the loss of aliphatic and ethyl terminal groups approaches 25%. Nonetheless, it is important to note that this loss of carbon-rich organic groups did not generally nullify the targeted increase of carbon content in the low-k films as shown in Table 3.3 demonstrating the results of surface XPS analysis.

The percentage of carbon in the films with new linking or terminal aryl-based groups has increased by 25-30% as compared to the reference low-k material. Only in the film including the ethyl group the carbon content remained almost at the same level as in the reference film.

Table 3.2. Atomic concentrations (at%) of elements extracted from angle-integrated XPS spectra collected on low-k films under study.

Material description	C (1s)	O (1s)	Si (2p)
Reference	23.4	48.43	28.17
O-Si-CH_2-CH_2-Si-O	29.08	44.57	26.35
O-Si-CH_2-CH_3	24.81	47.85	27.34
O-Si-C_6H_5	30.49	44.3	25.21
Si-C_2H_4-C_6H_5	29.43	44.88	25.69
Si-C_4H_8-C_6H_5	30.19	44.23	25.58

Table 3.3. The results of the quantitative analysis of IR absorbance spectra collected on low-k films featured with a new functional group mentioned in the material description.

Material description	Density of linking groups*, x10^{22} cm^{-3}	Density of terminal groups**, x10^{22} cm^{-3}	Weighted linking bond density, x10^{22} cm^{-3}	Mean connectivity number	Fraction of organic linking groups***	Fraction of Si-H groups****
Reference	1.82 ± 0.38	0.173 ± 0.021	1.93 ± 0.41	2.537	0.60	0
O-Si-CH_2-CH_2-Si-O	1.82 ± 0.38	0.184 ± 0.024	2.12 ± 0.46	2.530	0.59	0.02
O-Si-CH_2-CH_3	1.78 ± 0.37	0.200 ± 0.033	1.88 ± 0.40	2.516	0.57	0.12
O-Si-C_6H_5	1.55 ± 0.32	0.188 ± 0.031	1.63 ± 0.34	2.504	0.54	0.11
Si-C_2H_4-C_6H_5	1.41 ± 0.29	0.190 ± 0.031	1.47 ± 0.31	2.488	0.49	0.11
Si-C_4H_8-C_6H_5	1.49 ± 0.31	0.190 ± 0.021	1.55 ± 0.33	2.495	0.47	0.03

**Linking groups include Si-O, Si-CH_2-Si / Si-CH_2-CH_2-Si*

*** Terminal groups include Si-H, Si-CH_3, Si-CH_2-CH_3/ Si-C_6H_5/ Si-C_2H_4-C_6H_5/ Si-C_4H_8-C_6H_5*

****Fraction of Si-CH_2-Si or Si-CH_2-CH_2-Si groups in the set of organic functional groups present in the film.*

*****Fraction of Si-H groups is calculated with respect to the overall concentration of terminal groups*

Porosity and pore structure of SOG dielectrics. The pore structure and porosity of low-k dielectrics are known to have a strong impact on mechanical properties.[92,110] Since the purpose of this study was to highlight the role of the functional groups, all sol solutions were designed to minimize the differences in porosity and pore size distributions. This was achieved by employing the same Brij-type surfactant molecules and comparable loading of the sacrificial phase. The actual pore structure parameters were evaluated by ellipsometric porosimetry measurements with toluene as adsorbate. The results of the measurements are summarized in Table 3.4.

Table 3.4. The pore structure parameters of low-k films under study.

Sample ID	Material description	Open porosity, %	Average pore radius, nm
A1	Reference	41.9	1.50
A2	$O\text{-}Si\text{-}CH_2\text{-}CH_2\text{-}Si\text{-}O$	40.8	1.40
A3	$O\text{-}Si\text{-}CH_2\text{-}CH_3$	42.2	1.40
B1	$O\text{-}Si\text{-}C_6H_5$	47.4	1.35
B2	$Si\text{-}C_2H_4\text{-}C_6H_5$	50.5	1.55
B3	$Si\text{-}C_4H_8\text{-}C_6H_5$	47.8	1.40

The values in Table 3.4 show that the low-k films are characterized by two levels of porosity and nearly identical pore dimensions. The low level of porosity is centered around 41% and corresponds to the films with aliphatic terminal and linking groups (A1-A3). The higher porosities of about 48% were measured for the films which contain aryl-based terminal groups (B1-B3).

Mechanical properties of SOG dielectrics. Mechanical properties of the low-k dielectric films were evaluated using two different experimental setups. At first, Young's modulus and fracture toughness of blanket layers

were measured using nanoindentation. Then the cohesion/adhesion strength of the low-k dielectric and its interfaces to adjacent metal TaN/Ta and dielectric SiCN barriers was evaluated with a 4-point bending test and compared to the fracture toughness values obtained on pristine films.

a. Intrinsic mechanical properties of SOG via nanoindentation. The elastic modulus of the low-k films was measured by nanoindentation using a Hysitron TI950 Triboindenter equipment with a cube corner indentation probe. Substrate-independent film properties were obtained by applying the analytical approach from Li-Vlassak, who adopted Yu's solution for the elastic contact problem for indentation on a layered half-space and extended it to the plastic regime.[111] Recently, this approach was successfully demonstrated on a variety of porous low-k films with porosities in the range of 24% to 47% and for film thicknesses between 148 nm and 235 nm by Okudur and co-workers.[112] Fracture toughness of the low-k films was extracted from cube corner indentation tests, which were performed under displacement-control mode with predefined maximum penetration depths between 50 nm and 200 nm in order to generate radial cracks through the film thickness. To calculate the fracture toughness values, we employed the mechanics model developed by Morris and Cook, which relies on crack geometry and intrinsic low-k film properties including thickness, Young's modulus, and stress as input parameters.[84,85] The crack lengths were measured from high-precision topography maps of the indents and further verified with GHz-scanning acoustic microscopy (not shown). In turn, the intrinsic low-k film parameters were evaluated using spectroscopic ellipsometry, nanoindentation (see above), and wafer bow measurements, respectively. The latter are summarized in Table 3.5.

Table 3.5. The parameters of low-k films used for extraction of fracture toughness in the framework of Morris-Cook model.

Sample ID	Material description	Thickness, nm	Young's modulus, GPa	Film stress, MPa
A1	Reference	214	5.6 ± 0.4	38
A2	O-Si-CH_2-CH_2-Si-O	229	5.6 ± 0.2	54
A3	O-Si-CH_2-CH_3	220	4.9 ± 0.3	36
B1	O-Si-C_6H_5	235	4.3 ± 0.3	33
B2	Si-C_2H_4-C_6H_5	234	3.1 ± 0.2	23
B3	Si-C_4H_8-C_6H_5	242	2.9 ± 0.2	25

To witness the impact of the pore structure on the values of Young's modulus and fracture toughness, the latter were plotted as a function of open porosity (Figures 3.8a, 3.8d). Although the negative effect of increased porosity seems obvious when A1-A3 and B1-B3 material subsets are compared, the variation of modulus values within the subsets cannot be explained only in terms of porous volume. When the dependency of fracture toughness on porosity is considered, the correlation becomes vague even on the subset level. These findings suggest that in our experiment porosity has a stronger impact on Young's modulus than on fracture toughness for which the changes in the material composition may play a more essential role.

To assess the correlation between the mechanical properties and composition of the low-k films enriched with bulky organic groups, Young's modulus, and fracture toughness were plotted against the corresponding mean network connectivity numbers and weighted densities of linking bonds extracted during the quantitative analysis of IR spectra (Figures 3.8b, 3.8c, 3.8e, 3.8f). The selected parameters are related to the organosilica backbone and therefore should ideally negate the effect of porosity difference between A1-A3 and B1-B3 films.

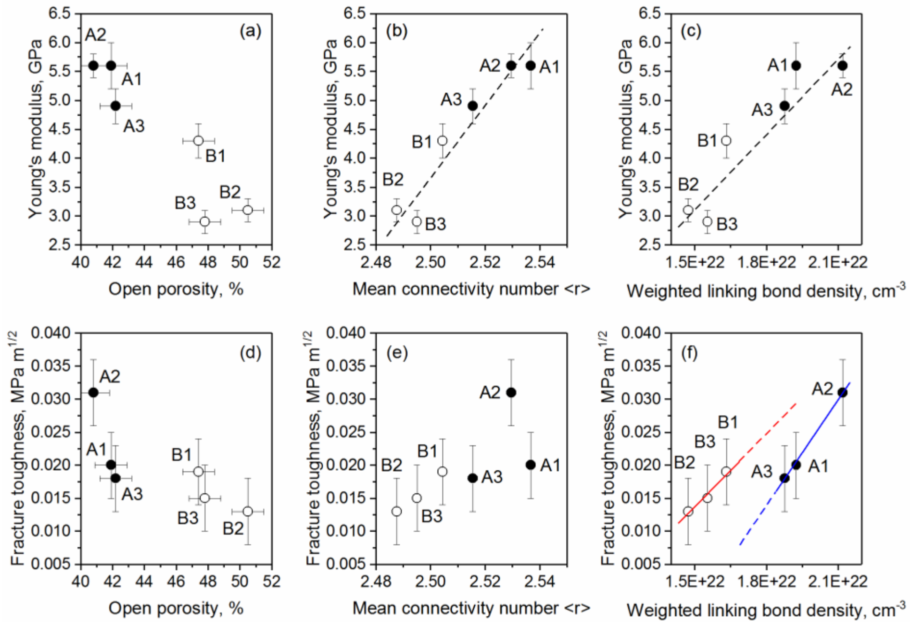

Figure 3.8. Young's modulus and fracture toughness as a function of open porosity (a, d), mean connectivity number (b, e), and weighted linking bond density (c, f).

In both plots showing the dependency of Young's modulus on organosilica matrix composition (Figure 3.8b, 3.8c) the positive linear trend well approximates the distribution of the experimental data, particularly with respect to the mean connectivity number. In contrast, the values of fracture toughness cannot be properly described with a single trend line in both coordinate systems (Figure 4e, 4f). However, such linear dependencies are clearly observed within the A1-A3 and B1-B3 subsets when the values of fracture toughness are plotted as a function of weighted linking bond density (Figure 3.8f). In coordinates of mean connectivity numbers, the linear trend is preserved only within the subset of B1-B3 films (Figure 3.8e).

To interpret the observed correlations, one should clarify the meaning of the employed composition-related parameters. Both parameters serve as indicators of the organosilica network connectivity. However, unlike the mean

connectivity number characterizing the network rigidity from the geometry viewpoint, the weighted density of linking bonds conveys information about the energy accumulated in covalent bonds forming the network. Based on these definitions, it is expected that the mean connectivity number would strongly positively correlate with the values of Young's modulus which are measured in the elastic regime, i. e. in the absence of bond breaking. Such a link between the mean connectivity number and Young's modulus observed in our study has been also confirmed in the works of H. Li and Y. Lin on computational models of organosilica materials and experimentally on PECVD low-k dielectric coatings.[94,113] In contrast, the phenomenon of film fracture is more complex on the molecular level because the crack propagation is realized via bond rapturing. So just geometrical considerations would not always explain the behavior of fracture toughness value like in the case of A1-A3 films in Figure 3.8e. To explain anomalously high cohesion strength in organosilica films containing ethylene bridges, G. Dubois *et al.* successfully applied the theory proposed by Lake & Thomas for polymers.[39] According to this theory, the crack growth is accompanied by the severing of every bond in the bridging group connecting the strained network nodes.[114] Our results nicely support this theory by showing that the best correlation between fracture toughness and network connectivity is achieved only when the dissociation bond energies of all linking groups are taken into account (Figure 3.8f).

Another important point to address is the mismatch of the fracture toughness linear trends plotted for A1-A3 and B1-B3 subsets in Figure 3.8f. The fact that comparable fracture toughness can be obtained in films with a lower weighted density of linking groups can be explained in terms of fracture concepts developed for organic polymer materials. In polymers, the fracture can occur by breaking primary covalent bonds and/or secondary van der Waals bonds through molecular "pull-out".[115] While in the above discussion on fracture toughness we were considering only the first contribution, we think

that the contribution of dispersive forces should not be ignored in the case of B1-B3 films containing bulky aryl-groups. We suppose that this additional term is able to effectively compensate for the lower density of linking covalent bonds in B1-B3 films.

b. Cohesion/adhesion analysis via 4-point-bending test. The interface adhesion strength of low-k dielectric films to TaN/Ta metal diffusion barriers and SiCN dielectric barrier was quantitatively measured using the four-point bending technique performed on a high-precision micromechanical test system from DTS Company.[116–118] To determine the crack location, both the detached surfaces were analyzed by XPS (not shown).

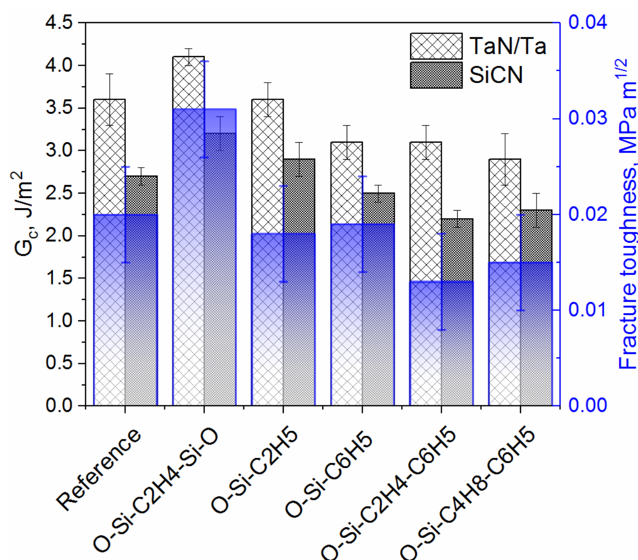

Figure 3.9. The cohesive strength as measured by the 4-point-bending test on stacks including the interface between the studied low-k films and TaN/Ta or SiCN. The results of fracture toughness measurements are laid over the bars with cohesive strength values to demonstrate a good correlation between them.

The results of the 4-point bending test are presented in Figure 3.9 together with the values of fracture toughness estimated on pristine films. The XPS analysis showed that in the stacks with TaN/Ta the crack was formed inside the low-k film close to TaN layer, while in the stacks with SiCN the crack appeared at the low-k/SiCN interface. Although the absolute values of energy release rate are generally higher for the stacks with TaN/Ta bi-layer, the relative changes of G_c-values between the low-k dielectrics under study follow the same pattern also matched by the values of fracture toughness. The perfect correlation between these three data sets allows concluding that the unmodified layer of low-k dielectric represents the weakest part in the employed stacks. This observation not only makes the employed nanoindentation methodology extremely valuable for the assessment of integration-relevant mechanical data, but it does also highlight the importance of thoughtful low-k material design as it directly affects the reliability of on-chip interconnects.

3.3.4 Conclusions

In this work, we studied five porous low-k materials derived from the reference film by modification of linking and terminal organic groups which corresponded to the replacement of 5-12% of the bonds in the material. The observed variations in YM, fracture toughness, and cohesion values highlight the importance of atomistic approaches for correct interpretation and assessment of mechanical properties in self-assembly-based oxycarbosilanes functionalized with bulky terminal or linking groups. While Young's modulus was found to follow mostly the geometrical network connectivity trends, fracture toughness was more sensitive to the type of bonds composing the organosilica network. For example, we demonstrated that the introduction of both long aliphatic linking groups and bulky aryl-based terminal groups are favorable for the enhancement of fracture toughness through the increase of

linking covalent bond density and through the increase of dispersive “matrix – pendant group” interactions, respectively. We hope that the material design guidelines provided in this study would allow other researchers to synthesize porous low-k dielectrics with the desired balance of carbon content and mechanical strength.

3.4 Leakage Current induced by Surfactant Residues in Self-assembly based Ultra Low-k Dielectric Materials

Abstract

In this work, we studied low-field leakage currents in the self-assembly based spin-on low-k dielectrics (k = 2.2) as it may be affected by the degree of the organic template decomposition. The distinct role of the template residues could be examined due to the remarkably different rates of organosilica matrix cross-linking and template decomposition during the hard-bake process. We found that the incomplete decomposition of the sacrificial organic phase is responsible for increased low-field leakage current through the dielectric. The analysis of photocurrent spectra and the results of electron resonance spectroscopy suggest that the degradation of electrical performance can be attributed to the presence of defect states ~5 eV below the insulator conduction band induced by the residues in the form of oxidized sp^3-carbon chains. The lowest leakage current is attained in the template-free material obtained by the introduction of additional broadband UV-assisted curing ($\lambda > 200$ nm).

3.4.1 Introduction

One of the major technological breakthroughs of the last two decades in IC On-Chip interconnects was the introduction of low-k materials which replaced the traditional silicon dioxide as an insulator in the first metallization layers[12,13]. Nowadays the mainstream approach for the formation of organosilica-based low-k dielectrics is plasma-enhanced chemical vapor deposition (PECVD), which is considered to be extendible to ultra low-k dielectrics with k-values in the range 2.0-2.5.[119] However, to reach such low

k-values, increased porogen/matrix precursor ratio should be used during the deposition. This condition induces the incorporation of unwanted graphite-like porogen residues into the low-k material, thus degrading its mechanical and electrical properties.[43,58,120,121] In contrast, solution-processed ultra low-k dielectrics including periodic mesoporous organosilica (PMO) films deposited by the spin-coating approach have demonstrated potential for superior mechanical stability achieved by appropriate selection of organosilica matrix precursors and better pore volume arrangement.[39,52,56] The role of porogen in such spin-on low-k dielectrics is fulfilled by surfactant molecules or so-called templating agents. During spin-coating accompanied by solvent evaporation, these amphiphilic molecules start forming micellar structures thus directing the assembly of the organosilica precursors and defining the pore structure of the film[93,122]. To make the film porous, the templating molecules need to be removed. The most common approach for extraction of the sacrificial phase in PMO powders is based on washing it away with acidified solvents before the organosilica matrix calcination.[123] However, the relatively long and complicated solvent extraction procedure is not favorable for PMO films in interconnects. Therefore, such self-assembly based low-k materials are typically processed in a way similar to PECVD films, i. e. by hardening of the organosilica matrix and decomposing the organic template in one high-temperature annealing step sometimes combined with exposure to UV-light.[124–127] The limited thermal budget of BEOL processes (T < 400°C) may result in only partial decomposition of this type of porogen which means that some organic residues may remain in the dielectric during the successive integration. Unlike the well-studied case of PECVD low-k materials, so far the porogen residues in self-assembly based spin-on low-k dielectrics did not get enough attention and the effect of these residues on electrical reliability is still not unraveled. In this work, we studied the impact of surfactant residues on the electrical properties of typical self-assembly based spin-on low-k dielectric films with a target k-value of 2.2 (SOG-2.2).

3.4.2 Experimental details

SOG-2.2 film preparation. The 200 nm thick films of SOG-2.2 were deposited from a proprietary sol on top of n-type 300mm Si wafers pre-passivated with thermally grown 1 nm thick SiO_2 (840°C, N_2O/H_2). The amphiphilic template molecules used in the sol consist of linear hydrophilic and hydrophobic blocks represented by polyethylene oxide (PEO) and saturated hydrocarbon $-(CH_2)_2-$ chains, respectively. After spin-coating and annealing at 150°C in air for 2 min (soft-bake), the films were sintered at 400°C in N_2 (hard-bake or HB) for different times to capture various stages of the surfactant decomposition. The selected hard-baked films were additionally UV-cured for 2 min using a broad-band spectrum lamp ($\lambda > 200$ nm) at the susceptor temperature of 385°C (this temperature corresponds to the wafer temperature of about 400°C).

SOG-2.2 film characterization. The IR absorbance spectra were recorded with a Nicolet 6700 spectrometer operating in transmission mode, while a sample was placed in a cell continuously purged with N_2.

The ellipsometric porosimetry measurements with water and toluene as adsorbate were carried out on a prototype porosimetry tool equipped with Sentech SE801 spectroscopic ellipsometer (400-800 nm wavelength range) mounted on a vacuum chamber.

The leakage current through SOG-2.2 films was measured on planar metal-insulator-semiconductor structures formed by thermal evaporation of 20 nm thick aluminum electrodes on top of low-k surface through the shadow mask with square holes of 700 μm x 700 μm. Additionally, a 0.3 μm thick aluminum blanket electrode was deposited on the back-side of the n-type Si-substrate. The current-voltage curves were recorded with Agilent 4156C parameter analyzer by sweeping the top electrode voltage in the range 0-100V. The current density through the stack (J) as a function of the electrical field

(E) was calculated by dividing the appropriate values of current and voltage by the contact pad area and the low-k film thickness, respectively. The obtained J-E curves were averaged over 8-11 single measurements for each of the tested stacks.

The ESR measurements were performed in K-band (~20.4 GHz) spectrometer at liquid He temperature (~4.2 K) on stacked samples of SOG-2.2 on top of thinned n-Si. Conventional adiabatic first derivative absorption spectra (dP_{μ}/dB, where P_{μ} represents the incident microwave power) were recorded at the applied magnetic field B parallel with the [100] normal to the sample surface. Defect densities and g-values were determined using a co-mounted calibrated Si:P marker sample ($g = 1.998696 \pm 0.00002$ at 4.2 K).

The extinction coefficient spectra of SOG-2.2 films were extracted from the spectra of reflection coefficients measured by a spectroscopic ellipsometer KLA-Tencor Aleris 8510 operating in the wavelength range of 150-850 nm. Three generalized harmonic oscillators were used to describe the dispersion of the optical properties of the SOG-2.2 layer in the employed optical model stack.

3.4.3 Results and discussion

Surfactant residues in SOG-2.2. We have previously shown that the employed hard-bake conditions during the preparation of SOG-2.2 films result in relatively fast solidification of the organosilica backbone – changes in infrared (IR) absorbance of organosilica-related peaks and thickness reduction induced by the condensation of unreacted silanols are negligible already after 2 min HB.[128] The aforementioned decoupling of the organosilica matrix cross-linking and the template decomposition process natively attainable in self-assembly based low-k dielectrics makes it possible to establish the direct link between the leakage current and surfactant residues.

The different phases of the template decomposition can be evidenced via combined analysis of IR absorbance spectra and ellipsometric porosimetry based on the adsorption/desorption of toluene and water vapors. The IR absorbance spectra in 2800-4000 cm^{-1} range (Figure 3.10a) contain fingerprints of the sacrificial organic phase in the form of peaks arising from the asymmetric C-H bond stretching in $C\text{-}H_2$ group (narrow peak at 2925 cm^{-1}) and from the stretching of hydrogen-bonded O-H groups (broad peak centered at around 3400 cm^{-1})[129]. The first peak is largely attributed to the hydrophobic aliphatic block of the surfactant molecule while the O-H peak reflects the presence of the hydrophilic PEO block and its decomposition by-products. One can clearly see the continuous decrease in the absorbance peak related to $\text{-}C\text{-}H_2\text{-}$ groups as the hard-bake time varies from 2 min to 120 min. The lowest $\text{-}C\text{-}H_2\text{-}$ absorbance is detected for the samples which were additionally UV-cured. On the other hand, the peak from –OH groups nearly disappears after hard-bake times longer than 30 minutes. This indicates the noticeably faster decomposition of the hydrophilic by-products derived from PEO part of the micelles. Similar observations have been made by E. Finocchioa *et al.* in the study on the thermal decomposition of PEO and PEO-$(CH_2)_x\text{-}CH_3$ surfactants intercalated into montmorillonite clays.[130] There it was shown that the decomposition of the embedded polymers occurs via fragmentation of PEO chain and successive formation of short-chain esters, aldehydes, alcohols, and esters. The final product of decomposition at high temperatures (in the range 350-450°C) is a thermally stable carbon-rich phase.[131]

Complementary to the FTIR analysis, we used ellipsometric porosimetry to trace the changes in the refractive index of the porous layer during the adsorption/desorption cycle of water or toluene. The refractive index of the low-k film measured at the saturation pressure of the adsorbate can be recalculated into its respective volume fraction using the Lorentz-Lorenz effective medium approximation.[89] In the case of toluene as adsorbate this

fraction corresponds to the open porosity of the porous layer, while in the case of water the volume fraction serves as an estimate of pore wall hydrophilicity.

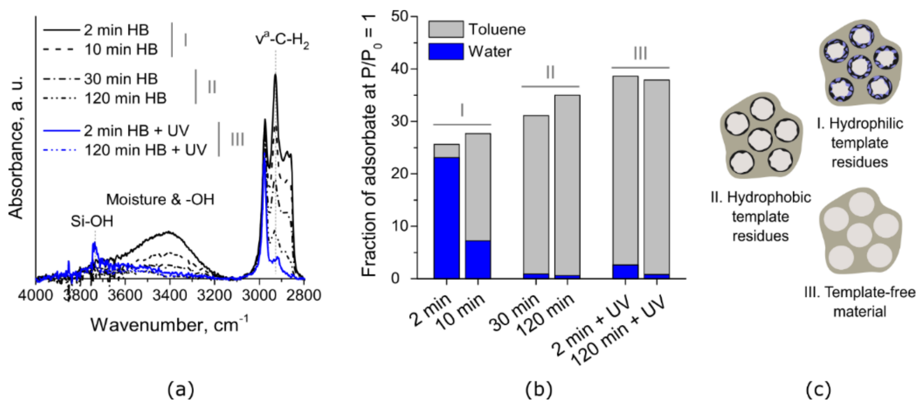

Figure 3.10. Changes in composition and pore structure of the SOG-2.2 films upon decomposition of the organic template during the hard-bake process are evidenced by the evolution of (a) IR absorbance and (b) adsorption capability of toluene and water related to open porosity and material hydrophilicity, respectively. (c) Schematic representation of three different stages of the template decomposition in SOG-2.2.

The fact of surfactant removal during the hard-bake process is reflected in Figure 3.10b by the simultaneous increase of open porosity upon longer annealing. The largest open porosity values are found in the UV-cured SOG-2.2 films, which confirms the high efficiency of this post hard-bake UV-treatment as porogen decomposition approach. Considering the UV-cured SOG-2.2 films as porogen-free coatings, one can get an estimate of how much organic residues are remaining in porous film by subtracting the porosity value from that of the UV-cured SOG-2.2 films. According to this estimate, the volume fraction of the residues in the hard-baked films varies from 3% to 13%. The results of the water adsorption test are in good agreement with the IR absorbance spectra. The amount of water adsorbed in the SOG-2.2 film hard-baked for 2 min is nearly the same as that of toluene which implies

pronounced hydrophilicity of the pore surface. There is less water adsorbed in the pores of SOG-2.2 film hard-baked for 10 min and after 30 min annealing the SOG-2.2 film becomes hydrophobic. Such behavior correlates well with the presence of hydroxy -OH groups on the surface of pores represented by the coating of surfactant decomposition by-products.

Summarizing the above observations, we can distinguish three types of pore wall surface functionality in hard-baked SOG-2.2 films (Figure 3.10c): hydroxyl-rich hydrophilic residue coating observed at the early stage of the surfactant decomposition (I), hydrophobic coating of carbon-enriched decomposition products formed after prolonged annealing exceeding 30 min (II) and surfactant-free organosilica pore surface achieved by additional UV-curing treatment (III).

Leakage current in SOG-2.2. The *J-E* curves recorded on the stack including SOG-2.2 films exhibit a strong impact of the hard-bake sequence – the leakage current variation at 2 MV/cm spans over 2 orders of magnitude (Figure 3.11). The largest leakage current is found in SOG-2.2 films hard-baked for 2 min and 10 min. Taking into account the hydrophilic nature of the surfactant residues in these cases, the adsorbed moisture can be considered the main cause for the degraded dielectric properties of the porous organosilica film. The presence of moisture in the integrated low-k dielectric layer is known to produce a hump in the *J-E* curve in the low-field range and to significantly reduce the time-to-breakdown of the porous dielectric[132–134]. The leakage current gets noticeably lower as soon as the pore surface of the hard-baked SOG-2.2 films becomes hydrophobic and reduces even further as the amount of the residues goes down reaching the lowest values in the UV-cured SOG-2.2 films.

To understand the origin of the observed correlation between the leakage current and the hydrophobic residues, we additionally investigated the SOG-2.2 films with internal photoemission (IPE) and electron spin resonance (ESR) spectroscopies, which proved to be helpful in the determination of the defect

level position in the band gap of organosilica dielectrics and in relating the corresponding defect levels to a certain defect representation, respectively[135–139].

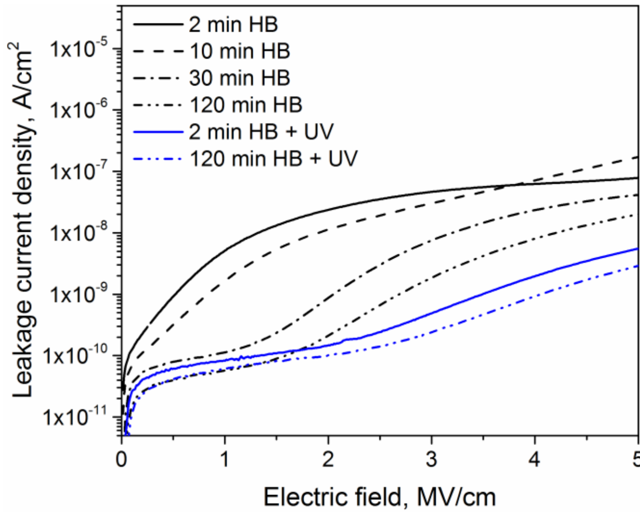

Figure 3.11. Leakage current density as a function of applied electric field recorded on MIS-structures with SOG-2.2 low-k films hard-baked (HB)/hard-baked and UV-cured (HB+UV) for different times.

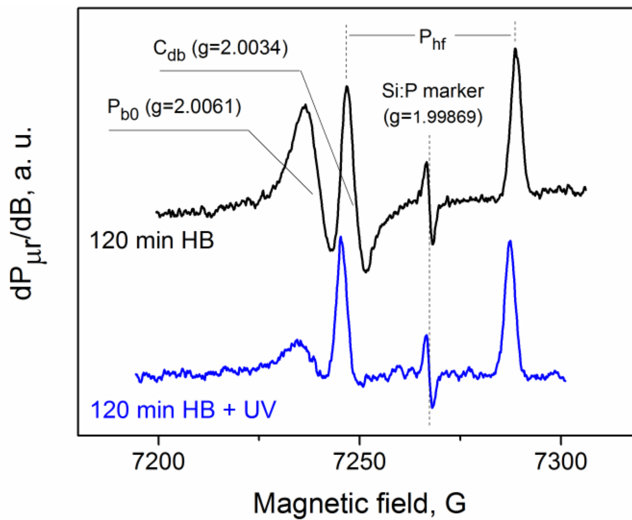

Figure 3.12. K-band ESR-spectra of spin-on low-k dielectric films hard-baked for 120 minutes (with and without extra UV-curing).

Table 3.6. Defects observed by ESR and their inferred areal density in SOG-2.2/n-Si stacks prepared with and without additional UV-curing; ΔB represents the peak-to-peak linewidth.

ESR defect type	g-value	ΔB, G	Areal density, cm^{-2}	
			120 min HB	120 min HB + UV
P_{b0}	2.0061	8.0	1.1×10^{13}	4.2×10^{12}
C_{db}	2.0034	3.3	1.4×10^{12}	5.9×10^{11}

At first, we checked the presence of paramagnetic defects in SOG-2.2 films hard-baked for 120 min. The recorded ESR spectra are shown in Figure 3.12, while the extracted defect densities and g-values are summarized in Table 3.6. Apart from the hyperfine-split doublet stemming from the phosphorous dopant atoms in the Si-substrate, two more absorption bands could be resolved in the ESR spectra of both the just hard-baked and additionally UV-cured SOG-2.2 films. The first paramagnetic defect positioned at g = 2.0061 concerns dangling Si-bond at the Si/SiO_2 interface (P_{b0}-type).[140] Since the silicon substrates were passivated with high-quality thermal oxide before deposition of the low-k films and the hard-bake process was done in an inert nitrogen atmosphere, the Si/SiO_2 interface traps are expected to remain unaffected (no passivation by hydrogen). Therefore, we exclude these defects from further consideration as a factor that would explain the observed strong variation of the low-field leakage current. The same applies to the sample subjected to the additional UV-curing, though the concentration of ESR-active P_{b0} states is reduced as a result of electron trapping induced by photoemission from the n-Si surface.[141] The second detected defect with characteristic g = 2.0034 can be attributed to the presence of carbon dangling bonds (C_{db}) in the bulk of the low-k dielectric. Based on the previously reported results of ab-initio g-tensor simulation of the carbon-dangling bond, one can infer that the carbon with an unpaired electron in SOG-2.2 samples is likely back-bonded to several oxygen atoms $(O_xC_y)\equiv C\bullet$.[142]

Since the formation of oxidized carbon-containing molecules is known to occur during PEO decomposition[143] and the thermal degradation of the hydrophobic $(CH_2)_n$-chain proceeds via the formation of multiple hydrocarbon radicals,[144] we suggest that the dangling carbon bonds likely originate from residues of the decomposed sacrificial organic phase. This conclusion is supported by the systematic study of T. Pomorski *et al.* who demonstrated the general link between the C_{db}-type defects and low-field leakage current in various types of organosilica low-k dielectrics.[139] Even more explicitly, the connection between the carbon dangling bonds and trap-assisted leakage current in low-k dielectrics has been evidenced via measurement of spin-dependent tunneling current on dense and porous PECVD low-k materials.[145] The two-fold reduction in density of the paramagnetic C_{db}-type defect concentration induced by UV-curing and the associated drop in leakage current nicely falls into this trend. Interestingly, unlike the sp^2-bonds enriched porogen residues in PECVD dielectrics[57,58], the decomposition by-products of the surfactant molecules seem to consist largely of an sp^3-hybridized carbon-based phase. This follows from the light absorption onset lying at $\lambda < 200$ nm in the SOG-2.2 films regardless of the hard-bake sequence as detected by the additionally performed vacuum ultra-violet spectroscopic ellipsometry (VUV-SE) measurements (Figure 3.13).[146]

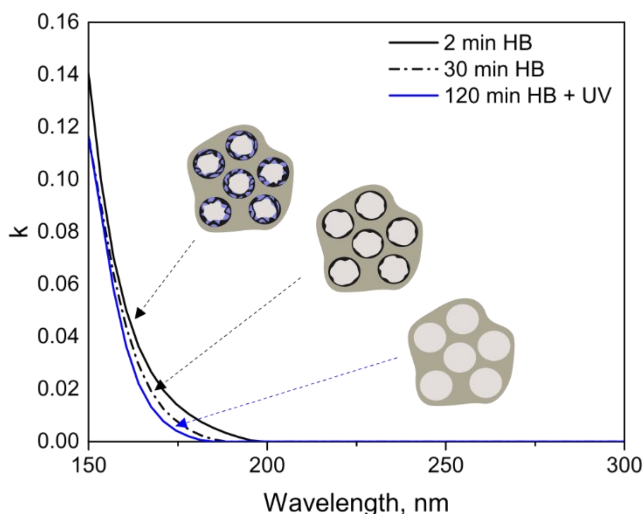

Figure 3.13. Extinction coefficient (k) spectra obtained by VUV-SE for SOG-2.2 films followed different hard-bake sequences. The inset sketches represent the stage of the surfactant decomposition.

The link between the hydrophobic organic residues and the leakage through SOG-2.2 films was studied by analyzing the photocurrent on two MIS stacks composed of SOG-2.2/n-Si and semi-transparent gold electrodes on top. The stacks were irradiated by monochromatic light with photon energies varied over the range 3.1-6.0 eV with a constant spectral resolution of 2 nm. The photocurrent spectra were recorded while applying various positive or negative bias voltages to the gold electrode. The quantum yield values defined as the photocurrent normalized on the incident photon flux are plotted using $Y^{1/3}$-hv coordinates to determine spectral thresholds as illustrated in Figure 3.14.[147]

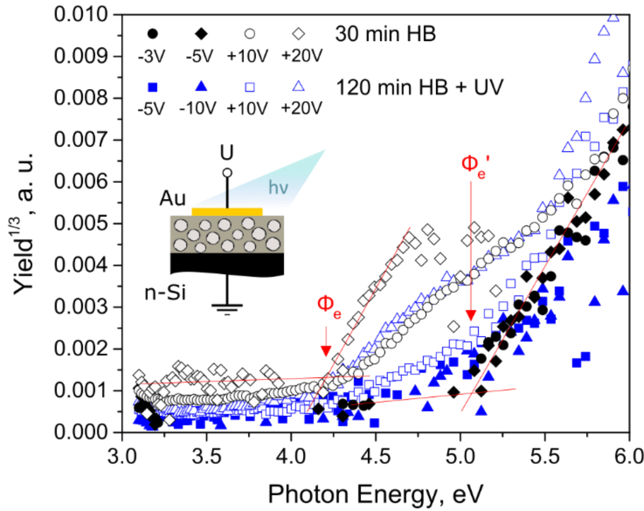

Figure 3.14. Spectral plot of the IPE quantum yield comparing results obtained on SOG-2.2 film containing hydrophobic template residues (30 min HB) and the surfactant-free version of SOG-2.2 layer (120 min HB + UV). Lines guide an eye; Vertical arrows indicate the spectral thresholds: $\Phi_e \approx 4.2$ eV – Si/SOG-2.2 electron IPE threshold; $\Phi_e' \approx 5$ eV – defect photo-depopulation threshold.

The photocurrent spectra measured under the positive and negative bias voltages show two distinct current onset points in both SOG-2.2 films situated at the photon energies $\Phi_e \approx 4.2$ eV and $\Phi_e' \approx 5$ eV, respectively. The absence of the former electron threshold under negative bias voltages suggests that it corresponds to electron transitions at the Si/SiO_2 interface. In particular, the extracted value of about 4.2 eV can be attributed to the emission of an electron from the valence band of the Si-substrate into the conduction band of the thin passivating SiO_2 layer[148]. When the negative bias is applied, electron transport through the MIS stack is possible via the emission of the electrons from the gold electrode or via depopulation of the defect states in the SOG-2.2 dielectric. There are several factors that speak in favor of the electron traps depopulation path. The first sign is given by the negligible variation of the

photocurrent under various negative bias voltages applied. Furthermore, one can discern a similar threshold of about 5 eV in the photocurrent spectra recorded under positive bias voltages. Such symmetry of the photocurrent implies the transfer of the charge carriers into the conduction band of SOG-2.2 independent of the adjacent interfaces at $h\nu > 5$ eV. In the IPE study of S. Shamuilia *et al.* in which various combinations of low-k dielectrics and metal electrodes have been screened,[136] the universally observed electron injection threshold around 4.5 eV was attributed to adsorbed moisture representing the common type of defects formed at the surface of the tested low-k dielectric. The current work demonstrates that the self-assembly based SOG-2.2 coatings show a higher electron injection barrier and are unlikely to be affected by the surface states in the form of adsorbed moisture after prolonged hard-bake (see Table 3.6). Instead, we suggest that the onset of the photocurrent at $h\nu \approx 5$ eV is caused by the depopulation of residues-related defect states dispersed in the bulk of SOG-2.2 films. The statement is supported by a somewhat lower photocurrent measured at $h\nu > 5$ eV in the SOG-2.2 film subjected to UV-curing, which was shown to possess a lower concentration of the C_{db}-type defects. This interpretation would also be consistent with the suggestion that the defects states associated with the carbon dangling bonds in PECVD low-k dielectrics lie in the lower part of the band gap (2-6 eV below the conduction band).[149]

3.4.4 Conclusions

To conclude, our study provides insight into the complex process of surfactant decomposition in PMO-like low-k materials and establishes the link between the organic decomposition by-products and the electrical reliability of the dielectric coatings. While the negative impact of the hydrophilic residues formed at the initial stage of the material preparation is rather obvious, the situation with the hydrophobic residual organics is less

straightforward due to its relatively small fraction and minimal impact on the overall dielectric constant. We demonstrated that the predominantly sp^3-hybridized hydrophobic surfactant decomposition by-products occupying 7% of the SOG-2.2 volume result in more than an order of magnitude increased leakage current. We identified the source of the degraded electrical performance as oxidized sp^3-bonded carbon chains which induce defect states energetically positioned in the bottom part of the dielectric band gap. These results bring awareness of the fact that the traditionally used route for removal of the surfactant in PMO-like dielectrics via simple hard-bake may not lead to the desired dielectric properties of the low-k films. At the same time, we showed that the additional short UV-curing with a broadband lamp ($\lambda > 200$ nm) serves as an efficient approach for the removal of the residual organic phase from the self-assembly based porous material.

3.5 Surfactant residues as protective coating against plasma-induced low-k damage

Abstract

The chapter describes a new approach for the reduction of plasma-induced damage in self-assembly based porous ultra low-k organosilica dielectrics. The concept is based on the retention of the partially decomposed sacrificial organic phase (template) into the pores of the low-k film during plasma exposure. The amount of template residues can be controlled by varying the hard-bake process time. It is shown that those residues are uniformly distributed throughout the film in the form of pore wall coatings. After plasma processing, the remaining residues are removed by means of a UV cure. Plasma damage to the underlying organosilica matrix was assessed by exposure of the differently hard-baked low-k films to fluorine-rich Ar/SF_6 plasma and to a commonly used Ar/CF_4 plasma. In the case of SF_6-based plasma, the thickest coating, estimated to be around 0.4 nm, enables a nearly damage-free etch process without any carbon depletion or k-value degradation along with limited shrinkage induced by post-etch UV-curing (< 4.5%). In contrast, the protection degree is lower in CF_4-based plasma which was attributed to the inability of the template residues to suppress the film degradation induced by VUV photons in the plasma. Nonetheless, the demonstrated results highlight the overall efficiency of a simple and scalable route for low-damage integration of highly porous self-assembly based low-k dielectrics.

3.4.1 Introduction

The degradation of intrinsic properties of porous organosilica (OSG) low-k dielectrics during the patterning process is one of the key challenges for the integration of these materials into the damascene interconnects fabrication process.[150,151] The problem is particularly severe for ultra low-k dielectrics with porosity exceeding 20-30%, i. e. beyond the percolation threshold.[152] In this case, the pores become fully interconnected which allows deep penetration of damaging plasma species and extraction of organic groups from the OSG matrix.[153]

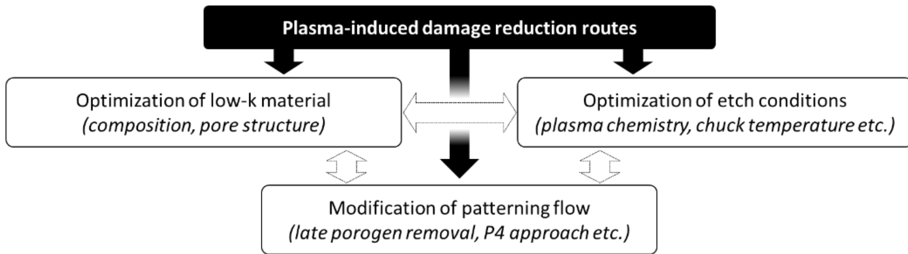

Figure 3.15. Three general routes for reduction of plasma-induced damage to low-k dielectric during the patterning process.

Over the last decade, different strategies for the mitigation of plasma damage to low-k dielectrics have been investigated. The proposed solutions can be roughly grouped into three categories (Figure 3.15).

The first group includes methods that focus on the optimization of composition and pore structure of low-k dielectrics. With respect to the composition of the organosilica materials, the most prominent example of such modifications is the increase of carbon content driven by the demonstrated positive correlation between the fraction of carbon in low-k dielectric and its stability in patterning plasma. The increase in carbon content

may be achieved with the addition of extra terminal Si-CH_3 groups.[102,154] However, the introduction of carbon in the form of Si-CH_2-Si bridging groups seems to be a preferred approach as in this case the carbon concentration can be increased without compromising the organosilica matrix connectivity and associated mechanical robustness.[39] Besides, the recent ab-initio study on the interaction of Si-CH_2-Si bridging groups with oxygen radicals showed that the groups may act as oxygen radical absorbers.[38] The discovered lower activation barrier for the reaction between oxygen radical and Si-CH_2-Si group as compared to the Si-CH_3 group may prevent deep penetration of oxygen radical and deep depletion of intrinsic organics from the low-k layer. On the other hand, the stability of porous low-k material in plasma can be strongly influenced not only by the fraction of porous volume but also by its distribution, i. e. by pore connectivity, by pore ordering, or by dimensions of pores and connections between them.[155] Taking the above factors into account, the ideal porous low-k dielectric would possess uniformly distributed closed micropores. In this respect, the closest to the ideal type of organosilica materials are periodic mesoporous organosilicas (PMOs), which are being actively investigated for applications as ultra low-k dielectrics.[52,156,157]

The second group of factors that has a strong and very diverse impact on the composition of the etched low-k material is etching gases. The typical plasmas for the etching of silica-based materials are based on fluorine-based species, which upon dissociation are able to convert silicon oxide into volatile silicon fluoride species. Since the interaction of just fluorine radicals with ultra low-k dielectrics was shown to lead to deep modification of the intrinsic organic groups and even pore structure, the reactivity and diffusivity of fluorine are often counter-balanced by using gases with a high C/F ratio, e. g. CHF_3, CH_2F_2, C_4F_8, *etc*.[158] The presence of carbon-rich species induces the formation of a fluorocarbon-based polymer layer at the etch front. The thickness and composition of the fluorocarbon layer define the ability of the passivating layer to limit the fluorine diffusion and thus mitigate the plasma-

induced damage. The modulation of the passivating fluorocarbon layer is complicated by its dependency on the composition, porosity, and pore structure of the low-k dielectric being etched. An alternative type of passivating layer limiting the diffusion of fluorine radicals was proposed by Posseme *et al.*[159] He showed that the use of carbon-free chemistries based on silicon-containing gases such as SiF_4 or $SiCl_4$ in combination with N_2 or O_2 can reduce carbon depletion due to the formation of SiN_x- or SiO_x-based sealing layers at the surface of etched porous material. Although O_2 or N_2 gases are sometimes added to modulate the passivation layer formation, the excess of these gases may lead to a situation when the interaction of oxygen or nitrogen radicals with the low-k film becomes the dominating damage mechanism. In particular, oxygen radicals are known to diffuse deeply inside the low-k layer depleting the organic groups.[160] Another important aspect in the patterning plasmas is VUV-radiation generated by excited plasma species. The common source of VUV photons in patterning plasmas are inert dilution gases, e. g. argon, which is responsible for the generation of intense resonant emission lines at 104.8 and 106.7 nm.[161] Though the radiation from other species like O-radicals and CH_x species should not be ignored.[162] This challenge is difficult to address from the plasma point of view. As a possible solution, pulsed plasma processing would effectively reduce the dose of VUV-radiation.[163,164] One more interesting approach which falls into the category of the plasma etch process optimization is low-k dielectric etching at cryogenic temperatures. It was shown by F. Iacopi *et al.* that at such low temperatures the penetration of plasma-generated radicals into a porous film is strongly limited due to the increase of both the sticking coefficient and recombination of the diffusing species.[165] The etch process performed with SF_6 at cryogenic temperatures has an additional mechanism of pore protection associated with the formation of relatively non-volatile etch by-products in the form of SiO_xF_y and -C_xH_yOH condensed inside the pores.[166,167] The removal of the condensate is achieved by simple post-etch annealing. Since the condensation of the

reactive by-products may negatively affect the composition of the low-k dielectric, and the required low process temperatures limit the applicability of the cryo-etch concept, the evolution of the approach was suggested. The key idea of the new method is to use high boiling point etchants which would enable both condensation and etching at higher temperatures. The optimal selection of the etchant molecule is not straightforward as it should enable the etching of the dielectric upon dissociation and maintain its stability in the condensed state to work as a protective phase.[168]

The last group of methods is related to the modification of the patterning flow by the addition of extra processing steps altering the composition or pore structure of the low-k layer before or after the plasma etching. The simplest example of the modified flow is a patterning process combined with a restoration post-treatment aimed at minimization of the low-k damage, i. e. recovery of the dielectrics' hydrophobicity and its k-value. This can be achieved by the elimination of silanol Si-OH groups and adsorbed moisture via silylation reactions,[169,170] exposure to methane-based plasmas,[171] or via annealing in an inert atmosphere with or without simultaneous exposure to UV-light.[172] Extensive research in the field of low-k dielectric restoration with various silylation molecules ($Si\text{-}(R)_3$) showed that the approach is efficient only when the plasma damage is concentrated at the surface of the low-k layer due to limited diffusivity of the silylation precursor. One recent attempt to alleviate this limitation was undertaken by researchers from Fraunhofer ENAS, who proposed to use plasma for the fragmentation of silylation molecules.[173,174] Nonetheless, it does not cancel the fundamental drawback of the silylation strategy – the increase of density and correspondingly dielectric constant of the material upon the incorporation of silyl-groups. Similarly, the post-treatment of etched low-k dielectric material with methane-based plasma suffers from limited restoration depth and results in the formation of a dense carbon-rich top layer. In contrast, a simple annealing/UV-curing of plasma-treated low-k layer aims at the reduction of the material density by promoting

moisture desorption and condensation of silanol groups.[175] However, the complete elimination of silanol groups requires temperatures above 600°C which are above the stability of organosilica dielectrics.[176]

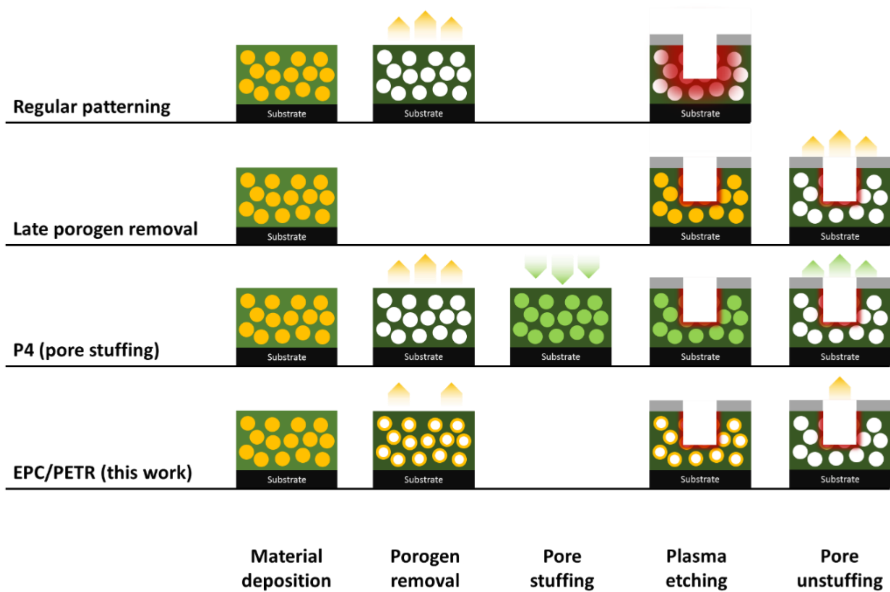

Figure 3.16. Modification of the regular patterning flow in late porogen removal, P4, and EPC/PETR low-k integration schemes. The carbon-depleted layer formed during etching is depicted in red. The intrinsic sacrificial phase (porogen) is shown in yellow and light green is used to denote the pore-stuffing polymer.

The imperfections of the above post-etch treatments can be compensated by employing the patterning strategies which strongly limit the depth of low-k damage. The core idea behind these innovative approaches is based on a temporary, partial, or complete elimination of porosity (Figure 3.16). The first solution suggested shortly after the initiation of research on porous low-k dielectrics prepared with sacrificial porogen phase was so-called porosity last

or late porogen removal strategies for low-k dielectric integration.[177,178] The strategies were assuming preservation of the sacrificial organic phase in the low-k dielectric during patterning and possibly even further – during metallization steps. However, the realization of this idea encountered several obstacles such as considerable shrinkage of the low-k dielectric of about 10% upon removal of the porogen phase which would increase the level of mechanical stress in metallization layers. Roughly a decade later this issue was addressed in the new Post-Porosity Plasma Protection (P4) method proposed by researchers from IBM.[179,180] This method, adopted from the membrane community, was based on the stuffing of pores of fully cured and mechanically stiff porous ultra low-k dielectric with polymer, which could be removed right after the patterning or CMP steps with nearly no shrinkage. Between the stuffing and unstuffing steps, the introduced polymer protects the organosilica framework of low-k dielectric from in-diffusing species during exposure to patterning plasmas or deposition of metal barrier. The P4 method was found to be particularly efficient for plasma damage reduction in highly porous materials. Despite these advances, the P4 method poses several application challenges such as the selection of optimal stuffing polymer (in terms of pore filling, plasma protection, thermal stability, *etc*.), the impact of possible polymer residues on electrical reliability as well as compatibility with low-k dielectrics of medium porosity (open porosity ~25%) which are currently favored by the semiconductor industry. One of the apparent shortcomings of P4 technology is its disruptive nature as compared to the late porogen removal approach. The need for the introduction of non-trivial stuffing and de-stuffing steps significantly complicates the integration flow. The compromise between the two methods is the effective porogen control (EPC) strategy which is based on a stepwise removal of the sacrificial phase from PECVD low-k dielectric.[181] The first portion of the porogen phase is removed right after the deposition of hybrid film via annealing. The thermal treatment hardens the organosilica matrix and lowers the shrinkage during the

second annealing step performed after patterning to complete the porogen removal. This approach allowed to mitigate the plasma-induced k-value increase by about 20%, though little or no information was provided by the authors about the efficiency of the post-etch porogen removal and film shrinkage. In this chapter, we investigate a similar approach applied to a solution-processed low-k material, the formation of which involves co-self-assembly of templating surfactant molecules and organosilica precursors. An outstanding representative of such dielectric materials is a family of periodic mesoporous organosilicas (PMOs), which are being actively investigated as a potential successor of PECVD dielectrics into advanced technology nodes. We showed that the partially decomposed polyethylene oxide based surfactant molecules commonly used during PMO synthesis can act as an efficient plasma protective phase and can be completely removed after the etching step with minimal film shrinkage, which forms prerequisites for damage-free patterning of the self-assembly based low-k films.

In the first part of this chapter, the concept of the post-etch template removal (PETR) strategy is introduced. Then the key assets of the proposed method are validated including the matrix cross-linking rate, uniformity of the surfactant residues distribution throughout the low-k layer and the efficiency of the residue removal process. The next part of the chapter reports on the interaction of the residue-containing low-k dielectric with Ar/SF_6 and Ar/CF_4 plasmas. The final part elaborates on the impact of VUV-photons generated in plasma on the template residues.

3.4.2 Template management strategy

In this work, the proposed concept of post-etch template removal was validated on self-assembly based low-k dielectric films targeting the k-value of 2.2 (SOG-2.2). The films were deposited on 300 mm n-type Si wafers from a sol containing a mixture of organosilica esters and amphiphilic molecules as

a template. The molecules consist of linear hydrophilic and hydrophobic blocks represented by polyethylene oxide (PEO) and polyethylene (PE) hydrocarbon chains, respectively. After spin-coating, the films were soft-baked at 150°C in air to remove the solvent and initiate cross-linking of the organosilica matrix. Further film hardening and organic template decomposition were realized by sintering at 400°C in N_2 (further referred to as hard-baked or HB) for different times to capture various stages of the template decomposition. The combination of 120 min hard-bake with an additional UV-curing (λ > 200 nm) at a susceptor temperature of 385°C for 2 minutes (further referred to as UV) was used as a reference condition producing a mechanically stable and template-free low-k film. Due to the additional heating induced by UV absorption, the actual wafer temperature during the UV-curing process was about 400°C. Schematically, the preparation of samples with different amount of the template residues described in this chapter is depicted in Figure 3.17.

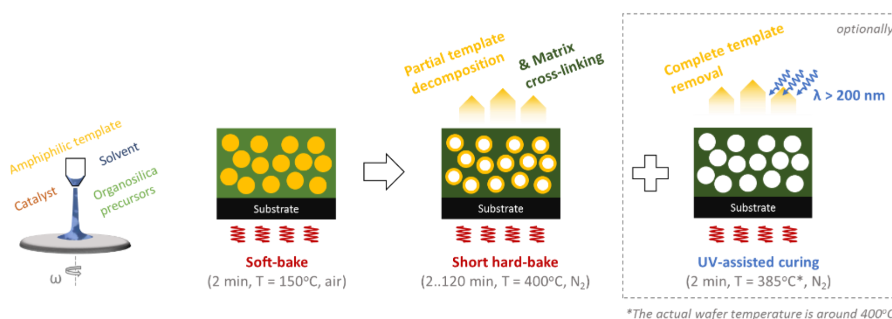

Figure 3.17. Preparation of self-assembly based low-k films with different amount of template residues.

The deposited SOG-2.2 films were characterized using FTIR spectroscopy (Nicolet 6800), spectroscopic ellipsometry (Sentech SE801), nanoindentation (Hysitron TI950 Triboindenter equipped with a cube corner indentation probe), TOF SIMS depth profiling (TOFSIMS IV from ION-TOF

GmbH operating in dual beam configuration) and ellipsometric porosimetry with toluene as adsorbate.[89]

The proposed approach for plasma damage reduction relies on three key elements: 1) fast OSG matrix cross-linking compared to the template decomposition rate; 2) the complete template residues removal during the post-etch UV-curing step; 3) stability of the sacrificial phase under exposure to patterning plasma represented by fluorine radicals and VUV photons as the most damaging species produced during the discharge. Here the focus will be on the validation of the first two aspects.

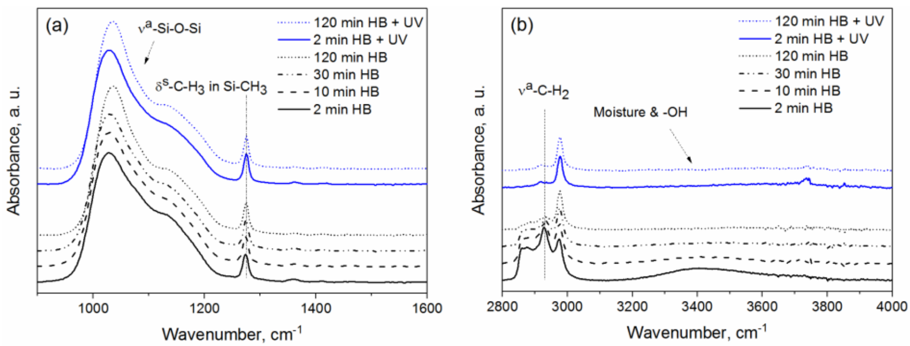

Figure 3.18. IR-absorbance spectra of SOG-2.2 low-k films hard-baked (HB)/ hard-baked and UV-cured (HB+UV) for different times.

To address the first element, we investigated how the properties of the low-k films evolve as a function of hard-bake time. Compositional changes of both the organosilica matrix and the sacrificial phase can be measured by FTIR,[129] see Figure 3.18. The absorbance in the wavenumber range 1000-1150 cm^{-1} corresponding to asymmetric Si-O-Si bond stretching experiences no significant changes already after the shortest tested hard-bake time (Figure 3.18a). Meanwhile, the absorbance from asymmetric C-H stretching in -CH_2-group at around 2925 cm^{-1}, which can be largely associated with the sacrificial phase in the pores, reduces continuously over 2 hours of hard-bake (Figure

3.18b). This indicates the possibility to have independent control of the organosilica matrix cross-linking and of the portion of the sacrificial organic phase in the pores.

Table 3.7. Properties of SOG-2.2 films prepared under different conditions of the hard-bake sequence.

Hard-bake sequence	Thickness, nm	Young's modulus, GPa	Average pore radius, nm	Open porosity, %
0 min HB	217.8 ± 0.9	2.00 ± 0.30	-	-
2 min HB	195.3 ± 2.1	4.79 ± 0.33	0.8	25.6
10 min HB	193.3 ± 2.0	6.04 ± 0.38	0.9	27.7
30 min HB	192.6 ± 1.9	6.39 ± 0.42	0.9	31.1
120 min HB	192.0 ± 0.9	6.39 ± 0.49	1.1	35.0
2 min HB + UV	191.1 ± 2.0	6.29 ± 0.45	1.1	38.6
120 min HB + UV	191.8 ± 0.5	6.23 ± 0.70	1.2	37.9

Another critical aspect such as template removal efficiency of the UV-curing was assessed by applying this treatment to the hard-baked films containing the smallest and the largest amount of sacrificial phase, i. e. hard-baked for 2 and 120 minutes. After UV cure, both films show the lowest FTIR absorbance in the range of wavenumbers corresponding to -CH_2- groups indicating effective removal of the template.

More evidence supporting the results of FTIR analysis can be found in Table I in the form of thickness values measured by spectroscopic ellipsometry and substrate-independent Young's modulus evaluated by nanoindentation. After 2 minutes bake, the film thickness reduces from ~218 nm down to ~195 nm, 2-3 nm above the steady-state value of ~192 nm reached after a long bake. Therefore, most of the film shrinkage associated with condensation of unreacted silanol (Si-OH) groups occurs over the first 2 minutes of the hard-bake. For extended bake time, the thickness variation does not exceed 3%. This tendency is consistent with changes in the mechanical

properties of hard-baked films – the increase of Young's modulus nearly saturates after 10 minutes of the hard-bake. Although the organosilica matrix hardening is not yet complete after 2 minutes according to the nanoindentation results, the UV-curing based template removal treatment is able to restore Young's modulus to the value of the reference template-free coating of about 6.3 GPa. Such fast matrix hardening can be attributed to a well-defined separation between the sacrificial template phase and the OSG matrix. The observed phase separation is generally prone to the self-assembly based spin-on low-k films and is even more prominent in the low-k material under test because of the relatively short PEO block within the surfactant molecule.[182] Considered together with FTIR results, these data indicate clearly that the OSG matrix cross-linking is a fast-occurring phenomenon in contrast to the template decomposition rate which is a noticeably slower process.

Regarding the pore structure of the hard-baked films, it can be noted that both open porosity and average pore radius simultaneously increase with hard-bake time. This supports the assumption of the uniform distribution of the template residues throughout the SOG-2.2 layer (validated in the next paragraph). In turn, it makes it feasible to assume that the template residues stay in the low-k films as pore wall coating. The thickness of this coating can be roughly estimated as a difference between the average pore radii measured in the film of interest and in the film cleaned from the template residues by long hard-bake and additional UV-curing. Following this approach, we calculated that after 2 min hard-bake the template residues take up to 30% of the open porous volume and cover the pore walls with a layer of about 0.3-0.4 nm thick.

To define how uniformly the decomposition of the sacrificial phase occurs throughout the low-k film, we additionally measured the carbon distribution using TOF SIMS depth profiling. Figure 3.19 compares the level of carbon (defined as a signal from C- ions in mass-spectra) in the films hard-baked for 2 min, 30 min, and in the reference template-free film obtained by

the combination of 120 min hard-bake and UV-curing. Besides the fact that the carbon content scales with the length of hard-bake process in agreement with the above measurements, the concentration of carbon stays nearly constant as a function of sputter time in each evaluated low-k film, thus indirectly confirming the uniformity of the template removal process and the interconnectivity of the pore structure existing already after 2 min hard-bake.

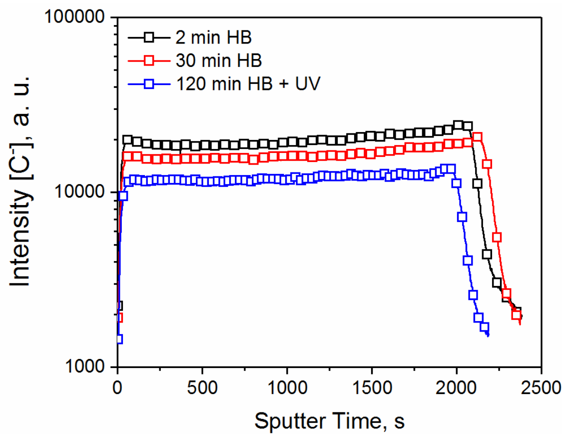

Figure 3.19. TOF SIMS carbon (C^-) depth profiles recorded as a function of sputter time on low-k films which followed a different hard-bake sequence.

To summarize, the thorough analysis of the composition, mechanical strength, and pore structure of the hard-baked films allowed validation of the two key aspects of the proposed post-etch template removal approach namely the possibility to obtain a controllable amount of uniformly distributed template residues within mechanically robust organosilica matrix and to remove it with an additional short UV-treatment.

3.4.3 Plasma-induced damage mitigation

To evaluate the efficiency of the template residues in protecting the organosilica matrix from patterning plasma-induced damage, the low-k films prepared with different hard-bake sequences were subjected to two different fluorine-based discharges. The first tested plasma was fluorine-rich Ar/SF_6 discharge ignited in a commercial magnetically enhanced dual-frequency CCP reactor Vesta™ from Tokyo Electron Ltd (Figure 3.20a). The plasma was maintained at 120 mTorr using total power of 500W (400W + 100W of 100 MHz and 13.7 MHz RF power supplies, respectively) and equal flows of Ar and SF_6 gases set to 100 sccm. The second tested treatment was Ar/CF_4 discharge, which represents a more common patterning plasma mixture. The Ar/CF_4 plasma was ignited in another dual-frequency CCP reactor Vigus™ from Tokyo Electron Ltd (Figure 6b). The plasma was maintained at 70 mTorr using total power of 350W (250W + 100W of 40 MHz and 13.7 MHz RF power supplies, respectively) and 1000 sccm Ar/100 sccm CF_4 flows.

The plasma-induced damage of the porous organosilica material is attributed to different interactions with species generated in the discharge, i.e. free reactive radicals, ions, or VUV photons. In the case of Ar/SF_6 plasma used in this work, the impact of fluorine radicals is considered the dominant low-k damage mechanism due to the strong plasma dissociation of the SF_6 molecule[183] compared to the relatively low VUV-induced damage caused by a small fraction of Ar in the total flow.[184] In contrast, the interpretation of Ar/CF_4 plasma interaction with the template-containing low-k films is complicated not only by the presence of CF_x radicals along with F-radicals but also by the abundance of argon in the discharge and therefore non-negligible contribution of VUV-radiation.

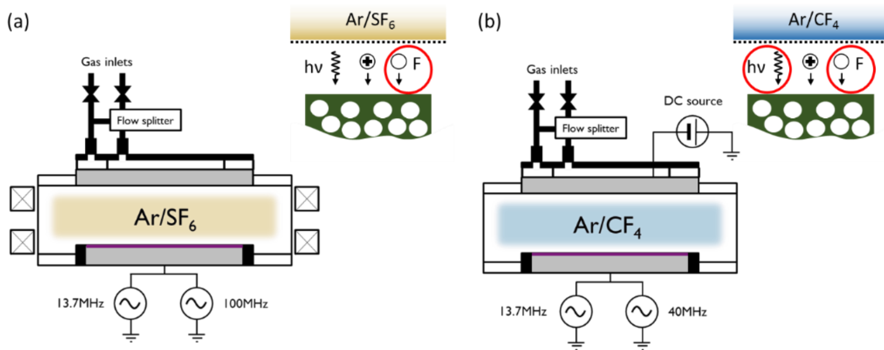

Figure 3.20. The set-ups for the patterning plasmas under study and the expected dominating low-k damage mechanisms: (a) AR/SF_6 plasma; (b) Ar/CF_4 plasma.

Apart from ellipsometry and FTIR, the analysis of the plasma-induced damage was performed with TOF SIMS depth profiling and complemented with an HF-dipping test (aqueous 0.2% HF, 60s) revealing the thickness of the carbon-depleted low-k layer.[185] The dielectric constant of the low-k films was estimated from capacitance measured with E4980A Precision LCR Meter on planar metal-insulator-semiconductor structures formed by evaporation of 70 nm Pt contact pads on top of n-Si/SOG-2.2 stacks.[88] Surface topography images (2 µm x 2 µm, 512 x 512 pixels) were recorded on low-k films in tapping mode (Nanoscope V from Bruker). The root-mean square (RMS) roughness values were calculated with Gwyddion 2.44.

3.4.3.1 Ar/SF_6 plasma

Samples with different levels of template residues (Table I) were exposed to the Ar/SF_6 plasma for 35s, then half of the etched samples was UV-cured to get template-free low-k films. To evidence the carbon-depleted top layer formed during the etch process, the UV-cured samples were pre-measured

with ellipsometry and then immersed into 0.2% aqueous HF solution for 60s. The observed thickness loss gives an estimate of the low-k damage depth. As can be seen in Figure 3.21, the thickness loss caused by HF-dip inversely correlates with the amount of the template residues present in the low-k films during etching. The largest damage depth of approximately 52 nm is found in the low-k layer UV-cured prior to the etch process, while this value is about 10 times smaller for the film hard-baked for 2 minutes and hosting ~30% of the templating organics.

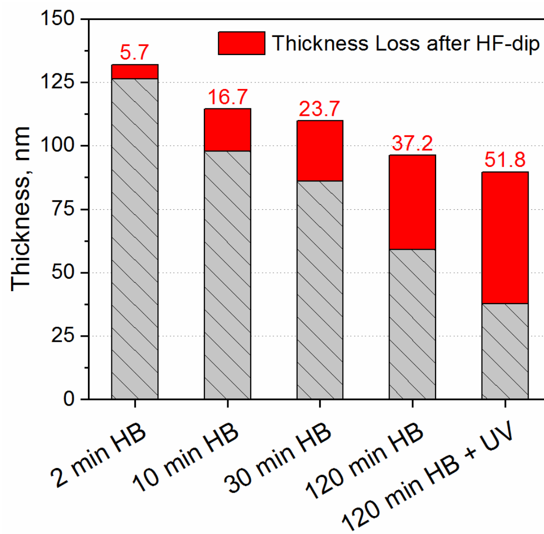

Figure 3.21. The thickness of the low-k films after 35s Ar/SF_6 etch and post-etch UV-treatment (pristine thickness ~ 200nm). The part of the film removed by the subsequent 0.2% HF dip is indicated in red.

While the HF-dip test provides an indirect indication of carbon depletion, TOF-SIMS depth profiling gives a better insight into the carbon distribution within the low-k layer. Figure 3.22 shows the C- intensity as a function of sputter time for the films with the largest and the smallest tested amount of the template residues retained before the etch process, i. e. for the hard-bake sequences referred to in Table I as “2 min HB” and “120 min HB + UV”,

respectively. The level of carbon in hard-baked films has already been compared in the previous part of the chapter and it was shown to have minimal variations over the layer's thickness. As expected, the most significant changes in the carbon profiles appear after the plasma etch. In agreement with the results of the HF-dip test, the carbon depletion is particularly significant in the material containing the lowest amount of the template residues before etching. In this case, the depleted region exceeds half of the film thickness. On the contrary, the C loss is almost negligible in the case of the film hard-baked for 2 minutes.

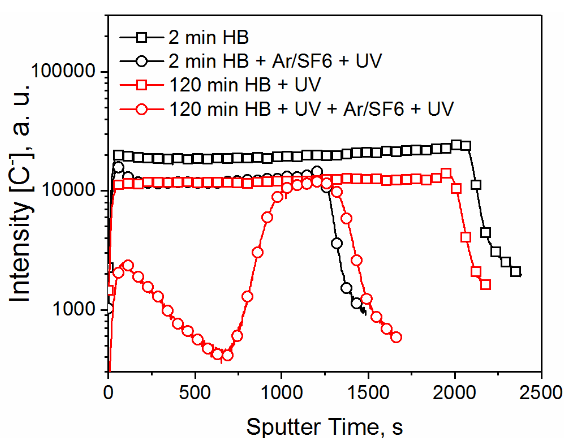

Figure 3.22. TOF SIMS carbon (C^-) depth profiles recorded as a function of sputter time on low-k films which followed different hard-bake sequences and exposure to Ar/SF_6 plasma with successive UV-cure.

To make sure that the carbon preserved in the organosilica matrix during etching is still present in its original form (Si-CH_3 groups), FTIR spectra of the samples before and after the plasma exposure were compared, as shown in Figure 3.23. Although the initial height and position of the Si-CH_3 peak at around 1275 cm^{-1} slightly varies (which might be related to the proximity of the template residues), the relative absorbance changes caused by the plasma

can be compared. The spectra support the previous findings and additionally provide evidence of the largely intact matrix organics in the case of 2 min hard-baked film. The slight decrease in the peak intensity after etching can be attributed to the partial replacement of $Si-CH_3$ groups with Si-H, Si-OH or its fluorinated form $Si-CH_xF_{3-x}$. However, since neither Si-H, Si-OH or concomitant moisture appear in the full spectra (Figures 3.23a, 3.23b), fluorination is the most plausible chemical change. Additionally, one can also notice the impact of the Ar/SF_6 plasma on the template residues in Figure 3.23a. The exposure to the plasma does not only lead to partial removal of the residues, which follows from the decrease of the $C-H_2$ absorbance peak, but it does also modify the composition of the template residues by increasing the concentration of C-OH bonds. The latter may appear due to the fragmentation of PEO chains of the sacrificial phase under plasma exposure.

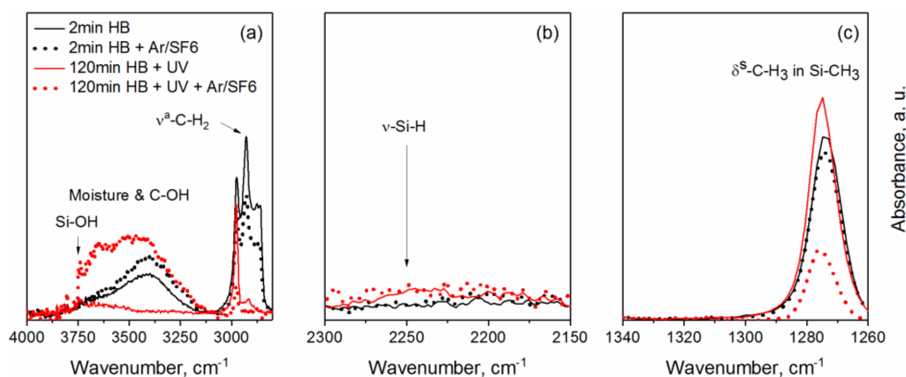

Figure 3.23. The IR absorbance peak (normalized by the film thickness) corresponding to C-H vibrations within the $Si-CH_3$ group recorded on low-k films before and after exposure to Ar/SF_6 plasma. The absorbance scale was modified on each graph to improve the visibility of the peaks of interest.

In order to understand the underlying damage reduction mechanism, we need to refer to the used plasma conditions. As it has been pointed out above,

the employed Ar/SF_6 plasma interacts with the low-k layer predominantly via fluorine radicals. The interaction between F-radicals and porous silica-based low-k films has been recently well described by Rakhimova et al.[186,187] Exposure to F-radicals forms the carbon-depleted layer in the low-k film as a result of two propagating processes – fluorination of $Si-CH_3$ groups as well as the material etching via elimination of $–CF_3$ groups and subsequent reaction with the exposed Si-O bonds of the matrix. The rate of both processes, relying on the diffusion of F-radicals, is strongly affected by the pore structure of the low-k dielectric. As a consequence, the protective impact of the template residue coating can be attributed to the substantially reduced open porosity and pore dimensions, reducing significantly F-radical diffusion through the porous matrix. In addition, the presence of sacrificial organics covering the pore walls could also sterically hinder the fluorination of $Si-CH_3$ groups thus protecting the organosilica matrix from unwanted modification even at the topmost part of the low-k film where the concentration of fluorine radicals is the highest.

From the mechanism of fluorine radical interaction with porous organosilica dielectric described by Rakhimova et al, it follows that the materials with larger pores would experience faster surface roughening. To check if the undesirable surface roughening can be mitigated when the reduced pore dimensions are attributed to the presence of organic template residues, we compared AFM topography images measured on SOG-2.2 films exposed to Ar/SF_6 plasma (Figure 3.24). According to the calculated RMS roughness values, the exposure to the F-radical rich plasma caused significant surface roughening, while the UV-curing had minimal impact on the surface morphology. On the positive side, one can notice about 30% lower roughness measured on the low-k films retaining the template residues.

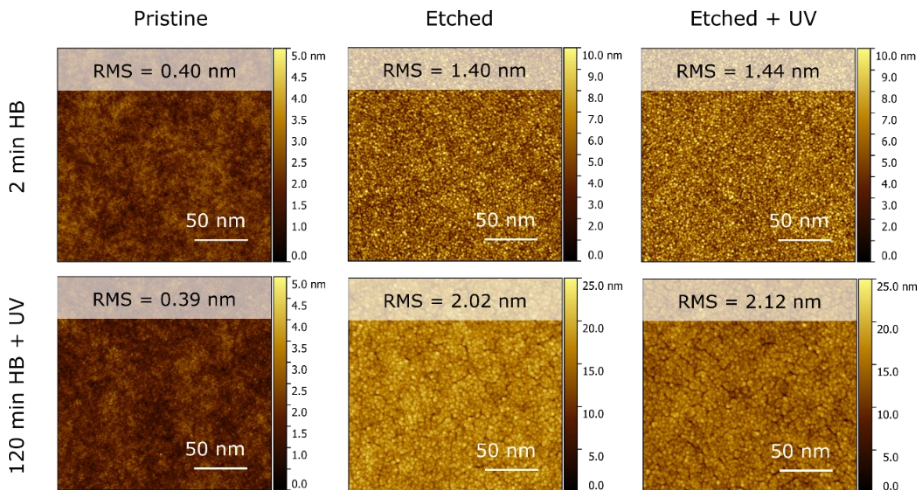

Figure 3.24. AFM surface topography of low-k films with associated root-mean square (RMS) roughness value measured at different stages of low-k processing.

Finally, the dielectric constant of low-k films exposed to Ar/SF_6 plasma and UV-cured afterward was measured to assess the ability of the proposed post-etch template removal approach to suppress the k-value increase (Figure 3.25). There is a clear correlation between the amount of the template residues controlled by the hard-bake sequence and the increase of dielectric constant of low-k films treated by fluorine-rich plasma. Interestingly, the shortest hard-bake time made the low-k film particularly resistant against the fluorine radicals thus demonstrating the potential of the proposed post-etch template removal approach to provide nearly damage-free patterning of self-assembly based low-k dielectrics.

However, it is important to note that a fluorine-rich plasma like SF_6 is not favored in the actual patterning process due to the poor selectivity of such plasmas towards non-organic hard-masks and associated difficulties with the etch profile control. Therefore, the efficiency of the organosilica backbone protection by the template residues was also studied in fluorocarbon-based Ar/CF_4 plasma.

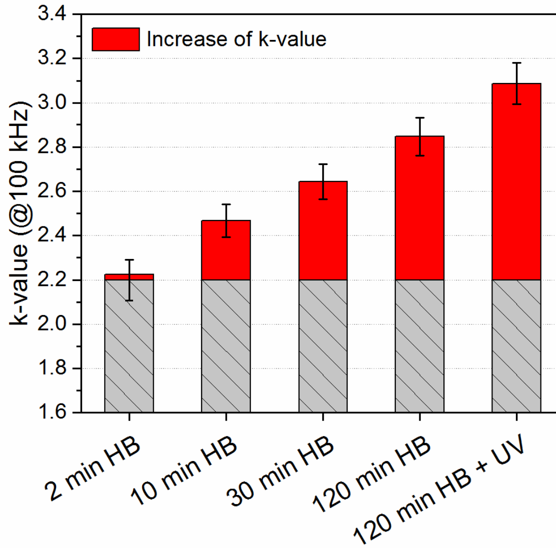

Figure 3.25. The dielectric constant of low-k films exposed to Ar/SF6 plasma. The k-value of the pristine template-free low-k film corresponds to the gray part of each bar. The increase of k-value induced by plasma etching is marked with red.

3.4.3.2 Ar/CF_4 plasma

The low-k films hard-baked for a different time were exposed to Ar/CF_4 plasma for 20-30s targeting removal of about 70 nm of the film. Then the etched films were subjected to the additional UV-curing to remove the sacrificial organics. The plasma-induced damage was characterized using an analogous set of techniques employed for the evaluation of Ar/SF_6 treated samples. The depth of carbon depletion was checked by measuring the thickness loss upon immersion of the processed low-k films in dilute HF solution (Figure 3.26a). The first important observation is the absolute values of the thickness loss. Even the largest thickness loss value in Figure 3.26a does not exceed the smallest one found in the experiment with Ar/SF_6 discharge. Another remarkable difference in the results of the HF dip test – the largest

amount of the template residues retained in the pores did not ensure the lowest plasma-induced damage. The plasma damage was minimal for the hard-bake conditions corresponding to the intermediate amount of organic residues in the pores. The above trends are also reflected in the chart showing the k-value increase in SOG-2.2 films treated with Ar/CF_4 plasma (Figure 3.26b).

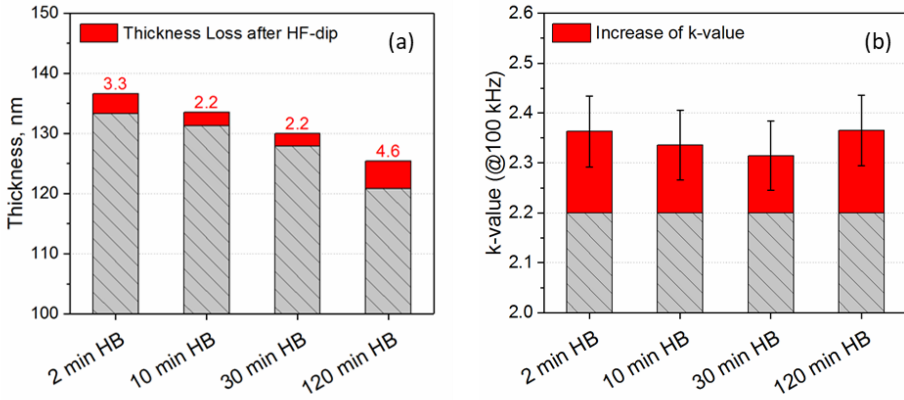

Figure 3.26. Characterization of low-k damage induced by Ar/CF_4 plasma. (a) Thickness loss after 0.2% HF dip is marked with red (thickness of SOG-2.2 before etching is ~ 200nm). (b) The dielectric constant of SOG-2.2 films. The k-value of the pristine template-free low-k film corresponds to the gray part of each bar. The increase of k-value induced by plasma etching is marked with red.

Figure 3.27 exhibiting the carbon TOF SIMS depth profiles compares the low-k materials before and after exposure to Ar/CF_4 plasma combined with UV-curing. The carbon depletion is limited to the very surface in both types of plasma-treated low-k films, and the deviation from the reference carbon profile of pristine template-free coating is relatively small. Nonetheless, one can discern slightly more carbon preserved in the low-k dielectric which contained template residues during etching. This is also consistent with the

slightly lower thickness loss measured on the analogous film during the HF test.

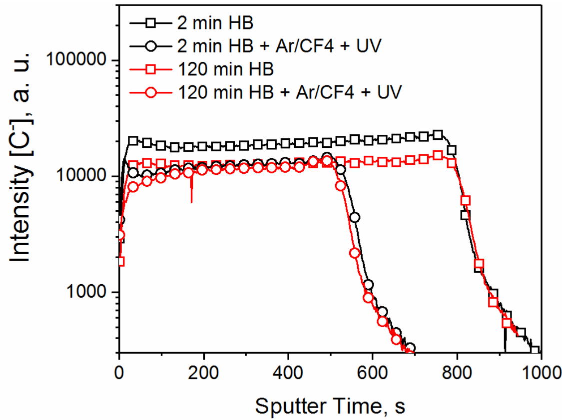

Figure 3.27. TOF SIMS carbon (C^-) depth profiles recorded as a function of sputter time on low-k films which followed different hard-bake sequences and exposure to Ar/CF_4 plasma with successive UV-cure.

To compare the efficiency and applicability of the proposed post-etch template removal approach in different plasmas, we summarized the information on the low-k damage and film shrinkage caused by UV-curing post-treatment in Table 3.8. The first parameter was estimated as a plasma-induced k-value increase relative to that on SOG-2.2 films with the lowest template fraction.

Table 3.8. The relative efficiency of plasma damage mitigation in Ar/SF_6 and Ar/CF_4 discharges and the corresponding film shrinkage upon post-etch template removal via a short UV-curing step.

Processing sequence	Ar/SF_6		Ar/CF_4	
	Damage	Shrinkage	Damage	Shrinkage
2 min HB + ETCH + UV	1.2%	4.5%	98.7%	1.0%
30 min HB + ETCH + UV	48.9%	1.6%	67.4%	0.8%
120 min HB + (UV) + ETCH + UV	100%	0.8%	100%	1.3%

The difference in damage mitigation efficiency between Ar/SF_6 and Ar/CF_4 plasmas could be related to the weight of factors responsible for it. Considering the high concentration of fluorine radicals as the major origin of the carbon depletion and of the associated k-value increase in the case of Ar/SF_6 plasma, one can conclude that the PEO-PE-based template residues efficiently block the interaction of fluorine radical with organosilica framework. In such fluorine-rich plasma, the damage mitigation efficiency scales with the amount of template residues residing in the pores during etching. Importantly, the lowest damage of about 1% was achieved at the expense of the film shrinkage of only 4.5% which is two times lower than the value reported for the late porogen removal approach.[178]

The absence of any plasma-protection effect in Ar/CF_4 discharge for the same low-k film hard-baked for 2 min indicates that damage factors other than just fluorine-based radicals should be considered. Moreover, the fact that the plasma damage reduction capability is partially restored when a smaller portion of the template residues is present in the film, suggests that the template residues themselves may be a source of the damage to the organosilica matrix under the employed plasma conditions. The lower concentration of F-radicals generated in the CF_4-based plasma can explain the generally lower level of damage in Ar/CF_4 and implies that another damage factor such as VUV radiation cannot be ignored. The potential source of the VUV-photons could be the excited Ar atoms (~105 nm) and CF_2 radicals (~140 nm). To understand whether the VUV impact could explain the difference in the observed damage mitigation efficiency between the tested plasmas, we explored the interaction of the template residues with VUV-light produced in Ar and Xe discharges.

3.4.4 VUV radiation-induced damage

The negative impact of plasma-emitted VUV radiation in semiconductor technology has long been associated with gate silicon oxide damage in the form of positive charge accumulated at the Si/SiO_2 interface.[188,189] Upon the introduction of the damascene process and especially after the addition of organic groups as an integral part of the low-k dielectric, the issues related to VUV radiation expanded to interconnects.[184,190] Apart from the previously known silica-related defects, the exposure of organosilica low-k dielectric to highly energetic VUV-light results in the breaking of Si-C bonds. In turn, the formed silicon dangling bond can be saturated with hydrogen (Si-H) or moisture (Si-OH) thus leading to degraded electrical reliability. Since plasma patterning of low-k dielectric is a regular step in a damascene flow where organosilica material gets irradiated by VUV light, the VUV component of plasma damage has been the subject of several studies. The VUV emission is strongly dependent on the chamber design, plasma conditions, and plasma chemistry. The latter aspect is of particular interest in the current study. Although the typical VUV-emission spectrum of Ar/CF_4 patterning plasma is rather complex and includes a series of transitions between excited species, one can point out the most intense peaks attributed to Ar (104.8 nm and 106.7 nm), CF_2 (~ 140 nm) and C (150-180 nm) resonant lines.[191]

Since the isolation of the respective VUV-photons from other plasma species such as radicals and ions is not trivial in Ar/CF_4 plasma, we simplified the task by analyzing the interaction of the low-k dielectric with Ar and Xe discharges, strongly emitting at ~105 nm and 147 nm, respectively.[192,193] In the context of the study, the VUV-light generated in Xe-plasma mimics the effect of VUV-emission of CF_2 species in Ar/CF_4 discharge. The effect of the VUV-emission of lower energy was not considered due to the higher transparency of the organosilica matrix in this energy range. Nonetheless, the use of pure inert gas plasmas does not eliminate the damage contribution from

ion bombardment of the sample surface. To eliminate the ion bombardment in Xe-plasma, the low-k film was covered with MgF_2 optical filter window characterized by a cut-off wavelength of about 120 nm.[194] While the MgF_2 window is transparent for the 147 nm photons, it is absorbing the VUV-emission from Ar-plasma. In an attempt to minimize the bombardment contribution in Ar-discharge, the treatment was done in an ICP chamber without any RF bias power applied to the bottom electrode. In this way, the ion accelerating voltage is equal to self-bias on the wafer chuck. The employed plasma set-ups and the corresponding damage mechanisms are schematically shown in Figure 3.28.

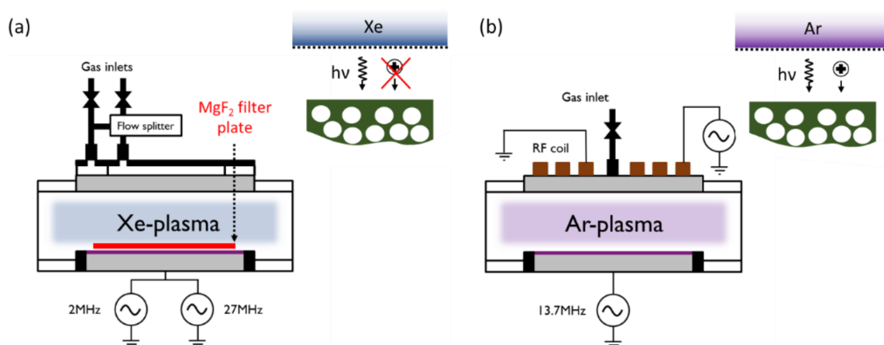

Figure 3.28. The set-ups for studying VUV-induced damage in SOG-2.2 films: (a) CCP-plasma chamber for Xe discharge; (b) ICP-plasma chamber for Ar discharge. The corresponding insets highlight the potential damage mechanisms (ions, VUV photons).

To examine the stability and the organosilica matrix protection capability of the template residues in the presence of VUV-light, we exposed the low-k film enriched with a large amount of the template residues and the template-

free low-k films to Xe-plasma and Ar-plasma for different times ranging from 5 s to 150 s. The employed plasma conditions are summarized in Table 3.9.

Table 3.9. The condition of CCP Xe and ICP Ar plasmas used in this work.

Plasma type	Pressure, mTorr	Gas flow, sccm	Power (frequency), W
Xe-plasma	120	120	1500 (27 MHz)
Ar-plasma	30	30	1000 (13.7 MHz)

The changes in the composition of the low-k film and its dynamics were analyzed using FTIR spectroscopy. At first, the wavenumber range featuring the modification of organic groups in the low-k films was studied (Figure 3.29). One can clearly see the reduction of -C-H_2 absorbance peak (~2925 cm^{-1}) corresponding to PE-PEO surfactant residue in both Xe and Ar plasmas signifying its removal from the pores of SOG-2.2. The dynamics of this process can be seen in Figure 3.30a. After a slightly steeper decrease in Ar plasma, the -C-H_2 peak height quickly saturates at the same level (~50% of the original intensity) for both plasma treatments.

The ability of the template residues to suppress or lower the VUV-induced cleavage of Si-CH_3 bonds of the SOG-2.2 organosilica matrix can be estimated by monitoring changes in the corresponding IR absorbance peak at ~1275 cm^{-1}. Figure 3.30b compares the evolution of the Si-CH_3 peak height in template-containing and template-free SOG-2.2 coatings exposed to Ar- or Xe-plasma. The nearly overlapping curves corresponding to the same type of plasma treatment indicate that the residual template organics cannot protect the organosilica matrix from damage by VUV photons.

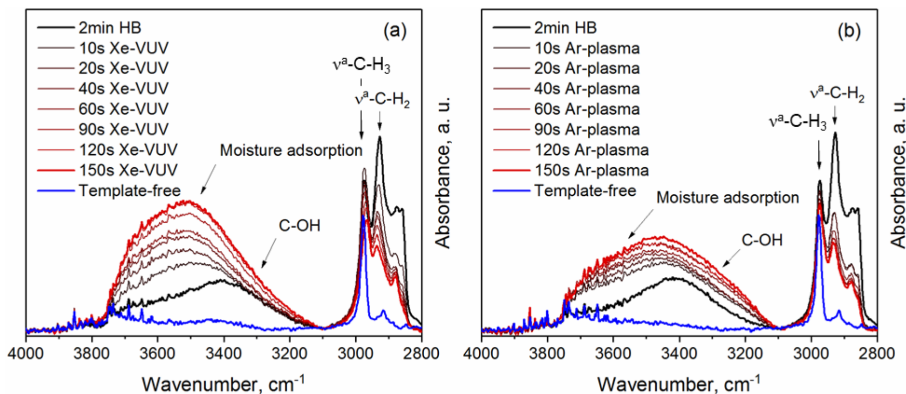

Figure 3.29. IR absorbance spectra of SOG-2,2 low-k films hard-baked for 2 min and exposed to VUV-radiation originating from (a) CCP Xe-plasma or (b) ICP Ar plasma. The IR absorbance spectrum of the template-free coating is added for reference.

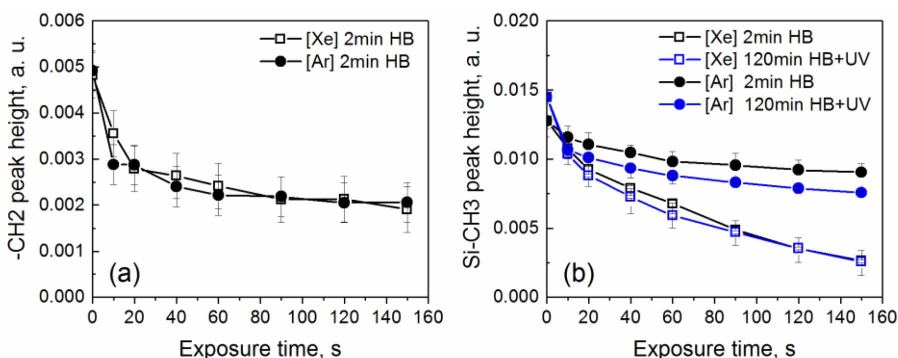

Figure 3.30. Evaluation of template removal and SOG-2.2 organosilica matrix damage under VUV-emitting plasmas via IR absorbance of corresponding peaks: (a) C-H_2 (~2850 cm^{-1}); (b) Si-CH (~1275 cm^{-1}).

To get more insight into the decomposition mechanism of the template residues and to evaluate the possible impact of the template decomposition process on the damage of the organosilica matrix, photolysis routes of short PEO and PE chains were studied by means of ab-initio calculations based on

density functional theory (DFT) method (Jaguar version 8.3).[195,196] In the performed calculations, triethylene glycol and dodecane molecules were used as model polymers representing PEO and PE-based fragments of the template residues, respectively. The geometry of the model molecules was first optimized at B3LYP/ 6–31(d,p) level.[197] Then the energies of the excited singlet and of the first triplet states were calculated with a time-dependent DFT approach at the same level of theory to define the VUV-absorbance spectrum (Figure 3.31) and the metastable triplet states as starting points for the successive dissociation of the excited model molecule. The thermodynamic parameters associated with the possible dissociation paths such as Gibbs free energy change (ΔG) and the enthalpies (ΔH) of the corresponding reactions at 298 K were estimated from frequency analysis applied to the triplet state of the model molecule and to the ground states of the dissociation products. The results of these calculations are presented in the form of a photodissociation scheme (Figure 3.32). The scheme demonstrates one of the probable paths of energy dissipation upon VUV photon absorption. When the photon energy is larger than the gap separating the highest occupied and the lowest unoccupied molecular orbitals (HOMO-LUMO gap), the molecule acquires one of the excited singlet states. The successive molecule thermalization process and associated non-radiative losses bring the molecule to the long-living metastable triplet state. Since the further de-escalation of the molecule excitation via photon irradiation is impeded by the selection rules, the dissociation of the excited molecule is one of the likely outcomes, the probability of which depends on the thermodynamic and kinetic parameters of the bond-breaking process.

The VUV-spectra calculated for PE and PEO model polymers (Figure 18) show that PE is generally transparent down to ~140 nm radiation, while the PEO short chain starts absorbing VUV photons with wavelengths below ~170 nm. This implies that the main VUV-line in Xe-plasma would be able to affect directly only the PEO-based residues. At the same time, both PE and

PEO polymers are strongly absorbing VUV-light around ~100 nm which corresponds to VUV Ar resonant emission lines. These findings are well consistent with the experimental observations if we assume that the absorption of VUV photons does lead to the dissociation of PE and PEO fragments. The fact that such reactions are thermodynamically favorable for both PE and PEO chains upon absorption of photon energies exceeding the HUMO-LUMO gap is evidenced by the large negative values of Gibbs free energies for each of the photolysis scenarios. To decide which of them is preferable, we should analyze the intramolecular electron rearrangement in the excited molecules. Since the symmetry of the first excited singlet (S_1) and triplet (T_1) states is generally the same, we can check the LUMO (S_1) orbital for the location of antibonding interactions between neighboring atoms (see the insets in Figure 3.32). In both PE and PEO blocks the antibonding is observed between either C-C or C-O atoms forming the backbone of the polymer thus favoring the X_1 dissociation reaction.

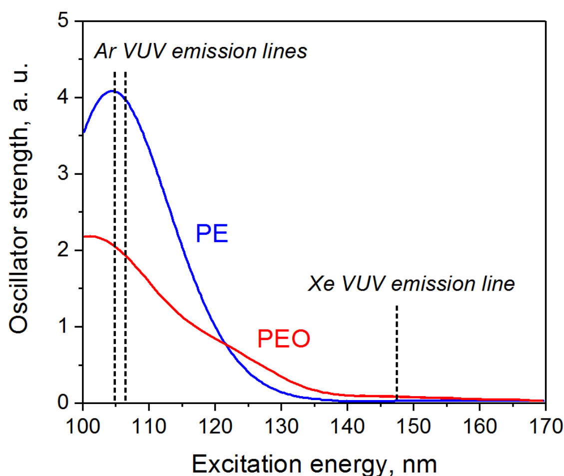

Figure 3.31. Simulated VUV absorption spectra for triethylene glycol (PEO) and dodecane molecules (PE).

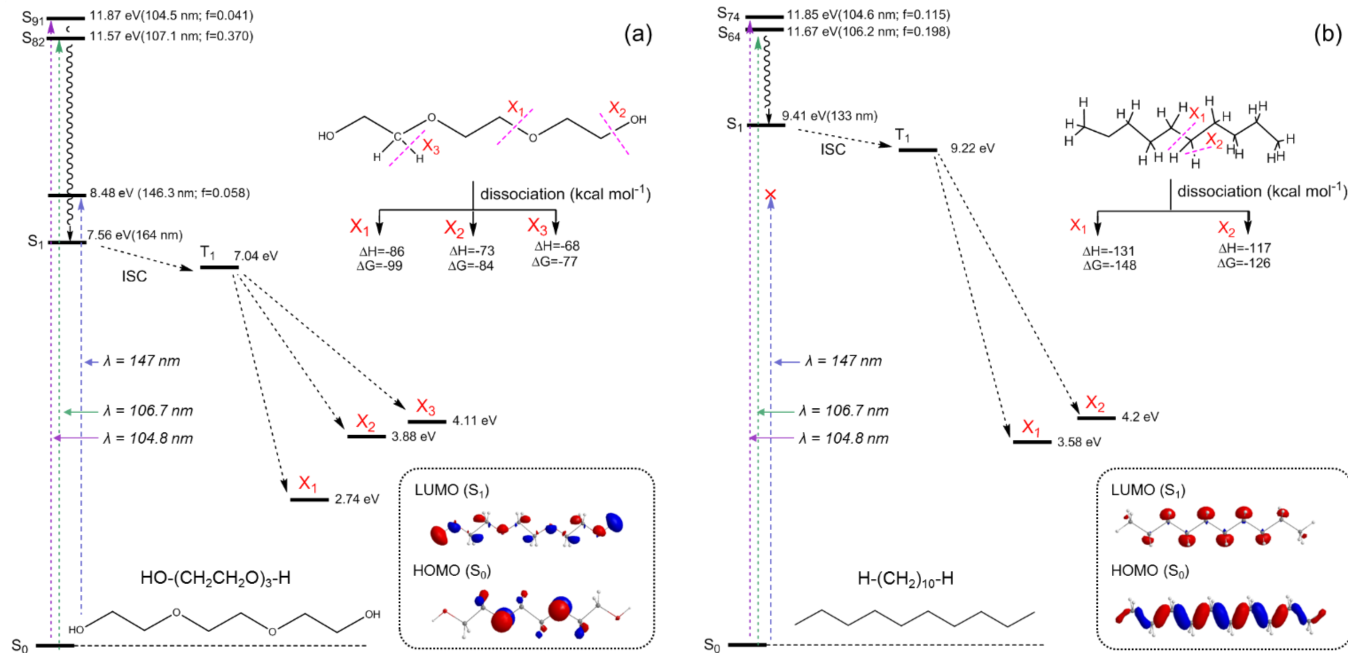

Figure 3.32. The photolysis energy diagram calculated for (a) triethylene glycol and (b) dodecane molecules interacting with VUV photons. The singlet states are denoted as S_i, and the triplet states as T_i. Besides the excitation path, the diagram contains the isosurfaces of HOMO/LUMO orbitals and thermodynamic parameters (Gibbs free energy ΔG and enthalpy ΔH) of the possible bond scission reactions X_i.

The generation of PEO and PE fragments terminated with oxygen or carbon dangling bonds upon photoinduced dissociation in the vicinity of the organosilica matrix may be considered as a potential mechanism promoting the removal of Si-CH_3 organosilica matrix groups from the pore surface. Therefore, in plasmas with non-negligible VUV-light emission, the layer of template residues does not only sterically protect the organosilica matrix from in-diffusing plasma radicals but also serves as a source of damaging species. This controversial role of the template residues is reflected in the non-monotonic dependence of the plasma-induced damage on the amount of the sacrificial organics (Figure 3.26). Similar concerns were mentioned in the pore-stuffing study of Liping *et al*. where PMMA or PEG chains were used as a pore-filling material. The potential damage by the fragments of dissociated molecules condensed in the pores of low-k dielectric was also an issue highlighted in the cryogenic etch study. One of the potential solutions would be to use surfactant chains that do not form radicals of strong oxidizing nature. In this context, the simple ammonium-based cationic surfactants containing a long hydrocarbon chain (e. g. CTAB) look rather appealing.

3.4.5 Conclusions

In this work, we proposed and studied the viability of a new patterning scheme for low-damage integration of self-assembly based low-k dielectrics. We demonstrated that the partial decomposition of the typical PEO-PE templating molecules during hard-bake process leads to the formation of protective organic coatings, which can be efficiently removed by an additional post-etch UV-curing step. These organic layers uniformly covering the pore surface of a mechanically robust OSG matrix act as a barrier against diffusing reactive F* plasma radicals. By optimization of hard-bake time, we achieved nearly damage-free plasma etching of highly porous dielectric films in fluorine-rich Ar/SF_6 plasma. However, we found that the template residue

coatings cannot protect the organosilica matrix against VUV radiation and may even promote damage to the organosilica matrix of the low-k dielectric. To avoid this, the plasma etch process should be appropriately modified to minimize the interaction of the low-k material with VUV-light. The application of a VUV-absorbing hard-mask above the low-k dielectric may be another option to compensate for the observed low VUV stability of the PE-PEO-based template residues. Alternatively, surfactants with functional blocks different from PE-PEO could be used for the preparation of the porous dielectric as a possible way to improve VUV compatibility by minimizing the generation of strongly oxidizing fragments upon photodissociation.

We believe that the proposed plasma damage mitigation strategy based on a simple modification of the standard damascene metallization flow could be of particular interest for the integration of such promising sub-class of self-assembly based low-k dielectrics as PMOs into advanced on-chip interconnects.

3.6 Metal barrier induced damage in self-assembly based organosilica low-k dielectrics and its reduction by organic template residues

Abstract

This study describes the damage caused by physical vapor deposition of TaN/Ta barriers on porous self-assembled organosilica low-k dielectrics for IC applications. It is demonstrated that the ion bombardment associated with TaN layer sputtering strongly influences the metal species in-diffusion and modifies the bulk dielectric and pore sealing characteristics. The modulation of the pore structure via controlled decomposition of the organic template, prior to the barrier deposition step, allows to mitigate this damage. The reduction of open porosity, from nominal 39% down to 26%, is realized by partial retention of the sacrificial organic porogen phase in the pores of the low-k dielectric, resulting in the suppression of deep Ta penetration and in the recovery of pore sealing. This approach is successfully tested in a 45 nm half-pitch damascene vehicle. The compatibility of the organic template residues with the subsequent steps of the interconnects integration process flow, such as hard-mask deposition and patterning, are discussed.

3.6.1 Introduction

As the density of transistors in advanced ULSI chips continues to increase, the critical dimensions in the advanced on-chip interconnects become ever smaller, reaching a few tens of nanometers. This is reflected in a growing RC-delay, impacting the overall performance of a chip. As a solution, copper and low-k dielectrics started replacing traditional aluminum wiring and silicon oxide insulation[12,13,198,199]. The reduction of inter- and intra-level

capacitance via the introduction of porous low-k dielectrics was the key knob for mitigating the signal propagation delay in the last decade. However, the significant increase of metal resistivity at the nanoscale made the line resistance play a dominating role in RC-delay factor[200–202]. Since the resistivity depends on the sectional area of the metal wire, a strategic solution is to reduce the thickness of the poorly conducting metal diffusion barriers, such as TaN/Ta bi-layer. The latter are typically deposited by magnetron sputtering. To make the porous low-k dielectrics compatible with the metal-barrier deposition and thickness reduction trends, attempts were made to eliminate the porosity locally or completely by pore sealing or pore stuffing[203–205]. While there was some success in this direction, the processes were rather difficult or expensive to implement. As an alternative, the approaches based on porogen retention in plasma-enhanced chemical vapor deposited (PECVD) material were proposed[177,178]. Though this approach was relatively simple to implement, the post-CMP removal of the sacrificial phase resulted in unacceptably high shrinkage values, leading to mechanical failure of the multi-layer interconnects structure.

Among the potential low-k dielectrics for insulation in the next generation on-chip interconnects, materials with ordered pore structure are preferred from the viewpoint of balance between mechanical stability and k-value[56]. In this respect, the self-assembly based materials, such as periodic mesoporous organosilicas (PMOs), provide a better alternative to conventional PECVD analogs for further down-scaling of the dielectric constant[52,156,157]. However, the mesoporous nature of PMOs or PMO-like materials imposes certain issues for the preservation of the material integrity during patterning and metal barrier deposition steps[158,206]. Recently, a new approach relying on the preservation of the surfactant residues in self-assembly based dielectrics was proposed for the elimination of the plasma-induced damage[128]. Unlike the aforementioned porogen retention methods, it relies on short pre-annealing of the soft-baked low-k dielectric film, which

enables sufficient mechanical strength of the organosilica framework combined with minimal loss of the sacrificial organics. The present paper assesses the role of surfactant residues in solving two main low-k dielectric integration challenges associated with the formation of a continuous metal barrier on top of a highly porous surface, namely the degradation of dielectric properties and the in-diffusion of barrier precursors into the pores. The above issues are addressed in the context of PVD TaN/Ta bi-layer deposited on blanket and patterned test structures featuring a PMO-like dielectric with target k-value of 2.2 and open porosity around 40%.

3.6.2 Experiment details

The low-k dielectric films, SOG-2.2, with a target k-value of 2.2 and thickness of about 200 nm, were prepared from a commercial solution (SBA Materials Inc.). The solution contains organosilica esters as precursors for the organosilica matrix and amphiphilic polyethylene oxide (PEO) based surfactant molecules as organic porogen. After spin-coating and a short soft-bake in air at 150°C for 2 minutes, the films were annealed at 350°C or 400°C in N_2 for varying times in the range of 2-120 minutes, allowing to control the amount of remaining sacrificial organics in the self-assembled pore structure. To achieve a surfactant-free version of the dielectric, the film with the longest bake time was additionally exposed to a short UV-cure ($\lambda > 200$ nm) at 385°C for 2 minutes.

The physical vapor deposition (PVD) of a 3 nm TaN/ 3 nm Ta bi-layer was realized on an Endura platform (Applied Materials). No reactive pre-clean (RPC, He/H_2 plasma) was used in this experiment to avoid possible impact on the remaining surfactant residues or on the organic functionalities embedded in the organosilica matrix[207,208]. The AC bias sputtering power for the TaN deposition step was varied between 0W and 800W, to determine the origin and scale of the low-k material degradation, while the AC bias was fixed at

800W during the subsequent Ta deposition step. The DC sputtering power was kept fixed at 15kW for both TaN and Ta steps. To quantify the impact of TaN/Ta deposition on the underlying low-k layer, blanket films were characterized by Rutherford backscattering spectroscopy (RBS), Fourier-transform infrared (FTIR) spectroscopy, and for k-value extraction, a metal-insulator-silicon (MIS) stack was measured by impedance measurements.

For the RBS results, the energy spectrum of He^+ ions accelerated to 1.523 MeV and backscattered at an angle 130° was recorded with a silicon surface barrier (SSB) detector in a customized scattering chamber developed at the Jülich Research Center. To extract the information about the penetration depth of the metal barrier inside the porous low-k dielectric, the signal corresponding to backscattering from tantalum atoms was fitted using a five-layer model: one layer on the top of low-k dielectric and 4 additional layers representing various diffusion depths. The ratio of diffused tantalum summed over the four bottom layers compared to the total amount of tantalum gives a good qualitative estimate of the metal-barrier in-diffusion into porous media.

Infrared absorbance was recorded in transmission mode using Nicolet 6700 FTIR Spectrometer (Thermo Scientific). The IR absorbance spectra with a resolution of 2 cm^{-1} were averaged over 100 scans and then normalized by the maximum absorbance peak at around 1035-1037 cm^{-1} corresponding to the stretching of Si-O-Si bonds in the organosilica matrix. In the current study, featuring stacks containing IR-absorbing conductive coatings like Ta, the chosen type of absorbance normalization is preferred over a more common normalization by the film thickness. The key advantage of the normalization by Si-O-Si peak value is that it allows a direct comparison of SOG-2.2 film composition regardless of the presence of thin conductive Ta coating on top. The justification for the use of Si-O-Si peak value as a reliable coefficient for IR absorbance normalization can be found in Appendix A (Figure S3.1).

To estimate the effective dielectric constant of blanket low-k dielectric films covered with the metallic barrier in a simple MIS planar capacitor

geometry, we deposited 70 nm thick Pt electrodes on top of the barrier layer through a nickel shadow mask and sputtered away the uncovered conducting TaN/Ta layer in a CCP Ar discharge. The MIS stack preparation procedure was checked to have no impact on the k-value of the underlying porous low-k dielectric. The k-values were calculated based on the expression of capacitance for planar capacitors relying on measured capacitance and dielectric layer thickness as inputs. The series capacitance was measured at 100 kHz with Keysight E4980A Precision LCR Meter, while the thickness was measured by ellipsometry (KLA-Tencor ASET-F5) before the deposition of the metal barrier. In the case of TaN/Ta layer deposited on the films containing surfactant residues, the assessment of the sputtering impact on the dielectric constant was done after the additional annealing at 400°C for 2 hours in N_2 which followed the removal of TaN/Ta in-between the Pt electrodes. The employed annealing condition has been opted for nearly complete removal of the sacrificial phase.

The pore sealing was checked with an EP-10 ellipsometric porosimeter, equipped with a Sentech SE801 ellipsometer mounted on the lid of the vacuum chamber. Toluene or methanol was used as an adsorbate. Since the construction of an accurate optical model is complicated by the presence of two absorbing layers in the stack and by the presence of diffuse interfaces, the porosimetry analysis was simplified to the recording of the absolute changes in Δ ellipsometric angle at a single wavelength (680 nm), during the adsorption/desorption cycle. As shown in [209–211], the most accurate way to quantify the pore sealing efficiency is to expose a stack of interest to the adsorbate saturation pressure while monitoring the transient optical properties of the stack. Since the adsorbate in-diffusion rate is linked to the density of pinholes in the sealant layer[212], the change of adsorbate pressure should occur as quickly as possible if films with relatively high pinhole densities are to be distinguished. In this work, we used a slightly different approach due to a rather slow increase of adsorbate pressure in the employed porosimetry

chamber. The pore sealing quality of various SOG-2.2/TaN/Ta stacks was compared by analyzing dynamic adsorption/desorption "isotherms" recorded at an identical rate of adsorbate pressure modulation (Figure S3.2).

Regarding the patterned single-damascene vehicle, the dies with patterned SOG-2.2 dielectric were characterized electrically by measuring the room temperature leakage current on 2 cm long, 45 nm half-pitch fork-fork structures. The IV-characteristics were recorded with an Agilent 1500A parameter analyzer by sweeping voltage from 0V to 50V with a step of 0.5 V.

TEM analysis of die cross-section was done on lamellas prepared with FEI Helios NanoLab 460HP dual-beam system. The images were captured with TEM FEI Titan at 120kV using STEM-HAADF and EDS detectors enabling information about the elemental composition of analyzed samples.

3.6.3 Results and discussion

3.6.3.1 PVD TaN/Ta barrier damage in template-free low-k dielectric

The surfactant-free UV-cured SOG-2.2 material with open porosity of 39%, average pore radius of 1.2 nm, and nominal dielectric constant of 2.2 was subjected to sputtering of a 3nm/3nm TaN/Ta bi-layer. The TaN sputtering process was studied, by varying the energy of ionized species accelerated towards the low-k dielectric surface, i. e. it used three different AC bias power levels. Similar to plasma-induced damage of low-k dielectrics, the exposure of porous organosilica surface to high kinetic energy ions may result in two types of material modification: 1) changes in the composition of the organosilica matrix; 2) changes in the structure of the porous layer at its top interface such as densification, roughening/smoothening, *etc*.

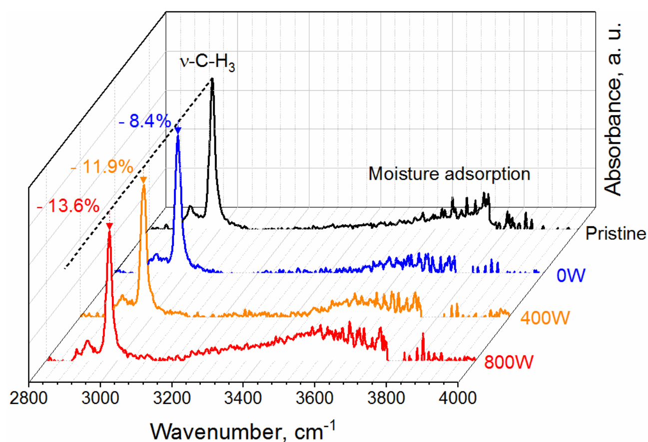

Figure 3.33. Normalized IR absorbance spectra recorded on SOG-2.2 films, pristine and after PVD TaN/Ta deposition with variable bias power of TaN sputtering step. The inset data shows the relative loss of $-CH_3$ groups as compared to the pristine SOG-2.2 coating.

In the context of TaN/Ta sputtering, the compositional changes may include depletion of intrinsic organic groups, adsorption of moisture, and incorporation of Ta into the top interface of the low-k film in the form of Ta-O or Ta-C bonds. The first two modifications can be evidenced in Figure 3.33, showing the normalized IR absorbance spectra, in the 2800-4000 cm^{-1} range, featuring the signals from $C-H_x$ and O-H stretching vibrations. Since the UV-cured material contains a negligible amount of sacrificial organics, the reduction of ν-$C-H_3$ peak intensity can be directly linked to the loss of $Si-CH_3$ groups responsible for the hydrophobicity of the low-k dielectric. In the case of 0W bias power, the loss of $-CH_3$ groups reaches about 8%, without any significant moisture accumulation. This damage may be partly attributed to VUV photons generated by the magnetron plasma containing excited Ar atoms. Nonetheless, unlike the study of Y. Wang et al.[210] on DC-sputtered metal barriers, this source of low-k damage does not appear to be dominating when the additional AC bias power source is on. The increase of AC bias

power to 400W and then to 800W results in a reduction of the normalized -CH_3 peak intensity, as compared to the uncoated low-k dielectric, by 11.9% and 13.6%, respectively. In addition, one can observe the associated increase of the moisture peak, indicating hydrophilization of the low-k film. To get a rough lower bound estimate of the material modification depth, one can multiply the thickness of the low-k layer (about 200 nm) by the calculated -CH_3 group loss values[166]. This FTIR-based equivalent damage layer (EDL) is around ~30 nm, which makes the damage induced by the deposition of the TaN/Ta barrier comparable to that observed in similarly porous low-k dielectrics exposed to fluorocarbon-based patterning plasmas[206]. Besides the removal of methyl groups, the process of TaN/Ta deposition is expected to induce the formation of Ta-O and Ta-C, which are more difficult to detect on the prepared stacks with a relatively thick TaN/Ta layer of 3 nm/3 nm. Therefore, the analysis of TaN/Ta incorporation into the low-k organosilica matrix was limited to the evaluation of tantalum in-diffusion into the porous dielectric.

Figure 2 shows the results of RBS measurements expressed in a calculated fraction of tantalum atoms present below the low-k layer/TaN interface. Without AC bias, a well-defined interface can be obtained, with minimal in-diffusion of metal barrier. As the power of the AC bias source increases, more metal species enter the porous layer. In the case of the highest studied bias power of 800W, nearly 25% of all sputtered tantalum is deposited inside the pores of the low-k dielectric. It is important to note, that the in-diffused species may not only bond to the matrix via polar Ta-O and Ta-C bonds[213], but also effectively reduce the thickness of the dielectric layer due to the presence of conductive TaN inclusions[214].

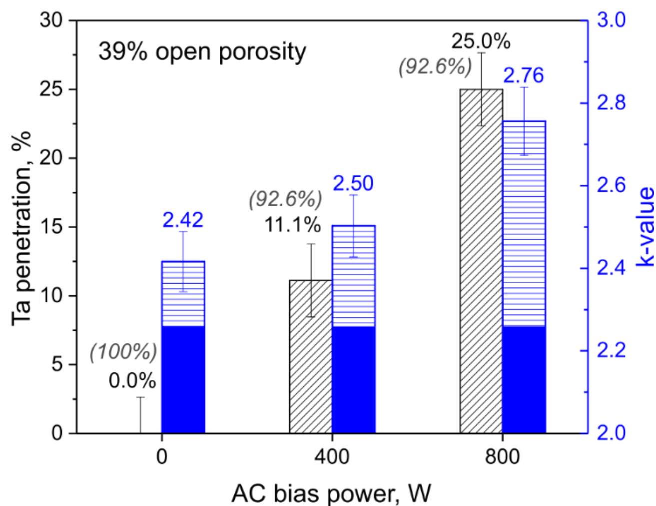

Figure 3.34. Impact of AC bias power during TaN sputtering step on tantalum penetration into SOG-2.2 (left columns) and on overall low-k damage expressed in terms of effective k-value (right columns). The values in brackets show the concentration of Ta atoms at the low-k dielectric surface relative to the 0W AC bias condition as estimated by RBS. The k-value of pristine SOG-2.2 film is 2.26.

The above compositional changes result in an increase of the dielectric constant, as shown in the same Figure 3.34 (right column). The estimated effective k-value is calculated using the thickness of the low-k dielectric before the TaN/Ta deposition and assuming the uniformity of the dielectric properties throughout the dielectric layer. It allows making a relative comparison of overall low-k damage between the different tested TaN/Ta sputtering conditions, while the actual role of damage-contributing factors such as carbon depletion, metal barrier penetration, and shrinkage remains debatable. In the case of TaN sputtering without bias, the dielectric constant rises from the initial 2.26 up to 2.42. Since this situation corresponds to negligible penetration of metal barrier into the low-k dielectric, one can

attribute the observed increase of k-value largely to the depletion of intrinsic organics from the organosilica matrix, as discussed above. The finite depth of carbon depletion in the absence of noticeable Ta permeation can be explained by the release and diffusion of O/H radicals generated upon bombardment of the low-k dielectric surface[215] as well as by the presence of a certain concentration of VUV photons attacking the Si-CH_3 groups in the bulk of the porous layer[216]. The addition of an extra AC bias source leads to additional degradation of the k-value. Remarkably, the seemingly minor increase of k-value is equivalent to the conversion of more than 30 nm of the pristine low-k layer into SiO_2 (k = 4.1) even in the case of bias-free barrier deposition (Table S3.1 in Appendix A). The significant part of the k-value increase can be attributed to physisorbed water which could be avoided in the properly integrated low-k dielectric, i. e. when the porous dielectric is sufficiently degassed before the metallization and not exposed to the atmosphere during the successive process steps[217]. Nonetheless, the estimated damage highlights how severe the low-k damage could be in case of inefficient encapsulation of the porous dielectric by barrier layers.

Therefore, it is crucial to estimate another performance criterion of a metal barrier deposited on a porous low-k dielectric – its pore sealing efficiency. The pore sealing in the current case is a complex interplay between the low-k pore structure changing under bombardment and the growth of 3 nm TaN/ 3 nm Ta layer. To test the continuity of the deposited barrier layer, we used ellipsometric porosimetry with toluene (C_7H_8) as a probe molecule. The adsorption/desorption isotherms in Figure 3.35 demonstrate that only in the case of zero-bias TaN sputtering, sealing is achieved. With AC bias power, the metal barrier layer fails the sealing check. Considering only the geometrical aspect of the pore sealing process with a PVD barrier, the minimal PVD layer thickness required for a continuous pinhole-free film can be estimated using an expression proposed by X. Wang et al.[211]. With the assumption that the average pore radius R is equal to the diameter of channels

connecting the pores, the minimum required thickness of the sealing layer t_{min} is given by $t_{min} = 16R/3$. For the template-free SOG-2.2 film used in the present work, $t_{min} \sim 6.4$ nm, which is close to the total nominal thickness of the deposited TaN/Ta barrier. The observation of pore sealing only for zero AC bias sputtering highlights the crucial role of ion bombardment for conditioning of the low-k dielectric surface.

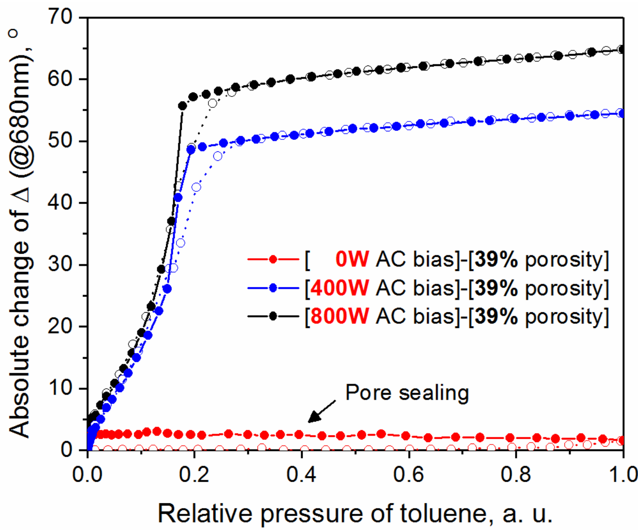

Figure 3.35. Relative changes in ellipsometric angle Δ (@680 nm) as a function of relative toluene pressure in the test chamber (both adsorption and desorption) recorded on template-free low-k films with three TaN/Ta bi-layers distinguished by different bias power of TaN deposition step.

To understand the reason for the pore sealing failure, it is insightful to have a look at the structure of the deposited metal barrier in detail. From the RBS results in Figure 3.34 (also see Table S3.2 in Appendix A), it follows that the concentration of Ta species at the surface deposited in the presence of AC bias is 7.4% lower as compared to the 0W AC bias case. This means that the process calibrated for deposition of 3 nm TaN on a dense SiO_2 surface fails to

deposit the same amount on porous substrates when bias is on. Since penetrated species are not expected to deposit in the pores as densely as they would do in the surface TaN phase, the effective dense barrier layer appears thinner and therefore more prone to discontinuity defects. Moreover, a relatively small concentration of such defects is needed to fail the toluene porosimetry test.[212] For example, no such barrier discontinuities are noticeable in 2.0 x 2.0 um^2 AFM scans (Figure S3.4 in Appendix A).

Although the above results suggest no apparent impact of the low-k dielectric material on the observed changes in the continuity of TaN/Ta layer, likely, the modification of the low-k dielectric surface by the bombarding species plays a key role in this phenomenon. F. Bailly *et al.* in his work studied the roughening of the low-k surface during etching in Ar/CF_x discharges and demonstrated that it is initiated by the formation of pits at the surface of the low-k dielectric, as a result of ion bombardment, inducing densification and cracking.[218] The formed pits then serve as diffusion paths for etching species such as fluorine radicals. This mechanism is applicable for PVD barrier deposition except that the in-diffused species in this case are not etching the low-k material, but instead remain in the pores thus degrading its dielectric properties. The formation of pits would explain the local character of TaN penetration into the porous low-k dielectrics (Figure 3.42). Their formation could also be directly linked to the thickness reduction of the dense TaN layer formed on top of the porous film. As the pits are created due to the cracking of the damaged top layer of the low-k layer, it is reasonable to assume that a higher concentration of such pits would appear under the sputtering conditions favoring surface bombardment or in a dielectric with higher porosity prone to low mechanical stability and fast surface densification. Based on this, two strategies can be proposed to solve the problem of pore sealing. The first one is to minimize the bias power component. This would lead to better pore sealing as well as to lower low-k damage. While this solution could work in the case of blanket films, the deposition of PVD barrier in high aspect ratio

trenches of damascene metallization layers requires finite bias to ensure a uniform step coverage of both the trench bottom and the side-walls. Moreover, the mere optimization of the sputtering component does not resolve the fundamental link between the porosity/pore dimensions and minimal thickness of the metal barrier needed to seal such pores, i. e. this solution is not scalable and cannot be easily extended to materials with lower k-value and larger pores. The second strategy relies on the optimization of the low-k dielectrics and their pore structure, e. g. by maintaining a temporary low porosity during the barrier deposition process. In the context of self-assembly based low-k dielectrics, we explored the benefits of using partially decomposed organic template molecules as the pore-protecting phase.

3.6.3.2 PVD TaN/Ta barrier damage in low-k dielectric with template residues

As the decomposition of the PEO-based surfactants starts at around 300-350°C[130,219], one can control the amount of the residues present in the pores by tuning the temperature or duration of the hard-bake process. The previous reports showed, that the template residues tend to decompose uniformly throughout the layer and remain on the surface of pores in the form of a protective coating, the thickness of which is modulated by the duration or temperature of the hard-bake process[128,220]. Also, the surfactant decomposition process takes much longer than the cross-linking of the organosilica process, which ensures a mechanically stable material. Therefore, we can consider the changes in the sacrificial phase and its amount as the only variables in the films. Here we prepared three low-k dielectric coatings from the same sol, using, after soft-bake, annealing times of 2 min, 30 min, and 120 min at 400°C in N_2. The latter type of coating was additionally UV-cured to achieve a template-free low-k material as a reference. The obtained set of three coatings had open porosity values of 26%, 31%, 39% and pore radii of 0.8 nm, 0.9 nm,

1.2 nm, respectively. To verify if the achieved effective reduction of the material porosity would solve the pore sealing issues during PVD TaN/Ta barrier deposition, the three types of low-k coating have been subjected to the deposition of 3 nm/ 3 nm TaN/Ta bi-layer under sputtering conditions with the highest AC bias power of 800W. The impact of the deposition process on low-k dielectric layer and the efficiency of its pore sealing have been tested using impedance measurements and ellipsometric porosimetry, respectively.

According to Figure 3.36, the retention of the template residues during TaN/Ta sputtering and the associated reduction of pore dimensions helps to suppress the penetration of Ta species into the bulk of the porous material. The level of Ta penetration, of about 3%, detected in the film with the largest template residue content (~30% of the total pore volume) becomes comparable to the result obtained under zero-bias TaN sputtering (Figure 2). As the damage contributions associated with the penetration of the conductive TaN phase and formation of polar Ta-O/Ta-C bonds are strongly reduced in the presence of template residues, the k-value of SOG-2.2 after TaN/Ta sputtering (and additional annealing to remove the template remnants) is approaching the value of 2.42 found in the case of no Ta penetration. This confirms the presence of low-k damage during the deposition of the PVD TaN/Ta layer, which can be attributed to sputtering-induced carbon depletion from the utmost surface and to deeper damage induced by VUV-photons which cannot be easily blocked by pore stuffing organics. It should be noted that in the current experiment, the procedure used for the removal of the template residues after TaN/Ta sputtering (annealing in N2 at 400oC for 120 min) is not as efficient as UV-cure. The UV-cured template-free SOG-2.2 material shows a k-value of 2.26, while the SOG-2.2 coating hard-baked at 400oC for 2 hours has a k-value of 2.36. Therefore, in Figure 4, some fraction of the trapped template phase could be responsible for increased k-values of the SOG-2.2 films initially hard-baked for shorter times.

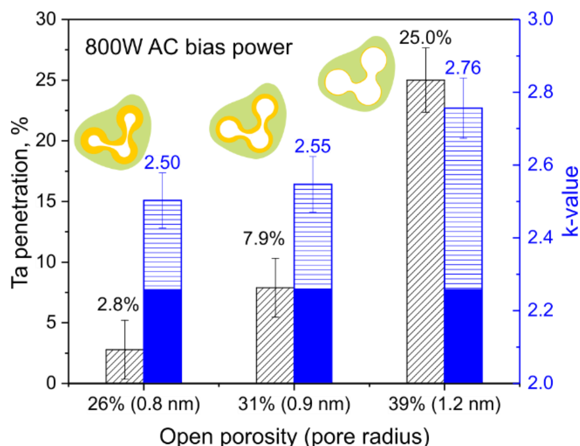

Figure 3.36. Impact of pore structure modified by the presence of template residues on tantalum penetration into SOG-2.2 and on its k-value. The k-values were estimated after an additional template removal step following the TaN/Ta sputtering.

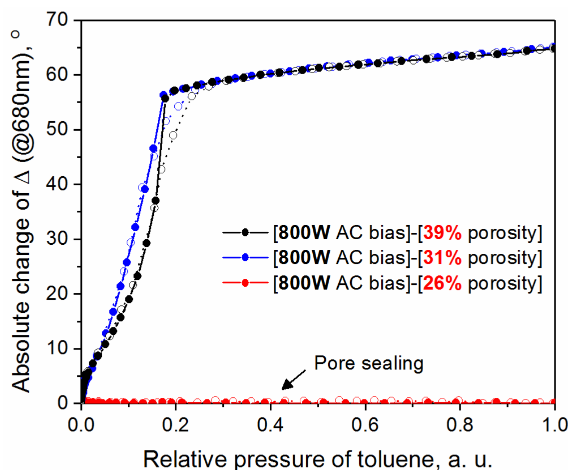

Figure 3.37. Relative changes in ellipsometric angle Δ (@680 nm) as a function of relative toluene pressure in the test chamber (both adsorption and desorption) recorded on SOG-2.2/TaN/Ta stack. The open porosity values in SOG-2.2 films have been defined by the amount of retained template residues.

According to Figure 4, the retention of the template residues during TaN/Ta sputtering and the associated reduction of pore dimensions helps to suppress the penetration of Ta species into the bulk of the porous material. The level of Ta penetration, of about 3%, detected in the film with the largest template residue content (~30% of the total pore volume) becomes comparable to the result obtained under zero-bias TaN sputtering (Figure 3.34). As the damage contributions associated with the penetration of the conductive TaN phase and formation of polar Ta-O/Ta-C bonds are strongly reduced in the presence of template residues, the k-value of SOG-2.2 after TaN/Ta sputtering (and additional annealing to remove the template remnants) is approaching the value of 2.42 found in the case of no Ta penetration. This confirms the presence of low-k damage during the deposition of the PVD TaN/Ta layer, which can be attributed to sputtering-induced carbon depletion from the utmost surface and to deeper damage induced by VUV-photons which cannot be easily blocked by pore stuffing organics[221]. It should be noted that in the current experiment, the procedure used for the removal of the template residues after TaN/Ta sputtering (annealing in N_2 at 400°C for 120 min) is not as efficient as UV-cure. The UV-cured template-free SOG-2.2 material shows a k-value of 2.26, while the SOG-2.2 coating hard-baked at 400oC for 2 hours has a k-value of 2.36. Therefore, in Figure 3.36, some fraction of the trapped template phase could be responsible for increased k-values of the SOG-2.2 films initially hard-baked for shorter times.

With respect to the pore sealing efficiency, one can notice the same positive trend. The partial occupation of pores with template residues compensates for the adverse effects of increased AC bias sputtering power. The isotherms in Figure 3.37 demonstrate, that only the low-k film containing the largest tested fraction of the template residues and pore radius of 0.8 nm can be sealed with a 6 nm TaN/Ta barrier. As we showed above, the pore sealing efficiency in the case of the 800W AC bias source depends not only on the pore geometry but also on the ability of the low-k dielectric to resist

surface modification such as densification and cracking under heavy ion bombardment. The presence of sacrificial organics in the pores appears to contribute to this resistance. Besides the mechanical support provided by the template residues as confirmed by the increased hardness of template-containing films (Table S3.3 in Appendix A), the sacrificial phase is additionally protecting the film from modification of the organosilica matrix composition and associated bond network relaxation, which has been demonstrated in our plasma damage mitigation study[128]. The importance of the minimal surface morphology modification is especially obvious in the case of the SOG-2.2 film which contained an intermediate amount of the template residues. According to the porosimetry analysis, the template residues occupying 20% of the porous volume in the film with 31% measured porosity reduce the average pore radius from 1.2 nm to 0.9 nm. This reduced pore radius would correspond to the minimal thickness of the sealing layer t_{min} of 4.8 nm. However, the deposition of 6 nm thick TaN/Ta on top of this low-k dielectric film did not show any pore sealing, indicating that despite smaller pore size, the surface morphology did not favor sealing.

In summary, the surface damage during PVD TaN/Ta deposition under high AC bias power conditions can be minimized in self-assembly based low-k dielectrics by keeping in the pores some partially decomposed sacrificial phase. These template residues enable efficient pore sealing with the lowest possible thickness of metal barrier, defined by the pore dimensions of the low-k dielectric.

3.6.3.3 Damascene integration using template residue retention

The demonstrated strategy for barrier damage mitigation and pore sealing enhancement can be integrated into damascene metallization schemes analogous to the post-CMP burn-out or post-porosity plasma protection approaches (Figure 3.38). However, its efficiency can be compromised by the

sensitivity of the template residues to the processes preceding the actual metal barrier deposition such as hard-mask stack formation, patterning, and post-etch wet clean. Unlike pore stuffing[203] or pore grafting[222] approaches, the method employing the template residues comes at nearly no cost as it does not require any additional precursors or stuffing process steps. On the other hand, the composition of the template residues is dictated by the choice of surfactant in the precursor solution. The commonly used surfactants are typically based on PEO, PPO, or PE chains[123,127], which tend to degrade at temperatures above ~300°C, are unstable in strongly oxidizing/reducing plasmas, and can decompose under VUV radiation. These factors are therefore expected to largely degrade, and remove partially decomposed surfactants, i.e. template residues, from the low-k dielectric. Therefore, the preservation of the template residues may need certain optimization of the integration process steps to avoid early decomposition.

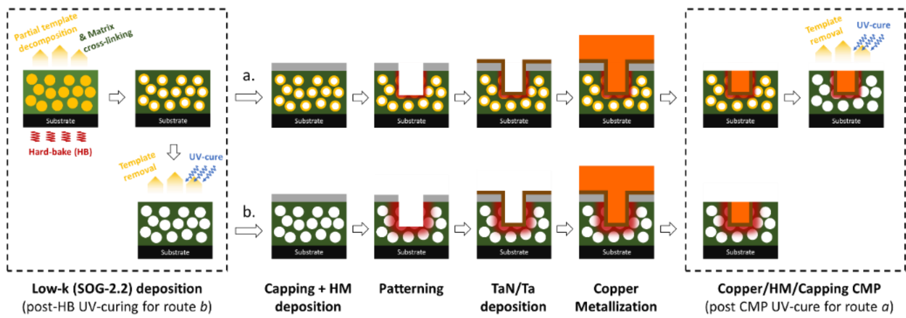

Figure 3.38. Schematic representation of single damascene metallization flows featuring the integration of SOG-2.2 self-assembly based low-k dielectrics (a) with template residue and (b) template-free. The red halo around the pattern area indicates the damaged/modified low-k dielectric (e. g. carbon depletion, Ta penetration, *etc*.).

The scheme in Figure 3.38 demonstrates the most important single damascene integration steps for the template-residues (top) and residue-free (bottom) routes. The only difference between the two integration flows under study is the point at which the sacrificial phase is removed. The removal of the template residues right after the hard-bake process corresponds to the standard integration of low-k dielectric. In the alternative flow, the template residues are preserved until the metallization is complete, then are moved by UV-cure, i.e. after the polishing (CMP) of copper together with the capping layer. Both integration routes start from the deposition of 200 nm SOG-2.2 dielectric, which is then hard-baked with specific hard-bake conditions aiming at maximizing the amount of the template residues. First, the hard-bake temperature was decreased from 400°C to 350°C; then its duration was adjusted to 30 min to allow sufficient time for the silanol condensation reactions within the organosilica matrix. A large enough organosilica matrix cross-linking is necessary to avoid excessive material shrinkage upon template removal. The optimized hard-bake conditions resulted in a rigid low-k film with shrinkage induced by UV-curing of only 2%, and with nearly 60% of the porous volume occupied by the template residues (Figure 3.39). This amount of residual organics is two-fold that detected in the pores of the film hard-baked at 400°C for 2 min and featured with open porosity of 26%. In Figure 3.39, the relative occupation of pores with the template residues at different steps of the low-k integration is calculated using Lorentz-Lorenz effective medium approximation from the measured refractive index of the low-k layer by assuming the refractive index of the template residues constant and equal to 1.533 (Figure S3.5 in Appendix A).

The lability of the PEO-based template residue phase means that its amount may decrease as the porous material is passing through different unit steps. The deposition of a silica-based capping layer preceding metal hard-mask (HM), using plasma-enhanced chemical vapor deposition (PECVD), is the first damaging process in the integration sequence. As shown in Figure

3.39, the plasma-based process of capping layer deposition removes roughly 10% of the template residues.

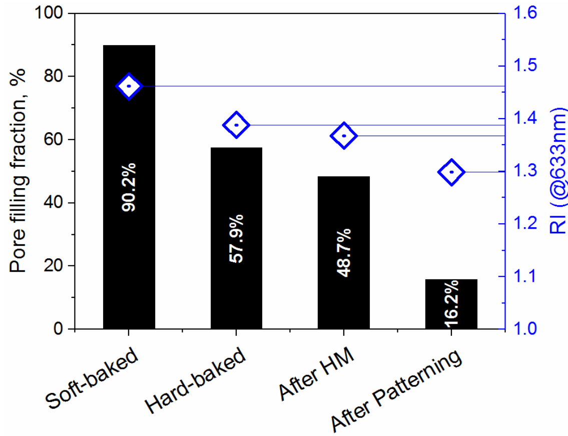

Figure 3.39. The loss of template residues and associated changes in refractive index (RI) of SOG-2.2 film induced by integration steps preceding the deposition of PVD TaN/Ta metal barrier. Spin-on HM is used.

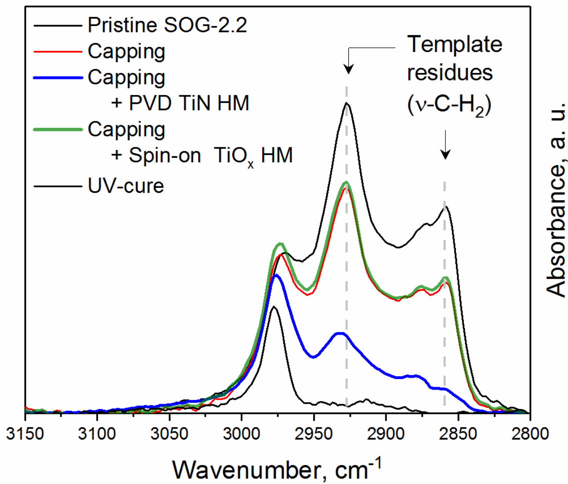

Figure 3.40. Impact of hard-mask stack formation on the preservation of the template residues in SOG-2.2 hard-baked at 350°C for 30 min in N_2.

At the next step of metal hard-mask formation, we compared two different deposition approaches – magnetron sputtering (PVD) and spin-coating complemented with additional soft-bake identical to the one used for the preparation of SOG-2.2 and hard-bake (spin-on). Both tested PVD TiN and spin-on TiO_x hard-mask layers have been deposited at temperatures not exceeding 350°C. Since the capping layer completely seals the SOG-2.2 dielectric, the deposition of the successive metal hard-mask layer is expected to have a minor impact on the template residues. To verify this, we analyzed transmission IR spectra recorded on the stacks with or without the capping layer. The TiN and TiO_x hard-mask layers were deposited on top of the capping layers and then dissolved in the ammonia-peroxide mixture (APM). The absence of any metallic layer on top of the capping film as well as the negligible presence of methylene bridging groups (-CH_2-) in the silica-based capping layer allows direct comparison of the template residue amount in the stacks of interest via -CH_2- IR absorbance signal (Figure 3.40). Besides the loss of the sacrificial phase caused by the deposition of the capping layer, one can clearly see that the deposition of the PVD TiN hard-mask led to an even greater reduction of the template residues. In contrast, the deposition of spin-on TiO_x coating did not have any impact on the composition of the underlying films. This is most likely due to the presence of VUV photons generated during magnetron sputtering of TiN target employing Ar as sputtering gas. The template residues could be decomposed by a fraction of VUV photons reaching the encapsulated low-k layer despite the relatively good VUV absorbing capability of the TiN layer[223]. To maximize the amount of sacrificial phase in the pores of SOG-2.2 at the PVD metal barrier deposition stage, we performed further integration of SOG-2.2 in combination with the spin-on TiO_x hard-mask.

In the current integration flow, the trenches within the SOG-2.2 layer were etched in CCP-discharge with Ar/CF_4/C_4F_8 gas mixture. While the PEO-based template residues demonstrated very good stability in SF_6-based

fluorine-rich etching plasma, their sensitivity to VUV light, abundant under the employed plasma conditions, may adversely affect their low-k damage mitigation function. What is more important in the context of this work, such a patterning process resulted in the decomposition of a sizable portion of the template residues. According to the data presented in Figure 3.39, the dry etching step is responsible for the decomposition of about two-thirds of the sacrificial phase. Therefore, the reduction of VUV emission during the patterning process is essential for compatibility with the PEO-based template residues.

The combined impact of the capping layer deposition and of the patterning process nullified the advantages of the optimized hard-bake conditions. The fraction of porous volume occupied by the template residues dropped from 60% to about 16% after patterning, i. e. before the PVD metal barrier deposition step. Such a high level of template dissociation indicates that the residues offered some protection against active radicals and VUV, during mask deposition and plasma etching. This pore occupation fraction of about 16% is close to what is obtained for SOG-2.2 film prepared by annealing for 30 min at 400°C. Since this blanket SOG-2.2 film could not be sealed with 3 nm TaN/3nm Ta bi-layer according to the data discussed above, the thickness of both TaN and Ta layers deposited on top of the patterned SOG-2.2 films was increased by 50% making the total nominal thickness of the metal barrier equal to 9 nm.

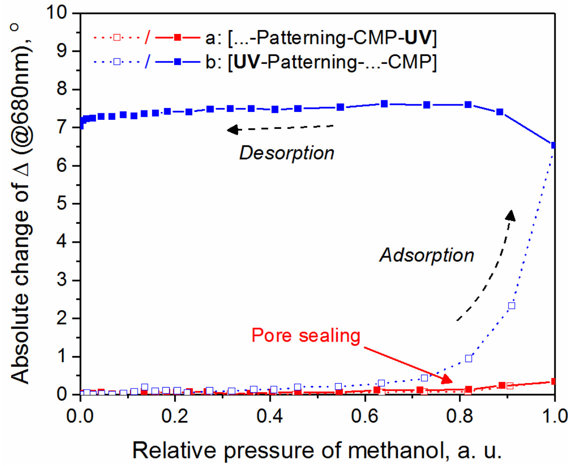

Figure 3.41. Relative changes in ellipsometric angle Δ (@680 nm) as a function of relative methanol pressure in the test chamber (both adsorption and desorption) recorded on the patterned SOG-2.2 after deposition of TaN/Ta barrier. The figure compares the template preserving (a) and the conventional template-free integration strategy (b).

The continuity of the barrier layer deposited on the patterned template-containing (route a) and template-free (route b) SOG-2.2 dielectrics was evaluated using ellipsometric porosimetry with methanol (CH_3OH) as a probe molecule (Figure 3.41). Compared with toluene, the smaller size of the methanol molecule makes the porosimetry test more sensitive to barrier discontinuities. Moreover, the similarity between the dimensions of methanol (0.38 nm) and water molecules (0.30 nm) makes such a test more integration relevant, as it allows assessing the water permeability of the barrier layer[224]. As the rate of pressure variation during the porosimetry measurements is fixed, the quality of the pore sealing layer, associated with a certain density of pinholes in it, can be estimated via the dynamics of the diffusion-controlled pore filling process. We can clearly see that the two integration routes under test have distinctly different dynamics of methanol adsorption into SOG-2.2

dielectric. The large hysteresis loop formed by adsorption/desorption curves in the case of template-free low-k dielectric provides evidence of a relatively small pinhole density in the TaN/Ta barrier film which prevents fast in-diffusion of methanol into the underlying porous layer. The pinhole density is expected to be lower than that in the thinner TaN/Ta metal barrier deposited on the blanket template-free SOG-2.2 dielectric (Figure 3.37). Nonetheless even the presence of a few pinholes of the size exceeding that of water molecules represents a serious reliability concern for interconnects. These local direct contacts between the damaged low-k dielectric and copper may induce corrosion of conducting lines[225]. In contrast, the TaN/Ta layer deposited on top of the low-k dielectric containing the preserved fraction of the template residues appears to be pinhole-free and is characterized by reversible adsorption/desorption isotherms. The small changes in ellipsometric angle Δ at the end of the adsorption process can be attributed to the larger surface area of the patterned films as compared to the blanket SOG-2.2 coatings.

The superior quality of the TaN/Ta barrier deposited on top of the template-containing SOG-2.2 dielectric is confirmed with TEM cross-section images recorded on a fully integrated single damascene metallization layer (Figure 3.42). Without template residues, the dark-field STEM images demonstrate significant in-diffusion of metal into the low-k dielectric, particularly at the trench bottom, where it appears in the form of metal streaks. The element maps show that the metal entering the low-k dielectric is tantalum and no discernable signal from copper can be detected in the areas around the conductor line. Although the tantalum in-diffusion could also be partially caused by the lamella preparation process (ion milling), there is an apparent difference in the severity of this phenomenon between the integration routes tested in this work.

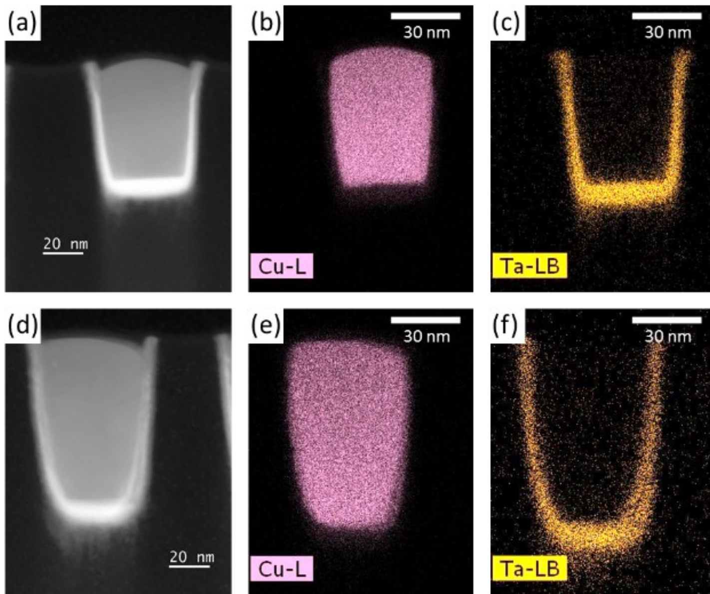

Figure 3.42. TEM cross-section analysis of 45 nm copper line integrated following the template preservation strategy (a)-(c) and the conventional template-free damascene integration (d)-(f), respectively. Cross-section images (a) and (d) are recorded in HAADF-STEM mode, while (b), (c), (d), (f) represent the respective EDS elemental maps of copper and tantalum.

The local penetration of the metal barrier supports the hypothesis pointing to the microcracks or pits formed under the bombardment-induced stress as the main reason for the pore sealing failures. It is also important to note that in the current process flow, the low-k dielectric surface experiences noticeable ion bombardment both during the TaN/Ta PVD sputtering and during patterning. Therefore, the observed reduced metal barrier infiltration in the case of the integrated template containing SOG-2.2 films should not be considered out of the context of the etching process which may strongly roughen a porous low-k dielectric surface.

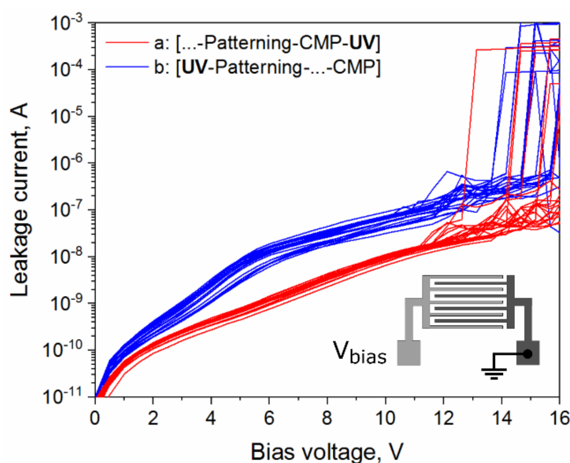

Figure 3.43. Leakage current measured on 21 fork-fork capacitors (45 nm half-pitch) prepared following the two integration routes under test.

To understand whether the observed differences at the SOG-2.2/TaN interfaces could influence the electrical properties of SOG-2.2 low-k dielectric, leakage current measurements were performed at room temperature on 45 nm half-pitch fork-fork capacitor structures (Figure 3.43). The capacitors prepared with a reference template-free approach demonstrate a generally higher level of leakage current. This difference could be related to the larger height of the copper wires (see TEM profiles in Figure 3.42). What makes the IV-curve series recorded on the reference capacitors particularly distinct is a leakage current "hump" at around 6 V, which is identified as an onset of a low-field conduction mechanism not evidenced for capacitors integrated with the template residue preservation strategy. Although based on the available electrical data, it is not possible to pinpoint the exact mechanism responsible for the increased leakage current, there are several reasons to associate it with the low quality of the barrier layer. The roughness of the TaN/low-k interface obtained during the reference processing may result in

increased Schottky emission[226], while the deeply in-diffused Ta atoms may act as shallow traps for the emitted electrons thus enhancing the Poole-Frenkel contribution to the leakage current[227]. Moreover, the pinholes in the metal barrier detected by the methanol porosimetry open the path for the drift of copper ions into the low-k dielectric. In turn, the presence of Cu ions in the organosilica-based low-k dielectrics has been shown to assist both Poole-Frenkel and Schottky emission mechanisms[228].

3.6.4 Conclusions

This work covers various aspects of porous low-k dielectric damage induced by magnetron sputtering of the TaN/Ta metal barrier. The extent of low-k material modification described in terms of its composition, surface morphology, and k-value strongly depends on the AC bias sputtering power of the PVD TaN process. In turn, the structural changes at the surface of the dielectric caused by ion bombardment appear to be responsible for the observed in-diffusion of tantalum into the porous layer and pore sealing failures. Therefore, the minimization of ion bombardment is necessary for the deposition of the thinnest possible continuous metal barrier defined by the intrinsic pore geometry of the low-k dielectric. PEO-containing template residues, uniformly distributed in the pores in self-assembly based low-k dielectrics, may be another scalable solution. Tests on blanket SOG-2.2 coatings show that the retention of about 30% of the template residues in the pores allows not only to achieve pore sealing with 6 nm TaN/Ta bi-layer under higher bias power conditions (800W AC bias) but also to reduce the average pore radius from the nominal 1.2 nm to 0.8 nm, which may enable deposition of even thinner pinhole-free metal barrier coatings. The proposed template retention strategy is validated for the low-k integration in a 45 nm half-pitch damascene structure. The main challenge in this implementation is to preserve template residues during hard-mask stack deposition and plasma etching. The

sensitivity of PEO-based template residues to VUV photons makes the template-containing SOG-2.2 low-k dielectric poorly compatible with PVD TiN hard-mask and plasmas with strong VUV emission. While the loss of the residues during the sputtering of the TiN hard-mask could be eliminated by replacing it with a spin-on TiO_x analog, the employed patterning plasma consumed nearly 60% of the sacrificial organic phase. Nonetheless, although not fully optimized, the current process flow demonstrates the advantages of the new strategy in comparison with the reference integration flow featuring template-free low-k dielectric. The modified flow, where the organic residues are decomposed at the end of the metallization, results in sharp pin-hole free interfaces between the porous low-k and the metal barrier layers, correlated with reduced low-field leakage current through fork-fork capacitors. Therefore, the proposed surfactant retention approach provides a simple yet efficient solution for the reduction of integration-induced damage in highly porous organosilica materials.

3.7 Chapter summary

As shown in Chapters 3.2 and 3.3, the optimal selection of sol components such as template and organosilica esters may have a significant impact on the mechanical stability of the low-k dielectric coating. The use of short-chain surfactants and organosilica esters featuring long bridging groups enhances the cohesion strength of the dielectric. Chapter 3.4 described UV-curing of the spin-on organosilica dielectrics as an approach for elimination of defect states associated with the template residues which are left inside the pores even after the prolonged conventional hard-bake process and undermine the electrical reliability of the dielectric. In contrast, Chapters 3.5 and 3.6 highlighted the benefits of the template residues, which can be temporarily left in the pores of a fully cross-linked organosilica framework to enhance its stability in plasma and facilitate pore sealing. Finally, the complete single damascene integration of porous SOG-2.2 dielectric with template residues preserved in the pores up until the copper CMP step demonstrated the improved electrical performance of 45 nm half-pitch capacitor devices as compared to the reference integration flow.

Chapter 4. Zeolitic imidazolate frameworks as low-k dielectrics

4.1. Chapter introduction

In this chapter, we explore the possibility to use zeolitic imidazolate frameworks (ZIFs), a sub-class of metal-organic frameworks, as ultra low-k dielectrics in on-chip interconnects. Sub-chapter 4.2.3 focuses on both evaluation of blanket ZIF-8 and ZIF-67 coatings formed via MOF-CVD approach and on testing the gap-filling capability of this deposition method.

This work was performed at imec in collaboration with the group of Prof. Rob Ameloot (cMACS, KU Leuven) whose research group pioneered the MOF-CVD approach used here for solvent-free deposition of zeolitic imidazolate framework films. The study was published in Nature Communications journal.

M. Krishtab, I. Stassen, T. Stassin, A. J. Cruz, O. O. Okudur, S. Armini, C. Wilson, S. De Gendt, R. Ameloot. Vapor-Deposited Zeolitic Imidazolate Frameworks as Gap-Filling Ultra-Low-k Dielectrics. *Nat. Commun.* 10 (1), 3729 (2019).

***Personal contribution*:** Design and arrangement of the experiments, collection and analysis of experimental data, direct involvement in fabrication of the patterned test structure, MOF film characterization (AFM, EP, k-value evaluation on both blanket and patterned test vehicles) and capacitance simulation.

***Support from co-authors and other contributors*:** The deposition of ALD ZnO, the MOF-CVD process as well as post-deposition characterization with GI-XRD were carried out by Alex John Cruz, Timothée Stassin and Ivo Stassen using the KU Leuven cleanroom and lab facilities. The

mechanical properties of thin MOF films were analyzed by Oguzhan Orkut Okudur via nanoindentation. Some analysis including XPS, RBS, TEM/TEM-EDS was performed by members of imec's MCA group.

4.2 Vapor-deposited zeolitic imidazolate frameworks as gap-filling ultra-low-k dielectrics

Abstract

The performance of a multi-layer interconnects system formed above a semiconductor chip is strongly related to the properties of insulating medium surrounding metal wires. The continuous demand for reduction of dielectric's k-value creates multiple integration challenges and encourages searching for materials beyond organosilica. Here we report a novel strategy for the integration of metal-organic frameworks (MOFs) as gap-filling low-k dielectrics in advanced on-chip interconnects. The method relies on the selective conversion of purpose-grown or native metal-oxide films on the metal interconnect lines into MOFs by exposure to organic linker vapor. The proposed strategy is validated for thin films of the zeolitic imidazolate frameworks ZIF-8 and ZIF-67, formed in 2-methylimidazole vapor from ALD ZnO and native CoO_x, respectively. Both materials show a Young's modulus and dielectric constant comparable to state-of-the-art porous organosilica dielectrics. Moreover, the fast nucleation and volume expansion accompanying the oxide-to-MOF conversion enable uniform growth and gap-filling of narrow trenches, as demonstrated for 45 nm half-pitch fork-fork capacitors.

4.2.1 Introduction

Since the invention of integrated circuits (ICs) 60 years ago, there has been a persistent incentive towards the miniaturization of IC components. An indispensable part of every contemporary IC is a multi-level wiring system fabricated on top of the semiconductor device layer. As transistors get smaller

and more densely packed, the complexity and the impact on performance of the on-chip interconnects rises. Modern chips can incorporate several billion transistors and require multilayered interconnects that have wire dimensions below 30 nm in diameter near the silicon surface[202,229]. The non-zero resistance (*R*) and capacitance (*C*) associated with the metal wires and the insulating medium between them induce cross-talk noise, limit the speed of signal propagation and contribute to the power consumption of a chip[201]. Both *R* and *C* tend to increase with further interconnect miniaturization, an effect particularly noticeable at wire diameters and spacings below 50 nm. To address this challenge, the materials used for on-chip interconnects have been significantly diversified in the last two decades[198]. Two major changes concerned (i) the replacement of traditional dielectrics such as silicon oxide with 'low-k' materials featuring a dielectric constant (or 'k-value') < 4.3 and (ii) the introduction of low-resistivity metals instead of aluminum. Currently, copper is the metal of choice due to its high conductivity and good resistance to electromigration, while state-of-the-art low-k dielectrics are typically porous organosilicas deposited from plasma or solution[12,13,35,105]. Due to difficulties associated with direct plasma etching of copper films[230], copper interconnect wires are formed via a 'damascene' process[231], This metallization route relies on first patterning the dielectric layer via anisotropic plasma etching before Cu electroplating and planarization. Plasma-induced damage of new potential low-k materials, especially porous ones, during this patterning step is a major roadblock to achieve k-values < 2.4[223,232]. An alternative metallization approach is to first pattern a sacrificial layer that can be removed after the formation of metal interconnect wires, leaving the latter as a patterned top layer[233]. In such an integration scheme, the low-k dielectric is subsequently deposited and needs to fill the gaps between the metal wires. Driven by the steep increase in copper resistivity at wire dimensions below 50 nm[234], this and other alternative metallization strategies relying on the initial formation of the metal pattern are quickly gaining attention[235–238], together

with a shift to beyond-Cu metals that perform better at these dimensions (e.g., Co and Ru)[9,199,239,240]. The common challenge shared between these alternative metallization approaches is gap-filling the narrow trenches (width < 50 nm, height/width ratio > 2) between metal interconnect lines with the low-k dielectric[241,242]. For the current state-of-the-art organosilica dielectrics deposited by plasma-enhanced chemical vapor deposition or spin-on methods, this task is not straightforward because of local deposition non-uniformity and post-deposition material shrinkage upon porogen removal. While current ultra-low-k dielectrics thus seem unsuitable for a novel, plasma-damage-free integration, the alleviated plasma stability requirement allows to significantly widen the range of potential low-k dielectrics.

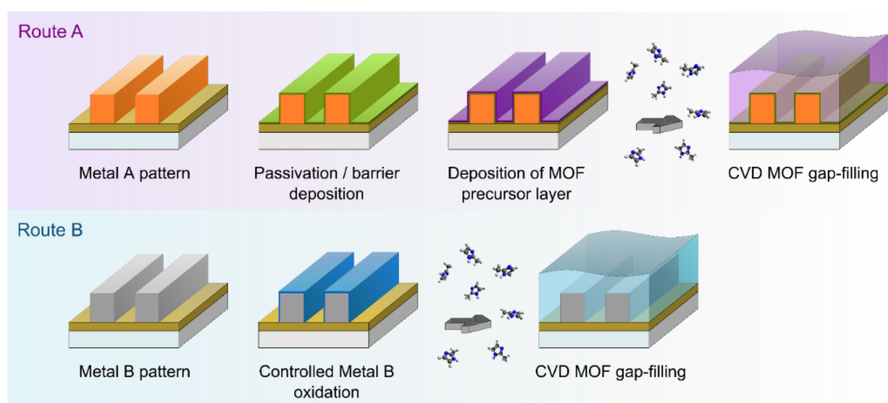

Figure 4.1. Two proposed routes for the integration of ultra-low-k MOF dielectrics in on-chip interconnects via the MOF-CVD process. Routes A and B differ in how the MOF precursor layer is formed around the interconnect wires. In route A, metal oxide to be converted into MOF is deposited after the passivation of metal lines, while route B relies on the selective conversion of metal oxide formed through controlled oxidation of the metal pattern.

One promising class of dielectric materials are metal-organic frameworks (MOFs)[243], which possess many properties sought for in interconnects: (i) uniformly distributed pores with diameters < 2 nm that significantly reduce possible infiltration during subsequent processing[211,244] and make the porous dielectric applicable in sub-10 nm inter-metal spacings[56,245]; (ii) a low dielectric constant and (iii) a suitable mechanical stability[13,105]. The potential of MOFs as advanced low-k dielectrics was first recognized by Zagorodniy et al., who used a simple Clausius-Mossotti model to estimate the dielectric constants of various MOFs[246]. Eslava et al. provided the first experimental validation of the k-value of solution-deposited films of ZIF-8 (k = 2.33)[76], a well-studied thermally and chemically stable MOF consisting of Zn(II) nodes and 2-methylimidazolate (2-mIm) linkers[80]. Since then, other MOFs have been studied as potential low-k dielectrics[247–250]. Despite these encouraging results, no integration of MOFs in interconnects has been shown to date, mainly because typical MOF thin film growth methods are solution-based, and therefore hard to scale and mostly incompatible with microelectronics fabrication infrastructure[251]. Nevertheless, recent advances in vapor phase deposition of MOF films[61,252,253] bridge this gap and make integration in on-chip interconnects possible.

In this work, we adapted the method of chemical vapor phase deposition of zeolitic imidazolate frameworks (ZIFs) proposed by Stassen et al. ('MOF-CVD')[251] to achieve gap-filling of narrow spacings between metal interconnect lines (90 nm pitch, 45 nm trench width, 90 nm trench height). In MOF-CVD, a metal oxide precursor film is consumed through a vapor-solid reaction with the organic linker and converted to a porous MOF film. In the case of ZIF-8 MOF-CVD, a previously deposited ZnO layer reacts with 2-methylimidazole vapor (2-HmIm). Importantly, ZIF-8 film growth is selective as it is restricted to the area covered by ZnO and the final film is significantly thicker than the initial ZnO layer (~16-17 times, based on theoretical crystal densities), because of the added organic content and the porous nature of the

MOF. Based on these characteristics of the MOF-CVD process, we propose two general integration routes for MOFs as gap-filling dielectrics into the interconnect metallization layer (Fig. 1). In both routes, gap-filling relies on localized material expansion during the precursor-to-MOF conversion. Route A targets gap-filling the trenches between passivated metal lines by first depositing a conformal oxide/hydroxide layer as MOF precursor. This route can be an optimal choice when a metal diffusion barrier is required (e.g., Cu interconnects). Route B is arguably more elegant since the MOF precursor layer is formed by the controlled oxidation of the metal line surface[254–256]. Since this route results in direct contact between the metal and the MOF, low metal ion diffusion through the dielectric is needed to avoid electrical reliability issues. Additionally, this route requires that the oxide-to-MOF conversion strictly halts at the metal/metal oxide interface so that the interconnect wire remains intact. Route B is particularly interesting for Co metallization since cobalt wires may not need a metal diffusion barrier[257] and at the same time form a CoOx precursor skin layer through surface oxidation[256]. In this proof-of-concept study, we focus on Zn(II)-based ZIF-8 and its isostructural Co(II)-based analog ZIF-67 to demonstrate the feasibility of routes A and B, respectively.

4.2.2 Experiment details

Preparation of MOF-CVD precursor layers on blanket wafer. The layers of ALD ZnO and PVD Co were prepared on highly-doped p++ Si substrates. ALD ZnO deposition was realized at 120 °C by 30 cycles of diethyl zinc (DEZ)/water precursor pulses separated by N_2 purge steps (Savannah S200, Veeco Instruments Inc.). PVD Co film was sputtered on Ar-plasma pre-cleaned Si-substrate (NC7900, Canon Anelva Corp.).

Preparation of MOF-CVD precursor layer on patterned wafer. The fork-fork capacitor structures featuring 45 nm line/space were prepared on p-

type 300 mm Si-wafers according to a modified integration route (Figure S4.2) based on using sacrificial amorphous carbon (a-C) layer to form a pattern of passivated copper wires[233]. The initial stack of layers above the substrate consisted of 1000 nm SiOx, 30 nm SiCN diffusion barrier, 90 nm a-C, and a multi-layer hard-mask stack. After the formation of a device pattern in the top positive resist coating with 193 nm immersion lithography, the pattern features were then transferred into the underlying a-C film. Following the wet removal of hard-mask residues, the exposed surfaces of a-C/SiCN were coated with 3 nm ALD TiN. The subsequent metallization steps included sputtering of 20 nm Cu seed, electroplating of 500 nm Cu, and chemical mechanical polishing (CMP) down to the a-C film. The removal of the a-C sacrificial layer was done in He/H2 remote plasma. Afterwards, the metallic lines were passivated with a non-conformal 3 nm PECVD SiCN barrier layer and then additionally covered with conformal 2 nm PEALD SiN_x film. The deposition of CVD Co was realized at 200 °C on VECTOR Excel tool cluster (Lam Research). Before deposition of CVD Co on the SiCN/SiN_x-passivated Cu pattern, the growth conditions were optimized on blanket SiN_x surface to obtain 4.0 ± 1.0 nm Co layer across 300 mm wafer (assessed by Rutherford backscattering spectroscopy). ALD ZnO deposition on the metal lines passivated with SiN_x layer was performed by applying the same growth conditions as used on blanket wafers (see above).

Vapor-phase conversion process (MOF-CVD). For the conversion to the appropriate ZIF layer, samples with precursor layers were placed in a glassware reactor (Figure S4.1). The glassware reactor was connected to a vacuum pump via a manual valve. Upon assembly, the reactor was checked for leaks. The glass tube containing 2-methylimidazole powder (99%, CAS #693-98-1, Sigma-Aldrich) was connected to one of the ports of the glassware reactor via another manual valve. The whole set-up was placed in a furnace pre-heated at 120 °C. After the temperature stabilization (15 min), the valve to the vacuum pump was opened, and the reactor was evacuated until pressure

stabilization below 10 mbar. The vacuum valve was then closed and the valve to the 2-methylimidazole tube opened. The exposure of samples to vapors of 2-methylimidazole was set to 120 min, after which the precursor valve was closed, and the sample area of the reactor was kept under dynamic vacuum for 15 min to remove the unreacted organic linker from the sample surface and pores of formed ZIF films (activation). Finally, the reactor was let to cool down before the samples could be taken out for further characterization.

X-Ray diffraction (XRD) patterns were obtained with PANalytical Empyrean diffractometer equipped with Cu Kα X-ray source and Pixcel3D detector. The surface-sensitive grazing incidence X-ray diffraction mode (GI-XRD) was employed with Omega fixed at 0.2° and 2*Theta scanned in the range 5-50° with a step size of 0.05°. The diffractograms were then manually baseline-corrected using b-spline interpolation.

Ellipsometric porosimetry (EP) measurements were performed on a custom-built tool featuring a vacuum chamber, a spectroscopic ellipsometer (Sentech SE801, 350–850 nm wavelength) mounted on it and a programmable adsorbate vapor supply platform. The isotherms were recorded at 23 °C (the temperature of the vacuum chamber). The temperature of the liquid sources (DIW and methanol) was maintained at 25 °C. The equilibration time at each pressure point was set to 30 s.

Atomic force microscopy (AFM) topography images (10 x 20 μm^2, 512 x 1024 pixels) were recorded in tapping mode with Dimension Edge microscope (Bruker). The image corrections (rows alignment, horizontal scars elimination) and plotting was performed with Gwyddion 2.44 software[258]. The latter was also used to calculate the arithmetic (R_a) and root-mean-squared (R_q) surface roughness.

Scanning electron microscopy (SEM) images were collected on manually cleaved samples with Hitachi SU8000 microscope operating at 10 kV with a secondary electron detector. Besides 70 nm Pt e-beam evaporated on top of ZIF layers (Pfeiffer PLS580) before cleaving, the cross-section

surface was additionally sputter coated with 1 nm Pt (Cressington 108) before the inspection. The extraction of average ZIF layer thickness (*d*) from the obtained cross-sectional images was done with a custom Python script based on OpenCV (Open Source Computer Vision Library). This involved locating more than 60 uniformly spaced points at ZIF/Pt interface (*N*). The uncertainty of the average thickness value was expressed via a 95% confidence interval [$d - 1.96*R_q$/sqrt(N); $d + 1.96*R_q$/sqrt(N)], where R_q, root-mean-squared surface roughness calculated from the appropriate AFM images, was used as an accurate estimate of standard deviation of ZIF layer thickness. As a result, the thickness of ZIF-8 and ZIF-67 films used in this work was defined as 24.0 ± 1.2 nm and 28.9 ± 2.2 nm, respectively.

X-Ray photoelectron spectroscopy (XPS) measurements were carried out in angle-resolved mode using a Theta300 system (Thermo Fisher Scientific). 16 spectra were recorded at exit angles between 22 and 78 degrees as measured from the normal of the sample. The measurements were performed using a monochromatized Al K_α X-ray source (1486.6 eV) and a spot size of 400 micrometers. Standard sensitivity factors were used to convert peak areas to atomic concentrations.

Rutherford backscattering spectroscopy (RBS). The RBS experiments were performed in a random rotation mode using 1.5 MeV He^+ ions from the 6SDH tandem accelerator (National Electrostatics Corporation) equipped with an Alphatross ion source. The experimental end-station was a 5-axis goniometer developed at the Forshungszentrum Jülich[86]. The angle between the sample normal and the beam was set to 11 degrees. The solid angle of the PIPS detector was 0.42 msr, the scattering angle was 170°. The beam spot was confined to 1x1 mm^2. In-house developed analysis software was used to fit the spectra and to deduce the areal density.

Nanoindentation (NI) measurement was performed using Hysitron TI 950 Triboindenter (Bruker). Continuous stiffness measurements (CSM) with a cube corner indenter were employed. The Li-Vlassak method[83] implemented

in a custom MATLAB script was applied to extract Young's modulus of the top ZIF layers. Poisson's ratio of the films was assumed 0.44 based on a previous study[259]. At least 10 CSM curves were analyzed per sample and the results were averaged. It should be noted that the method is in principle applicable only for bilayer stacks, i. e. thin film on a substrate. This complicates the extraction of elastic properties in the case of ZIF-67 film, which is formed on top of 20 nm Co/Si-substrate stack. Nonetheless, the additional elastic finite-element simulations demonstrated the negligible influence of the intermediate metallic Co layer on the load-displacement characteristics. This can be attributed to the same order of magnitude of Young's moduli for Co (200 GPa)[260] and Si (130 GPa)[261] in contrast to the much lower value of Young's modulus of ZIF films under test (< 5 GPa). As a result, the presence of the Co layer was ignored during the analysis of the stack containing ZIF-67 film.

Transmission electron microscopy (TEM) analysis of the fork-fork capacitor cross-section was done on 30-50 nm thick lamellas prepared with dual beam FIB/SEM Helios NanoLab 450HP (FEI). Before the FIB lift-out, the surface of the samples under test was coated with a protective coating consisting of three sequentially deposited layers: a drop-casted organic layer (SoC) soft-baked at 150 °C, e-beam (5 kV) and ion-beam (30 kV) deposited Pt layers. As a last step of the lamella preparation, there was a 5 kV ion beam milling step to reduce the surface damage. The TEM images and EDS element maps were captured with Titan3 G2 60-300 TEM (FEI) operating at 60 kV.

Impedance measurements were performed using high-precision LCR-meter E4980A (Keysight Technologies) in the frequency (f) range 10 kHz - 1 MHz. The measured impedance values were interpreted with an equivalent scheme consisting of a serially connected capacitor (C_s) and resistor (R_s). The dissipation factor (D) was estimated as $2\pi{*}f{*}R_s$. In the case of blanket ZIF films, their k-value was calculated from capacitance C_s measured on Metal-Insulator-Metal stacks using the formula for parallel plate capacitor: k =

C_s*d/(ε_0*S), where ε_0 – vacuum permittivity, S – the area of top 70 nm thick Pt circular electrodes e-beam evaporated though a Ni shadow mask (Pfeiffer PLS580), d – average thickness of ZIF layer extracted from cross-sectional SEM images.

2D capacitance simulation. The extraction of the k-value for the gap-filling phase in the case of fork-fork capacitors was performed by adapting the procedure which has been already successfully employed for the evaluation of integrated k-values of various porous low-k dielectrics[262]. At first, a model of the electrically characterized fork-fork capacitor is reconstructed based on previous knowledge about low-frequency dielectric constants of the constituting layers and on their profiles extracted from TEM cross-sectional images. The extraction of the profiles and layer dimensions of interest was implemented with a help of a custom Python script embedding OpenCV (Open Source Computer Vision Library) functionality. The profiles of the conducting lines (Cu + TiN liner) and of the passivating SiCN and SiN_x films were averaged over six different wire cross-sections. The other dielectric layers in the model were represented by perfect rectangular patches with an average height determined from TEM images. The capacitance simulation was done with 2D field solver implemented in Raphael program suite (Synopsys). The width of the simulation window could be reduced to only two structure pitches (180 nm) due to the employed reflective (Neumann) boundary condition. The capacitance of a model fork-fork capacitor was calculated as a product of simulated 2D capacitance and the capacitor's length (2 cm).

4.2.3 Results and discussion

Validation of the MOF-CVD process on blanket films. Figure 4.2a schematically shows the precursor-to-MOF conversion that was performed in a simple glassware reactor (Figure S4.1). Starting from 5.8 nm atomic layer deposition (ALD) ZnO on top of a Si substrate and from 3.2 nm native CoO_x

on top of 20 nm PVD Co, the conversion resulted in 24.0 nm ZIF-8 and 28.9 nm ZIF-67 respectively, as estimated from SEM cross-sectional images (Figure S4.3b). The crystalline structure and composition of the films were confirmed by GI-XRD (Fig. 4.2b) and XPS (Table S4.1).

The "effective" thickness expansion factors of 4.1 for ZnO and 9.0 for CoO_x based on ellipsometry and SEM data (Fig. 4.2a) appear significantly lower than the theoretical expansion of 17.0 and 20.4 calculated for wurtzite hexagonal ZnO and cubic CoO, respectively. The theoretical expansion factor calculated based on the metal density of ideal ZnO and CoO crystals is an upper limit since (i) precursor films can contain defects (e.g., hydroxyls) and therefore can have a lower metal content compared to pure oxide crystals and (ii) the precursor-to-MOF conversion might be incomplete. Both effects were investigated for the ALD ZnO and native CoOx precursor layers.

For the ALD ZnO film (45 DEZ/H_2O cycles at 120 °C), the volume concentration of Zn atoms was estimated by combining the Zn atom areal density ($30.8 \cdot 10^{15}$ atoms per cm^2) assessed by Rutherford backscattering spectroscopy (Figure S4.4) and the thickness (8.9 nm) measured by ellipsometry. The resulting density of Zn atoms equal to $3.45 \cdot 10^{22}$ atoms per cm^3 is lower than that of wurtzite ZnO by approx. 18%, which results in a proportional reduction of the thickness expansion and an expansion factor of 13.9. The lower Zn content of the ALD ZnO film likely originates from pending Zn-OH groups that remain unreacted during the low-temperature ALD process[263]. Based on the corrected expansion factor, it can be calculated that roughly 4 nm ZnO remains at the interface between the ZIF-8 film and the substrate. However, due to its relatively high conductivity[264,265], the remaining thin ALD ZnO layer has negligible impact on the measured MIM capacitance.

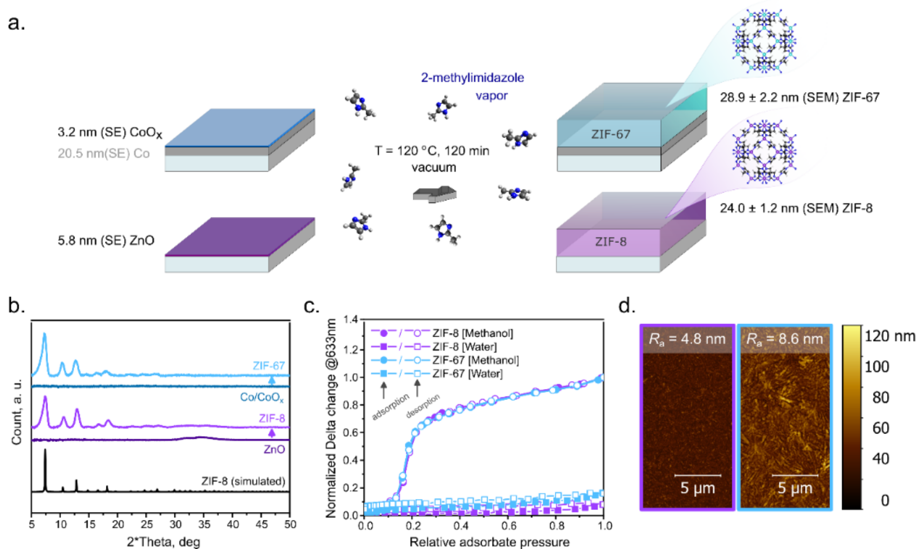

Figure 4.2. Validation of the MOF-CVD process and characterization of the deposited MOF thin films. (a) Schematic representation of the conversion of ALD ZnO and native CoO_x to ZIF-8 and ZIF-67 and the corresponding increase in thickness as measured by spectroscopic ellipsometry (SE) and from SEM cross-sectional images. (b) Baseline-corrected GI-XRD diffraction patterns together with simulated powder diffractogram for ZIF-8. (c) Ellipsometric porosimetry with methanol and water as adsorbates. The amount of adsorbate corresponds to the change of the ellipsometric angle Delta (@633nm) relative to the value recorded before introducing probe molecules. The values are normalized against the Delta change measured at methanol saturation pressure. (d) AFM topography images of MOF-CVD films: ZIF-8 (purple frame) and ZIF-67 (light blue frame).

The situation is more complicated for the native CoO_x layer formed on top of the sputtered Co film. While there is no doubt about the formation of ZIF-67 (based on GI-XRD, porosimetry, and XPS data), the presence of metallic Co prevents the use of the RBS methodology to correct the expansion factor and estimate how much CoO_x remains. Therefore, the aforementioned theoretical expansion factor for perfectly crystalline CoO was used to estimate the maximum thickness of the remaining CoO_x layer as 1.8 nm. In reality, the remaining CoO_x layer will be thinner because of a lower effective expansion factor[266,267]. Because of its higher resistivity, the presence of CoO_x at the interface between metallic Co and ZIF-67 should be taken into account for the estimation of the MOF k-value. However, the impact of this layer was negligible (Figure S4.5). Although in the current experiment some CoO_x remains, the conversion process would in any case be expected to stop at the metallic Co surface, thus preserving the metal line in analogy with a recent study on metallic Zn surfaces[268].

Ellipsometric porosimetry is a powerful technique for the evaluation of thin porous films. It is based on in-situ ellipsometry monitoring of the refractive index changes in the porous layer as a result of the adsorption/desorption of a probe molecule supplied at well-controlled partial pressures[89,269,270]. For a qualitative assessment of the resulting isotherms, one can avoid fitting the recorded Psi/Delta values by plotting the relative changes of these optical parameters as a function of adsorbate pressure (e.g., Delta at 633 nm) (Fig. 4.2c). Such ellipsometric porosimetry data obtained with methanol as a probe molecule show that both ZIF films display identical adsorption/desorption behavior, characterized by a step in the isotherm in the partial pressure range 0.1-0.2. This observation is consistent with previous reports of methanol adsorption measured for ZIF-8 powder samples[271,272]. The absence of secondary sorption at higher relative pressures, characteristic of intercrystallite mesoporosity, positively distinguishes the MOF-CVD ZIF layers from the pure-silica zeolite (PSZ) films that also have been considered

as potential low-k dielectrics[273,274]. Another advantage of the ZIF-8 and ZIF-67 frameworks is that they are intrinsically hydrophobic due to the methyl group on the organic ligand pointing towards the pore interior[275]. The MOF-CVD ZIF films do not absorb moisture, even at high relative humidity, as evidenced by water-based ellipsometric porosimetry. While pure-silica zeolite powders are also intrinsically hydrophobic[276], thin films of PSZ and PSZ-like materials often suffer from moisture uptake and a related k-value increase due to silanol-rich grain boundaries or the presence of amorphous silica[175,277,278].

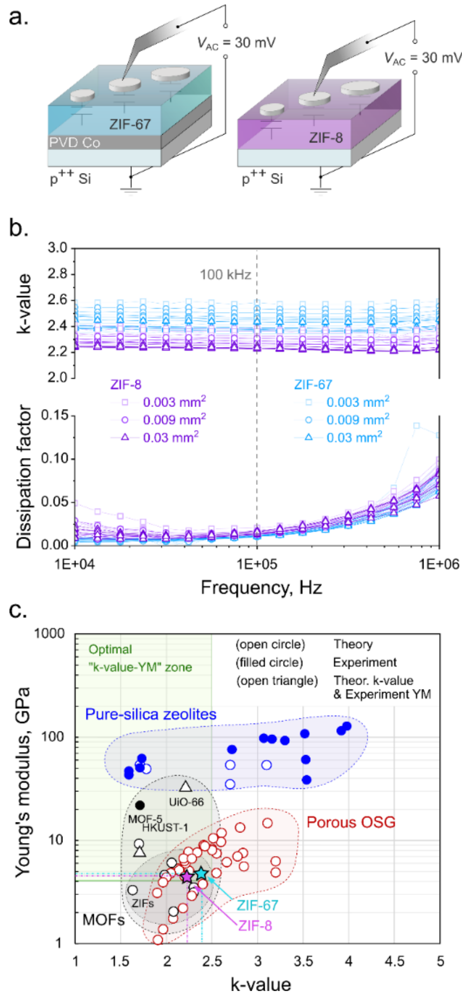

Figure 4.3. Dielectric constant and Young's modulus of MOF-CVD ZIF-8 and ZIF-67 films. (a) experimental set-up for k-value measurements; (b) k-value and dissipation factor spectra (10 kHz - 1 MHz) measured on MIM capacitors with three different top electrode areas; (c) positioning of MOFs on the Young's modulus/k-value map in comparison with other classes of advanced low-k dielectrics. The Young's modulus and k-value data measured on MOF-CVD ZIF-8 and ZIF-67 films (this work) are marked with stars. The theoretical and experimental values for Young's modulus and k-value in the graph are taken from [39,75,76,78,259,273,279–292].

Balance of dielectric constant and Young's modulus in MOF-CVD ZIF films. When considering MOFs as low-k dielectrics, it is essential to get an accurate value of the dielectric constant at low frequencies (< 1 MHz), conventionally used for the assessment and comparison of various low-k materials. Measurements on MOF-CVD films offer an advantage compared to the MOF powder pellets commonly studied, not only because of the absence of intercrystal voids[75,293] or potential pelletization-induced damage,[294] but as well because such high-quality pinhole-free films (Fig. 4.2b) allow to employ the standard measurement protocol for low-k dielectric coatings[88]. The k-value of the MOF-CVD ZIF layers was extracted from capacitance data measured at frequencies in the range 10kHz – 1MHz on planar Metal-Insulator-Metal (MIM) stacks. The latter are formed by e-beam evaporating round Pt electrodes of different diameters (195, 107, and 62 μm) on top of the MOF-CVD films deposited on conductive substrates (Fig. 4.3a). Measuring the capacitance on Pt electrodes of different sizes allows to check the uniformity and continuity of the MOF-CVD layers. Similar to good insulators such as silicon oxide or organosilica low-k dielectrics[88], the k-values measured for both ZIF-8 and ZIF-67 films demonstrate nearly no dispersion in the employed frequency range (Fig. 4.3b). Additionally, the k-values are insensitive to heating up to at least 150 °C (Figure 6). The absence of any significant conductivity or low-frequency dipole relaxation modes leading to the dissipation of electromagnetic field energy is also confirmed by a low dissipation factor (D = 0.01-0.02 at 100 kHz). The k-values extracted from the smaller capacitors tend to be slightly higher due to the effect of fringing capacitance[88,295]. The contribution of the latter is negligible for the k-values estimated on the largest electrodes: 2.23 ± 0.11 for ZIF-8 and 2.39 ± 0.18 for ZIF-67 at 100 kHz. The uncertainty for these k-values originates from the statistical variation of the thickness extracted from SEM images (Figure S4.3b). Interestingly, the obtained k-value for MOF-CVD ZIF-8 agrees well with earlier measurement of 2.33 ± 0.05 (at 100 kHz) by Eslava et al. on 10-

30 times thicker solution-deposited ZIF-8 films[76]. While the k-value of Zn-based ZIFs was shown to scale with the framework density[75], the impact of the metal ion node has not yet been reported. According to our results, the Co-based ZIF-67 possesses a slightly higher k-value than its Zn-based analog. A similar relation was reported for a pair of isostructural tryptophanate frameworks based on Zn (II) and Co (II) ions[296]. As the dielectric constant strongly depends on the polarizability of the bonds in the framework, the increased k-value of Co-based MOFs may be due to the more polar Co-N bonds as compared to Zn-N[297].

Another important characteristic of potential low-k dielectrics is their mechanical stability, typically assessed via nanoindentation and expressed as Young's modulus (YM). Since conventional data analysis techniques cannot provide a correct interpretation of measurements on sub-100 nm films due to substrate effects, we used an iterative data analysis algorithm proposed by Li and Vlassak[83] to extract the elastic modulus of the ZIF layers. This method was previously shown to yield consistent results for a wide range of thin low-k dielectric films[298]. Besides the low thickness, the measurement was challenged by the polycrystalline texture of the MOF-CVD films, by the associated surface roughness, and crystal facet-dependent elastic properties. Nevertheless, the average YM for ZIF-8 MOF-CVD films (3.44 ± 1.42 GPa) is in good agreement with the previously published isotropic (Voigt-Reuss-Hill averaged) experimental and theoretical YM values of 3.15 GPa[259]. The slightly higher YM of ZIF-67 MOF-CVD films (3.79 ± 1.83 GPa), reported here for the first time, could be ascribed to the larger stiffness of the Co-based framework as compared to ZIF-8[299]. The latter was attributed to the more ionic character of the Co-N bond.

To position the MOF-CVD ZIFs with respect to other porous materials considered as low-k dielectrics, the YM and k-values reported here were included in a summary plot of experimental and theoretical data for MOFs, PSZ, and porous organosilica glasses (Fig. 4.3c). The YM of state-of-the-art

porous organosilica glasses clearly decreases with a reduction of the k-value. This negative effect of the reduced density on the YM can be alleviated by incorporating stronger bonds[39,113], by introducing ordered instead of random pores[56] and by increasing the connectivity of the nodes[79,300]. Although the first two strategies may enable incremental improvements of the k-value versus YM trade-off for organosilica materials, breakthroughs are expected only from a transition to a different class of dielectrics. PSZ occupy an attractive area in the top left corner of the plot thanks to their crystallinity, microporosity, and strong covalent bonding. However, there is no scalable method yet for the deposition of PSZ films that produces uniform hydrophobic polycrystalline coatings without intercrystal porosity and a high concentration of silanol defects. MOFs lie mostly in the ultra-low-k range ($k < 2.5$) and are spread along the YM axis, as expected based on their diversity in terms of bond type and framework topology. Within the MOF family, ZIFs occupy the lower YM range, overlapping with porous organosilicas. Although ZIFs are equivalent to the latter state-of-the-art dielectrics in terms of mechanical and dielectric properties, their deposition via MOF-CVD has the distinct advantage of enabling gap-filling and therefore future interconnect integration schemes.

Gap-filling performance of MOF-CVD ZIFs. The gap-filling test for MOF-CVD ZIF-67 was performed on 45 nm pitch fork-fork capacitors formed by 90 nm thick copper lines passivated with a thin layer of PECVD SiCN diffusion barrier (~3 nm). A conformal film of 2 nm PEALD SiN_x was deposited to improve the nucleation of a nominally 4 nm CVD Co film that was exposed to air to form a CoO_x layer. The result of the precursor-to-MOF conversion process can be seen in Fig. 4.4a. The bright-field TEM cross-sections along with the EDS element maps before and after exposure to 2-HmIm vapor provide insight into the structural and compositional changes. The poor nucleation of the CVD Co layer on top of SiN_x results in a rough and non-conformal layer of oxidized Co agglomerates with a size of 10-15 nm on

top of the metal lines and 2-3 times smaller inside the trenches. During the vapor-phase conversion nearly all CVD Co is consumed and despite the initial non-uniform distribution of the Co precursor, the space in between and above the passivated copper lines is filled with ZIF-67, as also evidenced by the homogeneous Co and N EDS signal (Figure S4.7). To demonstrate that the voids in the ZIF-67 phase observed by TEM (Figure S4.8) are due to the beam damage or the preparation of the 30-50 nm thick lamellas[301,302], additional SEM cross-sectional images were recorded for the same fork-fork capacitors (Figure S4.9). The cross-section surface was prepared by manually cleaving the substrate and depositing 1 nm of Pt to eliminate any beam-induced damage. No voids can be observed in these high-resolution SEM cross-sections.

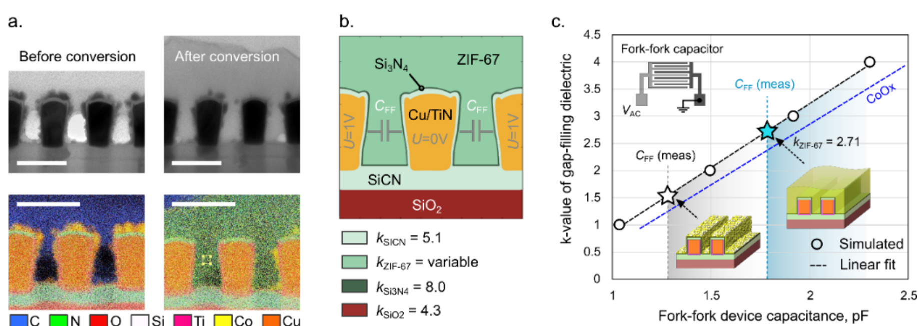

Figure 4.4. Validation of the MOF-CVD process and characterization of the deposited MOF thin films. (a) Schematic representation of the conversion of ALD ZnO and native CoOx to ZIF.

To evaluate the gap-filling performance of MOF-CVD ZIF-67, the effective k-value was extracted by means of 2D capacitance simulations. In these simulations, the capacitor geometry was taken from the TEM cross-sectional images (Fig. 4.4b), and the dielectric constant of the gap-filling medium was varied between 1.0 and 4.0 to generate a calibration curve (Fig.

4.4c). The resulting effective k-value of the gap-filling material determined from the capacitance data at 100 kHz (Figure 4S.10) is 2.71 and only slightly exceeds that of the flat ZIF-67 film (Fig. 3b).

CoO_x residues occur largely on top of the passivated Cu-lines and are caused by CVD Co agglomerates with dimensions in some cases exceeding 10-15 nm. To estimate the possible impact of these defects on the extracted ZIF-67 k-value, additional 2D capacitance simulations were performed (Figures S4.11-S4.12). The k-value of the CoO_x residues was assumed to be equal to that of CoO (k = 12.9)[303]. Since these simulations are two-dimensional, defects defined in a cross-section geometry extend in the 3rd dimension, along the Cu-lines. Therefore, the effect of defects on the simulated capacitance is strongly amplified and should be considered a worst-case scenario. Nevertheless, the addition of unconverted CoO_x residues decreases the extracted ZIF-67 k-value only by 0.35 for the largest simulated defect dimensions (Figure 4.4c). Noteworthy, despite the relatively small effect of these oxide residues on the overall capacitance, their impact on the leakage current between the capacitor forks can be severe (Figure S4.13). These effects are exclusively caused by the poor nucleation and agglomeration of CVD Co on the surface of the demonstrator capacitors. In the proposed integration route B (Figure 4.1), the use of Co metal lines would eliminate such issues since the CoO_x precursor would conformally cover the lines.

The fork-fork capacitors were also used to check gap-filling by MOF-CVD ZIF-8 starting from ~ 6 nm ALD ZnO deposited conformally on top of the SiN_x passivation layer. The corresponding TEM cross-sections (Figure S4.14) confirm the successful filling of 45 nm wide trenches with ZIF-8. Even though some unconverted ZnO remains, complete gap-filling is evidenced by the homogeneous Zn and N EDS signal.

4.2.4 Conclusions

In summary, MOF-CVD ZIF films do not only demonstrate dielectric and mechanical characteristics competitive with state-of-the-art porous organosilica dielectrics but may outperform them in future integration schemes because of the gap-filling nature of the deposition process. Besides validation of the proposed concept, the gap-filling experiments indicate that further control over the properties of the oxide precursors as well as the conversion process is desirable to avoid precursor residues. To achieve this goal, the MOF-CVD process will have to be implemented as an automated cleanroom unit operation instead of through the use of simple glassware reactors. Efforts are underway to achieve this goal and will be reported as a separate study. When implementing gap-filling MOF-CVD dielectrics, also further integration steps will have to be optimized. Different process flows can be proposed (Figure S4.15), in each of which potential points of concern with respect to MOF integration need to be investigated and addressed if necessary: (i) planarization of MOF films when the as-deposited roughness is too high for direct deposition of the next layer; (ii) deposition-induced damage of the MOF layer; (iii) plasma-MOF interactions, and (iv) MOF pore sealing. These topics are barely explored for MOF films and will need more attention in the future.

4.3. Chapter summary

The current chapter demonstrated the promising potential of MOFs as low-k dielectrics which is related to the favorable combination of low dielectric constant and Young's modulus as well as to the solvent-free deposition approach enabling area-selective and seamless formation of MOFs. The reported results can be considered a significant step forward in the field of MOF integration in nanoscale devices. Nonetheless, further development of the presented concept is necessary to address the pressing questions concerning the compatibility of MOF material with standard or alternative metallization process flows.

Chapter 5. General conclusions and outlook

5.1 General conclusions

The current study was initiated to explore the horizons of dielectric materials with a major focus on verification of their ability to compete and eventually replace the currently used organosilica materials deposited from plasma.

Based on the results reported in this thesis work one can conclude that the spin-on organosilica ultra low-k dielectrics would outperform the PECVD counterparts with the same target dielectric constant due to the following advantages of SOG films:

1) Possibility to decouple the correlation between the porosity and pore dimensions, thus ensuring a more uniform distribution of pore volume. As shown in Ch. 3.2, the latter makes the SOG materials more mechanically robust. According to Ch. 3.3, the cohesion strength of a SOG dielectric material could be further improved by adding longer carbon (ethylene) bridges into the organosilica matrix. This flexibility in defining the organosilica backbone composition and the pore structure is the unique property of porous SOGs which cannot be fully reproduced in plasma-deposited SiOCH low-k dielectrics. As the role of the bonding type within the organosilica matrix increases with material porosity, the superiority of SOG's mechanical properties is expected to stand out remarkably when highly porous materials are being considered for integration.

2) As shown in Ch. 3.4, unlike porogen molecules used during PECVD deposition, the PEO-based surfactants could be removed without leaving carbon-based residues, thus contributing to the material's

better electrical reliability. Also, it is worth noting that the proposed combination of a very short thermal annealing with UV-curing treatment used for the complete decomposition of the organic template allows to shorten the total SOG film preparation cycle by more than 20 times compared to the traditional calcination-based approach thus making the film deposition throughput comparable to that of typical PECVD low-k dielectrics.

3) The organic template residues uniformly covering the organosilica backbone can serve as a temporary protective layer against processing-induced damage. The complete removal of the sacrificial organics would be done using the UV-curing step right before the sealing of the porous low-k layer with a dielectric barrier layer. Since the proposed integration scheme relies on the PEO-based surfactant originating from the sol, it doesn't imply the introduction of any extra material. Despite the incomplete pore filling, the protective coating exhibits similar damage reduction performance to the more technically sophisticated pore stuffing method. In particular, in Ch. 3.5 it was shown that the template residues were able to suppress the damage of low-k dielectric in aggressive F-radical rich plasma. Another benefit of the proposed approach is displayed in Ch. 3.6 where the presence of the template residues on the pore walls was shown to enable improved pore sealing with a thin TaN/Ta metal barrier. These examples demonstrate how the thoughtful management of the original sacrificial material can help to extend the compatibility of traditional integration routes with highly porous low-k dielectrics.

Overall, the current work provides a rather complete guideline on the optimal design and integration of porous organosilica spin-on dielectrics.

The metal-organic framework films are still very new to the field of microelectronics and distinct from traditional amorphous silica-based materials. By comparing MOFs to silica-based low-k dielectrics in terms of the “k-value – Young’s modulus” balance (Figure 4.3c) one can note that MOFs occupy a sweet spot between pure-silica zeolites and porous organosilicas. This makes the search for integration routes of MOFs well justified. The current study focused on ZIF dielectrics is the first demonstration of MOFs integration into on-chip interconnects based on the newly developed MOF-CVD approach which is fully compatible with microelectronics processing.

While the measured dielectric and mechanical properties of ZIF-8 and ZIF-67 are comparable to competing porous organosilicas, the uniqueness of the MOF deposition process creates new opportunities for the low-k dielectric integration into interconnects. For example, the reported ability to gap-fill narrow geometrical high-aspect ratio features makes MOFs an appealing candidate for integration into post-damascene Ru-interconnects which are fabricated by pre-forming Ru pattern before the wiring insulation. Another opportunity is the area-selective deposition of MOFs following the conversion of respective metal oxide deposited in pre-defined areas. The latter would be of ultimate interest for self-alignment integration schemes being actively explored in microelectronics fabrication nowadays.

Besides the experimental gap-filling study, the work also offers the potential integration routes with highlighted process challenges (Figure S4.15) which can serve as a roadmap for future research on the integration of MOF-CVD gap-filling dielectrics into on-chip interconnects.

5.2 Outlook

For almost two decades of research in the field of ultra low-k dielectrics, no universal solution was found to break through the “red brick wall” firmly standing at an effective k-value of ~2.5. The manufacturability issues along with increasing contribution to RC-delay from down-scaled metal wires, made the semiconductor industry step back from the integration of highly porous dielectrics. This makes the future application of spin-on organosilicas as a direct replacement of PECVD SiOCH dielectrics rather doubtful despite the demonstrated advantages. Instead, porous SOG dielectrics may still be considered for integration into interconnects as auxiliary dielectrics in the schemes assuming planarization or gap-filling properties of the dielectric material.

One of such novel integration scheme is Ru-based metallization (Figure 1.8). As this route avoids direct dry etching of the dielectric material it allows to consider dielectrics for which gap-filling performance is more important than stability in plasma. Based on the results of the MOF-CVD study, this setup is particularly interesting for the integration of MOFs as low-k dielectrics. However, compared to the 90 nm half-pitch line pattern studied in this work, the pattern dimensions in the typical Ru interconnects are expected to be substantially more challenging for gap-filling namely with trench width below 20 nm and aspect ratio above 2. The study of MOF-CVD based gap-filling on such Ru patterns would be a logical extension of the current work.

Another integration scheme that potentially fits the MOF profile is so-called self-aligned via integration (Figure 5.1). In the proposed integration route, the selectively deposited low-k dielectric helps to prevent misplacement of the metal via and at the same time reduces the capacitive coupling between metal lines in adjacent layers (interlayer capacitance). Since the selective deposition of classical spin-on or PECVD porous organosilica materials is not

possible, the integration scheme is often exercised with high-k metal oxides such as AlO_x deposited via ALD. The MOF-CVD approach consisting in the local conversion of metal oxides into porous MOF dielectrics may potentially address this challenge. One potentially interesting aspect of using MOF-CVD materials as selective dielectrics compared to typical ALD dielectrics is that MOF-CVD growth proceeds via the re-assembly of the originally isotropic ALD precursor layer into MOF crystals. The alignment of such crystals may be guided by the underlying surface energy or recess pattern thus avoiding the change in critical pattern dimensions commonly observed for selectively-deposited isotropic coatings.

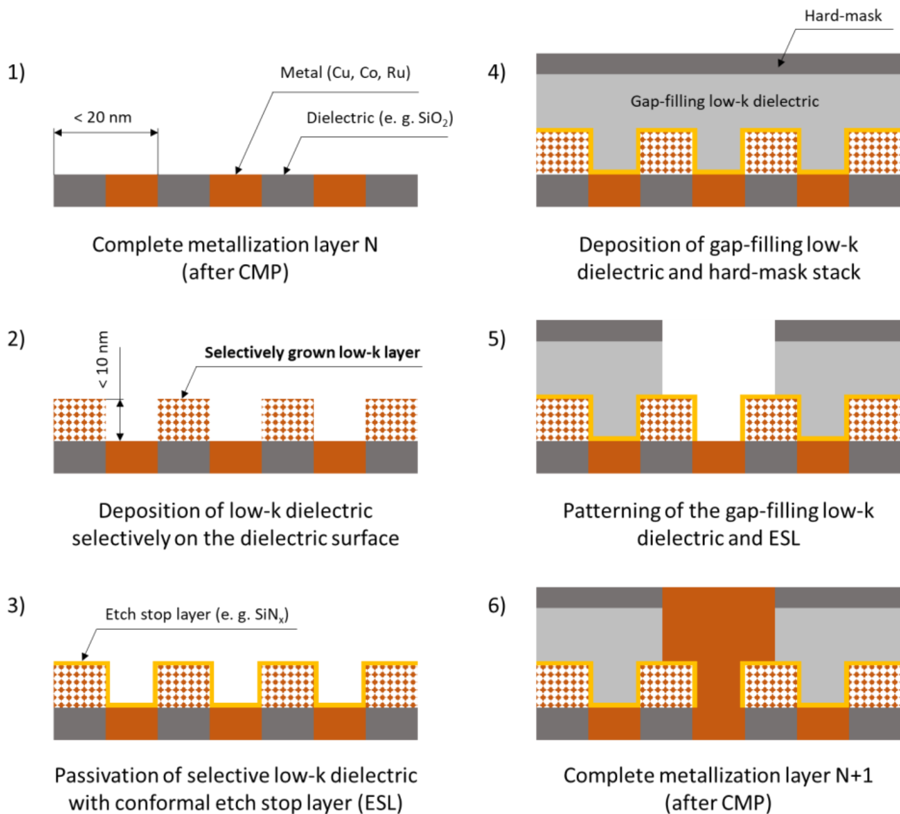

Figure 5.1. Self-aligned via integration scheme assuming selective deposition of a low-k dielectric.

Despite the abundance of literature exploring the application of MOFs in electronics, the electrical properties of MOFs are not often accurately measured or discussed in detail. Taking into account the polycrystalline nature of MOF layers as well as the potentially damaging interaction of MOFs with environmental species, the reliability aspects should become one of the central points of discussion on the applicability of a particular MOF type in nanoelectronics devices. Therefore, such critical fundamental aspects of MOF dielectrics as the mechanism of leakage current, the effect of point defects and grain boundaries on electrical properties are yet to be studied.

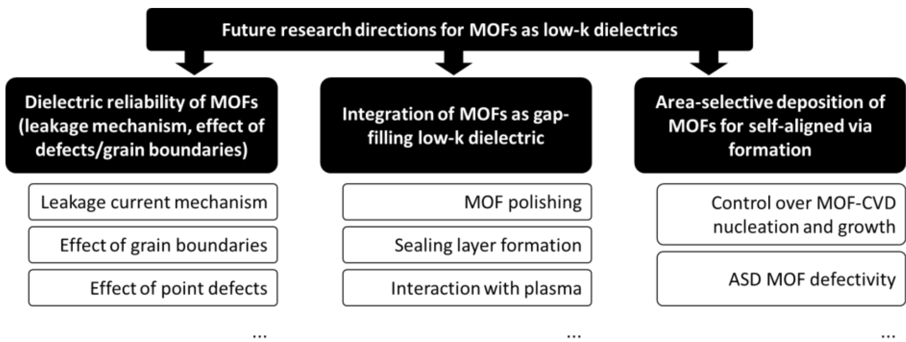

Figure 5.2. Potential future research directions for MOFs as low-k dielectrics.

Appendix A

Supporting information for Chapter 3.6

1. Normalization of IR absorbance by Si-O peak value

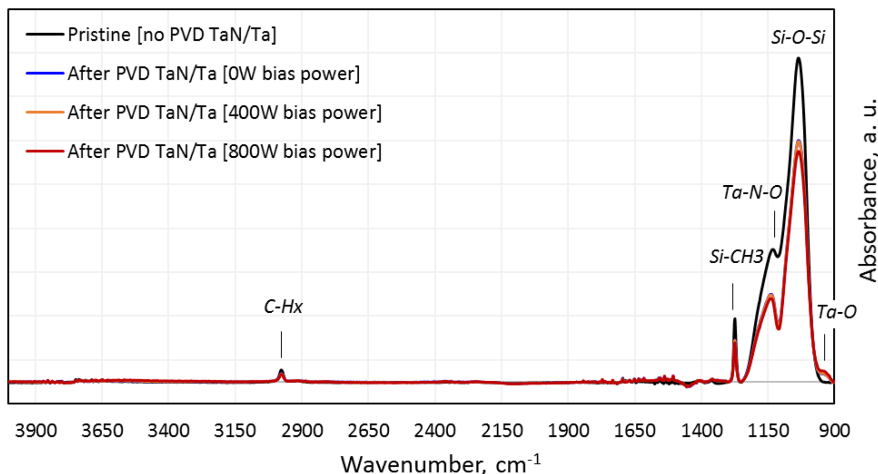

Figure S3.1. IR absorbance spectra normalized by the nominal thickness of pristine SOG-2.2 films. PVD TaN/Ta deposition was performed with variable bias power of the TaN sputtering step.

In this work, the analysis of IR spectra was based on a comparison of absorbance values normalized by the highest peak in the employed wavenumber range corresponding to Si-O-Si bond stretching (1035-1037 cm^{-1}). To justify the application of this normalization approach in the current study, it is necessary to show that the value of the Si-O-Si absorbance peak is not affected by the sputtering of TaN/Ta bi-layer on top of SOG-2.2 films.

The absorbance spectra normalized by the thickness of SOG-2.2 films measured before TaN/Ta deposition (Figure S3.1) allow to conclude that:

a. There is no direct overlapping of Si-O-Si absorbance peak (1035-1037 cm^{-1}) with those typically observed in TaO_x/TaN films[304,305]. The

corresponding Ta-N/Ta-O bond oscillations result in absorbance peaks located either below 900 cm^{-1} or above 1110 cm^{-1}.

b. There is no significant shift of Si-O-Si peak position (1035-1037 cm^{-1}) caused by the TaN/Ta sputtering process (its variation of 2 cm^{-1} is equal to the wavenumber scanning step), neither there is a positive correlation between the Si-O peak height and AC bias sputtering power. The above two observations imply that the organosilica matrix re-structuring is limited to the very top surface of the SOG-2.2 layer. In turn, the negative correlation between the Si-O peak intensity and AC bias power seen in Figure S3.1 may indicate the presence of an effectively larger thickness of the conductive layer.

As a result, the employed normalization by Si-O peak value may be used for a rough quantitative comparison of the compositional changes in SOG-2.2 coatings before and after the deposition of the TaN/Ta barrier.

2. Porosimetry measurement

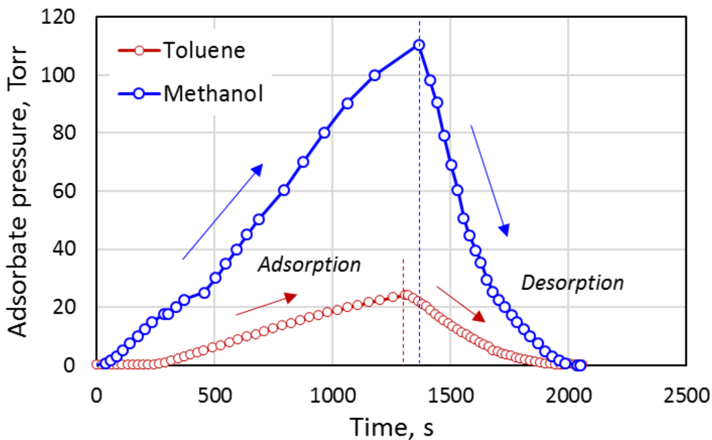

Figure S3.2. Rate of adsorbate (toluene or methanol) pressure change in the sample chamber during the adsorption/desorption cycle of porosimetry measurements.

Figure S3.2 demonstrates the typical rate of adsorbate pressure increase/decrease during the porosimetry measurement cycle. The use of the same adsorbate "pressure-time" pattern in all the performed porosimetry measurements allows qualitative comparison of pore sealing in different SOG-2.2/TaN/Ta stacks via monitoring of dynamic changes of their optical properties with in-situ ellipsometry.

3. Estimation of equivalent SiO_2-layer thickness in SOG-2.2/TaN/Ta stacks from measured impedance

Besides the reported effective k-values estimated from measured impedance (@100kHz) using parallel plate capacitor formula and a simple equivalent scheme consisting of serially connected resistor and capacitor (R_s)[88], we introduced another method of quantifying the induced low-k damage, which provides a thickness-independent estimate. The measured impedance data are interpreted using a two-layer model similar to what is done for the calculation of the equivalent damage layer (EDL) from the IR absorbance spectra[166]. For that, two layers with distinct dielectric constants are considered, corresponding to two capacitors connected in series (Figure S3.3). The top layer is defined as the damaged layer, with a dielectric constant set to 4.1 (SiO_2). The bottom layer is defined as the undamaged low-k dielectric, with a pristine dielectric constant of 2.26. With these assumptions, the capacitance-based equivalent damage depth is obtained by calculating the thickness of the SiO_2-like top layer.

By applying the above algorithm for the calculation of equivalent SiO_2 layer thickness in SOG-2.2 films subjected to TaN/Ta deposition, we obtained values exceeding 30 nm regardless of the applied AC bias power (Table S3.1).

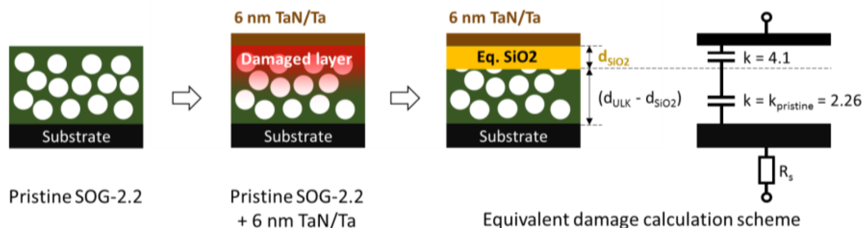

Figure S3.3. The two-layer approach for the interpretation of impedance measured on MIS stacks featuring surface-damaged low-k dielectric films.

Table S3.1. Estimation of low-k dielectric damage in SOG-2.2/TaN/Ta stacks from impedance measured on MIS capacitors by two methods based on different equivalent schemes.

TaN deposition conditions in TaN/Ta stack	SOG-2.2 thickness, nm	Effective k-value (@100kHz)	Eq. SiO_2 thickness within SOG-2.2, nm
0W AC bias	200.4	2.42	34.8
400W AC bias	200.8	2.50	48.9
800W AC bias	201.4	2.76	85.0

4. RBS analysis of SOG-2.2/TaN/Ta stacks

To extract the information about the depth of Ta penetration, the analysis on SOG-2.2/TaN/Ta stacks was performed based on simulations using in-house developed software ARRIBA with a multilayer model: one layer on the top and 4 additional layers representing various diffusion depths from the Ta/TaN bi-layer into the underlying SOG-2.2 porous film. Layer *n-1* is closest to the surface, while *n-4* is closest to the substrate. The fraction of Ta diffused

into the low-k layer, reported in the main manuscript, was calculated based on the fitting results presented in Table S3.2.

Table S3.2. Estimation of low-k dielectric damage in SOG-2.2/TaN/Ta stacks from impedance measured on MIS capacitors by two methods based on different equivalent schemes.

TaN deposition conditions in TaN/Ta stack	Ta thickness (10^{15} at/cm²)					
	Total	Surface	n-1	n-2	n-3	n-4
0W AC bias	27.0	27.0	0.0	0.0	0.0	0.0
400W AC bias	27.0	24.0	3.0	0.0	0.0	0.0
800W AC bias	32.0	24.0	8.0	0.0	0.0	0.0

5. AFM analysis of SOG-2.2/TaN/Ta stacks

The AFM measurements were performed with Bruker Dimension Edge microscope operating in tapping mode. The topographic images (512 x 512 pixels) were recorded on a scan area of 1x1 μm^2. The surface topography and corresponding value of root mean square roughness have been obtained on four stacks featuring template-free SOG-2.2 films before and after deposition of PVD TaN/Ta bi-layer with variable AC bias at TaN sputtering step (Figure S3.4).

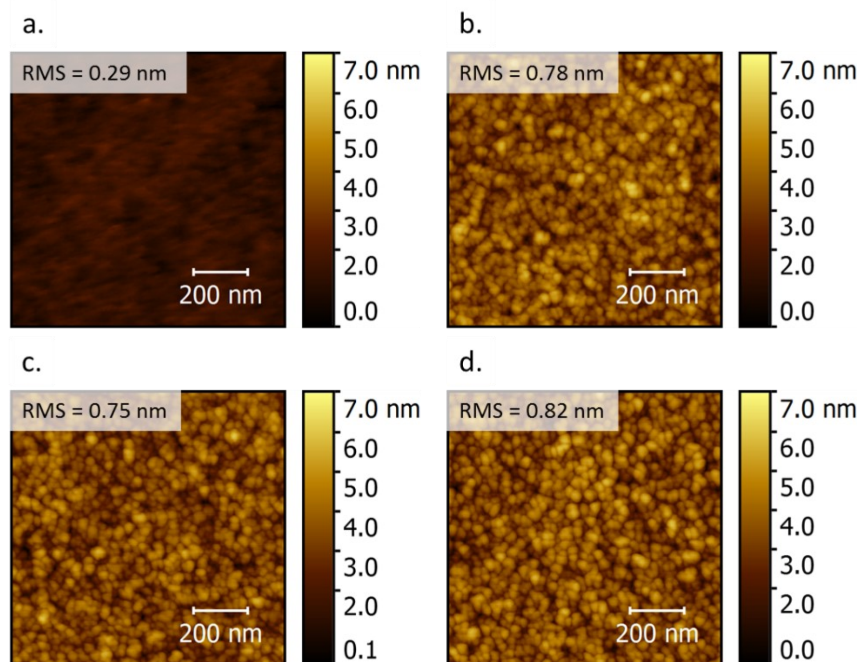

Figure S3.4. IR absorbance spectra normalized by the nominal thickness of pristine SOG-2.2 films. PVD TaN/Ta deposition was performed with variable bias power of the TaN sputtering step.

6. Nanoindentation analysis of template-free and template-containing SOG-2.2 films

The elastic modulus and hardness of the SOG-2.2 low-k films were measured by nanoindentation using a Hysitron TI950 Triboindenter equipped with a cube corner indentation probe. Substrate-independent Young's modulus was obtained by applying the analytical approach from Li-Vlassak, who adopted Yu's solution for the elastic contact problem for indentation on a layered half-space and extended it to the plastic regime[111]. In Table S3.3, Young's modulus and hardness are compared between the template-free SOG-2.2 film and the SOG-2.2 film characterized with ~60% porous volume occupied by template residues.

Table S3.3. Comparison of mechanical properties of template-containing and template-free SOG-2.2 coatings.

Hard-bake sequence	Pore filling fraction*, %	Young's modulus, GPa	Hardness, GPa
(120 min, 400°C, N_2) + UV	0.0	5.6 ± 0.4	0.65 ± 0.09
(300 min, 300°C, N_2)	44.8	5.4 ± 0.2	0.73 ± 0.06

**The parameter refers to the fraction of the porous volume occupied by residual organics and is estimated from the measured refractive index of the SOG-2.2 coating as explained in p. 7 of Appendix A.*

7. Evaluation of template residue content in SOG-2.2 with ellipsometry

The template residues in the pores of the low-k dielectric can be described in the framework of the theory commonly employed in ellipsometric porosimetry analysis[89]. The equations based on Lorentz-Lorenz effective medium approximation can be easily adapted for the case of the template residues. The fraction of template residues in the low-k film F can be expressed as

$$F = \frac{\frac{n_{meas}^2 - 1}{n_{meas}^2 + 2} - \frac{n_0^2 - 1}{n_0^2 + 2}}{\frac{n_{temp}^2 - 1}{n_{temp}^2 + 2}} \qquad \text{(S3.1)}$$

where n_{meas}, n_0, n_{temp} – refractive indices of template-containing low-k film of interest, of template-free low-k material, and of template residues, respectively. The unknown value of n_{temp} can be estimated from another expression linking the fraction of the template residues F to the value of open porosity P measured by regular toluene ellipsometric porosimetry:

$$F = P_0 - P \tag{S3.2}$$

where P_0 – open porosity measured on the template-free SOG-2.2 coating obtained by a combination of hard-bake process and UV-cure. The only unknown parameter in the above equation is n_{temp}. The values of F obtained from (2) have been fitted with (1) using the least square method, in which the measured refractive index n_{meas} was set as a variable and n_{temp} as a parameter. The wide range of experimental points (Figure S3.5) featuring SOG-2.2 films with a variable amount of template residues have been employed to get an accurate approximation of n_{temp}. The tested SOG-2.2 films have been prepared by subjecting the coatings to hard-bake at 400°C in N_2 for various durations (2-120 min). The calculated n_{temp} equal to 1.533 (@633 nm) has been used in this work to estimate the loss of the template residues caused by the damascene integration processes (Figure 7).

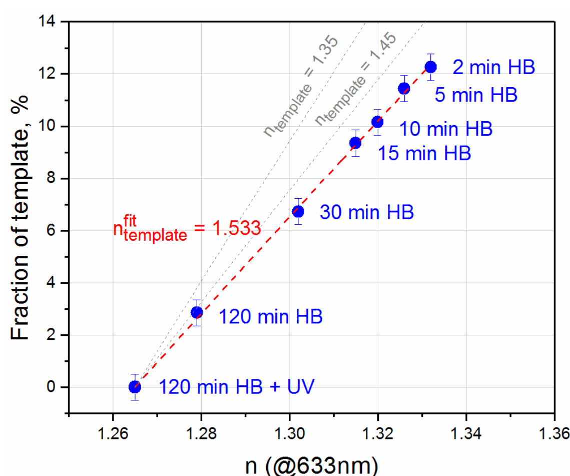

Figure S3.5. Fitting of the toluene porosimetry measurements results with the expression derived from Lorentz-Lorenz effective medium approximation (S3.1). The dashed curve (red) depicts the result of the least square fitting. The dotted curves (grey) are obtained from (S3.1) by assuming n_{temp} equal to 1.35 and 1.45.

Supporting information for Chapter 4.2

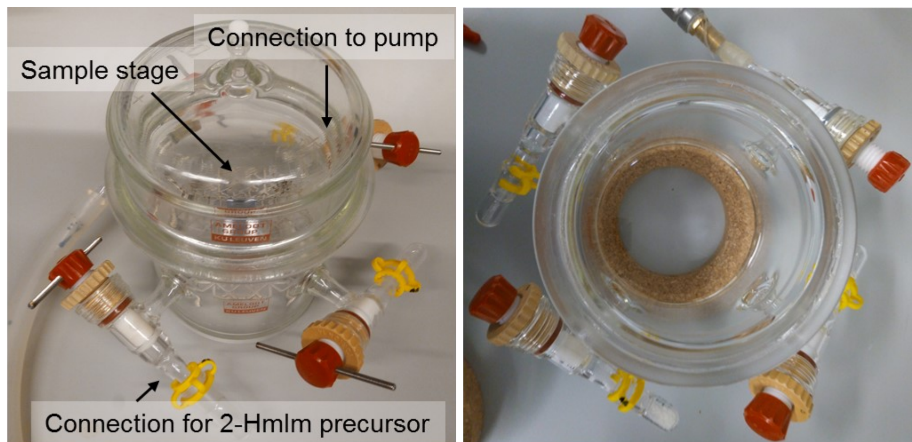

Figure S4.1. Validation of the MOF-CVD process and characterization of the deposited MOF thin films. (a) Schematic representation of the conversion of ALD ZnO and native CoOx to ZIF.

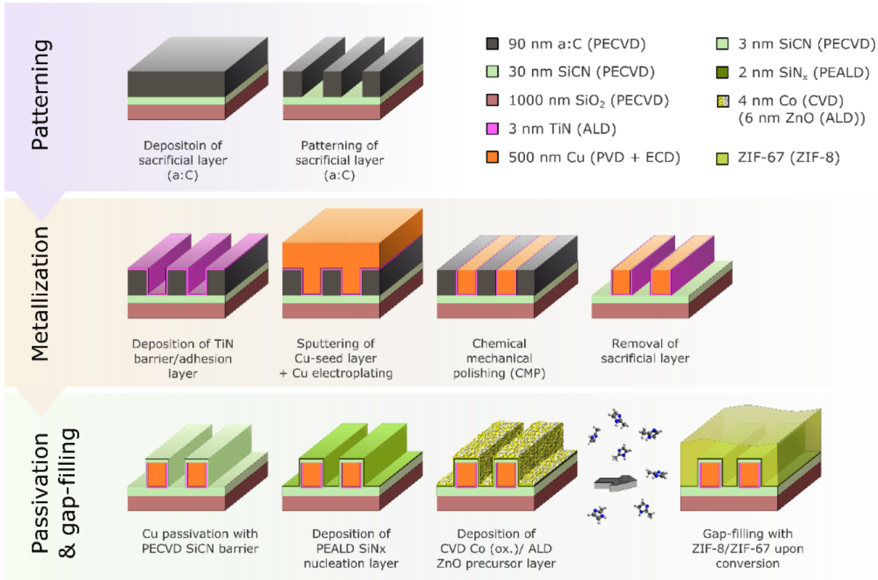

Figure S4.2. The schematic process flow depicts the preparation of 45nm half-pitch fork-fork capacitors and the subsequent MOF-CVD gap-filling step. The following deposition methods were employed: ALD = atomic layer deposition, PECVD = plasma-enhanced chemical vapor deposition, PVD = physical vapor deposition (magnetron sputtering), PEALD = plasma-enhanced atomic layer deposition, ECD = electrochemical deposition (electroplating).

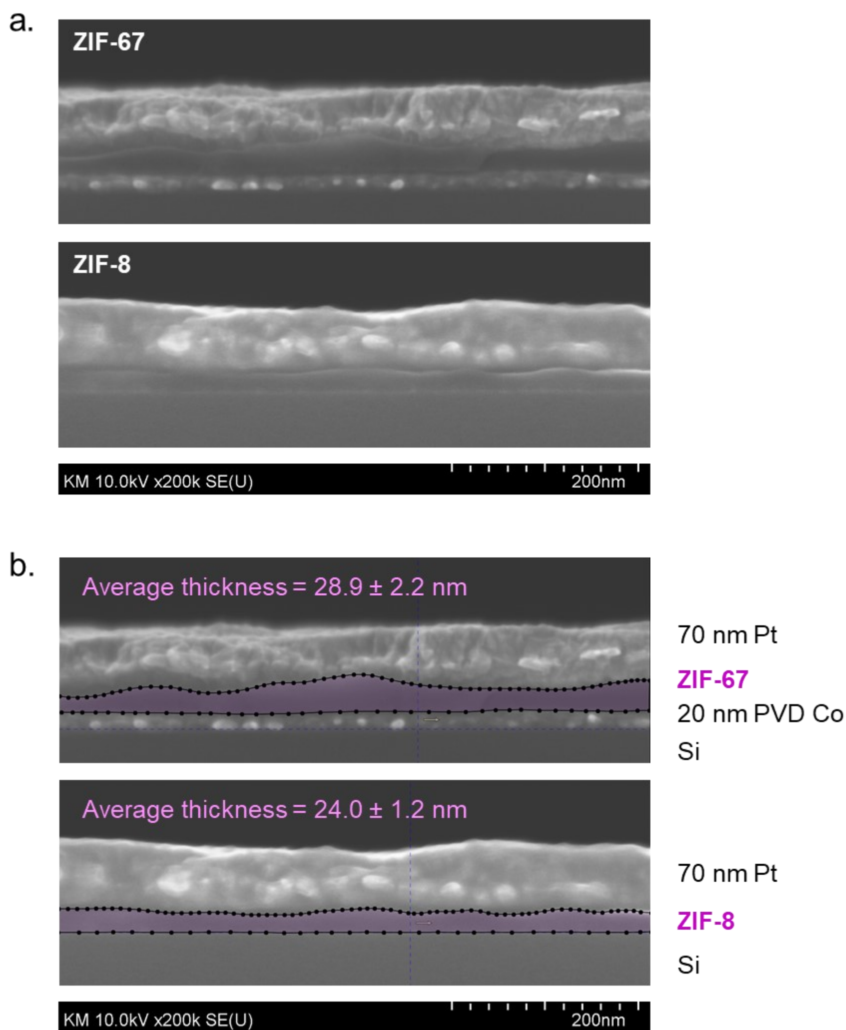

Figure S4.3. Cross-sectional SEM images of vapor-phase deposited ZIF-8 and ZIF-67 films covered with 70 nm e-beam evaporated Pt. The thicknesses of the MOF coatings extracted from these images were used for the calculation of k-values and for the estimation of unconverted metal oxide thicknesses. (a) Original cross-sectional SEM images; (b) SEM images containing a contour used for calculation of the MOF layer thickness.

Table S4.1. Comparison of relative atomic concentrations in vapor-phase deposited ZIF-8 and ZIF-67 films measured by XPS with those in ideal ZIF-8/ZIF-67 material determined from the unit cell composition.

Material	C 1s	N 1s	O 1s	Co 2p	Zn 2p
ZIF-67 (film)[a)]	61.9%	27.4%	3.9%	6.8%	-
ZIF-67 (ideal)	61.5%	30.7%	-	7.7%	-
ZIF-8 (film)[a)]	62.3%	27.2%	2.4%	-	8.2%
ZIF-8 (ideal)	61.5%	30.7%	-	-	7.7%

[a)] The XPS atomic concentrations are presented in angle-integrated mode (all angles summed).

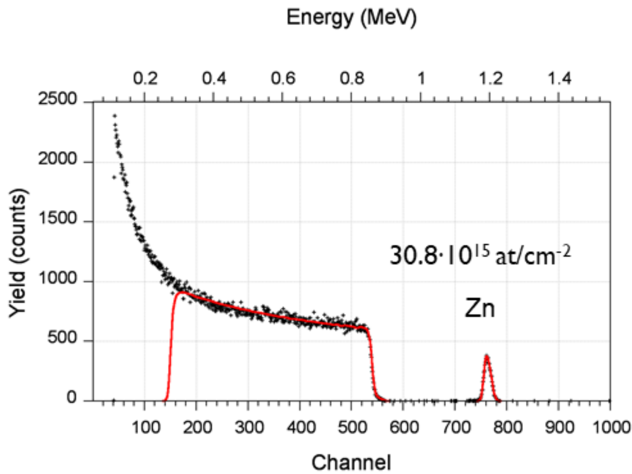

Figure S4.4. RBS spectrum (black) and fitting curve (red) recorded on 8.9 nm thick ALD ZnO film deposited on top of a Si/SiO_2 substrate.

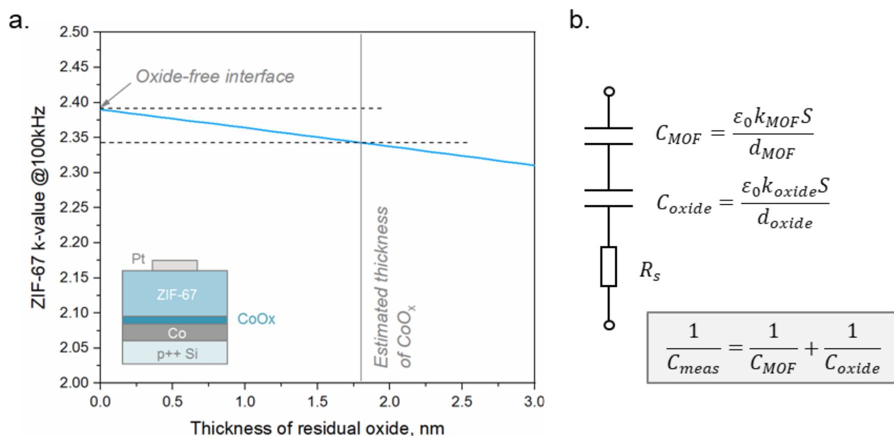

Figure S4.5. Impact of a residual CoO_x layer. (a) Dependence of the extracted ZIF-67 k-value on the thickness of the interfacial CoO_x layer; (b) equivalent circuit scheme for impedance measurements on the MIM stack. During the calculation, the k-value of the CoOx residue layer was assumed to be equal to that of CoO[303].

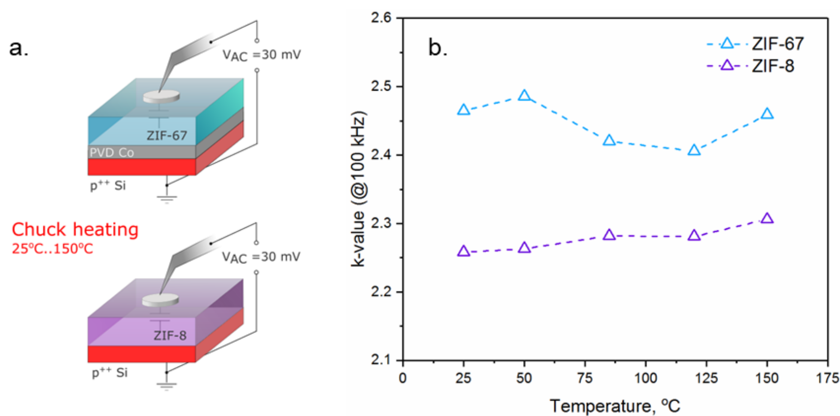

Figure S4.6. Temperature dependence of ZIF-8 and ZIF-67 k-value measured on parallel-plate metal-insulator-metal capacitors with 0.03 mm^2 Pt top electrodes. (a) Schematic representation of the experiment; (b) k-values of ZIF films extracted from capacitance recorded on the chuck-heated devices in air.

a. Before conversion reaction

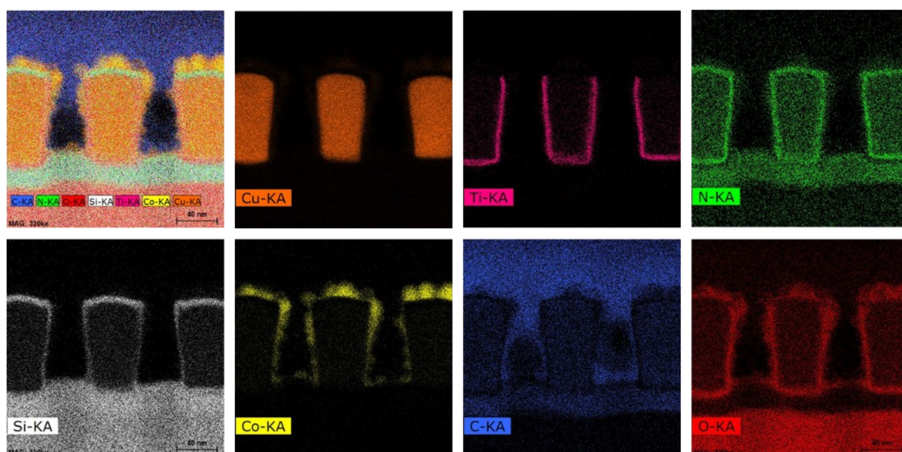

b. After conversion reaction

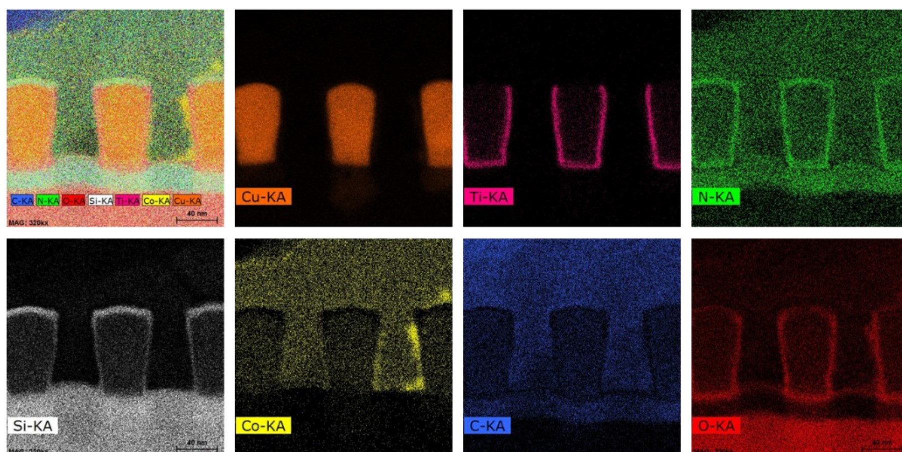

Figure S4.7. EDS-TEM element maps recorded on the cross-section of a 45 nm half-pitch fork-fork capacitor composed of passivated copper lines covered with oxidized CVD Co layer. (a) Before and (b) after the MOF-CVD conversion process.

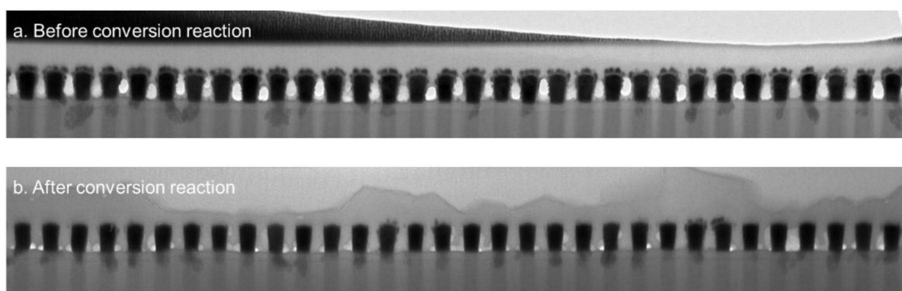

Figure S4.8. TEM review images demonstrating the gap-filling performance of the ZIF-67 phase on a 45 nm half-pitch fork-fork capacitor. (a) Before and (b) after the conversion of oxidized CVD Co into ZIF-67 in vapors of 2-methylimidazole.

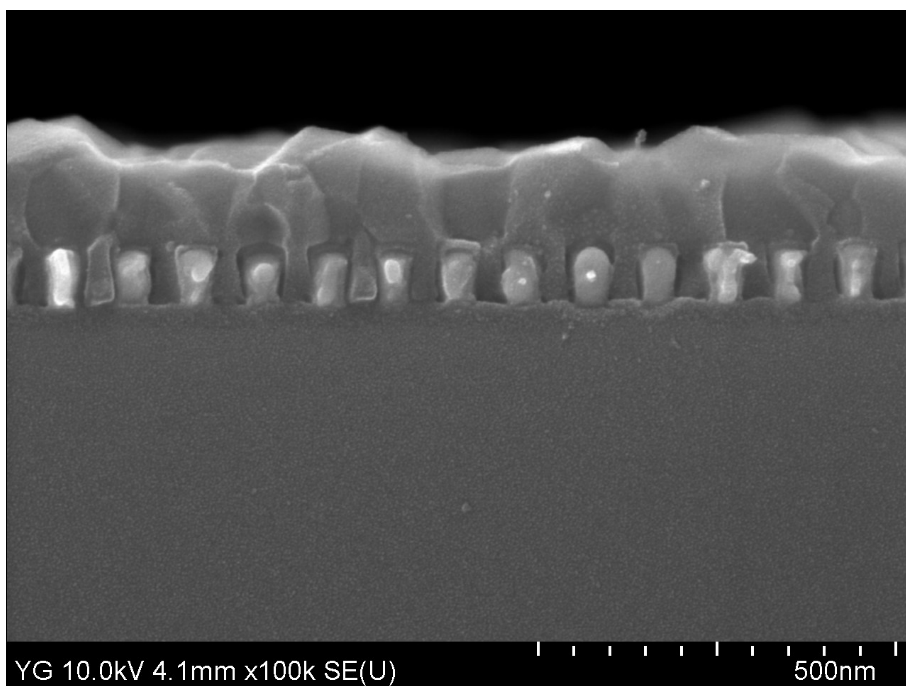

Figure S4.9. Cross-sectional SEM image of a manually cleaved substrate with 45 nm half-pitch fork-fork capacitors.

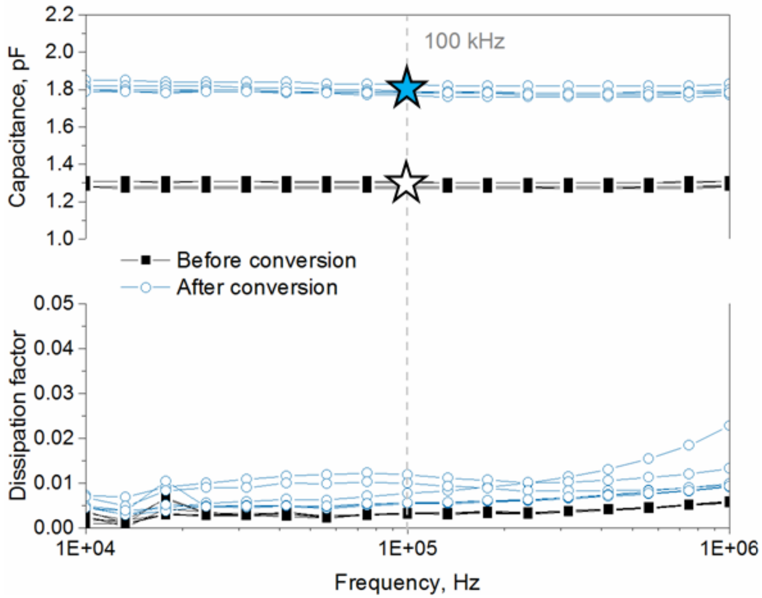

Figure S4.10. Capacitance and dissipation factor measured on six 45nm half-pitch fork-fork capacitors in the frequency range 10 kHz-1MHz before and after the MOF-CVD process. The average capacitance at 100 kHz measured on the samples after the MOF-CVD reaction was used for extraction of the effective k-value of the gap-filling phase.

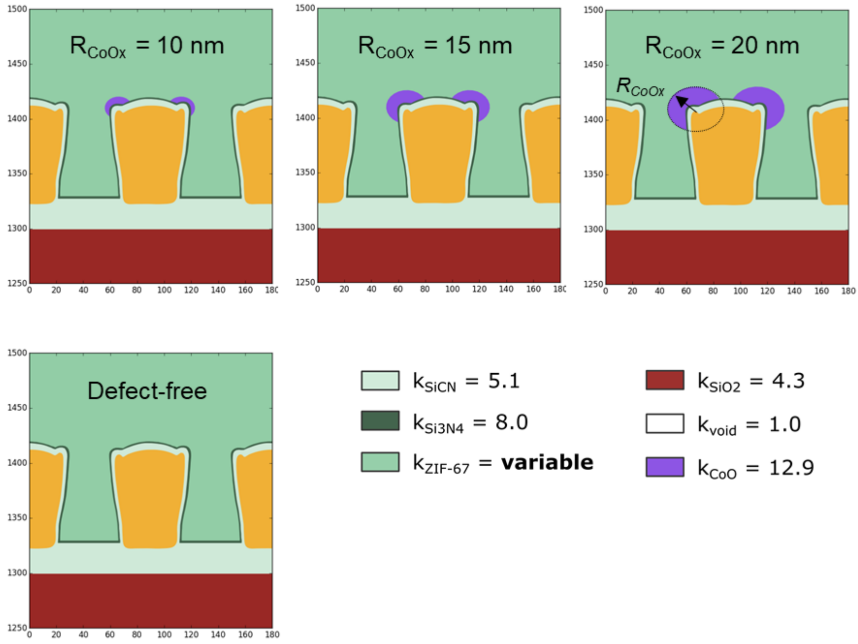

Figure S4.11. Modeled cross-sections of 45 nm half-pitch fork-fork capacitors featuring CoO_x residues of different sizes (defect radius R_{CoOx}).

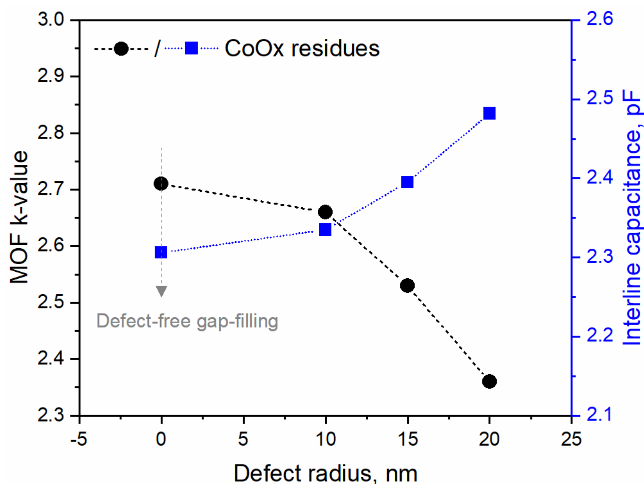

Figure S4.12. The effect of CoO_x residues of different sizes on the k-value of MOF-CVD ZIF-67 and on the total interline capacitance of a fork-fork device estimated by 2D capacitance simulations.

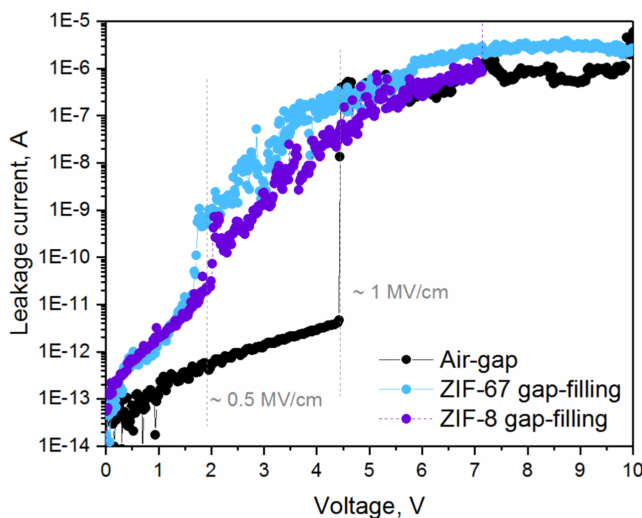

Figure S4.13. Leakage current measured on 45 nm fork-fork capacitors with different gap-filling media. The ZIF-67 and ZIF-8 phases were formed via vapor phase conversion of oxidized CVD Co and ALD ZnO films, respectively.

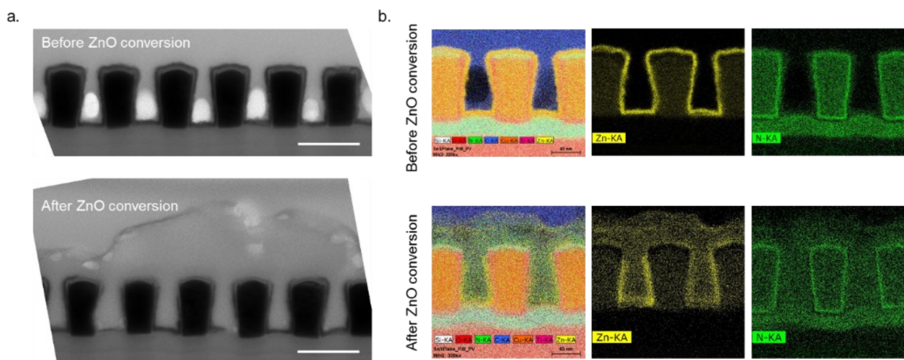

Figure S4.14. TEM analysis of lamellas cut out from the capacitor device covered with 6 nm ALD ZnO before and after the MOF-CVD process. (a) Bright-field TEM images; (b) EDS elemental maps. ALD ZnO is conformally covering the passivated copper lines. The 45 nm wide trenches appear gap-filled with ZIF-8 phase. There is also evidence of a thin unconverted ZnO underlayer largely present inside the trenches.

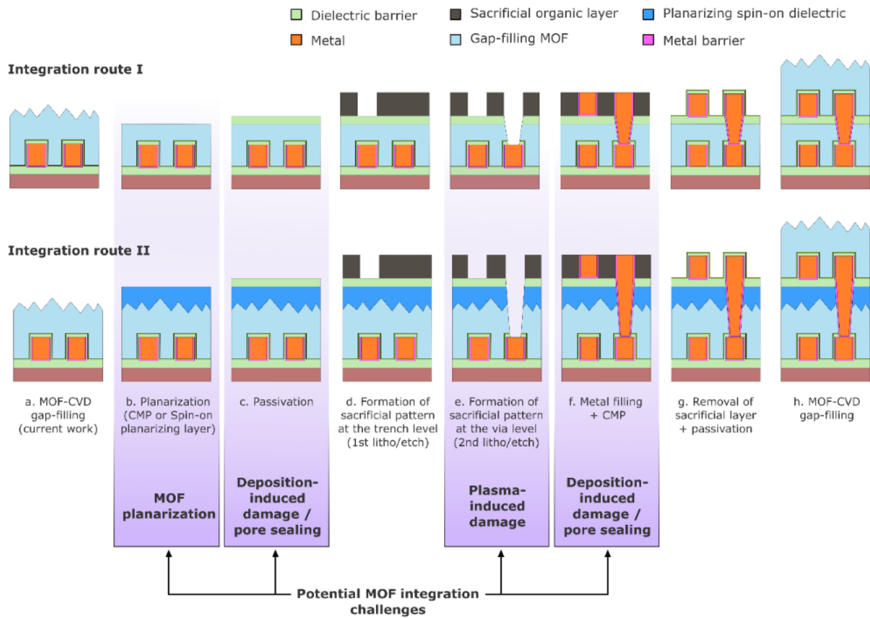

Figure S4.15. Two metallization routes for the integration of gap-filling MOF-CVD dielectrics. The integration routes differ in the selected planarization approach (step *b*). In integration route I, chemical-mechanical polishing (CMP) is used to remove the film roughness. Integration route II uses a spin-on dielectric as a planarization coating. This extra dielectric could be a low-k variation of spin-on glass (SOG) material, which is routinely used in photolithography for local planarization before the resist deposition. Besides planarization (step *b*), there are potential compatibility concerns in steps *c* and *f* related to deposition-induced damage and infiltration of subsequent layers (or building blocks thereof) into the porous MOF layer. Another question that needs to be addressed is the extent of plasma-induced damage during dry etching of the MOF layer at step *e*.

Appendix B

Safety, Health and Environment (SHE)

Most of the experiments in the present work were performed in imec cleanrooms and laboratories. All personnel should comply with the safety & environment policy defined by the EHS department. The purposes of the care system include preventing all accidents and losses, preventing incidental/gradual environmental damage, and preventing harm to the physical or psychosocial health of employees. Basic EHS training covers evacuation instructions, the use of personal protective equipment, and all other procedures that are needed to work safely. Trainings are mandatory for specific cleanrooms, labs, or technical buildings, including cleanroom behavior, safe use of chemicals, and handling emergency situations.

Since the work also involved handling various chemicals, special attention was paid to associated safety procedures. Prior to any chemical experiment, the material safety data sheet was consulted and potential EHS issues were discussed with the chemical department. Storage, distribution, and use of chemicals were under strict control. We took also additional safety precautions for highly dangerous processes. An example refers to hydrogen fluoride (HF) acid that used for the etching and cleaning of low-k dielectrics. It is a highly corrosive liquid and a powerful contact poison. Experiments with HF solutions were performed in a wet bench equipped with a special drain to avoid contamination issues. Personal protective equipment was worn including goggles, a face shield, thick gloves, and acid resistant apron.

For silicon wafer preparation, such as wafer cleavage and back-side scratching, particles hazard could be a major health issue. In this case, googles and mouth mask were employed.

Scientific activity

Peer-reviewed journals

1. **M. Krishtab**, I. Stassen, T. Stassin, A. J. Cruz, O. O. Okudur, S. Armini, C. Wilson, S. De Gendt, R. Ameloot. Vapor-Deposited Zeolitic Imidazolate Frameworks as Gap-Filling Ultra-Low-k Dielectrics. Nat. Commun. 10 (1), 3729 (2019).

2. **M. Krishtab**, J.-F. de Marneffe, S. Armini, J. Meersschaut, H. Bender, C. Wilson, S. De Gendt, Metal Barrier Induced Damage in Self-Assembly Based Organosilica Low-k Dielectrics and Its Reduction by Organic Template Residues. Appl. Surf. Sci., 485, 170–178 (2019).

3. K. Vanstreels, **M. Krishtab**, L. Garcia Gonzalez, S. Armini, Impact of organic linking and terminal groups on the mechanical properties of self-assembly based low-k dielectrics, Appl. Phys. Lett. 111 (2017). *– M. Krishtab and K. Vanstreels equally contributed to the published work.*

4. **M. Krishtab**, V. Afanas'ev, A. Stesmans, S. De Gendt, Leakage current induced by surfactant residues in self-assembly based ultralow-k dielectric materials, Appl. Phys. Lett. 111 (2017).

5. **M. Krishtab**, J.-F. de Marneffe, S. De Gendt & M. R. Baklanov. Plasma induced damage mitigation in spin-on self-assembly based ultra low-k dielectrics using template residues. Appl. Phys. Lett. **110**, 013105 (2017).

6. **M. Krishtab**, K. Vanstreels, T. Savage, M. Koichi, S. De Gendt, and M. Baklanov. Improvement of cohesion strength in ULK OSG materials by pore structure adjustment. Microelectron. Eng. 137, 75–78 (2015).

7. A. J. Cruz, I. Stassen, **M. Krishtab**, K. Marcoen, T. Stassin, S. Rodríguez-Hermida, J. Teyssandier, S. Pletincx, R. Verbeke, V. Rubio-Giménez et al. Integrated Cleanroom Process for the Vapor-Phase Deposition of Large-Area Zeolitic Imidazolate Framework Thin Films. Chem. Mater. 31 (22), 9462–9471 (2019).

8. I. Zyulkov, **M. Krishtab**, S. De Gendt, S. Armini, Selective Ru ALD as a Catalyst for Sub-Seven-Nanometer Bottom-Up Metal Interconnects, ACS Appl. Mater. Interfaces. 9 (2017).

9. M. Redzheb, S. Armini, T. Berger, M. Jacobs, **M. Krishtab**, K. Vanstreels, S. Bernstorff, P. Van Der Voort, J. Mater. Chem. C. 5 (2017).

10. A. Rezvanov, L. Zhang, M. Watanabe, **M.B. Krishtab**, L. Zhang, N. Hacker, P. Verdonck, S. Armini, J.-F.G.N.G. de Marneffe, J. Vac. Sci. Technol. B, Nanotechnol. Microelectron. Mater. Process. Meas. Phenom. 35 (2017).

11. M. Redzheb, L. Prager, S. Naumov, **M. Krishtab**, S. Armini, P. Van Der Voort, and M.R. Baklanov, Appl. Phys. Lett. 108, (2016). (doi: 10.1063/1.4939449)

12. A.P. Palov, E.N. Voronina, T. V. Rakhimova, D. V. Lopaev, S.M. Zyryanov, Y.A. Mankelevich, **M.B. Krishtab**, and M.R. Baklanov, J. Vac. Sci. Technol. B, Nanotechnol. Microelectron. Mater. Process. Meas. Phenom. 34, 041205 (2016).

13. Y. Sun, **M. Krishtab**, Y. Mankelevich, L. Zhang, S. De Feyter, M. Baklanov, and S. Armini, Appl. Phys. Lett. 108, 262902 (2016).

14. J.-F. De Marneffe, L. Zhang, M. Heyne, M. Lukaszewicz, S.B. Porter, F. Vajda, V. Rutigliani, Z. El Otell, **M. Krishtab**, A. Goodyear, M. Cooke, P. Verdonck, and M.R. Baklanov, J. Appl. Phys. 118, (2015).

15. A. Palov, T. V. Rakhimova, **M.B. Krishtab**, and M.R. Baklanov, J. Vac. Sci. Technol. B (2015).

16. M. Redzheb, L. Prager, **M. Krishtab**, S. Armini, K. Vanstreels, A. Franquet, P. Van Der Voort, and M.R. Baklanov, Microelectron. Eng. (2015).

17. S. Armini, J. Loyo Prado, **M. Krishtab**, T. Conard, J. Meersschaut, Q.T. Le, P. Verdonck, and M.R. Baklanov, ECS J. Solid State Sci. Technol. 3, N3106 (2014). (doi: 10.1149/2.017401jss)

18. S. Armini, J.L. Prado, **M. Krishtab**, J. Swerts, P. Verdonck, J. Meersschaut, T. Conard, M. Blauw, H. Struyf, and M.R. Baklanov, Microelectron. Eng. 120, 240 (2014).

19. I.E. Kononova, V.A. Moshnikov, **M.B. Krishtab**, and I.A. Pronin, Glas. Phys. Chem. 40, 190 (2014).

20. T.T. Olawumi, E. Levrau, **M. Krishtab**, C. Detavernier, J.W. Bartha, K. Xu, F. Lazzarino, and M.R. Baklanov, ECS J. Solid State Sci. Technol. 4, N3048 (2014).

21. T. V Rakhimova, A.T. Rakhimov, Y.A. Mankelevich, D. V Lopaev, A.S. Kovalev, A.N. Vasil’eva, S.M. Zyryanov, K. Kurchikov, O. V

Proshina, D.G. Voloshin, N.N. Novikova, **M.B. Krishtab**, and M.R. Baklanov, J. Phys. D. Appl. Phys. 47, 025102 (2014).

22. Y. Sun, **M. Krishtab**, H. Struyf, P. Verdonck, S. De Feyter, M.R. Baklanov, and S. Armini, Langmuir 30, 3832 (2014).

23. P. Verdonck, C. Wang, Q.T. Le, L. Souriau, K. Vanstreels, **M. Krishtab**, and M. Baklanov, Microelectron. Eng. 120, 225 (2014). (doi: 10.1016/j.mee.2013.10.028)

Conference proceeding

1. **M. Krishtab**, K. Vanstreels, S. De Gendt, and M. Baklanov, in 2015 IEEE Int. Interconnect Technol. Conf. 2015 IEEE Mater. Adv. Met. Conf. (IEEE, 2015), pp. 103–106.

2. Z. Tokei, I. Ciofi, P. Roussel, P. Debacker, P. Raghavan, M.H. van der Veen, N. Jourdan, C.J. Wilson, V.V. Gonzalez, C. Adelmann, L. Wen, K. Croes, O.V.P.K. Moors, **M. Krishtab**, S. Armini, J. Bommels, in: 2016 IEEE Symp. VLSI Technol., IEEE, 2016: pp. 1–2.

3. M. Redzheb, L. Prager, **M. Krishtab**, S. Armini, K. Vanstreels, A. Franquet, P. Van Der Voort, and M.R. Baklanov, in 2015 IEEE Int. Interconnect Technol. Conf. 2015 IEEE Mater. Adv. Met. Conf. (IEEE, 2015), pp. 99–102.

4. P. Verdonck, Q.T. Le, **M. Krishtab**, K. Vanstreels, S. Armini, A. Simone, M.P. Nguyen, M.R. Baklanov, and S. Van Elshocht, in IEEE Int. Interconnect Technol. Conf. (IEEE, 2014), pp. 155–158.

5. A. Zotovich, **M. Krishtab**, F. Lazzarino, and M.R. Baklanov, in Proc. SPIE - Int. Soc. Opt. Eng. (2014).

Patents

1. Resistless patterning mask, **M. Krishtab**, S. Armini, EP 19167248.4 (internal imec reference - PA 2019/016 EP1)

2. Selective deposition of metal-organic frameworks for self-aligned via formation in BEOL interconnects, **M. Krishtab**, Ivo Stassen, Silvia Armini, Rob Ameloot, US Patent App. 16/190,921

3. Method for etching porous organosilica low-k materials, F. Lazzarino, S. Tahara, **M. Krishtab**, M. Baklanov, US Patent App. 14/225,107

4. Method for Pore Sealing of Porous Materials Using Polyimide Langmuir-Blodgett Film, V. Luchinin, S. Goloudina, V. Pasyuta, A. Ivanov, M. Baklanov, **M. Krishtab**, US Patent App. 15/285,445

Conferences

1. **M. Krishtab**, J-F. de Marneffe, S. Armini, C. Wilson, S. De Gendt; "Metal-barrier induced damage in self-assembly based organosilica

low-k dielectrics and its reduction by surfactant residues", MAM2018 (Milan, Italy, 21.03.2018), Oral

2. **M. Krishtab**, I. Stassen, R. Ameloot, G. Pourtois, S. Armini, S. De Gendt; "Metal-organic Frameworks as Gap Filling Low-k Dielectric Material in Advanced Interconnects", MRS2017 Spring Meeting (Phoenix, USA, 18.04.2017), Oral

3. **M. Krishtab**, J.-F. de Marneffe, S. De Gendt; "Plasma induced damage mitigation in spin-on self-assembly based ultra low-k dielectrics using template residues", PESM2016 (Grenoble, France, 09.05.2016), Oral

4. **M. Krishtab**, T. Witters, S. De Gendt, M. Baklanov; "Impact of PVD barrier deposition sequence on ultra low-k dielectrics", MAM2016 (Brussels, Belgium, 09.05.2016), Poster

5. **M. Krishtab**, V. Afanas'ev, A. Stesmans, S. De Gendt, M. Baklanov; "Impact of Template Residues on Electrical Properties of Spin-on Ultra Low-k Dielectrics", SISC2015 (Arlington, US, 02.12.2015), Poster

6. **M. Krishtab**, K. Vanstreels, S. De Gendt, M. Baklanov; "Post-etch template removal strategy for reduction of plasma induced damage in spin-on OSG low-k dielectrics", IITC/MAM2015 (Grenoble, France, 18.05.2015), Poster

7. **M. Krishtab**, G. Pourtois, K. Vanstreels, M. Tsotsolas, H. Gliemann, C. Woll, S. De Gendt, M. Baklanov; "Low-k Dielectric Properties of HKUST-1 SURMOF Films", MRS2014 (San Francisco, US, 21.04.2014), Poster

8. **M. Krishtab**, K. Vanstreels, T. Savage, K. Matsunaga, S. De Gendt, M. R. Baklanov; “Improvement of cohesion strength in ULK OSG materials by pore structure adjustment”, MAM2014 (Chemnitz, Germany, 02.03.2014), Poster

Bibliography

1. Kilby, J. S. Invention of the integrated circuit. *IEEE Trans. Electron Devices* **23**, 648–654 (1976).
2. Warner, R. M. Microelectronics: its unusual origin and personality. *IEEE Trans. Electron Devices* **48**, 2457–2467 (2001).
3. Flamm, K. Has Moore's Law Been Repealed? An Economist's Perspective. *Comput. Sci. Eng.* **19**, 29–40 (2017).
4. Rupp, K. & Selberherr, S. The Economic Limit to Moore's Law. *IEEE Trans. Semicond. Manuf.* **24**, 1–4 (2011).
5. Maxfield, C. What's the total length of the tracks on a silicon chip? *EE Times* (2007). Available at: https://www.eetimes.com/whats-the-total-length-of-the-tracks-on-a-silicon-chip/.
6. Bohr, M. T. Interconnect scaling-the real limiter to high performance ULSI. in *Proceedings of International Electron Devices Meeting* 241–244 (IEEE). doi:10.1109/IEDM.1995.499187
7. Pamunuwa, D. & Tenhunen, H. Repeater insertion to minimise delay in coupled interconnects. in *VLSI Design 2001. Fourteenth International Conference on VLSI Design* 513–517 (IEEE Comput. Soc). doi:10.1109/ICVD.2001.902709
8. Andricacos, P. C. Copper On-Chip Interconnections: A Breakthrough in Electrodeposition to Make Better Chips. *Electrochem. Soc. Interface* **8**, 32–37 (1999).
9. Adelmann, C. *et al.* Alternative metals for advanced interconnects. in *IEEE International Interconnect Technology Conference* 173–176 (IEEE, 2014). doi:10.1109/IITC.2014.6831863
10. Liang Gong Wen *et al.* Ruthenium metallization for advanced interconnects. in *2016 IEEE International Interconnect Technology Conference / Advanced Metallization Conference (IITC/AMC)* 34–36

(IEEE, 2016). doi:10.1109/IITC-AMC.2016.7507651

11. Founta, V. *et al.* Properties of ultrathin molybdenum films for interconnect applications. *Materialia* **24**, 101511 (2022).
12. Maex, K. *et al.* Low dielectric constant materials for microelectronics. *J. Appl. Phys.* **93**, 8793–8841 (2003).
13. Volksen, W., Miller, R. D. & Dubois, G. Low Dielectric Constant Materials. *Chem. Rev.* **110**, 56–110 (2010).
14. Shamiryan, D., Abell, T., Iacopi, F. & Maex, K. Low- k dielectric materials. *Mater. Today* 34–39 (2004).
15. Gal, L. On-chip cross talk-the new signal integrity challenge. in *Proceedings of the IEEE 1995 Custom Integrated Circuits Conference* 251–254 (IEEE). doi:10.1109/CICC.1995.518179
16. Elgamel, M. A. & Bayoumi, M. A. Interconnect noise analysis and optimization in deep submicron technology. *IEEE Circuits Syst. Mag.* **3**, 6–17 (2003).
17. Darwish, T. & Bayoumi, M. Trends in Low-Power VLSI Design. in *The Electrical Engineering Handbook* 263–280 (Elsevier, 2005). doi:10.1016/B978-012170960-0/50022-0
18. Kaufman, F. B. *et al.* Chemical-Mechanical Polishing for Fabricating Patterned W Metal Features as Chip Interconnects. *J. Electrochem. Soc.* **138**, 3460–3465 (1991).
19. Woo, M., Fiordalice, B., Lin, J. & Kolar, D. Tungsten Cap Metallization for 0.5 μm Via Fill Technology. *J. Electrochem. Soc.* **142**, 3893–3896 (1995).
20. Graas, C. D., Le, H. A., McPherson, J. W. & Havemann, R. H. Electromigration reliability improvement of W-plug vias by titanium layering. in *Proceedings of 1994 IEEE International Reliability Physics Symposium RELPHY-94* 173–177 (IEEE, 1994). doi:10.1109/RELPHY.1994.307840
21. Deutsch, A. *et al.* Functional high-speed characterization and

modeling of a six-layer copper wiring structure and performance comparison with aluminum on-chip interconnections. in *International Electron Devices Meeting 1998. Technical Digest (Cat. No.98CH36217)* 295–298 (IEEE). doi:10.1109/IEDM.1998.746358

22. Brotherton, S. D., Ayres, J. R., Gill, A., van Kesteren, H. W. & Greidanus, F. J. A. M. Deep levels of copper in silicon. *J. Appl. Phys.* **62**, 1826–1832 (1987).
23. Havemann, R. H. & Hutchby, J. A. High-performance interconnects: an integration overview. *Proc. IEEE* **89**, 586–601 (2001).
24. Murdoch, G. *et al.* Semidamascene Interconnects for 2nm node and Beyond. in *2020 IEEE International Interconnect Technology Conference (IITC)* 4–6 (IEEE, 2020). doi:10.1109/IITC47697.2020.9515597
25. Murdoch, G. *et al.* Feasibility study of fully self aligned vias for 5nm node BEOL. in *2017 IEEE International Interconnect Technology Conference (IITC)* 1–4 (IEEE, 2017). doi:10.1109/IITC-AMC.2017.7968958
26. Feynman, R. P., Leighton, R. B. & Sands, M. The Feynman Lectures on Physics. in (Adison Wesley, 1966).
27. Atkins, P. & de Paula, J. Atkins' Physical Chemistry. in 622–629 (Oxford University Press, 2010).
28. Maex, K. *et al.* Low dielectric constant materials for microelectronics. *J. Appl. Phys.* **93**, 8793 (2003).
29. Endo, K., Kishimoto, K., Matsubara, Y. & Koyanagi, K. Plasma-Enhanced Chemical Vapor Deposition of FSG and a-C:F Low-k Materials. in 121–166 (2003). doi:10.1007/978-3-642-55908-2_5
30. Lucovsky, G. & Yang, H. Fluorine atom induced decreases to the contribution of infrared vibrations to the static dielectric constant of Si–O–F alloy films. *J. Vac. Sci. Technol. A* **15**, 836–843 (1997).
31. Kudo, H., Shinohara, R., Takeishi, S., Awaji, N. & Yamada, M.

Densified SiOF Film Formation for Preventing Water Absorption. *Jpn. J. Appl. Phys.* **35**, 1583–1587 (1996).

32. Passemard, G., Fugier, P., Noel, P., Pires, F. & Demolliens, O. Study of fluorine stability in fluoro-silicate glass and effects on dielectric properties. *Microelectron. Eng.* **33**, 335–342 (1997).
33. Kim, S. E. & Steinbrüchel, C. The interaction of metals and barrier layers with fluorinated silicon oxides. *Solid. State. Electron.* **43**, 1019–1023 (1999).
34. Kalla, R. & Sinharoy, B. POWER7: IBM's next generation server processor. in *2009 IEEE Hot Chips 21 Symposium (HCS)* 1–12 (IEEE, 2009). doi:10.1109/HOTCHIPS.2009.7478381
35. Grill, A. PECVD low and ultralow dielectric constant materials: From invention and research to products. *J. Vac. Sci. Technol. B, Nanotechnol. Microelectron. Mater. Process. Meas. Phenom.* **34**, 020801 (2016).
36. Grill, A. Low and Ultralow Dielectric Constant Films Prepared by Plasma-enhanced Chemical Vapor Deposition. in *Dielectric Films for Advanced Microelectronics* 1–32 (John Wiley & Sons, Ltd). doi:10.1002/9780470017944.ch1
37. Tada, M. *et al.* Chemical Structure Effects of Ring-Type Siloxane Precursors on Properties of Plasma-Polymerized Porous SiOCH Films. *J. Electrochem. Soc.* **154**, D354 (2007).
38. Chaudhari, M. & Du, J. Reaction mechanisms of oxygen plasma interaction with organosilicate low-k materials containing organic crosslinking groups. *J. Vac. Sci. Technol. A Vacuum, Surfaces, Film.* **30**, 061302 (2012).
39. Dubois, G. *et al.* Molecular Network Reinforcement of Sol–Gel Glasses. *Adv. Mater.* **19**, 3989–3994 (2007).
40. Chapelon, L. L. *et al.* Characterization and integration of a CVD porous SiOCH (k<2.5) with enhanced mechanical properties for 65 nm

CMOS interconnects and below. *Microelectron. Eng.* **76**, 1–7 (2004).

41. Shamiryan, D. G., Baklanov, M. R., Vanhaelemeersch, S. & Maex, K. Controllable change of porosity of 3-methylsilane low-k dielectric film. *Electrochem. Solid-State Lett.* **4**, F3–F5 (2001).
42. Verdonck, P. *et al.* Influence of the UV Cure on Advanced Plasma Enhanced Chemical Vapour Deposition Low- k Materials. *Jpn. J. Appl. Phys.* **50**, 05EB05 (2011).
43. Urbanowicz, a. M. *et al.* Improving mechanical robustness of ultralow-k SiOCH plasma enhanced chemical vapor deposition glasses by controlled porogen decomposition prior to UV-hardening. *J. Appl. Phys.* **107**, 104122 (2010).
44. Zhang, L. *et al.* Cu passivation for integration of gap-filling ultralow-k dielectrics. *Appl. Phys. Lett.* **109**, 232901 (2016).
45. Brinker, C. J. & Scherer, G. W. *Sol-Gel Science*. (Elsevier, 1990). doi:10.1016/C2009-0-22386-5
46. Baney, R. H., Itoh, M., Sakakibara, A. & Suzuki, T. Silsesquioxanes. *Chem. Rev.* **95**, 1409–1430 (1995).
47. Kim, H.-J. *et al.* Substituent Effects on Microstructure and Polymerization of Polyalkylsilsesquioxanes. *J. Am. Chem. Soc.* **123**, 12121–12122 (2001).
48. Ro, H. W. *et al.* High-Modulus Spin-On Organosilicate Glasses for Nanoporous Applications. *Adv. Mater.* **19**, 705–710 (2007).
49. Dubois, G. *et al.* Superior mechanical properties of dense and porous organic/inorganic hybrid thin films. *J. Sol-Gel Sci. Technol.* **48**, 187–193 (2008).
50. Hrubesh, L. W., Keene, L. E. & Latorre, V. R. Dielectric properties of aerogels. *J. Mater. Res.* **8**, 1736–1741 (1993).
51. Nitta, S. V. *et al.* Surface modified spin-on xerogel films as interlayer dielectrics. *J. Vac. Sci. Technol. B Microelectron. Nanom. Struct.* **17**, 205 (1999).

52. Hatton, B. D., Landskron, K., Whitnall, W., Perovic, D. D. & Ozin, G. A. Spin-coated periodic mesoporous organosilica thin films - Towards a new generation of low-dielectric-constant materials. *Adv. Funct. Mater.* **15**, 823–829 (2005).
53. Hatton, B., Landskron, K., Whitnall, W., Perovic, D. & Ozin, G. A. Past, present, and future of periodic mesoporous organosilicas-the PMOs. *Acc. Chem. Res.* **38**, 305–12 (2005).
54. Van der Voort, P. *et al.* Periodic Mesoporous Organosilicas: from simple to complex bridges; a comprehensive overview of functions, morphologies and applications. *Chem. Soc. Rev.* **42**, 3913–55 (2013).
55. Redzheb, M. A., Bernstorff, S., Sartori, B., Van Der Voort, P. & Armini, S. Periodic Mesoporous Organosilica Films with a Tunable Steady-State Mesophase. *ChemPhysChem* **18**, 2846–2849 (2017).
56. Michalak, D. J. *et al.* Porosity scaling strategies for low- k films. *J. Mater. Res.* **30**, 3363–3385 (2015).
57. Marsik, P., Verdonck, P., De Roest, D. & Baklanov, M. R. Porogen residues detection in optical properties of low-k dielectrics cured by ultraviolet radiation. *Thin Solid Films* **518**, 4266–4272 (2010).
58. Baklanov, M. R., Zhao, L., Besien, E. Van & Pantouvaki, M. Effect of porogen residue on electrical characteristics of ultra low-k materials. *Microelectron. Eng.* **88**, 990–993 (2011).
59. Zhou, H.-C., Long, J. R. & Yaghi, O. M. Introduction to Metal–Organic Frameworks. *Chem. Rev.* **112**, 673–674 (2012).
60. Bétard, A. & Fischer, R. A. Metal–Organic Framework Thin Films: From Fundamentals to Applications. *Chem. Rev.* **112**, 1055–1083 (2012).
61. Stassen, I., De Vos, D. & Ameloot, R. Vapor-Phase Deposition and Modification of Metal-Organic Frameworks: State-of-the-Art and Future Directions. *Chem. - A Eur. J.* **22**, 14452–14460 (2016).
62. Yang, D. & Gates, B. C. Catalysis by Metal Organic Frameworks:

Perspective and Suggestions for Future Research. *ACS Catal.* **9**, 1779–1798 (2019).

63. Li, D., Xu, H.-Q., Jiao, L. & Jiang, H.-L. Metal-organic frameworks for catalysis: State of the art, challenges, and opportunities. *EnergyChem* **1**, 100005 (2019).
64. Bavykina, A. *et al.* Metal–Organic Frameworks in Heterogeneous Catalysis: Recent Progress, New Trends, and Future Perspectives. *Chem. Rev.* **120**, 8468–8535 (2020).
65. Li, H. *et al.* Porous metal-organic frameworks for gas storage and separation: Status and challenges. *EnergyChem* **1**, 100006 (2019).
66. Li, H. *et al.* Recent advances in gas storage and separation using metal–organic frameworks. *Mater. Today* **21**, 108–121 (2018).
67. Stassen, I. *et al.* An updated roadmap for the integration of metal–organic frameworks with electronic devices and chemical sensors. *Chem. Soc. Rev.* **46**, 3185–3241 (2017).
68. Allendorf, M. D., Schwartzberg, A., Stavila, V. & Talin, a A. A roadmap to implementing metal-organic frameworks in electronic devices: challenges and critical directions. *Chemistry* **17**, 11372–88 (2011).
69. Stassen, I. *et al.* Chemical vapour deposition of zeolitic imidazolate framework thin films. *Nat. Mater.* **15**, 304–310 (2016).
70. Cruz, A. J. *et al.* Integrated Cleanroom Process for the Vapor-Phase Deposition of Large-Area Zeolitic Imidazolate Framework Thin Films. *Chem. Mater.* **31**, 9462–9471 (2019).
71. Stassin, T. *et al.* Vapour-phase deposition of oriented copper dicarboxylate metal–organic framework thin films. *Chem. Commun.* **55**, 10056–10059 (2019).
72. Zagorodniy, K., Seifert, G. & Hermann, H. Metal-organic frameworks as promising candidates for future ultralow-k dielectrics. *Appl. Phys. Lett.* **97**, 251905 (2010).

73. Redel, E. *et al.* On the dielectric and optical properties of surface-anchored metal-organic frameworks: A study on epitaxially grown thin films. *Appl. Phys. Lett.* **103**, 091903 (2013).
74. Usman, M. *et al.* Intrinsic low dielectric behaviour of a highly thermally stable Sr-based metal–organic framework for interlayer dielectric materials. *J. Mater. Chem. C* **2**, 3762–3768 (2014).
75. Ryder, M. R. *et al.* Dielectric Properties of Zeolitic Imidazolate Frameworks in the Broad-Band Infrared Regime. *J. Phys. Chem. Lett.* **9**, 2678–2684 (2018).
76. Eslava, S. *et al.* Metal-Organic Framework ZIF-8 Films As Low-κ Dielectrics in Microelectronics. *Chem. Mater.* **25**, 27–33 (2013).
77. Ryder, M. R., Donà, L., Vitillo, J. G. & Civalleri, B. Understanding and Controlling the Dielectric Response of Metal–Organic Frameworks. *Chempluschem* **83**, 308–316 (2018).
78. Tan, J. C., Bennett, T. D. & Cheetham, A. K. Chemical structure, network topology, and porosity effects on the mechanical properties of Zeolitic Imidazolate Frameworks. *Proc. Natl. Acad. Sci.* **107**, 9938–9943 (2010).
79. Wu, H., Yildirim, T. & Zhou, W. Exceptional Mechanical Stability of Highly Porous Zirconium Metal–Organic Framework UiO-66 and Its Important Implications. *J. Phys. Chem. Lett.* **4**, 925–930 (2013).
80. Park, K. S. *et al.* Exceptional chemical and thermal stability of zeolitic imidazolate frameworks. *Proc. Natl. Acad. Sci. U. S. A.* **103**, 10186–91 (2006).
81. Venna, S. R., Jasinski, J. B. & Carreon, M. A. Structural Evolution of Zeolitic Imidazolate Framework-8. *J. Am. Chem. Soc.* **132**, 18030–18033 (2010).
82. Stassen, I. *et al.* Solvent-free synthesis of supported ZIF-8 films and patterns through transformation of deposited zinc oxide precursors. *CrystEngComm* **15**, 9308 (2013).

83. Li, H. & Vlassak, J. J. Determining the elastic modulus and hardness of an ultra-thin film on a substrate using nanoindentation. *J. Mater. Res.* **24**, 1114–1126 (2009).
84. Morris, D. J. & Cook, R. F. Indentation fracture of low-dielectric constant films: Part I. Experiments and observations. *J. Mater. Res.* **23**, 2429–2442 (2008).
85. Morris, D. J. & Cook, R. F. Indentation fracture of low-dielectric constant films: Part II. Indentation fracture mechanics model. *J. Mater. Res.* **23**, 2443–2457 (2008).
86. Holländer, B., Heer, H., Wagener, M., Halling, H. & Mantl, S. New high-precision 5-axes RBS/channeling goniometer for ion beam analysis of 150 mm Ø wafers. *Nucl. Instruments Methods Phys. Res. Sect. B Beam Interact. with Mater. Atoms* **161–163**, 227–230 (2000).
87. Li, H. *et al.* Controlled fracture of Cu/ultralow-k interconnects. *Appl. Phys. Lett.* **103**, 231901 (2013).
88. Ciofi, I., Baklanov, M. R., Tőkei, Z. & Beyer, G. P. Capacitance measurements and k-value extractions of low-k films. *Microelectron. Eng.* **87**, 2391–2406 (2010).
89. Baklanov, M. R., Mogilnikov, K. P., Polovinkin, V. G. & Dultsev, F. N. Determination of pore size distribution in thin films by ellipsometric porosimetry. *J. Vac. Sci. Technol. B Microelectron. Nanom. Struct.* **18**, 1385 (2000).
90. Dauskardt, R. H., Lane, M., Ma, Q. & Krishna, N. Adhesion and debonding of multi-layer thin film structures. *Eng. Fract. Mech.* **61**, 141–162 (1998).
91. Vanstreels, K., Wu, C., Verdonck, P. & Baklanov, M. R. Intrinsic effect of porosity on mechanical and fracture properties of nanoporous ultralow-k dielectrics. *Appl. Phys. Lett.* **101**, 123109 (2012).
92. Li, H., Lin, Y., Tsui, T. Y. & Vlassak, J. J. The effect of porogen loading on the stiffness and fracture energy of brittle organosilicates.

J. Mater. Res. **24**, 107–116 (2009).

93. Grosso, D. *et al.* Fundamentals of Mesostructuring Through Evaporation-Induced Self-Assembly. *Adv. Funct. Mater.* **14**, 309–322 (2004).
94. Lin, Y., Tsui, T. Y., Vlassak, J. J. & Xiang, Y. PECVD low-permittivity organosilicate glass coatings: Adhesion, fracture and mechanical properties. *Acta Materialia* **56**, 4932–4943 (2008).
95. Lin, Y., Vlassak, J. J., Tsui, T. Y. & McKerrow, A. J. Subcritical Delamination of Dielectric and Metal Films from Low-k Organosilicate Glass (OSG) Thin Films in Buffered pH Solutions. *MRS Proc.* **795**, U8.1 (2003).
96. Guyer, E. P. & Dauskardt, R. H. Effect of solution pH on the accelerated cracking of nanoporous thin-film glasses. *J. Mater. Res.* **20**, 680–687 (2005).
97. Guyer, E. P., Patz, M. & Dauskardt, R. H. Fracture of nanoporous methyl silsesquioxane thin-film glasses. *J. Mater. Res.* **21**, 882–894 (2006).
98. Taek-Soo Kim & Dauskardt, R. H. Integration Challenges of Nanoporous Low Dielectric Constant Materials. *IEEE Trans. Device Mater. Reliab.* **9**, 509–515 (2009).
99. Wang, G., Ho, P. S. & Groothuis, S. Chip-packaging interaction: a critical concern for Cu/low k packaging. *Microelectron. Reliab.* **45**, 1079–1093 (2005).
100. Grill, A. PECVD low and ultralow dielectric constant materials: From invention and research to products. *J. Vac. Sci. Technol. B, Nanotechnol. Microelectron. Mater. Process. Meas. Phenom.* **34**, 020801 (2016).
101. Dubois, G. *et al.* Superior mechanical properties of dense and porous organic/inorganic hybrid thin films. *J. Sol-Gel Sci. Technol.* **48**, 187–193 (2008).

102. Ryan, E. T. *et al.* Property modifications of nanoporous pSiCOH dielectrics to enhance resistance to plasma-induced damage. *J. Appl. Phys.* **104**, (2008).

103. Brinker, C. J. Hydrolysis and condensation of silicates: Effects on structure. *J. Non. Cryst. Solids* **100**, 31–50 (1988).

104. Futamura, R., Jorge, M. & Gomes, J. R. B. Role of the organic linker in the early stages of the templated synthesis of PMOs. *Phys. Chem. Chem. Phys.* **15**, 6166–9 (2013).

105. Hatton, B. D. *et al.* Materials chemistry for low-k materials. *Mater. Today* **9**, 22–31 (2006).

106. Krishtab, M., Afanas'ev, V., Stesmans, A. & De Gendt, S. Leakage current induced by surfactant residues in self-assembly based ultralow-k dielectric materials. *Appl. Phys. Lett.* **111**, 032908 (2017).

107. Redzheb, M. *et al.* Effect of the C-bridge length on the ultraviolet-resistance of oxycarbosilane low-k films. *Appl. Phys. Lett.* **108**, 012902 (2016).

108. Lin, Y., Tsui, T. Y. & Vlassak, J. J. Octamethylcyclotetrasiloxane-Based, Low-Permittivity Organosilicate Coatings. *J. Electrochem. Soc.* **153**, F144 (2006).

109. Grandbois, M. How Strong Is a Covalent Bond? *Science (80-.).* **283**, 1727–1730 (1999).

110. Vanstreels, K. *et al.* Effect of Pore Structure of Nanometer Scale Porous Films on the Measured Elastic Modulus. *Langmuir* **29**, 12025–12035 (2013).

111. Yu, H. Y., Sanday, S. C. & Rath, B. B. The effect of substrate on the elastic properties of films determined by the indentation test — axisymmetric boussinesq problem. *J. Mech. Phys. Solids* **38**, 745–764 (1990).

112. Okudur, O. O., Vanstreels, K., de Wolf, I., Hangen, U. & Qiu, A. Substrate Independent Elastic Modulus of Thin Low Dielectric

Constant Materials. *Adv. Eng. Mater.* **19**, 1600653 (2017).

113. Li, H., Knaup, J. M., Kaxiras, E. & Vlassak, J. J. Stiffening of organosilicate glasses by organic cross-linking. *Acta Mater.* **59**, 44–52 (2011).

114. Lake, G. J. & Thomas, A. G. The Strength of Highly Elastic Materials. *Proc. R. Soc. A Math. Phys. Eng. Sci.* **300**, 108–119 (1967).

115. Kirk, J. Fracture Behaviour of Polymers. *Compos. Struct.* **2**, 373–374 (1984).

116. Dauskardt, R. H., Lane, M., Ma, Q. & Krishna, N. Adhesion and debonding of multi-layer thin film structures. *Eng. Fract. Mech.* **61**, 141–162 (1998).

117. Ma, Q. *et al.* Quantitative Measurement of Interface Fracture Energy in Multi-Layer Thin Film Structures. *MRS Proc.* **391**, 91 (1995).

118. Ma, Q. A four-point bending technique for studying subcritical crack growth in thin films and at interfaces. *J. Mater. Res.* **12**, 840–845 (1997).

119. Grill, A., Gates, S. M., Ryan, T. E., Nguyen, S. V. & Priyadarshini, D. Progress in the development and understanding of advanced low k and ultralow k dielectrics for very large-scale integrated interconnects—State of the art. *Appl. Phys. Rev.* **1**, 011306 (2014).

120. Jousseaume, V., Gourhant, O., Gonon, P., Zenasni, A. & Favennec, L. Dielectric Constant of Porous Ultra Low-κ Thin Films. *J. Electrochem. Soc.* **159**, G49 (2012).

121. Urbanowicz, A. M., Vanstreels, K., Shamiryan, D., De Gendt, S. & Baklanov, M. R. Effect of Porogen Residue on Chemical, Optical, and Mechanical Properties of CVD SiCOH Low-k Materials. *Electrochem. Solid-State Lett.* **12**, H292 (2009).

122. Lu, Y. *et al.* Continuous formation of supported cubic and hexagonal mesoporous films by sol–gel dip-coating. *Nature* **389**, 364–368 (1997).

123. Van Der Voort, P. *et al.* Periodic Mesoporous Organosilicas: from simple to complex bridges; a comprehensive overview of functions, morphologies and applications. *Chem. Soc. Rev.* 3913–3955 (2013). doi:10.1039/c2cs35222b
124. Goethals, F. *et al.* Ultra-low-k cyclic carbon-bridged PMO films with a high chemical resistance. *J. Mater. Chem.* **22**, 8281 (2012).
125. Jung, S. B. & Park, H. H. Concentration-dependent mesostructure of surfactant-templated mesoporous silica thin film. *Thin Solid Films* **494**, 320–324 (2006).
126. Jung, S.-B., Ha, T.-J., Seon, J.-B. & Park, H.-H. Phase behavior of ordered mesoporous silica film prepared by Brij-76 block copolymer. *Microporous Mesoporous Mater.* **111**, 188–193 (2008).
127. Volksen, W. *et al.* A Manufacturing Grade, Porous Oxycarbosilane Spin-On Dielectric Candidate with $K \leq 2.0$. *J. Electrochem. Soc.* **158**, G155 (2011).
128. Krishtab, M., de Marneffe, J.-F., De Gendt, S. & Baklanov, M. R. Plasma induced damage mitigation in spin-on self-assembly based ultra low-k dielectrics using template residues. *Appl. Phys. Lett.* **110**, 013105 (2017).
129. Grill, A. & Neumayer, D. A. Structure of low dielectric constant to extreme low dielectric constant SiCOH films: Fourier transform infrared spectroscopy characterization. *J. Appl. Phys.* **94**, 6697 (2003).
130. Finocchio, E., Cristiani, C., Dotelli, G., Stampino, P. G. & Zampori, L. Thermal evolution of PEG-based and BRIJ-based hybrid organo-inorganic materials. FT-IR studies. *Vib. Spectrosc.* **71**, 47–56 (2014).
131. Yariv, S. & Lapides, I. The use of thermo-XRD-analysis in the study of organo-smectite complexes. *J. Therm. Anal. Calorim.* **80**, 11–26 (2005).
132. Miyazaki, H., Kodama, D. & Suzumura, N. The observation of stress-induced leakage current of damascene interconnects after bias

temperature aging. in *2008 IEEE International Reliability Physics Symposium* 150–157 (IEEE, 2008). doi:10.1109/RELPHY.2008.4558877

133. Li, Y. *et al.* Influence of absorbed water components on SiOCH low-k reliability. *J. Appl. Phys.* **104**, 034113 (2008).
134. Kubasch, C., Ruelke, H., Mayer, U. & Bartha, J. W. Leakage Current and Breakthrough Measurements on Moisturized SiCOH. *ECS J. Solid State Sci. Technol.* **4**, N3118–N3121 (2014).
135. Atkin, J. M. *et al.* Photocurrent spectroscopy of low-k dielectric materials: Barrier heights and trap densities. *J. Appl. Phys.* **103**, 094104 (2008).
136. Shamuilia, S. *et al.* Internal photoemission of electrons at interfaces of metals with low-κ insulators. *Appl. Phys. Lett.* **89**, 202909 (2006).
137. Afanas'ev, V. V. *et al.* Electron spin resonance study of defects in low-κ oxide insulators (κ=2.5–2.0). *Microelectron. Eng.* **88**, 1503–1506 (2011).
138. Ren, H. *et al.* Defects in low-k organosilicate glass and their response to processing as measured with electron-spin resonance. *Appl. Phys. Lett.* **98**, 102903 (2011).
139. Pomorski, T. A. *et al.* Defect structure and electronic properties of SiOC:H films used for back end of line dielectrics. *J. Appl. Phys.* **115**, (2014).
140. Brower, K. L. Electron paramagnetic resonance studies of Si-SiO 2 interface defects. *Semicond. Sci. Technol.* **4**, 970–979 (1989).
141. Ren, H., Cheng, S. L., Nishi, Y. & Shohet, J. L. Effects of vacuum ultraviolet and ultraviolet irradiation on ultrathin hafnium-oxide dielectric layers on (100)Si as measured with electron-spin resonance. *Appl. Phys. Lett.* **96**, 192904 (2010).
142. Afanas'ev, V. V. *et al.* High-resolution electron spin resonance analysis of ion bombardment induced defects in advanced low-κ

insulators (κ = 2.0-2.5). *Appl. Phys. Lett.* **102**, 172908 (2013).

143. Voorhees, K. J., Baugh, S. F. & Stevenson, D. N. An investigation of the thermal degradation of poly(ethylene glycol). *J. Anal. Appl. Pyrolysis* **30**, 47–57 (1994).
144. Bockhorn, H., Hornung, A., Hornung, U. & Schawaller, D. Kinetic study on the thermal degradation of polypropylene and polyethylene. *J. Anal. Appl. Pyrolysis* **48**, 93–109 (1999).
145. Mutch, M. J., Lenahan, P. M. & King, S. W. Defect chemistry and electronic transport in low-κ dielectrics studied with electrically detected magnetic resonance. *J. Appl. Phys.* **119**, 094102 (2016).
146. Laidani, N., Bartali, R., Gottardi, G., Anderle, M. & Cheyssac, P. Optical absorption parameters of amorphous carbon films from Forouhi–Bloomer and Tauc–Lorentz models: a comparative study. *J. Phys. Condens. Matter* **20**, 015216 (2008).
147. Powell, R. J. Interface Barrier Energy Determination from Voltage Dependence of Photoinjected Currents. *J. Appl. Phys.* **41**, 2424–2432 (1970).
148. Goodman, A. M. Photoemission of electrons from silicon and gold into silicon dioxide. *Phys. Rev.* **144**, 588–593 (1966).
149. King, S. W., French, B. & Mays, E. Detection of defect states in low-k dielectrics using reflection electron energy loss spectroscopy. *J. Appl. Phys.* **113**, (2013).
150. Baklanov, M. R. *et al.* Plasma processing of low-k dielectrics APPLIED PHYSICS REVIEWS — FOCUSED REVIEW Plasma processing of low-k dielectrics. **041101**, (2013).
151. Lionti, K., Volksen, W., Magbitang, T., Darnon, M. & Dubois, G. Toward Successful Integration of Porous Low-k Materials: Strategies Addressing Plasma Damage. *ECS J. Solid State Sci. Technol.* **4**, N3071–N3083 (2015).
152. Lee, K. H., Yim, J. H. & Baklanov, M. R. Effect of the pore structure

on the properties of nanoporous silsesquioxane thin film. *Microporous Mesoporous Mater.* **94**, 113–121 (2006).

153. Darnon, M. *et al.* Impact of low-k structure and porosity on etch processes. *J. Vac. Sci. Technol. B, Nanotechnol. Microelectron. Mater. Process. Meas. Phenom.* **31**, 011207 (2013).

154. Safaverdi, S., Barkema, G. T., Kunnen, E., Urbanowicz, A. M. & Maes, C. Saturation of front propagation in a reaction diffusion process describing plasma damage in porous low-k materials. *Phys. Rev. B - Condens. Matter Mater. Phys.* **83**, 1–6 (2011).

155. Braginsky, O. V. *et al.* The mechanism of low-k SiOCH film modification by oxygen atoms. *J. Appl. Phys.* **108**, 073303 (2010).

156. Wang, W., Grozea, D., Kohli, S., Perovic, D. D. & Ozin, G. a. Water Repellent Periodic Mesoporous Organosilicas. *ACS Nano* **5**, 1267–1275 (2011).

157. Torres, J. M., Bielefeld, J., Blackwell, J., Michalak, D. J. & Clarke, J. S. Ordered porosity for interconnect applications. in *2016 IEEE International Interconnect Technology Conference / Advanced Metallization Conference (IITC/AMC)* 18–20 (IEEE, 2016). doi:10.1109/IITC-AMC.2016.7507644

158. Bruce, R. L. *et al.* Investigation of plasma etch damage to porous oxycarbosilane ultra low- k dielectric. *J. Phys. D. Appl. Phys.* **46**, 265303 (2013).

159. Posseme, N. *et al.* New fluorocarbon free chemistry proposed as solution to limit porous SiOCH film modification during etching. in *2013 IEEE International Interconnect Technology Conference - IITC* 1–3 (IEEE, 2013). doi:10.1109/IITC.2013.6615591

160. Worsley, M. A. *et al.* Effect of plasma interactions with low-κ films as a function of porosity, plasma chemistry, and temperature. *J. Vac. Sci. Technol. B Microelectron. Nanom. Struct.* **23**, 395 (2005).

161. Espinho, S., Felizardo, E., Henriques, J. & Tatarova, E. Vacuum

ultraviolet radiation emitted by microwave driven argon plasmas. *J. Appl. Phys.* **121**, 153303 (2017).

162. El Otell, Z. *et al.* Vacuum ultra-violet emission of CF4and CF3I containing plasmas and Their effect on low-k materials. *J. Phys. D. Appl. Phys.* **48**, (2015).

163. Tian, P. & Kushner, M. J. Controlling VUV photon fluxes in pulsed inductively coupled Ar/Cl 2 plasmas and potential applications in plasma etching. *Plasma Sources Sci. Technol.* **26**, 024005 (2017).

164. Jang, J. K., Tak, H. W., Shin, Y. J., Kim, D. S. & Yeom, G. Y. Plasma Induced Damage Reduction of Ultra Low-k Dielectric by Using Source Pulsed Plasma Etching for Next BEOL Interconnect Manufacturing. *IEEE Trans. Semicond. Manuf.* **33**, 302–309 (2020).

165. Iacopi, F., Choi, J. H., Terashima, K., Rice, P. M. & Dubois, G. Cryogenic plasmas for controlled processing of nanoporous materials. *Phys. Chem. Chem. Phys.* **13**, 3634 (2011).

166. Zhang, L. *et al.* Damage Free Cryogenic Etching of a Porous Organosilica Ultralow-k Film. *ECS Solid State Lett.* **2**, N5–N7 (2012).

167. Zhang, L. *et al.* Low Damage Cryogenic Etching of Porous Organosilicate Low-k Materials Using SF 6 /O 2 /SiF 4. *ECS J. Solid State Sci. Technol.* **2**, N131–N139 (2013).

168. Chanson, R. *et al.* Damage-free plasma etching of porous organo-silicate low-k using micro-capillary condensation above −50 °C. *Sci. Rep.* **8**, 1886 (2018).

169. Oszinda, T., Schaller, M. & Schulz, S. E. Chemical Repair of Plasma Damaged Porous Ultra Low-κ SiOCH Film Using a Vapor Phase Process. *J. Electrochem. Soc.* **157**, H1140 (2010).

170. Imada, T., Nakata, Y., Ozaki, S., Kobayashi, Y. & Nakamura, T. Systematic investigation of silylation materials for recovery use of low- k material plasma damage. *Jpn. J. Appl. Phys.* **54**, 071502 (2015).

171. Bao, J. J. *et al.* Mechanistic Study of Plasma Damage and CH4

Recovery of Low k Dielectric Surface. in *2007 IEEE International Interconnect Technology Conferencee* 147–149 (IEEE, 2007). doi:10.1109/IITC.2007.382366

172. Bao, J. *et al.* Mechanistic study of plasma damage of low k dielectric surfaces. *J. Vac. Sci. Technol. B Microelectron. Nanom. Struct.* **26**, 219 (2008).

173. Förster, A., Wagner, C., Schuster, J. & Gemming, S. Theoretical investigation of in situ k-restore processes for damaged ultra-low-k materials. *2015 IEEE Int. Interconnect Technol. Conf. 2015 IEEE Mater. Adv. Met. Conf. IITC/MAM 2015* **156**, 29–31 (2015).

174. Köhler, N., Fischer, T., Zimmermann, S. & Schulz, S. E. Experimental investigations on a plasma assisted in situ restoration process for sidewall damaged ultra low-k dielectrics. *2015 IEEE Int. Interconnect Technol. Conf. 2015 IEEE Mater. Adv. Met. Conf. IITC/MAM 2015* 353–355 (2015). doi:10.1109/IITC-MAM.2015.7325598

175. Eslava, S. *et al.* Ultraviolet-Assisted Curing of Polycrystalline Pure-Silica Zeolites: Hydrophobization, Functionalization, and Cross-Linking of Grains. *J. Am. Chem. Soc.* **129**, 9288–9289 (2007).

176. Vansant, E., Van Der Voort, P. & Vrancken, K. *Characterization and chemical modification of the silica surface*. *Characterization and chemical modification of the silica surface* (Elsevier Science, 1995).

177. Jousseaume, V. *et al.* Cu/ULK (k=2.0) integration for 45 nm node and below using an improved hybrid material with conventional BEOL processing and a late porogen removal. in *Proceedings of the IEEE 2005 International Interconnect Technology Conference, 2005.* 60–62 (IEEE, 2005). doi:10.1109/IITC.2005.1499923

178. Jousseaume, V., Favennec, L., Zenasni, A. & Passemard, G. Plasma-enhanced-chemical-vapor-deposited ultralow k for a postintegration porogen removal approach. *Appl. Phys. Lett.* **88**, 182908 (2006).

179. Frot, T. *et al.* Post Porosity Plasma Protection a new approach to

integrate k ≤ 2.2 porous ULK materials. in *2011 IEEE International Interconnect Technology Conference* 1–3 (IEEE, 2011). doi:10.1109/IITC.2011.5940272

180. Zhang, L. *et al.* Improved Plasma Resistance for Porous Low-k Dielectrics by Pore Stuffing Approach. *ECS J. Solid State Sci. Technol.* **4**, N3098–N3107 (2014).

181. Kagawa, Y. *et al.* Robust 45-nm Node Cu/LJLK Interconnects using Effective Porogen Control. in *2006 International Interconnect Technology Conference* 207–209 (IEEE, 2006). doi:10.1109/IITC.2006.1648689

182. Koganti, V. R., Das, S. & Rankin, S. E. In situ FTIR investigation of the kinetics of silica polycondensation in surfactant templated, mesostructured thin films. *J. Phys. Chem. C* **118**, 19450–19461 (2014).

183. Christophorou, L. G. Electron Interactions With CF[sub 3]I. *J. Phys. Chem. Ref. Data* **29**, 553 (2000).

184. de Marneffe, J.-F. *et al.* Vacuum ultra-violet damage and damage mitigation for plasma processing of highly porous organosilicate glass dielectrics. *J. Appl. Phys.* **118**, 133302 (2015).

185. Le, Q. T. *et al.* Removal of Plasma-Modified Low-k Layer Using Dilute HF: Influence of Concentration. *Electrochem. Solid-State Lett.* **8**, F21 (2005).

186. Rakhimova, T. V. *et al.* Interaction of F atoms with SiOCH ultra-low-k films: I. Fluorination and damage. *J. Phys. D. Appl. Phys.* **48**, (2015).

187. Rakhimova, T. V. *et al.* Interaction of F atoms with SiOCH ultra low-k films. Part II: etching. *J. Phys. D. Appl. Phys.* **48**, 175204 (2015).

188. DiMaria, D. J., Weinberg, Z. A. & Aitken, J. M. Location of positive charges in SiO 2 films on Si generated by vuv photons, x rays, and high-field stressing. *J. Appl. Phys.* **48**, 898–906 (1977).

189. Yunogami, T., Mizutani, T., Tsujimoto, K. & Suzuki, K. Mechanism of Radiation Damage in SiO 2 /Si Induced by vuv Photons. *Jpn. J.*

Appl. Phys. **29**, 2269–2272 (1990).

190. Braginsky, O. *et al.* Effects of VUV and EUV Radiation on Ultra Low-k Materials Damage. *MRS Proc.* **1559**, mrss13-1559-aa03-11 (2013).
191. Zotovich, A. *et al.* Comparison of vacuum ultra-violet emission of Ar/CF4 and Ar/CF3I capacitively coupled plasmas. *Plasma Sources Sci. Technol.* **25**, (2016).
192. Velchev, I., Hogervorst, W. & Ubachs, W. Precision VUV spectroscopy of Ar I at 105 nm. *J. Phys. B At. Mol. Opt. Phys.* **32**, L511–L516 (1999).
193. Zhang, S. & Zhu, S. Study of Xenon Discharges for 147 nm Emission. *Phys. Scr.* **66**, 476–479 (2002).
194. Lionti, K., Darnon, M., Volksen, W., Magbitang, T. & Dubois, G. The efficacy of post porosity plasma protection against vacuum-ultraviolet damage in porous low-k materials. *J. Appl. Phys.* **117**, (2015).
195. Becke, A. D. Density-functional thermochemistry. IV. A new dynamical correlation functional and implications for exact-exchange mixing. *J. Chem. Phys.* **104**, 1040–1046 (1996).
196. Lee, C., Yang, W. & Parr, R. G. Development of the Colle-Salvetti correlation-energy formula into a functional of the electron density. *Phys. Rev. B* **37**, 785–789 (1988).
197. Bauernschmitt, R. & Ahlrichs, R. Treatment of electronic excitations within the adiabatic approximation of time dependent density functional theory. *Chem. Phys. Lett.* **256**, 454–464 (1996).
198. Baklanov, M. R., Adelmann, C., Zhao, L. & De Gendt, S. Advanced Interconnects: Materials, Processing, and Reliability. *ECS J. Solid State Sci. Technol.* **4**, Y1–Y4 (2015).
199. Vyas, A. A., Zhou, C. & Yang, C. Y. On-Chip Interconnect Conductor Materials for End-of-Roadmap Technology Nodes. *IEEE Trans. Nanotechnol.* **17**, 4–10 (2018).
200. Prasad, D., Ceyhan, A., Pan, C. & Naeemi, A. Adapting Interconnect

Technology to Multigate Transistors for Optimum Performance. *IEEE Trans. Electron Devices* **62**, 3938–3944 (2015).

201. Ciofi, I. *et al.* Impact of Wire Geometry on Interconnect <italic>RC</italic> and Circuit Delay. *IEEE Trans. Electron Devices* **63**, 2488–2496 (2016).
202. Tokei, Z. *et al.* On-chip interconnect trends, challenges and solutions: How to keep RC and reliability under control. in *2016 IEEE Symposium on VLSI Technology* **2016-Septe**, 1–2 (IEEE, 2016).
203. Frot, T. *et al.* Post Porosity Plasma Protection a new approach to integrate k ≤ 2.2 porous ULK materials. *2011 IEEE Int. Interconnect Technol. Conf.* 1–3 (2011). doi:10.1109/IITC.2011.5940272
204. Zhang, L. *et al.* Integration of porous low- k dielectrics using post porosity pore protection. *J. Phys. D. Appl. Phys.* **49**, 505105 (2016).
205. Sun, Y. *et al.* Stuffing-enabled surface confinement of silanes used as sealing agents on CF4 plasma-exposed 2.0 p-OSG films. *Microelectron. Eng.* **137**, 70–74 (2015).
206. Darnon, M. *et al.* Impact of low-k structure and porosity on etch processes. *J. Vac. Sci. Technol. B Microelectron. Nanom. Struct.* **31**, 011207 (2013).
207. Baklanov, M. R. *et al.* Characterization of Cu surface cleaning by hydrogen plasma. *J. Vac. Sci. Technol. B Microelectron. Nanom. Struct.* **19**, 1201 (2001).
208. Fu, X. *et al.* Advanced Preclean for Integration of PECVD SiOCH (k=2.5) Dielectrics with Copper Metallization Beyond 45nm Technology. in *2006 International Interconnect Technology Conference* 51–54 (IEEE, 2006). doi:10.1109/IITC.2006.1648644
209. Shamiryan, D., Baklanov, M. R. & Maex, K. Diffusion barrier integrity evaluation by ellipsometric porosimetry. *J. Vac. Sci. Technol. B Microelectron. Nanom. Struct.* **21**, 220 (2003).
210. Wang, Y. *et al.* A non-destructive, fast evaluation of PVD diffusion

barriers deposited on porous low-k dielectrics. *Microelectron. Eng.* **198**, 22–28 (2018).

211. Wang, X. *et al.* Study of CoTa alloy as barrier layer for Cu/low- k interconnects. *J. Phys. D. Appl. Phys.* **50**, 405306 (2017).
212. Shamiryan, D., Abell, T., Le, Q. T. & Maex, K. Pinhole density measurements of barriers deposited on low-k films. *Microelectron. Eng.* **70**, 341–345 (2003).
213. Iacopi, F. *et al.* Factors affecting an efficient sealing of porous low- k dielectrics by physical vapor deposition Ta(N) thin films. *J. Appl. Phys.* **92**, 1548–1554 (2002).
214. Zhao, L. *et al.* Study of metal barrier deposition-induced damage to porous low-k materials. *Microelectron. Eng.* **88**, 3030–3034 (2011).
215. Posseme, N., Chevolleau, T., Joubert, O., Vallier, L. & Rochat, N. Etching of porous SiOCH materials in fluorocarbon-based plasmas. *J. Vac. Sci. Technol. B Microelectron. Nanom. Struct.* **22**, 2772 (2004).
216. Rakhimova, T. V *et al.* Low- k films modification under EUV and VUV radiation. *J. Phys. D. Appl. Phys.* **47**, 025102 (2014).
217. Proost, J., Baklanov, M., Maex, K. & Delaey, L. Compensation effect during water desorption from siloxane-based spin-on dielectric thin films. *J. Vac. Sci. Technol. B Microelectron. Nanom. Struct.* **18**, 303 (2000).
218. Bailly, F. *et al.* Roughening of porous SiCOH materials in fluorocarbon plasmas. *J. Appl. Phys.* **108**, 014906 (2010).
219. Pielichowski, K. & Flejtuch, K. Non-oxidative thermal degradation of poly(ethylene oxide): kinetic and thermoanalytical study. *J. Anal. Appl. Pyrolysis* **73**, 131–138 (2005).
220. Krishtab, M., Afanas' ev, V., Stesmans, A. & De Gendt, S. Leakage current induced by surfactant residues in self-assembly based ultralow-k dielectric materials. *Appl. Phys. Lett.* **111**, 32908 (2017).
221. Zhang, L. *et al.* Improved Plasma Resistance for Porous Low-k

Dielectrics by Pore Stuffing Approach. *ECS J. Solid State Sci. Technol.* **4**, N3098–N3107 (2014).

222. Rezvanov, A. *et al.* Pore surface grafting of porous low-k dielectrics by selective polymers. *J. Vac. Sci. Technol. B, Nanotechnol. Microelectron. Mater. Process. Meas. Phenom.* **35**, 021211 (2017).
223. de Marneffe, J.-F. *et al.* Vacuum ultra-violet damage and damage mitigation for plasma processing of highly porous organosilicate glass dielectrics. *J. Appl. Phys.* **118**, 133302 (2015).
224. van Leeuwen, M. E. Derivation of Stockmayer potential parameters for polar fluids. *Fluid Phase Equilib.* **99**, 1–18 (1994).
225. Cheng, Y. *et al.* Effect of moisture on electrical properties and reliability of low dielectric constant materials. *Microelectron. Eng.* **114**, 12–16 (2014).
226. Kim, Y. S. The Influence of Surface Roughness on the Electric Conduction Process in Amorphous Ta[sub 2]O[sub 5] Thin Films. *J. Electrochem. Soc.* **146**, 3398 (1999).
227. Ou, Y. *et al.* Conduction Mechanisms of Ta/Porous SiCOH Films under Electrical Bias. *J. Electrochem. Soc.* **155**, G283 (2008).
228. Suzumura, N. *et al.* A New TDDB Degradation Model Based on Cu Ion Drift in Cu Interconnect Dielectrics. in *2006 IEEE International Reliability Physics Symposium Proceedings* 484–489 (IEEE, 2006). doi:10.1109/RELPHY.2006.251266
229. IEEE International Roadmap for Devices and Systems. Available at: https://irds.ieee.org/roadmap-2017.
230. Steinbrüchel, C. Patterning of copper for multilevel metallization: reactive ion etching and chemical-mechanical polishing. *Appl. Surf. Sci.* **91**, 139–146 (1995).
231. Edelstein, D. *et al.* Full copper wiring in a sub-0.25 μm CMOS ULSI technology. in *International Electron Devices Meeting. IEDM Technical Digest* **4**, 773–776 (IEEE, 1997).

232. Baklanov, M. R. *et al.* Plasma processing of low-k dielectrics. *J. Appl. Phys.* **113**, 041101 (2013).
233. Zhang, L. *et al.* Damage free integration of ultralow-k dielectrics by template replacement approach. *Appl. Phys. Lett.* **107**, 092901 (2015).
234. Josell, D., Brongersma, S. H. & Tőkei, Z. Size-Dependent Resistivity in Nanoscale Interconnects. *Annu. Rev. Mater. Res.* **39**, 231–254 (2009).
235. Wu, F., Levitin, G. & Hess, D. W. Low-Temperature Etching of Cu by Hydrogen-Based Plasmas. *ACS Appl. Mater. Interfaces* **2**, 2175–2179 (2010).
236. Wen, L. *et al.* Direct etched Cu characterization for advanced interconnects. *2015 IEEE Int. Interconnect Technol. Conf. 2015 IEEE Mater. Adv. Met. Conf. IITC/MAM 2015* **7**, 173–175 (2015).
237. Paolillo, S. *et al.* Direct metal etch of ruthenium for advanced interconnect. *J. Vac. Sci. Technol. B* **36**, 03E103 (2018).
238. Kanarik, K. J., Tan, S. & Gottscho, R. A. Atomic Layer Etching: Rethinking the Art of Etch. *J. Phys. Chem. Lett.* **9**, 4814–4821 (2018).
239. Sankaran, K., Clima, S., Mees, M. & Pourtois, G. Exploring Alternative Metals to Cu and W for Interconnects Applications Using Automated First-Principles Simulations. *ECS J. Solid State Sci. Technol.* **4**, N3127–N3133 (2015).
240. Dutta, S. *et al.* Thickness dependence of the resistivity of platinum-group metal thin films. *J. Appl. Phys.* **122**, 025107 (2017).
241. Ahner, N., Schulz, S. E., Blaschta, F. & Rennau, M. Thermal stability and gap-fill properties of spin-on MSQ low-k dielectrics. *Microelectron. Eng.* **84**, 2606–2609 (2007).
242. Oh, H., Kim, J. H. & Jang, J. Narrow gap filling in 25nm shallow trench isolation using highly porous organosilica. *Thin Solid Films* **562**, 166–171 (2014).
243. Batten, S. R. *et al.* Terminology of metal–organic frameworks and

coordination polymers (IUPAC Recommendations 2013). *Pure Appl. Chem.* **85**, 1715–1724 (2013).

244. Sun, Y. *et al.* Impact of Plasma Pretreatment and Pore Size on the Sealing of Ultra-Low- k Dielectrics by Self-Assembled Monolayers. *Langmuir* **30**, 3832–3844 (2014).

245. Farrell, R., Goshal, T., Cvelbar, U., Petkov, N. & Morris, M. A. Advances in Ultra Low Dielectric Constant Ordered Porous Materials. *Interface Mag.* **20**, 39–46 (2011).

246. Zagorodniy, K., Seifert, G. & Hermann, H. Metal-organic frameworks as promising candidates for future ultralow-k dielectrics. *Appl. Phys. Lett.* **97**, 251905 (2010).

247. Usman, M. *et al.* Intrinsic low dielectric behaviour of a highly thermally stable Sr-based metal–organic framework for interlayer dielectric materials. *J. Mater. Chem. C* **2**, 3762 (2014).

248. Yu, S.-S., Yuan, G.-J. & Duan, H.-B. The low dielectric constant and relaxation dielectric behavior in hydrogen-bonding metal–organic frameworks. *RSC Adv.* **5**, 45213–45216 (2015).

249. Usman, M., Mendiratta, S. & Lu, K.-L. Metal-Organic Frameworks: New Interlayer Dielectric Materials. *ChemElectroChem* **2**, 786–788 (2015).

250. Mendiratta, S., Usman, M. & Lu, K.-L. Expanding the dimensions of metal–organic framework research towards dielectrics. *Coord. Chem. Rev.* **360**, 77–91 (2018).

251. Stassen, I. *et al.* Chemical vapour deposition of zeolitic imidazolate framework thin films. *Nat. Mater.* **15**, 304–310 (2015).

252. Lausund, K. B. & Nilsen, O. All-gas-phase synthesis of UiO-66 through modulated atomic layer deposition. *Nat. Commun.* **7**, 13578 (2016).

253. Lausund, K. B., Petrovic, V. & Nilsen, O. All-gas-phase synthesis of amino-functionalized UiO-66 thin films. *Dalt. Trans.* **46**, 16983–

16992 (2017).

254. Bridges, D. W., Baur, J. P. & Fassell, W. M. Effect of Oxygen Pressure on the Oxidation Rate of Cobalt. *J. Electrochem. Soc.* **103**, 614 (1956).

255. Birks, N., Meier, G. H. & Pettit, F. S. Oxidation of pure metals. in *Introduction to the High-Temperature Oxidation of Metals* 75–100 (Cambridge University Press). doi:10.1017/CBO9781139163903.006

256. Tompkins, H. G. & Augis, J. A. The oxidation of cobalt in air from room temperature to 467°C. *Oxid. Met.* **16**, 355–369 (1981).

257. Bekiaris, N. *et al.* Cobalt fill for advanced interconnects. in *2017 IEEE International Interconnect Technology Conference (IITC)* 1–3 (IEEE, 2017). doi:10.1109/IITC-AMC.2017.7968981

258. Nečas, D. & Klapetek, P. Gwyddion: an open-source software for SPM data analysis. *Open Phys.* **10**, 181–188 (2012).

259. Tan, J.-C. *et al.* Exceptionally Low Shear Modulus in a Prototypical Imidazole-Based Metal-Organic Framework. *Phys. Rev. Lett.* **108**, 095502 (2012).

260. Tromans, D. Elastic anisotropy of HCP metal crystals and polycrystals. *Int. J. Res. Rev. Appl. Sci.* **6**, 14 (2011).

261. Hopcroft, M. A., Nix, W. D. & Kenny, T. W. What is the Young's Modulus of Silicon? *J. Microelectromechanical Syst.* **19**, 229–238 (2010).

262. Ciofi, I. *et al.* Improved Methodology for Integrated k -Value Extractions. *IEEE Trans. Electron Devices* **59**, 1607–1613 (2012).

263. Beh, H. *et al.* Quasi-metallic behavior of ZnO grown by atomic layer deposition: The role of hydrogen. *J. Appl. Phys.* **122**, 025306 (2017).

264. Min, Y.-S., An, C.-J., Kim, S.-K., Song, J.-W. & Hwang, C.-S. Growth and Characterization of Conducting ZnO Thin Films by Atomic Layer Deposition. *Bull. Korean Chem. Soc.* **31**, 2503–2508 (2010).

265. Beh, H., Hiller, D., Laube, J., Gutsch, S. & Zacharias, M. Deposition temperature dependence and long-term stability of the conductivity of

undoped ZnO grown by atomic layer deposition. *J. Vac. Sci. Technol. A Vacuum, Surfaces, Film.* **35**, 01B127 (2017).

266. Moyes, R. B. & Roberts, M. W. Interaction of cobalt with oxygen, water vapor, and carbon monoxide - X-Ray and ultraviolet photoemission studies. *J. Catal.* **49**, 216–224 (1977).
267. Rice, D. W. Atmospheric Corrosion of Cobalt. *J. Electrochem. Soc.* **126**, 1459 (1979).
268. Yim, C., Abuzalat, O., Elsayed, M., Park, S. & Kim, S. Rapid Fabrication of Metal–Organic Framework Films from Metal Substrates Using Intense Pulsed Light. *Cryst. Growth Des.* **18**, 6946–6955 (2018).
269. Licitra, C., Bouyssou, R., Chevolleau, T. & Bertin, F. Multi-solvent ellipsometric porosimetry analysis of plasma-treated porous SiOCH films. *Thin Solid Films* **518**, 5140–5145 (2010).
270. Lépinay, M. *et al.* Probing the microporosity of low-k organosilica films: MP and t-plot methods applied to ellipsometric porosimetry data. *Microporous Mesoporous Mater.* **217**, 119–124 (2015).
271. Zhang, K. *et al.* Alcohol and water adsorption in zeolitic imidazolate frameworks. *Chem. Commun.* **49**, 3245 (2013).
272. Yim, C. *et al.* Adsorption and desorption characteristics of alcohol vapors on a nanoporous ZIF-8 film investigated using silicon microcantilevers. *Chem. Commun.* **51**, 6168–6171 (2015).
273. Wang, Z., Wang, H., Mitra, A., Huang, L. & Yan, Y. Pure-Silica Zeolite Low-k Dielectric Thin Films. *Adv. Mater.* **13**, 746–749 (2001).
274. Eslava, S. *et al.* Evidence of Large Voids in Pure-Silica-Zeolite Low-k Dielectrics Synthesized by Spin-on of Nanoparticle Suspensions. *Adv. Mater.* **20**, 3110–3116 (2008).
275. Ortiz, A. U. *et al.* What makes zeolitic imidazolate frameworks hydrophobic or hydrophilic? The impact of geometry and functionalization on water adsorption. *Phys. Chem. Chem. Phys.* **16**,

9940–9949 (2014).

276. Flanigen, E. M. *et al.* Silicalite, a new hydrophobic crystalline silica molecular sieve. *Nature* **271**, 512–516 (1978).

277. Li, Z. J., Li, S., Luo, H. M. & Yan, Y. S. Effects of Crystallinity in Spin-On Pure-Silica-Zeolite MFI Low-Dielectric-Constant Films. *Adv. Funct. Mater.* **14**, 1019–1024 (2004).

278. Eslava, S. *et al.* Characterization of spin-on zeolite films prepared from Silicalite-1 nanoparticle suspensions. *Microporous Mesoporous Mater.* **118**, 458–466 (2009).

279. Yang, L.-M., Ganz, E., Svelle, S. & Tilset, M. Computational exploration of newly synthesized zirconium metal–organic frameworks UiO-66, -67, -68 and analogues. *J. Mater. Chem. C* **2**, 7111–7125 (2014).

280. Redzheb, M. *et al.* On the mechanical and electrical properties of self-assembly-based organosilicate porous films. *J. Mater. Chem. C* **5**, 8599–8607 (2017).

281. Bailey, S. *et al.* Mechanical properties of high porosity low- k dielectric nano-films determined by Brillouin light scattering. *J. Phys. D. Appl. Phys.* **46**, 045308 (2013).

282. Zhou, W. *et al.* Elastic properties of porous low-k dielectric nano-films. *J. Appl. Phys.* **110**, 043520 (2011).

283. Poloni, R. & Kim, J. Predicting low-k zeolite materials. *J. Mater. Chem. C* **2**, 2298–2300 (2014).

284. Tiriolo, R. *et al.* Sub-Micrometer Zeolite Films on Gold-Coated Silicon Wafers with Single-Crystal-Like Dielectric Constant and Elastic Modulus. *Adv. Funct. Mater.* **27**, (2017).

285. Li, Z. *et al.* Mechanical and Dielectric Properties of Pure-Silica-Zeolite Low-k Materials. *Angew. Chemie Int. Ed.* **45**, 6329–6332 (2006).

286. Redel, E., Wang, Z., Walheim, S., Liu, J. & Gliemann, H. On the dielectric and optical properties of surface anchored metal-organic

frameworks : A first study on epitaxial grown SURMOF thin films. (2013).

287. Bundschuh, S. *et al.* Mechanical properties of metal-organic frameworks: An indentation study on epitaxial thin films. *Appl. Phys. Lett.* **101**, 101910 (2012).

288. Zheng, B. *et al.* Theoretical prediction of the mechanical properties of zeolitic imidazolate frameworks (ZIFs). *RSC Adv.* **7**, 41499–41503 (2017).

289. Warmbier, R., Quandt, A. & Seifert, G. Dielectric Properties of Selected Metal–Organic Frameworks. *J. Phys. Chem. C* **118**, 11799–11805 (2014).

290. Bahr, D. F. *et al.* Mechanical properties of cubic zinc carboxylate IRMOF-1 metal-organic framework crystals. *Phys. Rev. B* **76**, 184106 (2007).

291. Zhou, W. & Yildirim, T. Lattice dynamics of metal-organic frameworks: Neutron inelastic scattering and first-principles calculations. *Phys. Rev. B* **74**, 180301 (2006).

292. Sun, Y., Hu, Z., Zhao, D. & Zeng, K. Mechanical Properties of Microcrystalline Metal–Organic Frameworks (MOFs) Measured by Bimodal Amplitude Modulated-Frequency Modulated Atomic Force Microscopy. *ACS Appl. Mater. Interfaces* **9**, 32202–32210 (2017).

293. Titov, K. *et al.* Probing Dielectric Properties of Metal–Organic Frameworks: MIL-53(Al) as a Model System for Theoretical Predictions and Experimental Measurements via Synchrotron Far- and Mid-Infrared Spectroscopy. *J. Phys. Chem. Lett.* **8**, 5035–5040 (2017).

294. Chapman, K. W., Halder, G. J. & Chupas, P. J. Pressure-Induced Amorphization and Porosity Modification in a Metal−Organic Framework. *J. Am. Chem. Soc.* **131**, 17546–17547 (2009).

295. Chuang, W.-C., Wang, C.-W., Chu, W.-C., Chang, P.-Z. & Hu, Y.-C. The fringe capacitance formula of microstructures. *J. Micromechanics*

Microengineering **22**, 025015 (2012).

296. Mendiratta, S. *et al.* Anion-Controlled Dielectric Behavior of Homochiral Tryptophan-Based Metal–Organic Frameworks. *Cryst. Growth Des.* **14**, 1572–1579 (2014).
297. Krokidas, P. *et al.* ZIF-67 Framework: A Promising New Candidate for Propylene/Propane Separation. Experimental Data and Molecular Simulations. *J. Phys. Chem. C* **120**, 8116–8124 (2016).
298. Okudur, O. O., Vanstreels, K., de Wolf, I., Hangen, U. & Qiu, A. Substrate Independent Elastic Modulus of Thin Low Dielectric Constant Materials. *Adv. Eng. Mater.* **19**, 1600653 (2017).
299. Krokidas, P., Castier, M. & Economou, I. G. Computational Study of ZIF-8 and ZIF-67 Performance for Separation of Gas Mixtures. *J. Phys. Chem. C* **121**, 17999–18011 (2017).
300. Nordell, B. J. *et al.* Conquering the Low-k Death Curve: Insulating Boron Carbide Dielectrics with Superior Mechanical Properties. *Adv. Electron. Mater.* **2**, 1–7 (2016).
301. Patterson, J. P. *et al.* Observing the Growth of Metal–Organic Frameworks by in Situ Liquid Cell Transmission Electron Microscopy. *J. Am. Chem. Soc.* **137**, 7322–7328 (2015).
302. Wiktor, C., Meledina, M., Turner, S., Lebedev, O. I. & Fischer, R. A. Transmission electron microscopy on metal–organic frameworks – a review. *J. Mater. Chem. A* **5**, 14969–14989 (2017).
303. Rao, K. V. & Smakula, A. Dielectric Properties of Cobalt Oxide, Nickel Oxide, and Their Mixed Crystals. *J. Appl. Phys.* **36**, 2031–2038 (1965).
304. Capilla, J. *et al.* Characterization of amorphous tantalum oxide for insulating acoustic mirrors. in *2011 Joint Conference of the IEEE International Frequency Control and the European Frequency and Time Forum (FCS) Proceedings* 1–6 (IEEE, 2011). doi:10.1109/FCS.2011.5977833

305. Jong, C.-A., Gan, J.-Y. & Chin, T.-S. Microstructure and Thermal Diffusivity Investigations of RF-Sputtered Tantalum Nitride Films. *Jpn. J. Appl. Phys.* **41**, 5367–5371 (2002).